Myelin disruption and ectopic K_V1 channels in mouse optic nerve axons of cuprizone-induced model of demyelination contribute to aberrant conduction

Thesis submitted for the degree

of

Doctor of Philosophy

by

Bandita Bagchi, B.Sc., M.Sc., B.Ed

Supervised by

Prof. Oliver Dolly

Co-supervised by

Dr. Saak V Ovsepian

International Centre for Neurotherapeutics

Dublin City University

Ireland

January 2013

Declaration

I hereby certify that this material, which I now submit for assessment on the programme of study leading to the award of Doctor of Philosophy is entirely my own work, and that I have exercised reasonable care to ensure that the work is original, and does not to the best of my knowledge breach any law of copyright, and has not been taken from the work of others save and to the extent that such work has been cited and acknowledged within the text of my work.

Signed: _____ (Candidate) ID No.: 58102817 Date: _____

Acknowledgements

First and foremost, my thanks go to Prof. J. Oliver Dolly for his invaluable guidance through all the phases of my research. I would also like to thank him for giving me the opportunity to undertake an interesting project and for nurturing my thoughts.

As an overseas postgraduate student of Dublin City University, I would like to acknowledge PRTLI–IV funding through Higher Education Authority under Targeted Therapeutics and Theranostics (T3) program for the excellent opportunity to conduct research. Special thanks to Dr Saak Ovsepian for conceiving, executing and interpreting the functional recordings of compound action potential for this study. Thanks to all colleagues at ICNT, present and past for their encouragement, support and co-operation. I appreciate the constructive and discerning inputs provided by Drs Gary Lawrence, Marie LeBere-Mostert, Liam O'Hara, Ahmed Al sabi, Jiafu Wang, Jianghui Meng, Tom Zurawski and Dimitri Scholz (UCD). Special thanks to Tiina Toivonen and Cormac O' for their help.

My sincere gratitude to Ms Carolyn Wislon, Gillian O' Meara, Catherine Hagedorn, Dr Neal Lemon and Mr Peter Nowlan, without whom, it would not have been possible to carry out the animal work for this project.

Not to forget, my colleagues and friends Sharon Whyte, Sanjay Boddul and Marie O' Connell, with whom I have shared several special moments and their support made it possible to submit this thesis, even after having left Dublin. Thanks to the long list of people who kept me inspired and going during the difficult days. Deep regards to my parents, who have always had tremendous faith in my capabilities and have been a constant source of enthusiasm. Support from all my family members, especially my dear husband, who made it possible for me to stay away from home and pursue my interest.

Publication and presentations

Publication

Bandita Bagchi, Saak Ovsepian, Ahmed Al-Sabi, Seshu Kaza, Valerie O'Leary, D.Scholz, J Oliver Dolly, Axonal Changes and Ectopic K_v1 Channels Contribute to Temporal Dispersion of Compound Action Potentials and Reduced Excitability of Mouse Optic Nerve in a Cuprizone-Induced Model of Demyelination (Manuscript submitted).

Oral Presentations

Bandita Bagchi, Exploiting a unique K_v1 channel in multiple sclerosis, Biannual external review by the funding agency, Dublin City University, Dublin, Ireland, 16th June 2010.

Bandita Bagchi, Dimitri. Scholz, J.Oliver Dolly, K_v1 expression in neurofilament aberrant optic nerve axons of a multiple sclerosis murine model, Neuroscience Ireland 2011, National University of Ireland, Maynooth, Ireland. September 1st - 2nd 2011. **(Oral presentation, poster and abstract)**

Posters

Bandita Bagchi, Saak Ovsepian, J.Oliver Dolly, K_v1 channels as therapeutic targets in multiple sclerosis and other demyelinating diseases, SFI meeting, Dublin City University, Dublin, Ireland, 20th October 2009.

Bandita Bagchi, Saak Ovsepian, Dimitri Scholz, J.Oliver Dolly, Axonal K_v1 channel as a therapeutic target for multiple sclerosis, pharmaceutical and Pharmacological Sciences Research Day, Dublin City University, Dublin, Ireland, 11th January 2011.

List of abbreviations

3, 4 DAP, 3, 4 Diaminopyridine

AHP, After hyperpolarization

4-AP, 4 aminopyridine

8W, 8 week time point

8W+, Post 8 week time point (within 9 weeks)

ACSF, Artificial cerebrospinal fluid

APC, Adenopolymatous-supressor polyposis coli

ASPET, American Society for Pharmacology and Experimental Therapeutics

AU, Arbitrary unit

BRU, Bio-Resource Unit

BSA, Bovine serum albumin

BCA, Bicinchoninic acid

Caspr, Contactin associated protein

CA, Cornu ammonis

CAP, Compound action potential

CCx, Cerebellar cortex

CDMS, Clinically definite MS

CM, Cerebellar marrow

CNPase, 2'3'-Cyclic nucleotide 3' phosphodiesterase

CNS, Central Nervous System

CSF, Cerebrospinal fluid

CSPD, Disodium 3-(4-methoxyspiro 1,2-dioxetane-3,2'-(5'- chloro)tricyclo[3.3.1.13,7] decan-4-yl) phenyl phosphate

Cx, Connexin

CV, Cresyl violet

CZ, Cuprizone

DIV, Days in vitro

DRG, Dorsal root ganglion

DTXk, Dendrotoxin-K

DTT, Dithiothreitol

EAE, Experimental allergic encephalomyelitis

ECL, Enhanced chemiluminescence

EDTA, Ethylenediamintetracetic acid

EGTA, Ethylene glycol bis (β-aminoethyl ether)-N,N,N',N'-tetraacetic acid

E_k: Equilibrium constant

ELISA, Enzyme linked immunosorbent assay

ER, Endoplasmic reticulum

EU, European Union

FF, Floating fraction

gK, Membrane conductance

GL, Grannule layer

GM, Grey matter

GPI, Glycosyl-phosphatidyl inositol

GST, Glutathione- S- transferase

HBSS, Hanks buffered salt solution

HGNC, HUGO Gene nomenclature committee

HUGO, Human Genome Organization

IF, Immunofluorescence

IHC, Immunohistochemistry

IN, Interpositous nucleus

IP, Immunoprecipitation

IPL, Intra-period line

IUPHAR, International Union of Pharmacology

JXP, Juxtaparanode

K_v, Voltage-gated K^+ channel

KCN, K^+ channel nomenclature

KSP, Lysine-serine-proline

LCN, Lateral cerebellar nucleus

LFB, Luxol fast blue

MAG, Myelin associated glycoprotein

MBP, Myelin basic protein

MCN, Medial cerebellar nucleus

MDL, Major dense line

ML, Molecular layer

MOG, Myelin oligodendrocyte glycoprotein

MRI, Magnetic resonance imaging

MS. Multiple sclerosis

NAA, N-acetlyaspartate

NAWM, Normal appearing white matter

Na_v, Voltage gated Na^+ channel

NF, Neurofilament

NFH, Neurofilament heavy chain

NrCAM, Neuronal cell adhesion molecule

NFM, Neurofilament medium

ON, Optic nerve

PBS, Phosphate buffered saline

PCR, Polymerase chain reaction

PFA, Paraformaldehyde

PL, Purkinje layer

PLA, Proximity ligation assay

PLP, Proteolipid protein

PMSF, Phenylmethylsulfonyl fluoride

PNS, Peripheral Nervous System

RCA, Rolling circle amplification

RCK, Rat cortex K^+ channel

REC, Review Ethics Committee

RGC, Retinal ganglion cell

RLU, Relative luminescence unit

RRPMS, Remitting relapsing phase of MS

ROI, Region of interest

SDS-PAGE, Sodium dodecyl sulfate polyacrylamide gel electrophoresis

SLI, Schmidt-Lanterman incisures

SMI, Sternberger Monoclonals Inc.

T, Cuprizone treated

T1, 8 week CZ treatment

T2, 9 week CZ treatment

TAG, Transient axonal glycoprotein

TD, Trypsin DNase

TEA, Tetraethylammonium

TEM, Transmission electron microscopy

TM, Transmembrane

TsTX-K, Tityustoxin-K

UT, Untreated control

VEP, Visually evoked potential

VGIC, Voltage-gated-like ion channels

WB, Western blot

WM, White matter

List of units

µM, micromolar

kD, kilodalton

mA, milliampere

mM, millimolar

mV, millivolt

µm, micrometer

nm, nanometer

mm, millimeter

MΩ, megaohm

Hz, hertz

kHz, kilohertz

Table of contents

List of figures

List of tables

Abstract

Aim: Inhibition of K^+ efflux through voltage-activated K^+ channels (K_v) in demyelinated nerves can overcome conduction block in axons; hence, this approach should offer therapeutic potential for multiple sclerosis (MS). Use of 4-aminopyridine (4-AP), an indiscriminate K_v blocker, has proved effective but with adverse epileptogenic effects due to off-site actions. Identification of a specific homo-tetrameric $K_v1.1$ channel in MS autopsies (Dolly, unpublished) opened up a promising avenue for pursuing, effective therapeutic options. Hence, this study aimed to establish 'MS like' features in an animal model, so that CNS axonopathy and the role of K_v1 channels in the dysfunction could be explored.

Results: Sub-chronic, systemic demyelination in the central nervous system (CNS) was induced in young adult mice, by feeding a moderate dose of cuprizone (bis-cyclohexanone oxaldihydrazone) (CZ), to establish a model with several features closely related to human MS. Robust loss of myelin was produced and clearly documented in anatomically-identified regions (Corpus callosum and limbic areas). Disruption of myelin membrane periodicity was one of the main demyelinating features of optic nerve (ON) axon, elucidated by transmission electron microscopic analysis of its ultrastructure. In addition, an apparent activation of glial cells and increased levels of hypo-phosphorylated neurofilament, were implicated. This type of demeylination was marked by perturbed levels of lipophilin like proteolipid protein (PLP) and its variant DM20. A relative decrease in their ratio (PLP/DM20) in CNS myelin was observed after CZ treatment. Presence of three K_v1 α-subunits - $K_v1.1$, 1.2 and 1.4 in the ON of both the untreated and treated group was confirmed, with $K_v1.1$ and 1.2 α-subunits forming the major juxtaparanodal (JXP) component. Fluorescence microscopic analysis of K_v1 subunits and nodal voltage-gated sodium (Na_v) channels showed a notable alteration in apposing JXPs adjoining the nodal gap. Expression of K_v and Na_v channel became ectopic after CZ treatment. K_v channels were prevalent in internodal areas of the affected axons, whereas the remaining intact JXPs showed decreased content of $K_v1.2$ relative to 1.1 close to the nodal gap, indicating acquisition of atypical role by these two α-subunits. Compound action potentials based

pharmacological analysis using K^+ channel blockers like 4-AP and tetraethylammonium showed an increase in K^+ conductance. Application of $K_v1.1$ and 1.2-specific inhibitors namely dendrotoxin-K and tityustoxin-K further indicated an increase in $K_v1.1$-mediated currents, raising the possibility of emergence of oligomers having higher numbers of $K_v1.1$ than $K_v1.2$ α-subunit.

Conclusions: Taken together these results provide explicit evidence for the applicability of this murine model of CZ-induced systemic CNS demyelination in MS research. ON was demonstrated to have several features similar to MS associated axonopathy, which included loss of myelin periodicity, elevated levels of hypo-phosphorylated neurofilament, reduced lipophilin ratio (PLP/DM20), ectopic expression pattern of JXP K_v1 and nodal Na_v channels leading to a functional deficit largely mediated by $K_v1.1$ containing α-subunit.

CHAPTER 1

GENERAL INTRODUCTION

1.1. Axon organization

Axons are slender neuronal processes, which possess molecular specializations for generating and propagating nerve impulses; thus these are indispensible units integral for the promotion and survival of nervous system (Kandel et al., 1991, Siegel, 2005, Squire et al., 2008). These can be myelinated or unmyelinated, depending on the presence or absence of myelin, a dielectric (electrically insulating) material (Kandel et al., 1991, Squire et al., 2008, Waxman, 2005) wrapped along the axon. Myelin sheath is a compacted membrane stack of glial cells namely oligodendrocytes or Schwann cells, in the central and peripheral nervous systems, respectively. It helps regulate the development, anatomy, and molecular differentiation of an axon into node, paranode, juxtaparanode, and internode **(**Figure 1**)**. These structural specializations isolate segments of an axon into electrically defined compartments so that a fast mode of impulse propagation known as saltatory conduction becomes possible in myelinated axons. Several axons packed densely as an isolated structure form a nerve. Myelinated fibers have evolved to provide the body with a rapid and efficient transfer of information from peripheral receptors to the central nervous system (CNS) (afferent), from the CNS to peripheral effectors (efferent), and between different centers within the CNS. Myelin associated trophic support of these axons is derived from their interaction with the glial cells **(Figure 1, Figure 2B).** For example, CNS oligodendrocytes synthesize and maintain myelin sheaths for up to 40 neighboring axons, whereas one PNS Schwann cell is responsible for myelination of one axon/axonal internode segment (Siegel, 2005). These axons can vary in diameter owing to the extent of myelination (Squire et al., 2008, Chomiak and Hu, 2009). Such features are of great significance as it allows them to maintain their ability to generate and propagate repetitive

nerve impulses at a high speed. Thus, CNS coordination largely depends on the myelinated axons—a highly complex biological structure, which has been characterized as ". . . the most unique cytological feature in the animal kingdom . . ." (Schnapp and Mugnaini, 1978, Waxman, 2005).

1.1.1. Structural sub-domains of an axon and its segregation into compartments

The structure of CNS axons is less well understood relative to PNS myelinated axons, though knowledge of the former is vital for analyzing the functional deficits arising due to axonal dysfunction in diseases, like multiple sclerosis (MS). Both types of axons have structural similarities and they (motor axons, preganglionic autonomic axons, primary sensory axons) course uninterrupted from the CNS to the PNS or vice versa. This continuous and efficacious interaction between nerves is vital for fidel functioning in the nervous system. The intricate association between neuronal axon and glial myelin are key to their maintenance (Waxman, 2005).

Owing to alliance between the two cells, namely myelinating glia and neuron, myelin is a specialized compact layer of membranes which segregates the axon into several cytoplasmic domains. Electron microscopically, myelin has several alternating electron-dense and electron-lucent layers. The major dense line (MDL) or period line is formed where the cytoplasmic surfaces of the plasma membrane spiraling oligodendrocyte / Schwann cell processes appose. The fused outer leaflets facing the extracellular space form intraperiod line (IPL), or minor dense line, which is sometimes split. Longitudinally, a myelinated axon is also organized into several repetitive segments. Each of these segments has domains of unique structure containing molecular complex (es).

1.1.1.1. Myelin (glial membrane stack)

The condensed myelin spiraled around axon, forming an insulation sheath for the segmented domains required for saltatory (fast mode) conduction **(Figure 2A)** (Brazhe et

al., 2011, Debanne, 2004, Devaux and Gow, 2008), was earlier viewed as rudimentary amorphous stack of lipid bilayers. However, its biophysical properties were later recognized as an insulator with high resistance and low capacitance of large diameter fibers common to PNS. This notion falls short in accounting for the small myelinated axons that are widely distributed in the CNS, specifically optic nerve. The CNS axons face a greater constraint in terms of space limitation, energy utilization and information processing. Further on, cis- and trans- protein interactions of the myelin membrane are vital for maintaining of axon function; which are being noted to be different in CNS and PNS (Ogawa et al., 2010, Arroyo et al., 2001).

Owing to axo-myelin interactions, the compact myelin deprives the axoplasm of free access to nutrients in the extracellular milieu, except for widely spaced short gaps (nodes of Ranvier). The encapsulated axons reside in a milieu conditioned by the glia that can, thereby, support axonal energy metabolism. Non-compacted myelin forms a channel system that is continuous with the glial cytoplasm and brings metabolites close to the periaxonal space. Locally, the Schmidt-Lanterman incisures (SLIs) of non-compacted myelin in PNS spiraled around the axon is linked by gap junctions in these stacks. CNS oligodendrocytes are also coupled by gap junctions to astrocytes that extend to the blood-brain barrier. In addition to simple diffusion, cytosolic perfusions attenuate concentration differences of metabolites with high axonal turnover. Similar to fast axonal transport, glial intercellular transport depends on the tubular tracks and fine architecture of this type of channel system. For the postulated transfer of metabolites across the internodal axon, the adjacent glial and axonal compartments may function as a counter-current system. This axo-glial association is highlighted in disorders wherein metabolite fuelling of mitochondria by glia is hampered leading to axonal swellings in oligodendrocyte-specific defects, such as multiple sclerosis (MS) **(Figure 1, Figure 2B)** (Nave, 2010a, Nave, 2010b).

1.1.1.2. Axolemma (axon membrane)

The axolemmal membrane (8nm thick) on the other hand has proteins organized in clusters responsible for flow of ions mainly K^+ and Na^+ which maintains segregation of ionic gradient within the sub-compartments, entailing potential difference. These are known as ion channels and transporters. Energy dependent ion transporters or pumps utilize adenosine tri-phosphate (ATP) to restore the ionic gradient following generation of an action potential **(Figure 3).**

1.1.1.3. Axon cytoskeleton

Axon cytoskeleton provides the basic framework for maintenance of neuron cable essential for propagation and processing of information. This includes structures like microtubules, neurofilaments and microtrabecular matrix. Longitudinally microtubules are 25-nm thick, unbranched discontinuous tubes. A major function of microtubules is to provide tracks for fast anterograde transport, mediated by kinesin, and fast retrograde transport mediated by dynein (Nave, 2010a, Berthold and Rydmark, 1995, Alberts et al., 2002). Neurofilaments (a type of intermediate filament) are the major neuron-specific cytoskeletal element, which are 10nm unbranched stable fibers. There are 150-300 neurofilaments/μm^2 axoplasm irrespective of the axon size. Three types of NF protein (NF-L, ~68 kD; NF-M, ~150 kD; NF-H, ~200 kD) co-assemble into heteropolymers *in vivo*. The NF are linked together by protein cross-bridges contributing to the tensile strength of an axon and accounting for the regular inter-filament spacing (Alberts et al., 2002). Myelination promotes axon radial growth by promoting an accumulation of NFs due to induced phosphorylation (Lunn et al., 2002, Yabe et al., 2000, Waxman, 2005).

1.1.1.4. Nodes of Ranvier

Successive myelin sheaths are separated by short gaps the 'nodes of Ranvier', where the axolemma is exposed to the extracellular space over a length **(Figure 1, Figure 2A)**. It remains juxtaposed to the astrocytic processes. Nodal axolemma exhibits a distinct Na^+ channel immuno-reactivity and a high binding of their probe, saxitoxin (Waxman, 2005).

The node of Ranvier is characterized by regularly spaced, short gaps in the myelin sheath where voltage-dependent Na^+ channels (Na_v) are clustered at high density. These mediate the inward Na^+ currents responsible for the depolarization of nodal membrane and propagation of the action potential (Hille, 2001, Rasband, 2004).

1.1.1.5. Paranode

Nodes are flanked by two paranodes, where the myelin lamellae attach to the axolemma. Some previous investigators, including Ranvier himself, used the term 'paranode' to describe a longer part of the myelin sheath, including both the paranodal myelin attachment zones and the juxtaparanode. Longitudinally, each myelin lamella terminates as a lateral loop **(Figure 2B).** Here, the MDL splits and forms a membrane-bound drop shaped cytoplasmic compartment containing few microtubules, occasional vesicle(s) and varying amounts of electron-dense particles. Since each loop occupies a specific length, the paranodal axon allows direct apposition of a limited number of loops. Relative to the unspecialized internodal part of the axon, the paranodal part is slightly constricted in thin fibers. The paranodal junction is not tight in the conventional sense since small tracer molecules, but not larger ones, can reach the periaxonal space from the node gap (Waxman, 2005)**.** The nodal gap and the periaxonal space (space in between the axolemma and myelin membrane) seem to be connected by a narrow helical channel. Overall, the paranode has been attributed to a variety of functions: a) to anchor myelin lateral loops to the axon, b) to form a partial diffusion barrier from the node gap into the periaxonal space, c) to demarcate axonal domains by limiting lateral diffusion of membrane components, d) to be a site for signaling between axons and myelinating glial cells, and/or to play an active role in the ion exchange underlying saltatory conduction (Schnapp and Mugnaini, 1978, Peles and Salzer, 2000). Thus, these paranodes form the largest junction adhesion complex in vertebrates (Waxman, 2005, Rasband, 2004, Rosenbluth, 1995) with several functional attributes.

1.1.1.6. Juxtaparanode

Finally, just inside the innermost axoglial junction of the paranode is a 5–15µm-long domain called the juxtaparanode (JXP), which is characterized by the high-density

clustering of voltage-gated K^+ channels (K_v), specifically K_v1 subtype **(Figure 2A)** (Chiu and Ritchie, 1980, Wang et al., 1993, Rasband, 2004). In a thick myelinated PNS axon, this region extends some 35µm in an abnodal direction from the paranodes (Waxman, 2005). Their restricted and concealed localization underneath the myelin membrane is vital for action potential propagation. This is essentially due to the high density of K_v1 channels that aggregate in proximity to the node, on the axolemmal surface of JXP. This together with the nodal Na_v form small structural units spaced at regular intervals along the axon, which are vital for action potential propagation. These axolemmal proteins lodged in segregated compartments work in co-ordination to ensure effective information propagation **(Figure 2).**

1.1.1.7. Internode

The segment of a myelinated axon extending between the JXPs is known as internode. However, this term is more appropriately used to define the entire myelin sheath covered stretch of an axon **(Figure 1, Figure 2).** These segments are sometimes referred as unspecialized sections of an axon. They have CNS myelin sheath separated from the axolemma by a space, namely the intra-myelinic periaxonal space of at least 12nm. In myelinated PNS axons, the inner aspect includes a thin cytoplasmic lamella terminating in a small inner loop that is part of the inner mesaxon. Whereas in the oligodendroglia cytoplasm is associated with the outer aspect of internodal segment of myelin sheath, and limited to a small outer tongue and the outer mesaxon of thin myelinated CNS axons (Hirano and Llena, 1995).

1.1.2. Functional organization of an axon

The described structural organization of a myelinated axon is vital for coordinated functioning of the nervous system. An axon is a cable like structure with segregated ionic sub-compartments containing molecularly differentiated domains (Waxman, 2005). Patho-mechanisms perturb these structural elements which are reflective of hindered electrotonic properties affecting the spread of electric current generated by ionic changes (Rash, 2010).

In MS such functional deficits produce symptoms early on, but the structural co-relate remains undetected due to the inability to discriminate using currently available diagnostic tools (Compston and Coles, 2002). In unmyelinated axon, which lack such defined compartments, the conduction is slow and energy consumption less relative to the myelinated axons **(Figure 2, Figure 5, Figure 6).** Axo-myelinic associations in a myelinated axon of the nervous system allow segregation of potassium (K^+) and sodium (Na^+) along an axon **(Figure 1, Figure 6).** The reliable expression of axolemmal proteins like ion channels: voltage-gated K^+ channel (K_v) and voltage gated Na^+ channels (Na_v), and sodium-potassium transporters: Na^+/K^+ pump known as Na^+/K^+ ATPase, allow the generation of potential difference due to the ionic gradient across the membrane length **(Figure 3, Figure 4, Figure 5).** Synchronous and energy-dependent activity of these structural elements is the basis of information propagation along an axon in the form of action potentials. Myelin wrap produce the requisite insulation against leak of ions, between the axon sub-compartment or amongst the adjoining axons (ephaptic cross-talk).

These facts emphasize that axolemma and myelin are equal contributors towards the conduction of information. The daunting task of conducting nerve impulses is achieved by the axon owing to a constant delivery of organelles of their respective site of functioning and turnover of metabolites. Thus major consumption of ATP is entailed. Owing to this energy demand by myelinated axons, recent studies have advocated the transport, distribution and function of axonal mitochondria as a part and parcel of its functioning (Kiryu-Seo et al., 2010). Additionally, energy demand is also levied on the insulating myelin membranes in fast conducting axons. These features indicate that myelin assisted trophic support is essential for long-term axon survival, specifically when axon performs with an increased velocity or frequency of conduction (Trapp and Nave, 2008).

1.2. Action potential propagation and ion channels

Action potential was first demonstrated by Alan Hodgkin and Andrew Huxley in squid axons in 1939 when they showed that they are electrically polarized at a resting phase. The

membrane exhibits a resting potential of -60mV inside versus outside. Generation of action potential involves removal of the polarized state of the membrane (referred as depolarization) and a rapid swing toward, and even past -0mV. Depolarization is followed by another rapid swing the repolarization of membrane potential to more negative values, a process referred to as hyperpolarization. The membrane potential following an action potential typically becomes more negative than the original value of -60mV and this period of increased polarization is referred to as the after-hyperpolarization (AHP) or the undershoot (Squire et al., 2008) **(Figure 4).**

For a human neuron, the resting potential is -70mV. Action potential generation involves a co-ordinated sequence of events:

1. First response to a stimulus leads Na_v channels of the node to be activated and Na^+ flows inside the cell. If the inflow of Na^+ is sufficient to drive the interior potential from -70mV up to -55mV, then action threshold is achieved
2. Action threshold allows more Na_v channels to open and Na^+ influx drives the interior of the cell membrane up to about +30mV leading to depolarization. This stimulates deactivation of already activated Na_v channels.
3. Gradually all the inactivated Na_v channels close and K_v channels open in response to depolarization in order to repolarize the membrane. Since the K_v channels are much slower to open (slow activating) the depolarization peak is achieved and both Na_v and K_v channels remain open in response to these ionic influx. This synchronized activity of both the channels drives the system towards neutrality.
4. Gradually as the K_v channels remain open, the membrane begins to repolarize back towards its resting potential.
5. This repolarization typically overshoots the resting potential even up to -90mV in many cases. Even though this hyperpolarization would seem to be counter productive, it is actually important in the transmission of information. Hyperpolarization prevents the neuron from receiving another stimulus during this time, or at least raises the threshold for any new stimulus. Part of the importance of hyperpolarization is in preventing any stimulus already sent up an axon triggering

another action potential in the opposite direction. In other words, hyperpolarization assures that the signal proceeds in one direction.

6. After hyperpolarization, the Na^+/K^+ATPase pump eventually brings the membrane back to its rest state of -70mV. For every 3 Na^+ pumped out 2 K^+ is pumped into the neuron and an ATP is hydrolysed and this equals to 2/3 energy expenditure in a neuron **(Figure 3)** (Charand, 2012) (http://hyperphysics.phy-astr.gsu.edu/hbase/biology/actpot.html) accessed on 1st May 2012.

Thus, the two principal mechanisms which allow K^+ to cross the axolemma involve transporters and ion channels, which work in conjunction with several enzymes, cell adhesion molecules and myelin membrane proteins. For K^+ to be transported against its electrochemical gradient the expenditure of energy is supplemented by the ATP hydrolysis or from the electrochemical gradient of another ion. The Na^+/K^+ATPase pump achieves this transport of K^+ at a lower rate in order to maintain the resting concentration gradient across the neuron membrane. Ion channels on the other hand permit ions to flow across the membrane at a much higher rate and can thus affect the membrane potential of the cell rapidly. Ion channels do not permit the flow of ions when they are not activated, i.e., when they are in the resting condition. Instead they need to receive a physical or chemical activating stimulus to change the conformation of their pore region to permit ion flow (Squire et al., 2008).

With such operations in place and special ionic buffering, owing to the presence of myelin membrane and astrocyte (a glial cell type), they maintain precise internal concentrations of Na^+, K^+, Cl^-, and Ca^{2+} **(Figure 3)**. At a membrane potential, when there is no net flow of K^+ (the same number of K^+ enters and leave the cell per unit time) these ions are said to be in equilibrium (E_k) and is referred as equilibrium potential. The equilibrium potential is determined by:

1) concentration of ion inside and outside the cell,
2) temperature of the solution,
3) valence of the ion, and
4) amount of work required to separate a given quantity of charge.

The equation that describes the equilibrium potential was formulated by a German physical chemist Walter Nernst in 1888. According to Nernst equilibrium potential

$$E_{ion} = RT/zF.In([ion]_o/[ion]_i)$$

Here,

E_{ion} = membrane potential at which the ion species is at equilibrium,

R = gas constant (8.315J per Kelvin per mole ($JK^{-1}mol^{-1}$),

T = temperature in Kelvin (T_{kelvin}-273.16+$T_{celcius}$),

F = Faraday's constant [96,485 coulombs per mole ($Cmole^{-1}$)]

z = the valence of the ion

$[ion]_o$= concentration of ion outside the cell

$[ion]_i$ = concentration of ion inside the cell

The concentration of $[K^+]_o$ and $[K^+]_i$ in mammalian neurons and glial cells is 3.1mM and 140mM respectively, hence the equilibrium constant at the body temperature T = 37ºC is

$$E_k = 61.5 \log_{10} (3.1/140) = -102mV$$

At membrane potentials positive to -102mV, K^+ flow across the membrane (i.e., increasing the conductance of the membrane to K^+ (gK) causes the membrane potential to become negative, or hyperpolarized, due to the exit of positively charged ions from inside the cell. At membrane potentials negative to -102mV, K^+ tend to flow into the cell; increasing the gK causing the membrane to become more positive, or depolarized, due to the flow of positive charge into the cell. The specific membrane potential at which net current "flips" direction is referred as reverse potential (Squire et al., 2008).

Global functioning of the nervous system is dependent on the synchronized activity of ion channels and action potentials which serve a very different function in neuronal cell bodies, where they encode information in their frequency and pattern, than in axons, where they serve primarily to rapidly propagate signals over distance. So, the precise location of these ion channels with different functional attribute is vital for the fine tuning of a neuron, which

is an important aspect of neuro-modulation. Most neuronal cell bodies (in both vertebrate and invertebrates) can fire over a far wider range of frequencies and can respond to small changes in input currents with significant changes in firing frequency. This richer firing behavior depends on the expression of more types of voltage-dependent ion channels. There has been a gradual realization of just how many distinct voltage-dependent conductances are expressed by individual neurons in the mammalian brain — commonly including

- 2 or 3 types of Na^+ current,
- 4 or 5 different voltage-dependent calcium (Ca^{2+}) currents,
- at least 4 or 5 different voltage-activated K^+ currents,
- at least 2 to 3 types of calcium-activated K^+ currents,
- the hyperpolarization-activated current *I*h, and others

Because of this complexity, our understanding of how different conductances interact to form the action potentials of even the best-studied central neurons is still incomplete (Debanne, 2004). Such synchronized activity of several factors lead to appropriate functioning of a nerve and any breach owing to the emergence of an ectopic component leads to disruption of a well established neural code. In diseases like MS where demeylination occurs which, in turn affects various aspects of the neural network, rift of normative function(s) is eminent. As nerves are made of several thousands of axons, enwrapped in layers of connective tissue, the algebraic sum of their action potentials is referred as compound action potential (Patten et al., 1999). Each nerve has a characteristic CAP feature and demyelination affects it variously (Gordon et al., 1988). Optic nerve is the most susceptible target in MS associated demeylination (Soderstrom, 2001).

1.3. Compound action potential

Action potentials propagate along an axon; they produce electric potentials that can be recorded from the surface of nerve. When a nerve bundle is stimulated many axons produce

potentials synchronously. The resulting electric responses recorded from the surface of the nerve are called compound action potentials to distinguish from action potentials generated by individual axons (Patten et al., 1999).

CAP is measured using stimulus electrodes applied to one end of the nerve and recording electrode located along the nerve. Upon application of sufficient current pulse the action potentials produced in fibers propagate towards the recording electrodes. The aggregate effect of many action potentials is an extracellular potential, moving along the surface of the nerve. If the recording electrodes are widely spaced, the wave of negative potential produces a negative pulse recorded as voltage.

1.4. K_v1 channel: Background, Structure and function

As described above, the flow of K^+ across the plasma membrane is critical for all neuronal tissue. Stimulus induced ion channel activation and its conformational changes lead to depolarization of membrane and permit ion flow. For the K_v1 channels, the direction in which K^+ will flow is normally from inside the cell to outside tending to oppose depolarization that evoked their flow. This K^+ efflux tends to reduce the amplitude of the depolarization. One channel molecule could perform various functions in different neurons if the resting voltages of the neurons differ (Pinto and Klumpp, 1998, Kandel et al., 1991).

K_v1 channels are also known as 'Shaker channels' because of its origin which stems in to the *Shaker* locus of *Drosophila melanogaster* mutants which provided the first tools for cloning and characterization of these membrane proteins. Shaker flies exhibited a peculiar phenotype under ether based anesthesia marked by shaking of their legs, wings and abdomen. Voltage clamp experiments with these flies revealed defects in the transient K^+ current associated with each of their different Shaker alleles. This locus appeared to encode the affected voltage gated K^+ channel. Later chromosome walking strategies by several groups allowed cloning of cDNAs and molecular characterization of these clones. These studies revealed that they were closely related and were products of alternatively spliced

mRNAs (Judge and Bever, 2006, Papazian et al., 1987, Kamb et al., 1987). Sequence determination of one of these clones revealed a predicted protein with several putative transmembrane (TM) helices (Tempel et al., 1988). Thus combined molecular and electrophysiological, approaches brought forth an unexpected and vast diversity of K_v channels.

1.5. K_v channel subfamilies and nomenclature

In mammals distinct genes encode the molecular structure of each type K^+ channel subunit. Many voltage-activated K_v channels have been cloned and sequenced from several tissues in different species, including human (Pongs, 1992, Pongs et al., 1988, Wulff et al., 2009) (IUPHAR Compendium of Voltage-Gated Ion Channels, 2002; http://www.iuphar-db.org/iuphar-ic/). Four subfamilies of distinct K_v genes were originally identified in Drosophila. The initial cloning of members of the Shaker (Sh) subfamily of K_v channels (Kamb et al., 1987, Papazian et al., 1987, Pongs et al., 1988, Tempel et al., 1988, Wulff et al., 2009) was quickly followed by isolation of the Shab (Sb), Shaw (Sw), and Shal (Sl) subfamily genes (Wulff et al., 2009). Homologous subfamilies of vertebrate genes were subsequently found in Xenopus, mouse, rat, and man and were commonly referred as (Sh) ''K_v1'', (Sb) ''K_v2'', (Sw) ''K_v3'', and (Sl) ''K_v4'' which formed part of an original standardized nomenclature (Judge and Bever, 2006, Gutman et al., 2005) for K_v channels with a description of 6 subfamilies (''K_v1''–''K_v6''). This system was proposed as a means of simplifying the burgeoning list of human K_v gene names and their species homologues. Later a supposedly simpler nomenclature was introduced based on the ''sequence homology'' of their genes (channels sharing 65% sequence identity being classified as a single subfamily). This was quickly expanded to include standardized nomenclatures for Ca^{2+}-activated (KCa) and inwardly rectifying (Kir) K^+ channels prior to the successful sequencing of the human genome, which initially identified 67 human K^+ channel proteins under the International Human Genome Mapping Consortium (Venter et al., 2001). The human genome organization (HUGO) developed and introduced new guidelines for naming human genes in 1997 (White et al., 1997). Although the original standardized nomenclature

needed updating, the HUGO KCN (K^+ channel nomenclature) only introduced renewed confusion by removing all intuitive identifiers and failing to logically classify channel genes based on the molecular relationships between ion channel proteins. As a result, the use of the HUGO KCN nomenclature has been more often parenthetic. Subsequently, The International Union of Pharmacology (IUPHAR) together with the American Society for Pharmacology and Experimental Therapeutics (ASPET) convened multiple subcommittees to resolve these prevailing confusions and introduced a comprehensive and rational nomenclature that reinserted fundamental intuitive identifiers; classification based on molecular relatedness, and is presently meeting with wide acceptance within the ion channel field. To date, 12 subfamilies of K_v channel genes have been identified (Gutman et al., 2005, Gutman et al., 2003) **(Figure 7, Figure 8).**

The phylogenetic tree of all K^+ channel genes, as identified by protein sequence comparisons, divides first into 4 structural classes based on whether the pore forming structure or α-subunits comprising a given K^+ channel contain 2 [2TM; i.e., inward rectifiers and ATP-regulated K^+ channels (Kir)], 4 [4TM; i.e., background, leak, or tandem 2-pore K^+ channels (K2P)], 6 [6TM; i.e., delayed rectifiers, rapidly inactivating (A-type), and small/intermediate conductance voltage and calcium-activated K^+ channels (KCa)], or 7 [7TM; i.e., large conductance Ca^{2+} activated K^+ channels (KCa)] TM domains. The family of K_v channels belongs to the 6TM structural class. Originally, the 6TM structural class was comprised of 6 K^+ channel families including K_v, KQT-type, cyclic nucleotide-gated Ca^{2+}-activated (CNG), ether-a-go-go-related (eag, erg, or elk), small/intermediate conductance Ca^{2+}-activated (SK/IK), and large conductance Ca^{2+}-activated (slo, maxi KCa, or BK) K^+ channels (Judge and Bever, 2006, Hille, 2001). The formerly separate families of KQT and CNG K^+ channels have been reclassified as members of the K_v family, whereas the family of large conductance Ca^+-activated K^+ channels is now recognized as a separate structural class (7TM); channel subunits contain a 7TM segment due to the extracellular location of the N-terminus as opposed to its intracellular location in 6TM K^+ channels (Gutman et al., 2003, Gutman et al., 2005, Judge and Bever, 2006) **(Figure 9A).**

1.5.2. α-and β-subunits of K_v1 channels

1.5.2.1. α-Subunits

All mammalian K_v1 channels are large (Mr ~ 400 kDa) sialoglycoprotein complexes (Parcej et al., 1992) composed of 4 pore-forming α-subunits (K_v1.1-1.6) and 4 auxiliary, cytoplasmically associated β-subunits **(Figure 9B)** (Orlova et al., 2003, Dolly and Parcej, 1996, Parcej et al., 1992, Rettig et al., 1994, Scott et al., 1994a). K_v1 channels are tetrameric surface proteins. Each subunit of a tetramer has six conserved integral membrane spanning segments, namely S1-S6 which is connected by intracellular and extracellular loops or linkers and both the N- and C-termini being located intra-cellularly. A functional channel consists of 4 α-subunits arranged around a central axis forming the ion conduction pathway. S1-4 of an α-subunit are responsible for voltage sensing, and wrap around the pore of the adjacent subunit The S4 helix contains a positively charged amino acid (arginine) at every third residue, interspersed with hydrophobic residues, and is generally thought to function as the main voltage-sensor (Jan and Jan, 1992). The ion conduction pore consists of S5, the S5-S6 loop and S6 (Long et al., 2005b). The S5-S6 loop contains a conserved sequence which acts as a K^+ selectivity filter (Li et al., 2006). The S4-S5 linker connects the pore and voltage sensing components of α subunits **(Figure 9, Figure 10)** (Long et al., 2005a).

1.5.2.2. T1 domain

The N-terminus preceding S1, the first membrane spanning helix of an α-subunit, forms a T1 or tetramerization domain (within the cell). These domains (1 from each α-subunit) form a tetrameric complex at the intracellular membrane providing a docking platform for β-subunits **(Figure 10A, B, Figure 13)** (Long et al., 2005a). The T1-S1 linker maintains separation between the pore of these channel and the intracellular regions. A wide space between the T1 domain and pore is achieved by the radial direction of the linkers, allowing the inner pore helices to undergo large movements during pore opening without

interference. This also results in diffusion pathways, called side portals, between the cytoplasm and pore entrance which provide a means for communication and allows the flow of K^+. The 4 side portals of a complete channel attract cations due to negatively charged amino acids on their rims and surface. They also have a role in inactivation (Long et al., 2005a).

1.5.2.3. β Subunits

The β-subunits are non-glycosylated, hydrophilic proteins with 367 (β_2) or ~ 400 (β_1, β_3) residues. There are three types of β-subunits identified, namely β1, β2, and β3. The inactivation rate is greatly accelerated for several K^+ channels by the cytoplasmic association of β-subunits, *via* binding of a ball formed from the N terminus of the α-subunit, to the central cavity and the inner mouth of the pore **(Figure 10).** The main role of β2 is to act as a chaperone to increase the expression of K_v1 channels at the plasma membrane (Orlova et al., 2003, Shi et al., 1996)

1.6. Molecular determinants of K_v channel function

1.6.1. N- type and C- type inactivation

Ionic gradient and resulting potential difference across the axolemma creates an electric field. This induces structural rearrangements in K_v channel TM which allows the opening of its translocation pore. Such a change renders the channel to be either conducting (Hoopengardner et al., 2003) or non-conducting (closed or inactivated). In response to appropriate changes in the TM electric field, the non-conducting channel undergoes conformational rearrangements, which open (activation) or close (deactivation) the ion translocation pore (McCormack et al., 2002) **(Figure 10E)**. There are two mechanisms which take effect for the inactivation of a channel. If the pore is occluded due to the binding of a hydrophobic N-terminal “ball” to the cytoplasmic vestibule of the pore and this is

called rapid or N-type inactivation (Isacoff et al., 1990). This is common for rapidly inactivating channels. The latency is dependent on the length of the N-terminal chain and is typically in milliseconds. After a period of binding, the inactivation ‘‘ball’’ releases in a process called ‘recovery from inactivation’. Multiple inactivation domains have been identified in the amino terminal ‘ball and chain’ region of the K_v1.4 α-subunit (Ruppersberg et al., 1991). In addition, solution structures have also been determined for the N- terminal inactivation domain as well as the K_vβ subunits which confer rapid inactivation or non-inactivation or slow inactivation of K^+ channels (Wissmann et al., 2003, Gulbis et al., 2000, Judge and Bever, 2006). A second form of inactivation, termed ‘C-type inactivation’, also emerges with prolonged depolarization leading to decreased current flow due to structural changes that constrict the extracellular end of the ion translocation pore (Yellen et al., 1994).

Detailed models (Bezanilla et al., 1991, Bezanilla, 2008, Elinder et al., 2007) mathematically describe the steady/open state probability and their kinetic transitions taking place during activation and conformational changes in K_v channels **(Figure 10C, F, G, H).** Such models are based on the ability to measure gating currents that reflect, not the movement of charged ions (ionic currents) through the pore, but the intramolecular movement of charges or dipoles (gating currents) within the subunits of the channel protein itself (voltage-dependent action of the channel voltage sensor thought to be the S4 TM segment in K_v) (Bezanilla et al., 1991, Bezanilla, 2000, Bezanilla, 2006).

1.6.2. Voltage sensing models and conformational changes

How the voltage-sensing region translates TM voltage changes into structural conformational changes that leads to the opening or closing of the ion translocation pore remains unresolved and controversial but it entered an exciting era in 2003 with the first crystallization of a K_v channel. Using X-ray crystallography techniques, the MacKinnon laboratory crystallized the bacterial K_v channel from Aeropyrum *pernix* (K_vAP;(Jiang et al., 2003b, Jiang et al., 2003a). Their results reinvigorated research in this area by yielding an unexpected visualization of the voltage sensing region that conflicted with prevailing views

on the structure and movement of the voltage-sensing S4 segment in a K_v channel. It was the tertiary structure (not the primary or secondary structures) in K_vAP that came as a surprise. Unlike the long-standing and experimentally supported view that each of the S1–S4 segments spanned the TM region, the C terminus half of S3 and the S4 segment in K_vAP appeared to form a ‘‘paddle-like’’ structure lying alongside the intracellular surface of the membrane ‘‘translocating’’ charge through the membrane while S1 and S2 were approximately parallel to the surface of the membrane encircling the pore-forming S5–P–S6 domain **(Figure 10, Figure 11)** (Judge and Bever, 2006, Elinder et al., 2007).

In contrast, the voltage-sensing S1–S4 region of the recently determined K_v1.2 crystal structure has the anticipated TM topology with a tertiary structure very similar to that of the second K_vAP crystal structure of an isolated voltage-sensing domain. The MacKinnon lab (Jiang et al., 2003b) recognized that the voltage-sensing domain of the full-length K_vAP crystal structure is distorted from its native conformation, as a probable result of the antibodies used in the purification and crystallization process and/or the fact that the detergent solubilized protein does not exist in its native bilayer. K_v1.2 crystal structure confirms early proposals that the S4–S5 linker forms an amphipathic α-helix that lies parallel to the cytoplasmic surface of the membrane. Numerous models have been proposed for the voltage sensing mechanism of activation gating. The best known of these are the ‘helical screw’, the ‘gating pore’, the ‘transporter’, and the ‘paddle’ (Jiang et al., 2003b, Jiang et al., 2003a) **(Figure 10F, G, H)** (Judge and Bever, 2006, Elinder et al., 2007).

1.6.3. Ion and gating currents

Voltage-gated ion channels largely depend on membrane voltage. This voltage dependence suggests that around 12 elementary charges are required to move through the membrane electric field to open the channel (Keynes and Elinder, 1999, Swartz, 2004). Thus, there are three charges per subunit in the tetramer. When these charges are moving, they should cause a tiny gating current. This was realized already by Hodgkin and Huxley in their classical studies from 1952. However, due to its smallness and the consequent contamination by ion currents it withstood measurements for a long time. The first

measurements were possible only after development of efficient signal averaging techniques and were published 30 years ago. With the development better techniques it has now been demonstrated that even though there is no channel opening at -40mV potential difference across the axolemma, there is a large gating current. Larger voltage steps (-20 mV) move more charges and open the channel. The major gating current component precedes the opening of the channel. Still higher voltage steps (0 mV) speeds the movement but do not increase the total gating charge. The integrated gating current vs. voltage, Q(V) curve is typically to the left of the G(V) curve (conductance vs. voltage) **(Figure 11 C, D).** This means that the voltage sensors have to move before the channel can open (Keynes and Elinder, 1999).

1.6.4. The voltage-sensor movement

1.6.4.1 Early helical-screw and helical-twist models

The first model to describe the S4 movement was the helical-screw model. As depicted in **Figure 10** the positive charges are lined up in a spiral around S4. They are supposed to pair with conserved negative counter charges in S2 and S3. Upon activation, S4 moves to new stable positions by rotating 60° and translating 4.5 Å per step. Three steps, thus a rotation by 180° and a translational movement of 13.5 Å, are required to transfer three charges per subunit to open the channel (Keynes and Elinder, 1999). This relatively large scale movement of S4 was almost generally accepted as charge transfer mechanism in voltage-gated channels, until it was challenged by the helical-twist model, involving a much smaller movement, as shown in **(Figure 10G)** — a 180° rotation with no translational movement. Narrow, water-filled crevices make it possible to transfer the charges during gating.

1.6.4.2. Electrostatic interactions suggest a novel helical-screw model

The location of S4 within the channel has also been a matter of debate. Most investigators have placed S4 buried in the channel protein, in direct contact with the pore-forming

domain, and shielded from the lipid bilayer by surrounding S1 to S3. In contrast when it occupied a lipid facing position in the periphery of the channel the charge on the extracellular surface of the channel, close to S4, would electro statically interfere with the movement of the positively charged S4 —a position close to S4 would have a larger effect than a charge further away. A positive charge would decrease and a negative charge would increase the outward movement.

Introduction of extra charge on the channel surface at different distances from S4 allows measurement of the effect induced on the G (V) curve. A position at the extracellular end of S5 (residue 419) showed the largest effect on the G(V) curve compared to the other investigated positions, shifting the curve to ±8.2 mV. This study showed positioning of the charges of S4 8 Å outside S5 — not in the crevice between two adjacent subunits as previously assumed. The other segments, S1–S3, were placed to satisfy electrostatic interactions and to fill in structural gaps in the molecule. With this arrangement charges of S4 face S1–S3 and the hydrophobic side of S4 face the lipid bilayer. Thus it was suggested that such an unorthodox solution allows large-scale movements of S4 with little friction from the fluid lipid bilayers (Elinder et al., 2007).

The magnitude of the S4 movement was also measured using an electrostatic strategy. It was reasoned that a voltage sensor close to our mutated residue would attract negatively charged reagents, and increase the rate of reaction, while it would repel positively charged reagents, and decrease the rate of reaction. Depending on the position of S4 in open and closed states we would expect different reaction rates. This study found that S4 increased the local potential with 35 mV at the extracellular end of S5 when the channel was in open state. The top charge (residue 362) alone contributed 19 mV. Electrostatic calculations suggested that the top of S4 moved from a distant position (N20 Å) to a position close to S5 (8 Å) upon activation. Thus, they reasoned that it is compatible with a helical- screw motion with the helix located as suggested in **Figure 10F.** It is apparent that in diseases like MS where demeylination is most predominant feature and membrane protein-lipid dynamic is distorted, the axolemmal ion channels are also variously affected (Elinder et al., 2007).

1.7. Brief overview of multiple sclerosis (MS) and demyelination

Multiple sclerosis (MS) is a chronic, disabling disease that affects 2 million people worldwide, especially young adults in industrialized societies. It is typically diagnosed between 20 and 40 years of age. A study on European MS epidemiology found an overall estimated prevalence of 83 per 100,000 with higher rates in northern countries (Pugliatti et al., 2006). MS is an inflammatory demyelinating (loss of myelin) disease of the CNS (Martin et al., 1992) and a leading cause of nontraumatic neurological disability (Trapp and Nave, 2008, Compston and Coles, 2002, Dutta and Trapp, 2010).

MS derived its name because the patients have multiple attacks separated both in time and location, affecting different parts of the CNS. The disease often displays a relapsing–remitting pattern of demyelination associated symptoms early in its course, and then recovers during remissions. There is cumulative acquisition of neurological deficits in some patients either at a later stage (secondary progressive MS), or at the beginning of disease onset (primary progressive MS) which do not remit (Bitsch et al., 2000, Waxman, 2006). Demyelination involves CNS glial cell; namely, the oligodendrocyte as a principal target. Effects of unfavorable conditions during disease progression and associated mechanisms alter its interaction(s) with neurons and initiate symptoms (Lassmann et al., 2007, Smith, 2011, Smith and Hall, 2001, Smith and McDonald, 1999) due to CNS lesions. MS lesions denote loss/damage of oligodendrocyte coupled with axon degeneration (Dutta and Trapp, 2010, Prineas and Wright, 1978, Kuhlmann et al., 2002). Progressive axonal loss is the major cause of prolonged neurological disability (Dutta and Trapp, 2010, Bitsch et al., 2000). Morphological analysis of brain tissue (Trapp and Nave, 2008, Campbell et al., 2011, Lassmann et al., 2001) has further established this fact (Dutta and Trapp, 2011, Trapp and Stys, 2009). Alteration or disruption of axonal cyto-architecture impacts axonal functioning which in turn leads to conduction blocks of varying degrees due to differential levels of neuro-degeneration (Haider et al., 2011, Prineas and Wright, 1978, Lassmann et al., 2001).

1.8. Etiology and clinical symptoms of MS

The actual cause of MS remains unexplained and is a debatable issue. It is attributed to various causes like virus, toxin, genetic or environment induced leading to CNS inflammatory response followed by demyelination. Demyelination and axon loss begins right at the onset, which continues leading to chronic effects on axon and gliosis while the disease progresses as the inflammatory phase wanes off in due course **(Figure 12).** Focal CNS plaques of primary demyelination with a variable degree of impact on the axon and neuron are a characteristic feature of disease progression (Lassmann et al., 2007). Clinically T2-weighted magnetic resonance imaging (MRI) scan is used to detect the total number of lesions (lesion load) and disease burden. These are hyper-intense lesions, which appear as bright spots on the MRI image. The T2-weighted scan is part of conventional MRI technology which is used to monitor and diagnose MS, usually in conjunction with a T1-weighted scan and with gadolinium enhancement.

About 50-70% of patients present themselves with a clinically isolated syndrome (CIS) (i.e., a single relapse of the sort seen in MS). They are affected within the optic nerve, brain stem, or spinal cord which readily disseminates into the cerebral white matter lesions and is very typical of MS. Most of such individuals later develop clinically definite MS with follow-ups. MS patients display phenotypic heterogeneity, some may present with atypical clinical patterns, while others could be asymptomatic. But as the disease progresses and demyelination sets in individuals exhibit characteristic tiring during physical and cognitive tasks, taking longer to recover.

Demyelination can initially results in the expression of “negative” symptoms, namely loss of function resulting in deficits such as blindness, paralysis, and numbness. During the next few weeks the axon adapts to its demyelinated state, resulting in a gradual increase in excitability and then, if conditions are favorable, conduction through the demyelinated lesion(s) may be restored. Where this occurs, it contributes to clinical recovery and the remission of the negative symptoms – remitting relapsing phase of MS (RRPMS), although conduction remains insecure and some residual deficits may persist. Some axons may

become hyperexcitable, resulting in the expression of "positive" symptoms such as tingling sensation or pain (Waxman, 2005).

1.9. Factors leading to axonal conduction block

Axonal conduction block is an outcome of demeylination associated disruption of its function owing to the structural changes. Several elements of this change contribute differently leading to a perturbed homeostasis as the disease progresses. Briefly structural changes in an axon account for the following conditions.

1.9.1. Segmental demyelination involving complete loss of myelin over a single internode which is more than sufficient to block conduction completely.

1.9.2. Nodal widening: Sometimes demyelination does not involve the whole internode, but only the paranodes, resulting in widening of the nodal gap. In agreement with predictions made by computer modeling (Chiu and Ritchie, 1981, Koles and Rasminsky, 1972), nodal widening is also sufficient to block conduction (Waxman, 2005).

1.9.3. "g" ratio/myelin index*:* It is a measure of myelin thinning. The ratio of the inner axonal diameter to the total outer diameter or 'g' ratio is widely utilized as a functional and structural index of optimal axon myelination. Rushton was the first to derive an optimal theoretical 'g' ratio of 0.6 (Rushton, 1937). In this classic study, the calculation was based on the speed of fiber conduction. 'g' ratio=di/do (Rushton, 1951, Chomiak and Hu, 2009), and myelin index = do/di (Nashmi and Fehlings, 2001).

1.9.4. Soluble factors: There is an inevitable dysregulation of the composition of extracellular fluid bathing axons, including the appearance of other agents of various origins.

- Nitric oxide (NO): is a reactive agent that can have direct or indirect effects on Na^+ channels (Smith, 2007) and K^+ channels (Yang et al., 2007c); it also causes

membrane depolarization and inhibits mitochondrial metabolism. Any of these mechanisms would be expected to impair conduction.

- QYNAD/endocaine: An endogenous pentapeptide Gln-Tyr-Asn-Ala-Asp (QYNAD), which acts like a local anesthetic lidocaine and is found at 14-fold higher levels in CSF, producing Na_v channel blocking effects.
- Cytokines: like TNF-α and γ-interferon act indirectly.
- Antibodies: anti-GM1 etc.(Smith and Hall, 2001).

1.10. Compensatory mechanisms in demyelination, a structure function co-relate

Although conduction might be initially blocked by segmental demyelination, the block is not necessarily permanent. The loss of the myelin triggers a series of adaptive responses in the axon. These might be kicking in of several compensatory mechanisms that lead to restoration of axon conduction in the presence or absence of myelin loss. There are two most widely known facts:

1.10.1. Altered distribution and expression of ion channels

Atypical expression of ion channels, and their expression in different proportions and locations, can be expected to contribute to the complex neurological manifestations of demyelinating diseases. Although at present our understanding of the roles of individual types of channel is limited, increased knowledge is anticipated from studies conducted on several types of animal models including transgenic knock-outs of particular ion channels (Smith and Hall, 2001) Changes in the ion channel population along the demyelinated membrane is an adaptive response. Experimental allergic encephalomyelitis (EAE) optic neuritis induces dispersion of Na^+ channels into paranode and internode region, and the timings of this altered distribution correlates with the symptoms produced. Functional studies on dorsal root ganglion (DRG) and sciatic nerve also support this view. On the other hand, diffuse paranodal and JXP expression of K_v channels owing to destabilization of these structures in demeylination or hypomyelination (Rasband et al., 1999b) or lack of galactolipids is known. Axotomised DRGs show reduced immunoreactivity to K_v1.1, 1.2

.1.3 and 2.1. In MS and EAE demyelinated axons may express channels Ca^{2+} (Kornek et al., 2001) and Na_v (Smith, 2007, Waxman, 2006) that are not normally present (Smith and Hall, 2001).

The restoration of conduction to demyelinated axons involves substantial remodeling of demyelinated axolemma at the molecular level. The nature of these changes is becoming clearer with the advent of suitable antibodies for immuno-histochemistry (IHC), and it is now possible, to view the exquisite precision with which $Na_v1.6$ sodium channels are segregated at nodes of Ranvier (Arroyo and Scherer, 2000, Black et al., 2002) or K_v1 channel at the JXP (Rasband, 2004). Earlier morphological evidence that Na_v density can increase in demyelinated axons (Kazarinova-Noyes and Shrager, 2002) has been augmented by the discovery that two different isoforms of voltage-sensitive Na^+ channels**,** $Na_v1.2$ and $Na_v1.6$, become expressed along demyelinated axons (Craner et al., 2004). On the other hand, nothing is known about any kind of K_v channel subunit changes in demyelination.

1.10.2. Microsaltatory conduction

This is a property involving restoration of conduction to demyelinated axons in the presence of remyelination. Conduction in lysolecithin-induced demyelinated axons proceed in a discontinuous manner, by adopting a microsaltatory mode of conduction, perhaps reflecting the organization of Na^+ channels into new node-like foci, termed phi-nodes or reformation of shorter internodes. Thus, conduction may be possible even in “open” MS lesions, where there is a paucity of glial processes and a greatly expanded extracellular space. The presence of conduction in demyelinated axons can also explain the observation that large, but clinically “silent” (i.e., asymptomatic) demyelinating lesions can occur in patients in pathways where symptoms may have been expected (Waxman, 2005).

1.11. Persistence of conduction block and failure of regulatory mechanisms

Why these mechanisms fail and lead to persistence of conduction block? Does it involve modulation? There could be several answers to it. Although conduction can be restored to demyelinated axons, conduction block remains a common feature of such axons. Whether conduction is restored in practice depends on a number of factors; those favoring the persistence of conduction block include:

1. large axon diameter (Bostock et al., 1978);
2. long internode preceding the demyelinated region (especially if the internode is partially demyelinated);
3. long overall length of demyelination (e.g., many internodes lost);
4. dysregulation of extracellular fluid composition, for example due to the failure of blood-brain barrier; the presence of factors deleterious for conduction such as nitric oxide and other factors associated with inflammation;
5. absence of any glial ensheathment;
6. short period of time elapsed since the occurrence of demyelination;
7. recent (seconds/minutes) history of sustained impulse conduction (see later);
8. an inopportune composition of ion channels and pumps along the demyelinated axolemma, perhaps theoretically influenced by genetic background; and
9. warm body temperature (Ulthof's phenomenon) **(Section 1.13.4).**

Some of these points deserve further comment, and with regard to axon diameter, it is known that conduction can occur in demyelinated axons as large as 5.5 mm in diameter. As most demyelinated axons are smaller than this, especially in the CNS, it is likely that most peripheral and central demyelinated axons are capable of conduction if conditions are optimal. Also with regard to the preceding list, a long internode before the demyelinated region impedes the depolarization of the demyelinated axolemma by reducing the local current available at this site due to capacitative and resistive loss over the internode (Waxman, 2005).

1.12. Safety factor for conduction

The concept of safety factor is useful in the pathophysiology of demyelination. It is defined as the “current available to depolarize the axolemma, divided by the current necessary to do so” (Rushton, 1937, Waxman, 2005) .

- In normal myelinated axons, the action potential at an individual node generates approximately three to seven times more current than is actually required to fire the next node along the axon (Tasaki, 1953, Waxman, 2005), giving a safety factor of 3 to 7.
- In demyelinated axons, however, several factors conspire to reduce the safety factor and in some axons it falls to around unity. This is a critical level, because if the safety factor is fractionally higher than 1, the axon will conduct and the patient will have few symptoms; but if the safety factor is fractionally lower, conduction will be blocked and a neurological deficit may ensue.

Some patients have many axons with a safety factor near unity, can result in noticeable, quite sudden changes in the severity of symptoms, because the safety factor is not absolutely fixed for any particular axon and it can be modulated slightly by small changes in the environment of the axons, especially temperature. In fact, even subtle changes in temperature can have dramatic effects on the success of conduction and, thereby on the expression of symptoms. Thus, the low safety factor of demyelinated axon means that conduction along the axon is not only particularly sensitive to changes in temperature but also vulnerable to chemical factors that may impair conduction

An increased nodal gap can block conduction because the loss of the myelin means that the local current generated by the driving node (i.e., the last intact node before the demyelinated region) is now dispersed across a much wider area of axonal membrane than normal and, in particular, the nodal capacitance is greatly increased. Cell membranes, like axolemma, have a significant amount of capacitance and as they are very thin, and this capacitance has to be discharged as the axon is depolarized. The nodal capacitance is effectively determined by the area of the denuded axolemma, so demyelination can dramatically increase nodal capacitance, thereby, increasing the amount of local current

required for depolarizing the membrane to its firing threshold. The dispersal of the current and the increase in capacitance both serve to reduce the safety factor for conduction**.** Even myelin thinning along the internode can be sufficient to cause conduction failure, and failure is especially likely if an equivalent quantity of myelin is lost from the paranodes, resulting in widening of the nodal gap (Waxman, 2005).

1.13. Collative functional impact on axon

1.13.1. Slow conduction - impedance mismatch. Why?

Although demyelinated axons can sometimes conduct impulses successfully, they never conduct as well as the normal axons. Conduction remains much slower and less secure than normal (McDonald and Sears, 1970, Bostock et al., 1978). It has proven to be particularly valuable clinically, assisting in the diagnosis of demyelinating disease because of delays in the latency of the sensory or motor compound action potentials in patients with peripheral neuropathy, or in delays in the latency of the visual, somatosensory, or auditory-evoked potentials in patients with MS.

1.13.2. Refractory period of transmission (RPT) or conduction of pairs of impulses

The slow conduction along demyelinated axolemma inevitably limits the ability of the axons to transmit pairs (and trains) of impulses because the second action potential of a pair, traveling close behind the first, will run into the relative and absolute refractory periods of the first impulse as this is slowed at the site of demyelination. McDonald and Sears (McDonald and Sears, 1970) coined this deficit the refractory period of transmission (RPT), defining the RPT as the maximum interval between two conducted impulses such that the second impulse fails to be conducted successfully through the lesion. In a subsequent study of central axons proven to be segmentally demyelinated, the refractory period of the normal portion of the axon was always in the range 0.5 to 1.4 m/sec, but this was prolonged to 1.0 to 6.0 m/sec if the site of demyelination was included in the conduction pathway (Waxman, 2005).

1.13.3. Conduction of trains of impulses

The problems associated with conducting pairs of impulses are magnified when considering the conduction of trains of impulses. One consideration is that the RPT of the second and later impulses is longer than that of the first (McDonald and Sears, 1970, Waxman, 2005), slightly increasing with increasing numbers of impulses until a plateau is reached. This effect is due, in part, to the fact that the second impulse conducts across the demyelinated region in the relative refractory period of the first, and so conducts a little more slowly, and so on. The maximum frequency of transmission therefore slowly declines over time. These latter frequencies are within the physiological range, and so the phenomenon raises the likelihood of impairing normal sensation and motor function, contributing to the reduced flicker fusion frequency in some patients, to the "fading" or blurring of vision upon prolonged fixation of gaze, and to the progressive weakness experienced by some patients upon walking only a short distance (Waxman, 2005) **(Figure 15 B,C).**

1.13.4. Uhthoff's phenomenon or temporary exacerbation caused by warming

The security of conduction in demyelinated axons is markedly affected by temperature, and this effect can readily be demonstrated in the laboratory in both central (Smith et al., 2000) and peripheral experimentally-demyelinated axons. The effects can be sufficiently strong that even subtle changes in body temperature can have a profound effect on the expression of symptoms by patients with MS.

Indeed, many patients with MS exhibit a worsening of some symptoms upon body warming, and the worsening is sufficiently robust and reproducible that at one time the phenomenon was used in the diagnosis of MS in the form of the "hot bath test". The effect was first described in 1890 by Uhthoff, and the phenomenon now bears his name. Uhthoff-like phenomena can be provoked by a hot shower, sunbathing, exercise, or even by the normal circadian change in body temperature. Just as warming can be deleterious to function, so cooling can be beneficial and can sometimes be realized after a cool bath or simply after drinking cold water. Indeed, improvement in vision has been documented after drinking iced water, and these functional improvements are accompanied by an increase in the amplitude of the visual-evoked potential (Waxman, 2005).

1.14. Consequences of sustained impulse activity

1.14.1. Activity dependent conduction block

Axonal activity failure is also caused by axonal hyperpolarization resulting from activity of electrogenic Na^+/K^+ ATPase. Pump activity is prompted by the raised intra-axonal Na^+ concentration as a result of preceding impulse activity. Hyperpolarization can effectively and abruptly turn demyelinated axons 'off' for a period (e.g., 0.2-2s) and its intermittent appearance can cause a continuous train of impulses to be divided into short bursts separated by silent periods. The phenomenon has now been demonstrated in normal human axons and human axons affected by chronic demyelination (Smith and Hall, 2001).

1.14.2. Hyperexcitability and ephaptic transmission

Apart from the negative symptoms in MS (e.g., paralysis, blindness, numbness) positive symptoms (tingling sensation) are also known. Such symptoms are believed to arise primarily from spontaneous impulse activity, which is generated by axons rendered hyperexcitable by their response to demyelination. What leads to hyperexcitability is an open debate (Smith and Hall, 2001), but one consequence of it is the possibility of ephaptic transmission, namely the excitation of neurons/axons by activity in neighboring neurons/axons, at a site other than a synapse (Walz, 2000).

1.15. Inhibition of K_v1 channels and challenges

After protein kinases and G-protein coupled receptors (GPCRs), voltage-gated ion channels (VGICs) constitute the third largest group of signaling molecules encoded by the human genome. Even though about 40 K_v channels encoded by the human genome have been cloned and their biophysical properties characterized, it often remains a challenge to determine precisely which channel underlies the K^+ current in a native tissue. This is because within subfamilies, such as the K_v1 or K_v7 families, the α-subunits can heteromultimerize relatively freely, resulting in a wide range of possible channels tetramers

with different biophysical and pharmacological properties (Wulff et al., 2009, Gutman et al., 2005). K_v channel-interacting proteins (Long et al., 2005b, Long et al., 2005a, Wulff et al., 2009) enhance the surface expression (McKeown et al., 2008) and alter the function of K_v4 channel α-subunits (Gutman et al., 2005). In addition to this 'mixing and matching' of α- and β-subunits of K_v channel leads to properties that can be further modified by phosphorylation, dephosphorylation (Singer-Lahat et al., 1999, Yang et al., 2007a, Park et al., 2008), ubiquitination (Manganas et al., 2001), sumoylation (Plant et al., 2011, Dai et al., 2009) and palmitoylation (Gubitosi-Klug et al., 2005). In terms of drug discovery, this molecular diversity creates a challenge. However, it also provides an opportunity to achieve selectivity by designing modulators that discriminate between homotetramers and heteromultimers or that binds to tissue specific β-subunits (Wulff et al., 2009). The non-canonical (nonconductive) properties of K_v channels are increasingly found to be of importance. For instance K_v channels also play an important part in Ca^{2+} signaling, volume regulation; secretion proliferation (Wickenden, 2002, Chittajallu et al., 2002) and migration (Coma et al., 2003). Although no K_v channels have been found to have direct intrinsic catalytic functions, they induce indirect effect, since they are often a part of large supramolecular complexes. The behavior of these complexes can be influenced by the channel in the absence of ion flow. Thus inhibiting K_v channels by a certain blocking strategy remains a major challenge in drug discovery (Wulff et al., 2009).

1.16. Channel modulation strategies and pharmacological targeting

Agents that modulate K_v channels can be broadly divided into three chemical categories: metal ions, organic small molecules (molecular weight 200–500 dalton) and venom peptides (molecular weight 3–6 kD). These substances affect K_v channel function by blocking the ion-conducting pore from the external or internal side, or modifying channel gating through binding to the voltage sensor domain or auxiliary subunits. Similar to other proteins expressed on the cell surface, K_v channels can be targeted with antibodies (molecular weight 150 kD) which can inhibit channel function, lead to channel internalization or deplete channel-expressing cells by complement or cell-mediated cytotoxicity. Antibodies and toxins can also be engineered to serve as carriers for the

delivery of active compounds to channel-expressing cells, or can be conjugated to cytotoxic drugs, isotopes or other molecules **(Figure 13)** (Wulff et al., 2009).

In terms of channel inhibition, one study has reported the development of monoclonal antibodies (specific for K_v10.1); polyclonal antibodies have been obtained in several cases using extracellular parts of the pore loop as antigen. Peptide toxins typically bind either to the outer vestibule or the voltage sensor of K_v channels. By contrast, small molecules — as exemplified by the hydrophobic cations like tetrabutylammonium, d-tubocurarine and verapamil — block K_v channels by physically occluding the inner pore and inserting their ammonium group into the ion permeation pathway (Wulff et al., 2009).

The inner pore of K_v channels can also be targeted by nucleophilic molecules such as the K_v1 channel blocker correolide, which fits neatly into the hydrophobic surface of the S6 helix with its lipophilic domain and chelates a permeating K^+ with its polar acetyl groups. Typical blockers of K_v11.1 enter the channel from the intracellular side and seem to reside in a pocket in the inner mouth, where they interact mostly with two aromatic residues. The wide range of drugs that this pocket can accommodate might be due to the lack of a cluster of proline residues, which induces a kink in the intracellular channel pore opening of K_v channels, in contrast to other K^+ channel families. This produces a broader opening in K_v11.1 that allows entry of a wide range of molecules of varying sizes and shapes (Wulff et al., 2009).

In addition to the inner pore, small molecules can also bind to the 'gating hinges'. This occurs in the case of the K_v7 channel activator retigabine, which has been found by mutagenesis to bind to a putative hydrophobic pocket that is formed following channel opening between the cytoplasmic parts of S5 and S6. Another interesting mechanism of action for channels with α-subunits is the so-called disinactivators that disrupt the interaction between α- and β-subunits and, thereby, modify channel behavior (Wulff et al., 2009, Lu et al., 2008).

As evident several strategies can be adopted for K_v channel modulation; therefore, typically a blocking molecule is usually identified through high-throughput screening (Wacker et al., 2012) or serendipity, and then optimized through classical medicinal chemistry. Lead identification is usually achieved by ion flux assays (mostly using isotopes and/or atomic absorption spectroscopy) or fluorescent dye assays. More recently, it has been achieved through automated electrophysiological measurements, which can offer quality levels comparable to that of manual patch clamp assays and has a reasonable throughput. Detailed studies on functional drug–target interactions can be achieved through patch clamping, which allows the behavior of a single ion channel to be studied on the microsecond timescale. Subsequently, the identified compound can be pipelined for pre-clinical animal studies (Wulff et al., 2009).

1.17. Principal goals of this study

Several years back a biochemical analysis (unpublished results) conducted by Prof. J.O. Dolly's laboratory on human brain autopsy tissue of MS patient from a brain bank based in London, UK, indicated the appearance of an intriguing and conserved diagnostic form of K_v1 channel. This observation emphasized greater significance of $K_v1.1$ subunit compositions and their stoichiometry in functional tetrameric organization of K_v1 channels. This form of $K_v1.1$ channel(s) has been hypothesized as a likely therapeutic target, which could contribute to the underlying cause of benefits rendered by 4-AP like drugs. Even though benefits of 4-AP like drug in demyelinated axon is known for a long time (Sherratt et al., 1980), its clinical application remains restricted due to its off-site action and subsequent epileptogenic side-effects (Judge and Bever, 2006).

A great deal of progress has been achieved in the lab to decipher the biophysical profiles of $K_v1.1$ oligomeric forms (Shamotienko et al., 1999, Shamotienko et al., 1997, Wang et al., 1999) and identify an appropriate pharmacological inhibitor, i.e., a molecule, which can effectively block the K^+ flow through K_v1 channels (Al-Sabi et al., 2010) in order to restore the conduction in demyelinated axons. This has to be achieved by inhibiting the K^+ efflux from a demyelinated axon allowing improvement of toxic-to-therapeutic ratio. This

work has been specifically designed to explore the features of $K_v1.1$ channel in an animal model mimicking MS.

It could be anticipated that several demyelinating axon features are associated with subunit composition and specialized sub-cellular distribution of K_v1 channels which contribute to the functional diversity. Exploring such features in a demyelinating CNS nerve is contemplated to contribute towards eventually improving the specificity of K_v1 blocking agent. Hence, the aim of this research project is to establish the features of MS in an animal model, followed by elucidation of $K_v1.1$-containing channels in disease state, such that it can be used as an established model for *in vivo* screening of pharmacophore that is being currently developed under our research program.

1.18. Animal models for multiple sclerosis

MS is a complex disease and hence involves several aspects of research. *In vitro* studies have addressed issues specific to mechanisms like T-cell activation by a myelin epitope, migration across the blood-brain barrier and demyelination whereas *in vivo* models have mostly encompassed approaches based on experimental allergic encephalomyelitis (EAE), as well as transgenic and mutant strains (Altmann and Boyton, 2004, Schmandt et al., 2006). Various types of demyelinating models have been developed and used to address specific issues of research interest (Merrill, 2009).

EAE models require immunization using CNS tissue in adjuvant to produce inflammatory disease in species of animals like mouse, rats, macaques, marmosets and rhesus monkeys. This approach has been instrumental in basic discoveries about the nature of disease. It has also been affected for pre-clinical testing of monoclonal antibody based therapies targeted against p40 receptor of interleukin IL-12 and IL-23 and against CD40. However, these models suffer major limitations with respect to translational MS research, one being that disease is not spontaneous; hence, investigation of interactions between environmental factors and their susceptibility is not possible. Furthermore, most therapies are tested in

EAE by giving the treatment at the time of disease induction, an unrealistic test compared with the clinical context of requirement to treat a patient in the midst of an ongoing and potentially irreversible pathogenic process of unknown duration (Altmann and Boyton, 2004). EAE induces a highly inflammatory multifocal CNS disorder with a largely unpredictable distribution pattern of the lesion and, hence, has proved less appealing compared to demyelination or dysmyelination models (Schmandt et al., 2006). Virus (Theiler and Semliki Forest Virus) induced models are also used which is argued to induce pathological patterns of MS (the III and IV lesions) (Lucchinetti et al., 2000) and has been instrumental in identifying some of the steps involved in T-cell migration to the CNS.

On the other hand mutant models have shed light on some forms of dysfunctional or damaged myelin sheath by spontaneous or experimentally conducted mutation of genes specific for CNS constituents. Although it is not widely believed that a key component of susceptibility to MS resides in genetic malformation of myelin, the notion of some form of highlighted glial vulnerability to inflammatory damage has been plausible. Some of these models include, Shiverer mice (MBP deletion) which fail to develop compact myelin and die by 22 weeks of age, Jimpy mouse (PLP mutation) result in hypomyelination and oligodendrocyte death, Twitcher mice have deficiency of galactosyl-ceramidase b-galactosidase resulting in distended 'globoid' macrophages, impaired myelin formation and myelin breakdown (Altmann and Boyton, 2004). MAG mutants show hypomyelination (50% unmyelinated axons in optic nerve) (Schmandt et al., 2006) and double knockout mice of MAG and the non-receptor src-type tyrosine kinase Fyn show higher levels of hypomyelination as compared to the single mutant (Schmandt et al., 2006).

Models of chemical demeylination use gliotoxic/neurotoxic agents like ethidium bromide (Guazzo, 2005), lysolecithin or cuprizone (Matsushima and Morell, 2001). Affinity and DNA chelating properties of ethidium bromide not only destroys oligodendrocytes but also their progenitors and astrocytes. Cuprizone (CZ) feeding leads to systemic defects representing an intermediate model where it leads to oligodendrocyte death and subsequent demeylination. It interferes with mitochondrial function and has been shown to affect the

expression of myelin genes and to cause apoptosis of oligodendrocytes (Schmandt et al., 2006).

In vivo models are important for defining "whole animal" aspects of disease with respect to immune system or CNS interactions, which are vital for designing and testing new therapies (Altmann and Boyton, 2004). Depending on the specific patho-mechanism or disease component to be targeted, different animal models offer distinct advantages for probing experimental therapies. It is generally believed that the immunological mechanisms responsible for inflammation in MS are similar to those in EAE, an experimental paradigm of Th1-mediated autoimmune disease, and immuno-modulatory therapeutic strategies that work in EAE should also be beneficial in MS. Unfortunately, in many instances this approach has been disappointing (Lassmann et al., 2001). The inflammatory models induce brain inflammation, mediated by T cells and local activation of hematogenous macrophages or microglia which in turn impairs the blood–brain barrier. That allows circulating demyelinating antibodies and complement components to enter the CNS and destroy myelin, either by complement activation or an antibody-dependent cellular cytotoxicity reaction. The pathological hallmark of such lesions is the local precipitation of the lytic terminal complement complex on the surface of myelin sheaths and oligodendrocytes. However, other mechanisms that have been identified could induce myelin damage during the course of an inflammatory process in the CNS. Thus, the major challenge for future research, is to define which of these mechanisms operate in demyelinating MS plaques (Groebe et al., 2009, Norkute et al., 2009, Soderstrom, 2001), so that a successful therapeutic strategy can be worked.

1.18.1. Developing animal model for in vivo screening of K_v channel blocker

MS is distinguished from that of other inflammatory diseases of the nervous system by the presence of large, multifocal, and chronic demyelinated plaques with reactive glial scar formation (Lassmann et al., 2001). The existing data regarding myelin status in chronic injury is incomplete and its correlation between rodent and human studies appalling (Lasiene et al., 2008). In order to develop a CNS demyelinating model, it is imperative to

contemplate the basic fact that myelin sheaths not only ensure successful propagation of action potentials but also participate in axonal maturation, transport and survival (Lasiene et al., 2008). So, an understanding of the state of axons during disease progression is of prime importance in order to develop the most appropriate therapeutic strategies.

1.18.2. Chronic demyelination

Although myelin sheaths are primarily targeted during MS disease progression, neurons their axons and astrocytes are also affected though to a lesser extent. Initially, demyelination was thought to be caused by necrosis of oligodendrocytes; however, it is unclear what causes prolonged oligodendrocyte death weeks and months after injury. Acute axonal injury is frequent in demyelinating MS lesions and this leads to 50–70% reduction in neurite density in chronic plaques (Lassmann et al., 2001). The concept of chronically demyelinated axons is based on anatomical, pharmacological and cell based studies (Lasiene et al., 2008) and it has remained difficult to establish the lesion pattern in the most popular EAE model of demyelination (Altmann and Boyton, 2004, Schmandt et al., 2006). MS lesions are classified under three categories:

1. Type I (Acute): With numerous T cells (CD3+ cells) and macrophages (CD68+ cells) throughout. These can be of two subtypes
    - With macrophages
    - Without macrophages
2. Type II (Active chronic): Centre of the lesion contains few macrophages and T cells but there are more of these cells at the border between demyelinated and normally myelinated tracts
3. Type III (Chronic): Few or no macrophages and T cells in the centre or periphery of the lesion (Ferguson et al., 1997) but with oligodendrocyte apoptosis.

1.18.3. Cuprizone induced demeylination and multiple sclerosis

Oral administration of Cuprizone (CZ) or biscyclohexanone oxaldihydrazone is known to produce status spongiosus and demyelination in the CNS plus hepatic lesions (Suzuki and

Kikkawa, 1969); induction in young adult mice is synchronous and consistent. Loss of myelin occurs in lesion sites large enough to allow detection of changes in the relevant cellular, molecular, biochemical and morphological parameters (Hiremath et al., 1998, Matsushima and Morell, 2001) and has been used to investigate demyelination as well as remyelination processes (Matsushima and Morell, 2001, Kipp et al., 2009, Crawford et al., 2009). The action of CZ involves copper chelation, which produces the same effects as chronic copper deficiency (Benetti et al., 2010). Copper being a co-factor of mitochondrial cytochrome-C oxidase, its deprivation by presence of CZ is assumed to cause strong impairment of energy production, neuron viability and their proliferation. However, CZ is not a neurotoxic molecule capable of directly acting on CNS neurons. Degeneration of oligodendrocytes precedes disruption of the myelin sheath (Pasquini et al., 2007). It leads to early observable myelin loss, without damage to other cell types in the CNS. This is evidently due to disturbance of energy metabolism marked by decrease in the activities of the various respiratory chain complexes, indicating a disruption of mitochondrial function resulting in demyelinating lesions (Pasquini et al., 2007).

Why oligodendroglia is preferentially susceptible to copper deficit is not known, although an obvious and most plausible hypothesis is that the perikaryon of this cell type has to maintain a vast expanse of myelin and this extraordinary metabolic demand (Waxman, 2005) places it in jeopardy if the demand cannot be met (Stidworthy et al., 2003, Binder and Steinhauser, 2006, Matsushima and Morell, 2001). CZ challenge for oligodendrocytes mimics a form of demeylination where oligodendrocyte apoptosis predominates, and resembles the so-called type III lesions of MS (Franklin and Ffrench-Constant, 2008, Lassmann et al., 2001, Kipp et al., 2009, Hiremath et al., 1998). Hence, this model facilitates testing of several strategies in an easily inducible, very predictable and consistent manner in C57BL/6J strain of mice. The use of this particular strain is advantageous as it bestows an easy comparative analysis with other mouse models for demyelination, such as the *twitcher* mouse that also has the same genetic background. Thus, similar hypotheses can be tested and corroborated in several models of demyelination, and that should lend credence to any discovery (ies) and, perhaps, provide insights in to broad implications of any finding(s). Additionally, there are many genetically altered mice are of the C57BL/6J

genetic background; therefore, comparison of demyelination in these mutant mice to the wild type may further implicate roles for additional effector molecules (Hiremath et al., 1998).

1.18.4. Optic nerve and clinical relevance

Although demyelination has profound effects on axonal function, in most lesions the initial occurrence of demyelination has no detectable consequences for the patient because the lesions may occur in clinically "silent" areas (Lassmann et al., 2001, Waxman, 2005) of the brain where even the local complete destruction of nerve tissue does not produce symptoms and remain asymptomatic. However, optic nerve (ON) lesion always has major consequences for the patient, causing profound neurological deficits (Waxman, 2005, Edgar et al., 2004, Fairless et al., 2012). Development of a lesion in such a neural pathway can produce a clinical relapse. The form of the relapse (e.g., whether it is sensory or motor) and the modality or body part affected are determined directly by the location of the lesion and, thus, by the axons affected. The occurrence of even large lesions with similar pathology in silent areas of the brain would be overlooked by both patient and physician during the life-time, in absence of diagnostic imaging.

ON is one such clinically symptomatic tissue and has always been used for visually evoked potential (VEP) based diagnosis in delineating demyelination-associated features of a suspected patient, before they are identified as clinically defined MS (CDMS) **(Figure 15).** ON or second cranial nerve is sensory in nature which projects from the eye and is a well-studied, characterized system. Here in this study, it is considered as one of the most appropriate tissues for analyzing K_v1 channels of demyelinating axon due to the reasons below:

a) Structurally, it is a CNS nerve fiber exhibiting axon and oligodendrocyte interaction; its axonal conduction is sensitive to 4-AP, a general blocking agent for K_v1 (Kocsis et al., 1986, Smith et al., 2000).
b) A relatively homogenous population of axonal K_v1 channels can be analyzed there.

c) Demyelination can be reproducibly induced.

Anatomically, the eye is protected from mechanical injury by being enclosed in a socket or orbit, derived from several skull bones. These together form a four-sided pyramid like structure, the apex of which points back into the head. The orbit floor comprises parts of maxilla, zygomatic and palatine bones, while the roof is made up of the orbital plate of frontal bone with the sphenoid behind it. Optic foramen forms the opening of the optic canal. The superior surface of the sphenoid bone is bound behind by a ridge, which forms the anterior border of a narrow, transverse groove, the chiasmatic or optic groove. Above and behind it lies the optic chiasm. The groove ends on both side of an optic foramen, from which the ON and ophthalmic artery emerge into the orbital cavity. The ON is ensheathed by the three meningeal layers (dura-meter, arachnoid and pia-meter) rather than epineurium, perineurium and endoneurium of peripheral origin. Since the fiber tracks of CNS (as opposed to peripheral nerves) are incapable of regeneration, and nerve damage readily exhibit vision associated symptoms. These features further strengthen its clinical relevance.

To summarize, the set goal under this PhD project entailed experiments designed to achieve them in four major steps. This involved

- Establishment of a murine model with MS like demyelinating features,
- Verification of CNS axon demyelination in ON
- Identification of changes in K_v1 channel expression of the myelinated axon and
- Elucidation of induced functional deficit (s).

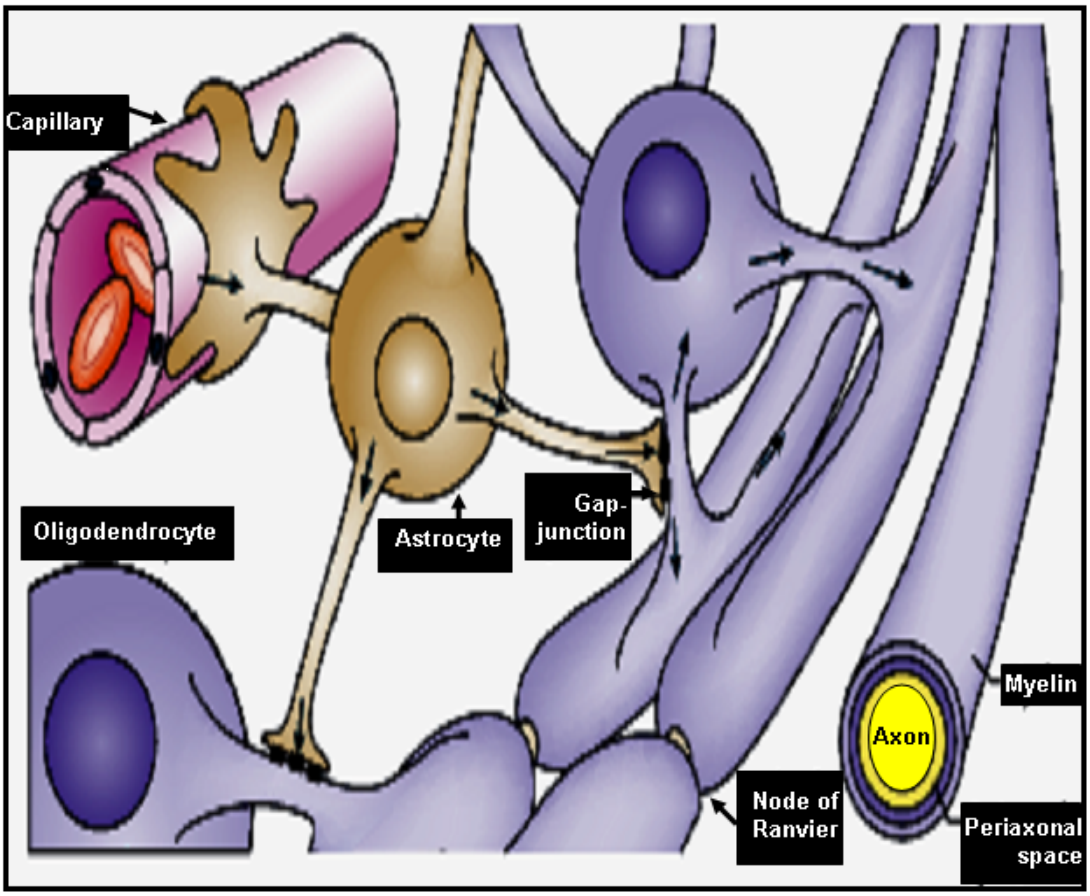
Capillary
Oligodendrocyte
Astrocyte
Gap-
junction
Myelin
Axon
Node of
Ranvier
Periaxonal
space

Figure 1: Axo-glial associations and structure of myelin membrane.

Oligodendrocyte (purple) and astrocyte (brown) processes form a cytosolic perfusion network by coupling of gap junctions in between the cells. This network terminates by adhering to the blood - brain barrier (Nave, 2010b), which form the essential metabolite transport system (shown by black arrows) (Adopted from Nave 2010b).

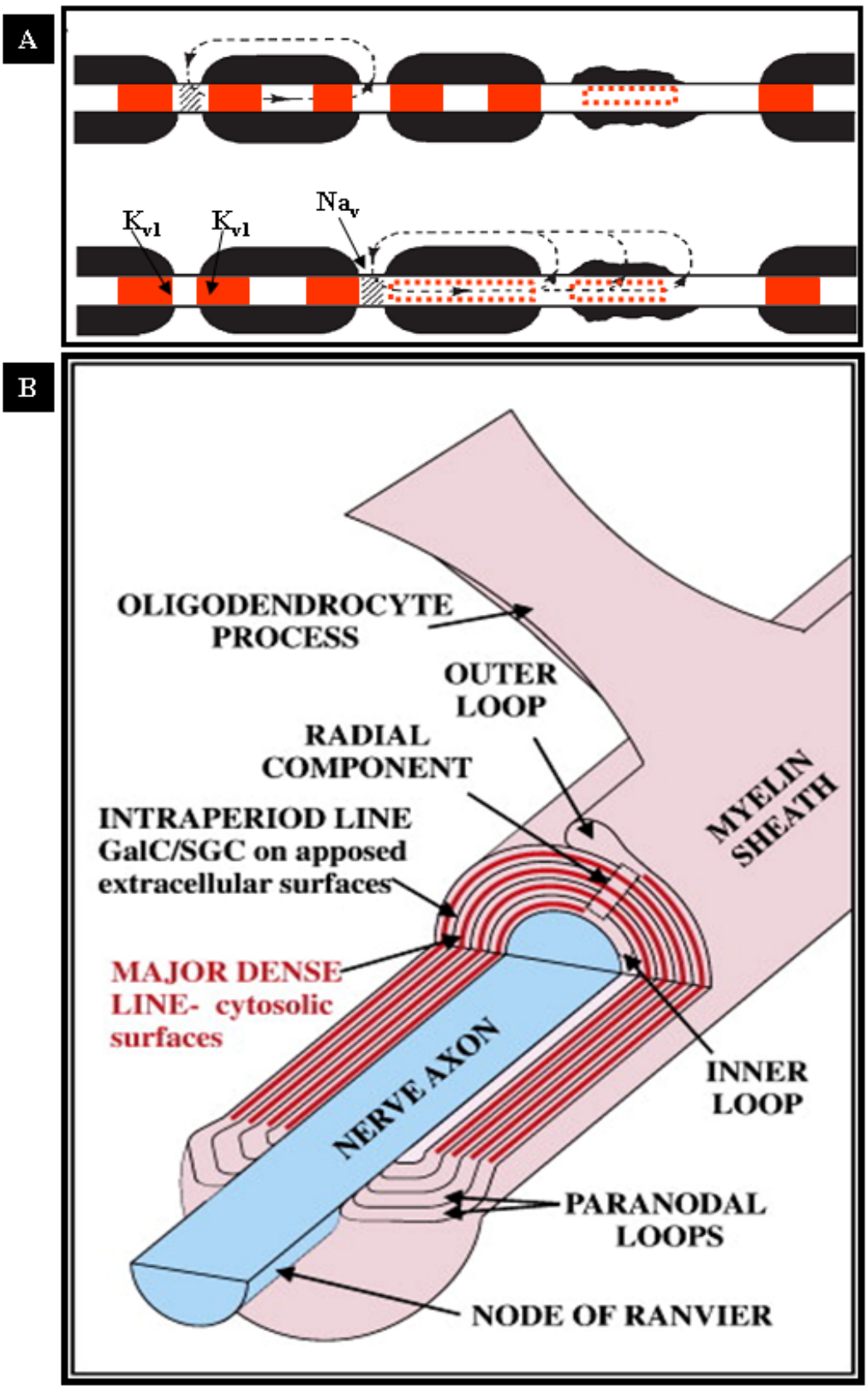
A
K_{v1}
K_{v1}
Na_v
B
OLIGODENDROCYTE PROCESS
OUTER LOOP
RADIAL COMPONENT
INTRAPERIOD LINE
GalC/SGC on apposed extracellular surfaces
MAJOR DENSE LINE- cytosolic surfaces
MYELIN SHEATH
NERVE AXON
INNER LOOP
PARANODAL LOOPS
NODE OF RANVIER

Figure 2: Axo-glial associations for conduction.

A. *Myelin enables the axon with saltatory conduction such that the action potentials travel from one node to the other (dashed line) which is staggered and interrupted due to demyelination and becomes discontinuous. Discrete location of juxtaparanodal* K_v1 *(orange color) and nodal* Na_v *(shaded region) on the axons plays a vital role for this mode of conduction, which are adversely affected (dashed orange lines) in demyelination.* ***B****. Diagrammatic representation of an oligodendrocyte process which forms myelin sheath. It is formed by thick dense stacked layers of membranes (Meister and Berry, 1999) which surround the axon. Myelin membranes face each other on apposed extracellular surfaces at the intraperiod line (thin black line) in compact myelin. Cytosolic surfaces adhere at the major dense line (red line) which is mediated by MBP. The paranodal outer and inner loops contain glial cytosol. The radial component consists of a series of tight junctions and contains actin, and tubulin.*

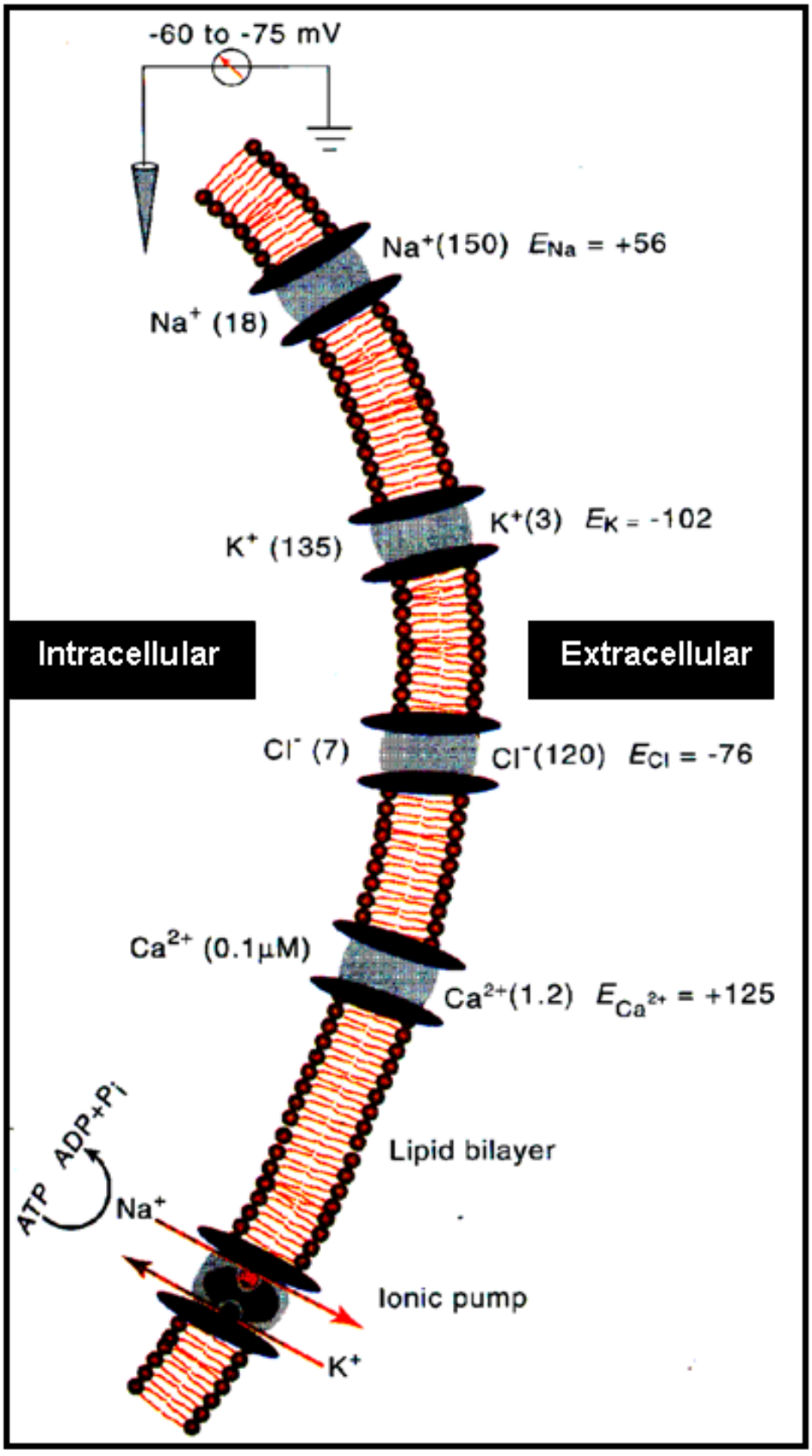
-60 to -75 mV
Na+(150) ENa = +56
Na+ (18)
K+(3) EK = -102
K+ (135)
Intracellular
Extracellular
Cl- (7)
Cl-(120) ECl = -76
Ca2+ (0.1μM)
Ca2+(1.2) ECa2+ = +125
Lipid bilayer
ATP
ADP+Pi
Na+
Ionic pump
K+

Figure 3: Electrochemical gradient, ion channels and transporters of a neuronal membrane.

Distribution of ions inside and outside the plasma membrane of neurons and neuronal processes, showing ionic channels for Na^+, K^+, Cl^-, and Ca^{2+}, as well as an electrogenic Na^+-K^+ ionic pump. Concentrations (in millimoles except that for intracellular Ca^{2+}) of the ions are given in parentheses; their equilibrium potentials (E_{Na}, E_k, E_{Cl}, E_{Ca}) for a typical mammalian neuron are indicated (Charand, 2012) http://hyperphysics.phy-astr.gsu.edu/hbase/biology/actpot.html) accessed on 1st May 2012.

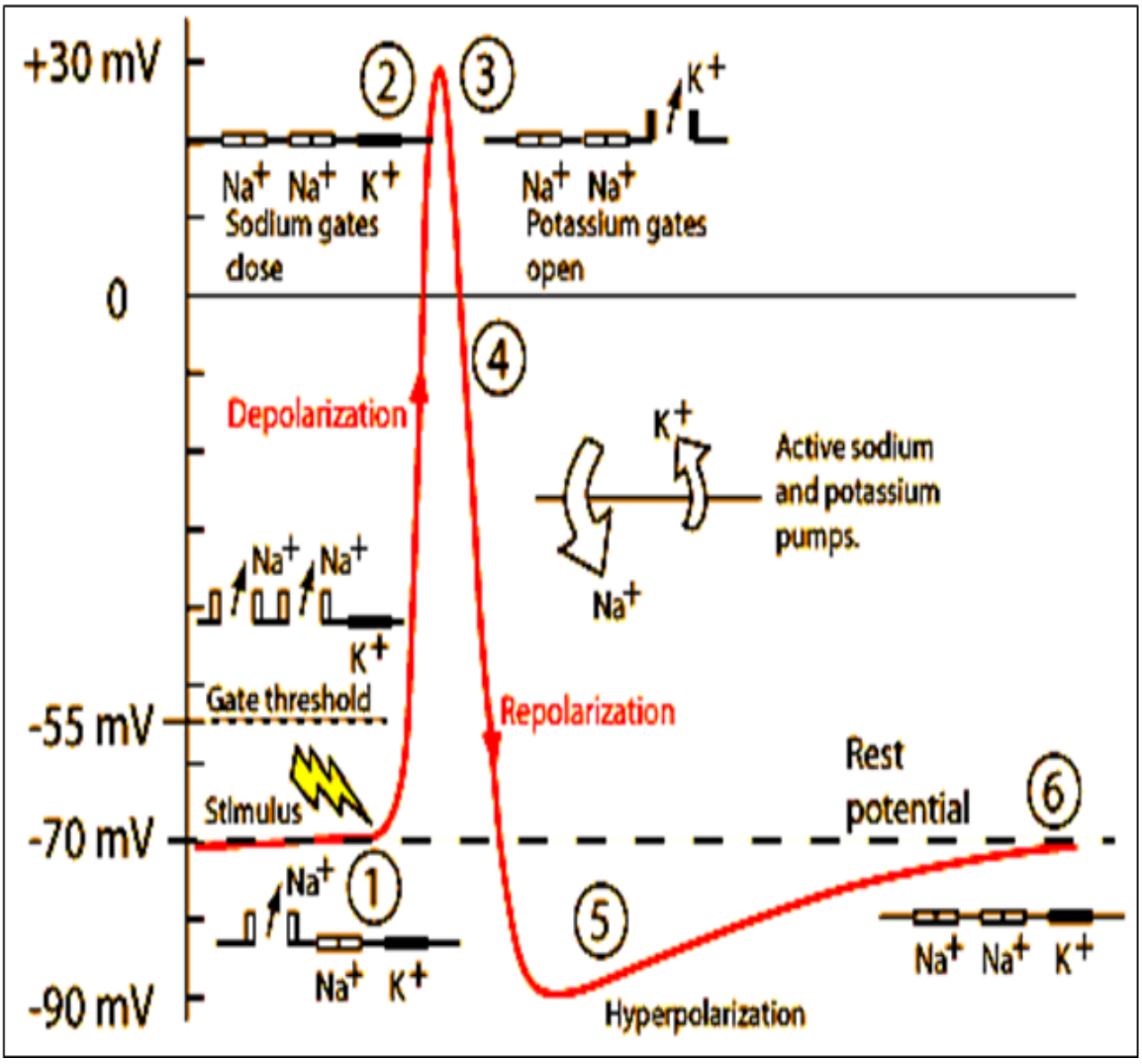
+30 mV
0
-55 mV
-70 mV
-90 mV
2
3
Na+ Na+ K+
Sodium gates close
Na+ Na+
K+
Potassium gates open
4
Depolarization
K+
Active sodium and potassium pumps.
Na+
Na+ Na+
K+
Gate threshold
Repolarization
Rest potential
6
Stimulus
1
Na+
Na+ K+
5
Hyperpolarization
Na+ Na+ K+

Figure 4: Electrochemical gradient and involvement of ion channels and transporters in action potential generation.

Action potential generation and the role of K_v and Na_v ion channels in depolarization (1 & 2) repolarization (3 & 4) and hyperpolarization (5 & 6) phases (Charand, 2012) http://hyperphysics.phy- astr.gsu.edu/hbase/biology/actpot.html) accessed on 1st May 2012. This involves several steps 1-6 as shown in the schematic representation.

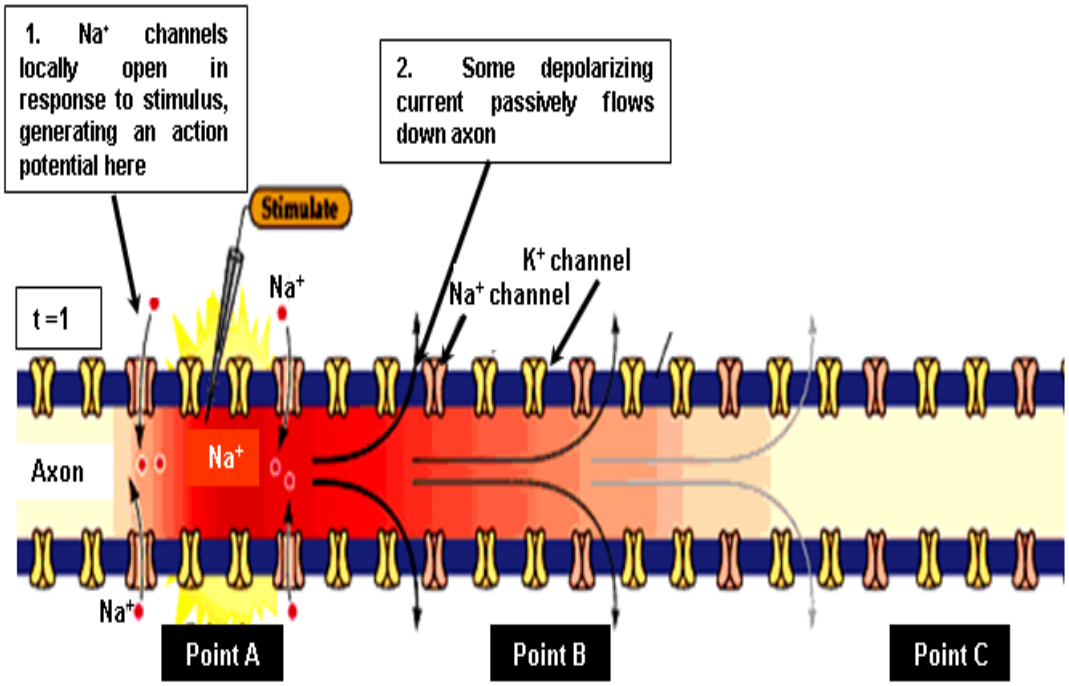
1. Na+ channels locally open in response to stimulus, generating an action potential here
2. Some depolarizing current passively flows down axon
Stimulate
Na+
K+ channel
Na+ channel
t =1
Axon
Na+
Na+
Point A
Point B
Point C

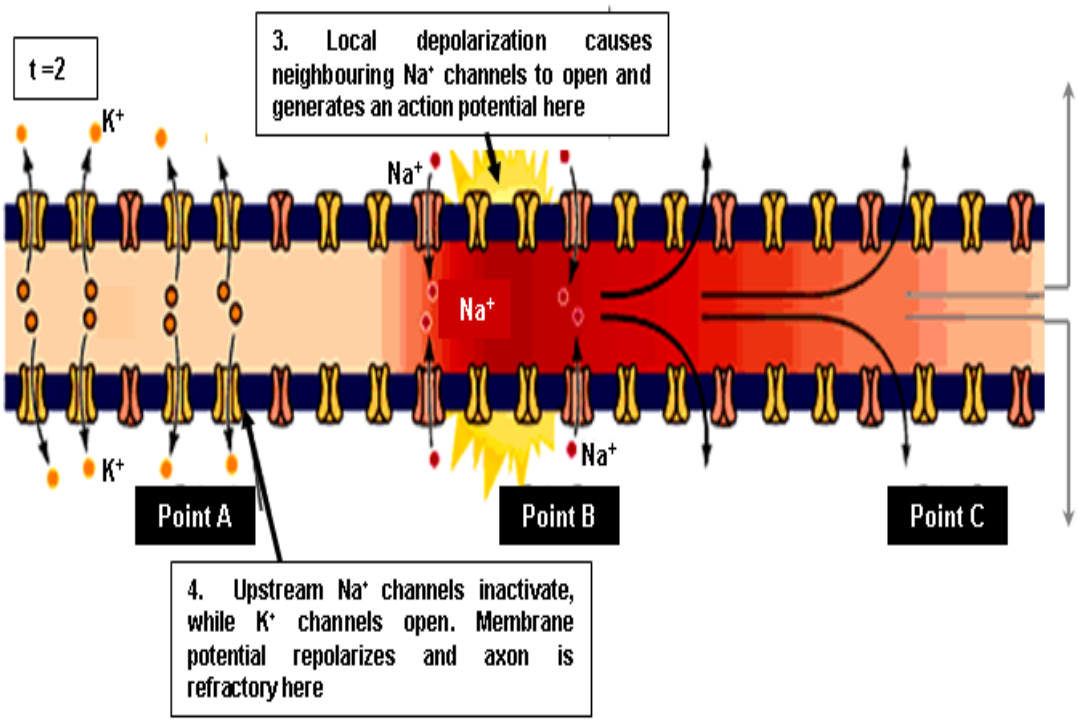
t =2
3. Local depolarization causes neighbouring Na+ channels to open and generates an action potential here
K+
Na+
Na+
K+
Na+
Point A
Point B
Point C
4. Upstream Na+ channels inactivate, while K+ channels open. Membrane potential repolarizes and axon is refractory here

Figure 5: Action potential propagation in an unmyelinated axon.

Synchronised and sequential activation of Na_v and K_v channels lead to propagation of action potentials. The axon has been represented at two time points (t1 and t2) to demonstrate the upstream (point A) and downstream (point B, C) effects of a stimulus. The inactivation of upstream Na_v channels ensures unidirectional propagation of action potential. Top panel shows the generation of action potential in response to a stimulus, which opens Na_v channels, and the bottom panel show the opening of neighbouring Na_v channels due to local depolarization. These events lead to the propagation of action potential (Fleming, 2012) http://www.arts.uwaterloo.ca/~bfleming/psych261/lec4se21, accessed on 1st May 2012.

Action potential propagation

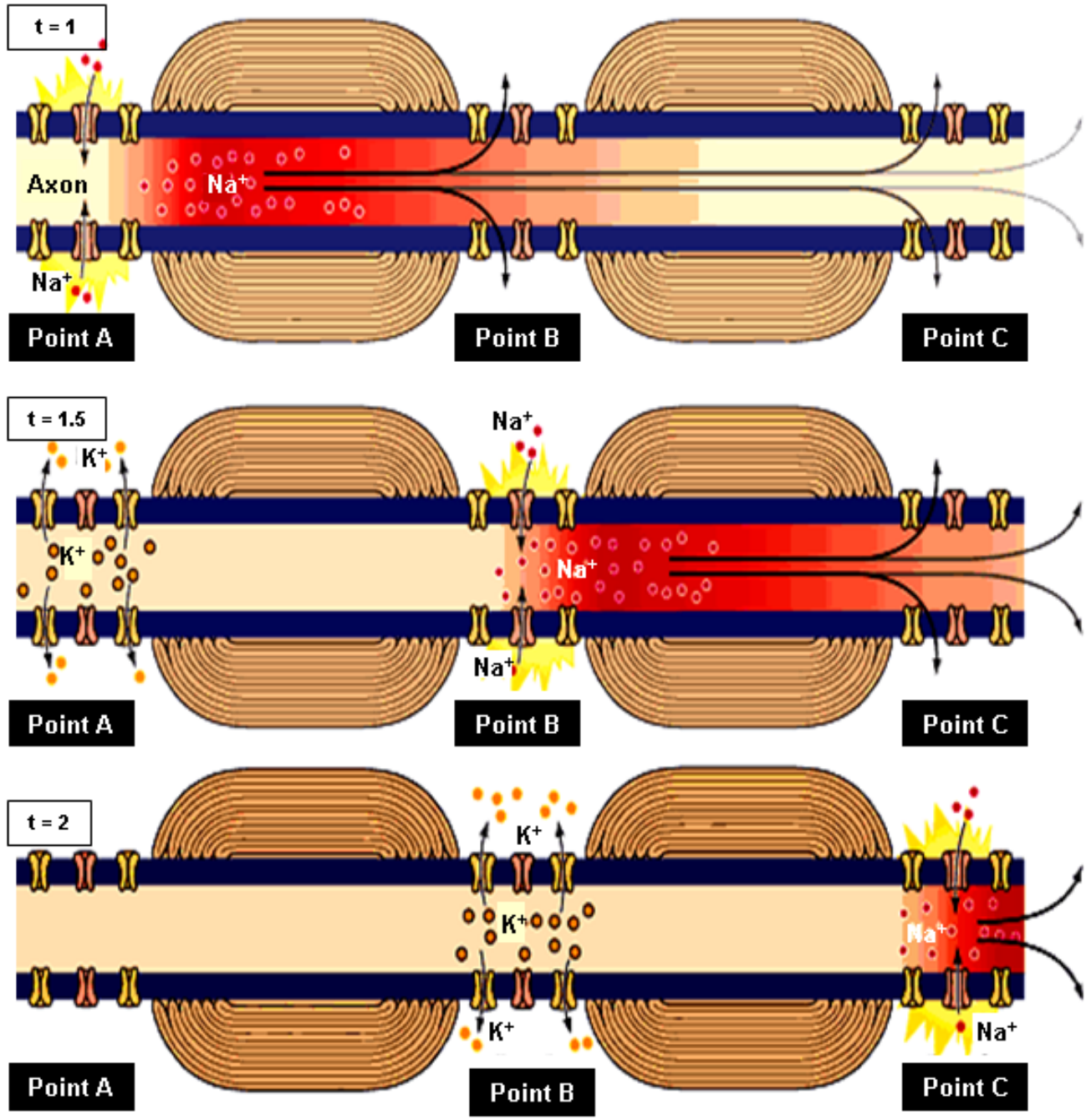

Figure 6: Myelination of axon is a specialization for saltatory conduction.

Synchronised activity of Na_v channels at the node (point A, B and C) and JXP K_v channels (red gradient along the axoplasm) lead to action potential propagation from one node to another node, thus allowing a fast movement in such axons. Note from Fig. 3, where the distance travelled by the action potential is less within the same time as compared to this case when the axon is myelinated (t1, t1.5 and t2 represent the time points). This highlights the benefits of sub-compartmentalised structure of this type of axon (Fleming, 2012) http://www.arts.uwaterloo.ca/~bfleming/psych261/lec4se21, accessed on 1st May 2012.

.

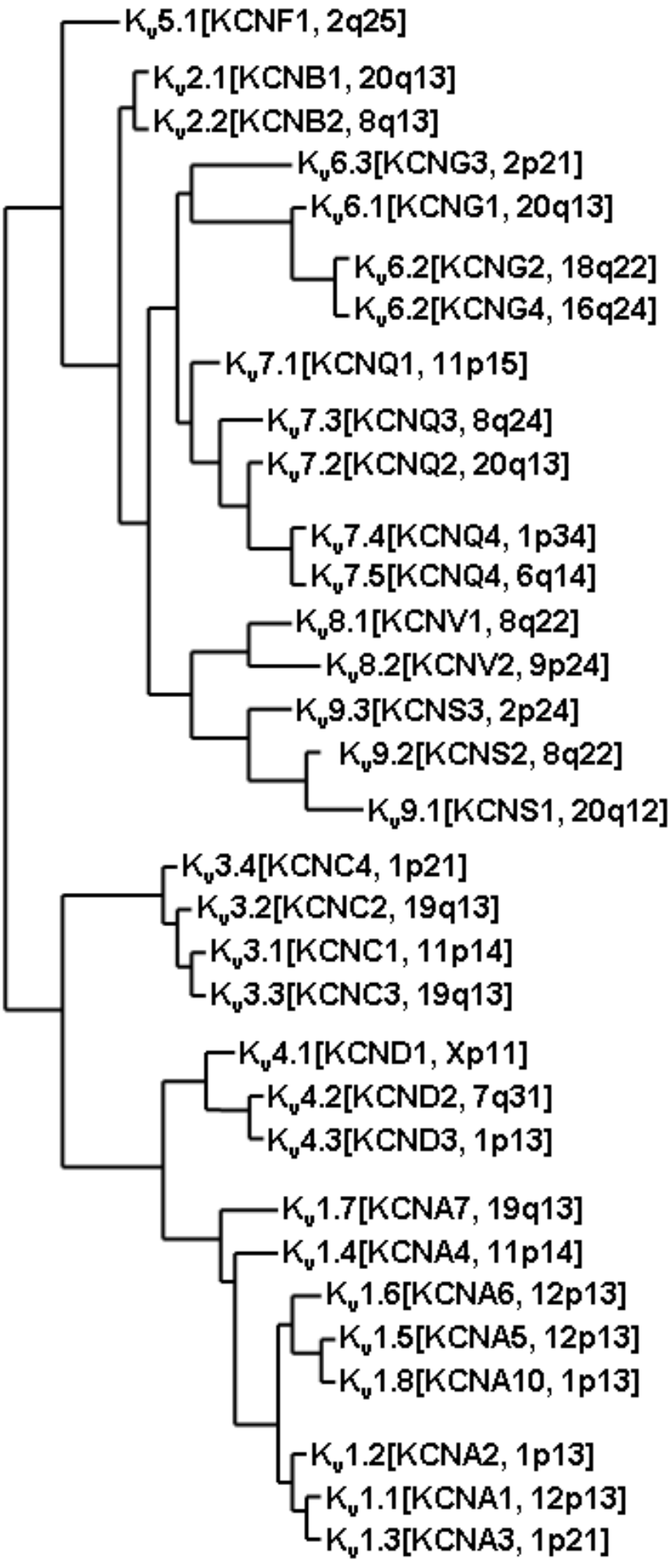
K_v5.1[KCNF1, 2q25]
K_v2.1[KCNB1, 20q13]
K_v2.2[KCNB2, 8q13]
K_v6.3[KCNG3, 2p21]
K_v6.1[KCNG1, 20q13]
K_v6.2[KCNG2, 18q22]
K_v6.2[KCNG4, 16q24]
K_v7.1[KCNQ1, 11p15]
K_v7.3[KCNQ3, 8q24]
K_v7.2[KCNQ2, 20q13]
K_v7.4[KCNQ4, 1p34]
K_v7.5[KCNQ4, 6q14]
K_v8.1[KCNV1, 8q22]
K_v8.2[KCNV2, 9p24]
K_v9.3[KCNS3, 2p24]
K_v9.2[KCNS2, 8q22]
K_v9.1[KCNS1, 20q12]
K_v3.4[KCNC4, 1p21]
K_v3.2[KCNC2, 19q13]
K_v3.1[KCNC1, 11p14]
K_v3.3[KCNC3, 19q13]
K_v4.1[KCND1, Xp11]
K_v4.2[KCND2, 7q31]
K_v4.3[KCND3, 1p13]
K_v1.7[KCNA7, 19q13]
K_v1.4[KCNA4, 11p14]
K_v1.6[KCNA6, 12p13]
K_v1.5[KCNA5, 12p13]
K_v1.8[KCNA10, 1p13]
K_v1.2[KCNA2, 1p13]
K_v1.1[KCNA1, 12p13]
K_v1.3[KCNA3, 1p21]

Figure 7: Phylogenetic tree of K_v1–9 channel families.

Classification of human K_v channels on the basis of amino acid sequence alignments represented as trees comprising the K_v1-K_v6 and K_v8-K_v9 families. IUPHAR and HGNC names are shown together with the genes' chromosomal localization and other commonly used names (Gutman et al., 2005).

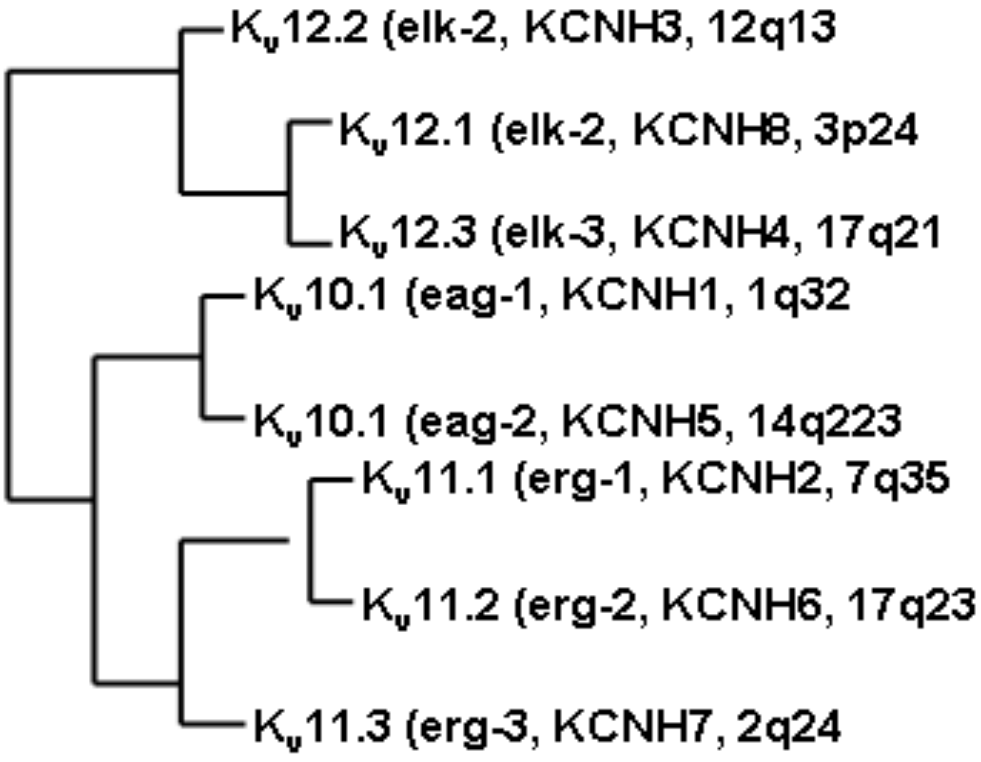

Figure 8: Phylogenetic tree of K_v10–12 channel families.

The IUPHAR and HGNC names are shown together with the genes' chromosomal localization and other commonly used names (Gutman et al., 2005).

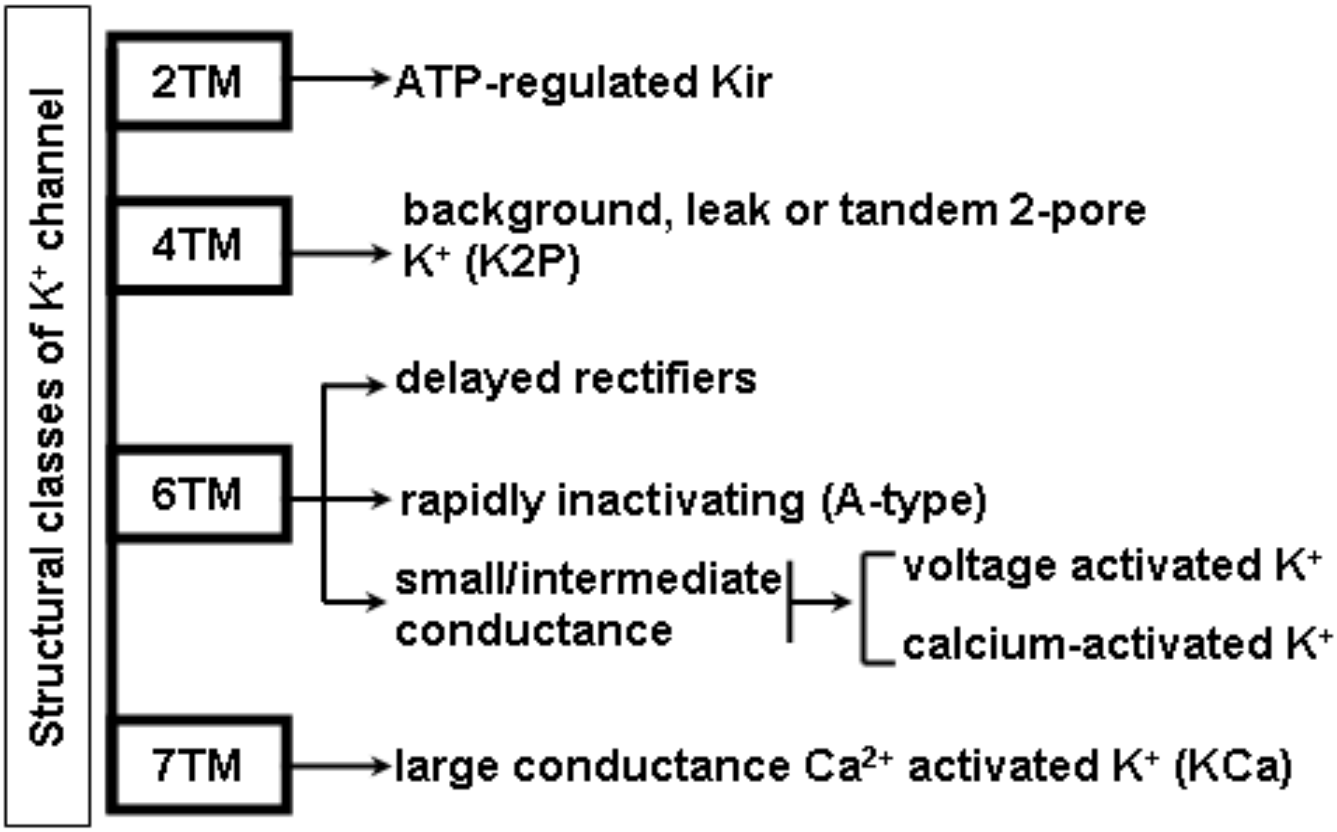

Figure 9: Structural classes of K_v channels.

Four major classes of K_v channels based on the number of TM spanning units and their functional relevance.

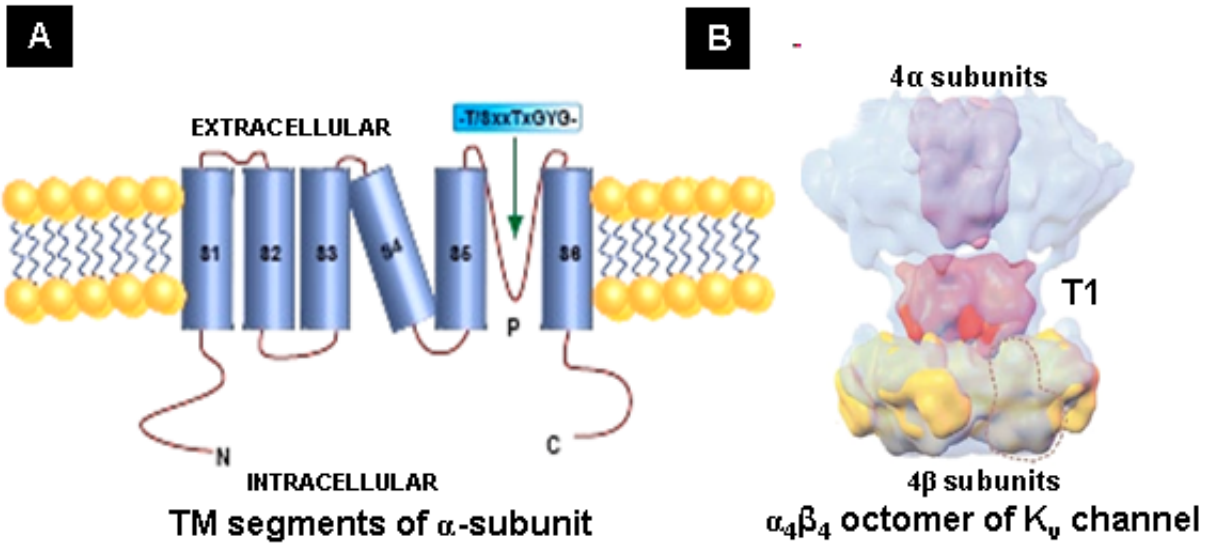
A
EXTRACELLULAR
S1
S2
S3
S4
S5
S6
P
N
C
INTRACELLULAR
TM segments of α-subunit
B
4α subunits
T1
4β subunits
α4β4 octomer of Kv channel

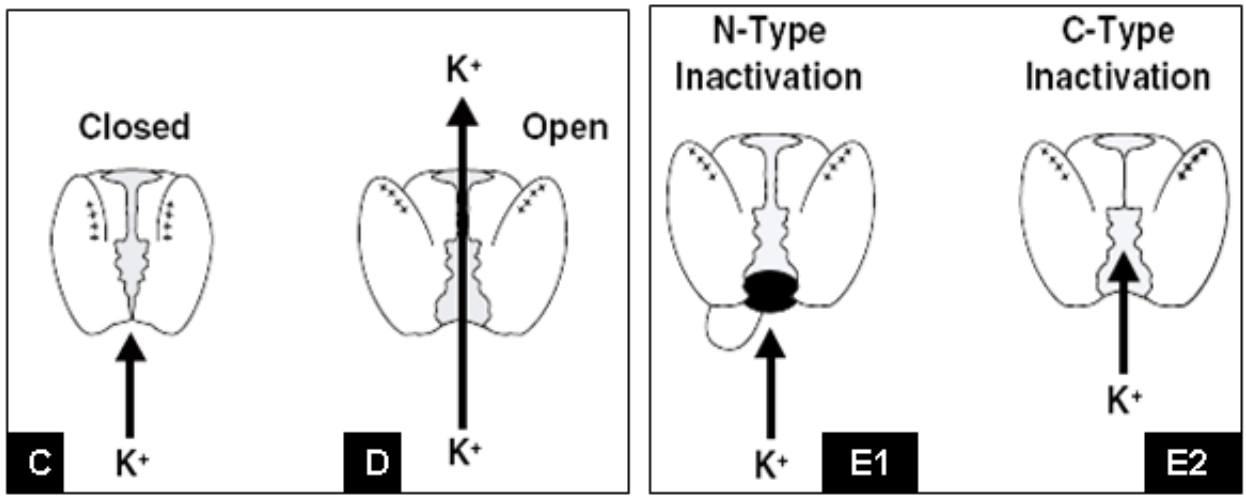
Closed
Open
K+
C
D
N-Type
Inactivation
C-Type
Inactivation
E1
E2

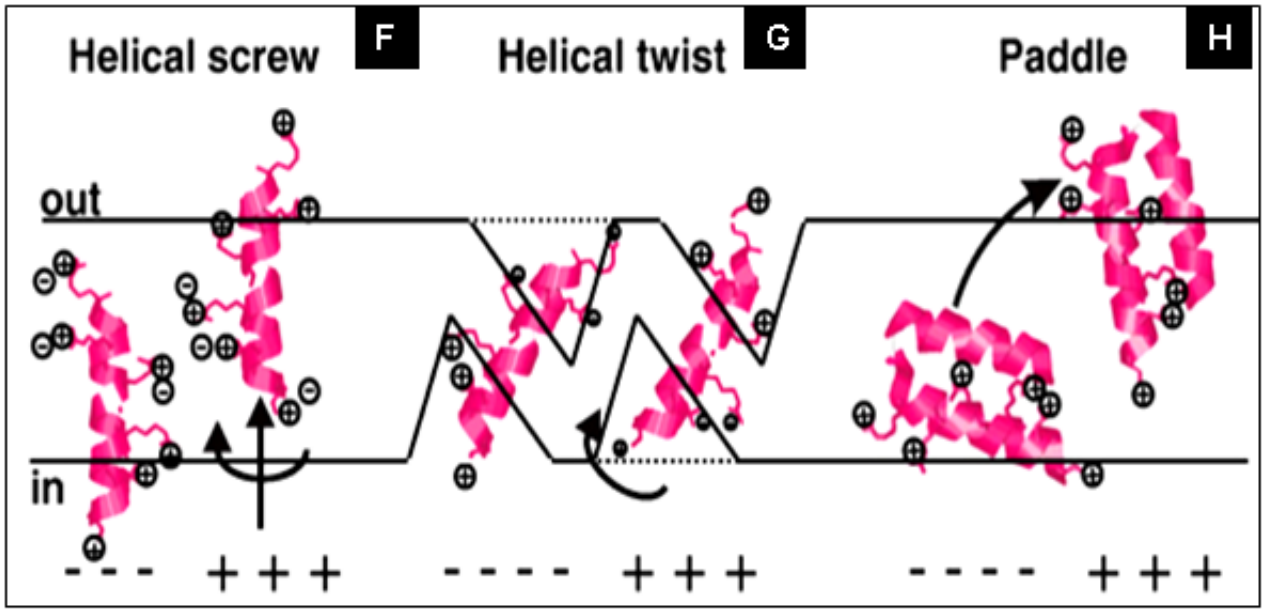
Helical screw
F
Helical twist
G
Paddle
H
out
in

Figure 10: Schematic presentation of K_v channel in various conformations and TM voltage sensing models.

A. *K_va-subunit has a 6TM structure (S1-S6), with a P-loop in between S5 and S6. The N- and C-terminus are intracellular.* ***B.****Octomeric K_v channel has 4a-subunits and 4β-subunits and a T1 domain where N- terminus of each subunit tetramerize to acquire this conformation (Orlova et al., 2003).* ***C.*** *Schematic view of closed, non-conducting channel, and* ***D.*** *Open, conducting channel in which the voltage sensor region (lined by +ve charges) has moved up and out so that the critical S4 charges are accessible from the extracellular surface* ***(Fig. 9A-C). E1.*** *Open, non-conducting channel following N-type inactivation in which the channel is occluded by the binding of the N-terminus 'ball' in a rapidly inactivating K^+ channel, at the intracellular mouth of the pore.* ***E2****. Open, non-conducting channel in which the process of C-type inactivation has produced a molecular rearrangement closing the selectivity filter* ***(Fig. 9B, C)*** *(Judge and Bever, 2006). Three molecular models for location and movement of S4 voltage sensor* ***(F, G, H)*** *after activation of the channel namely helical screw* ***(F)****, helical twist* ***(G)*** *and paddle* ***(H)****.*

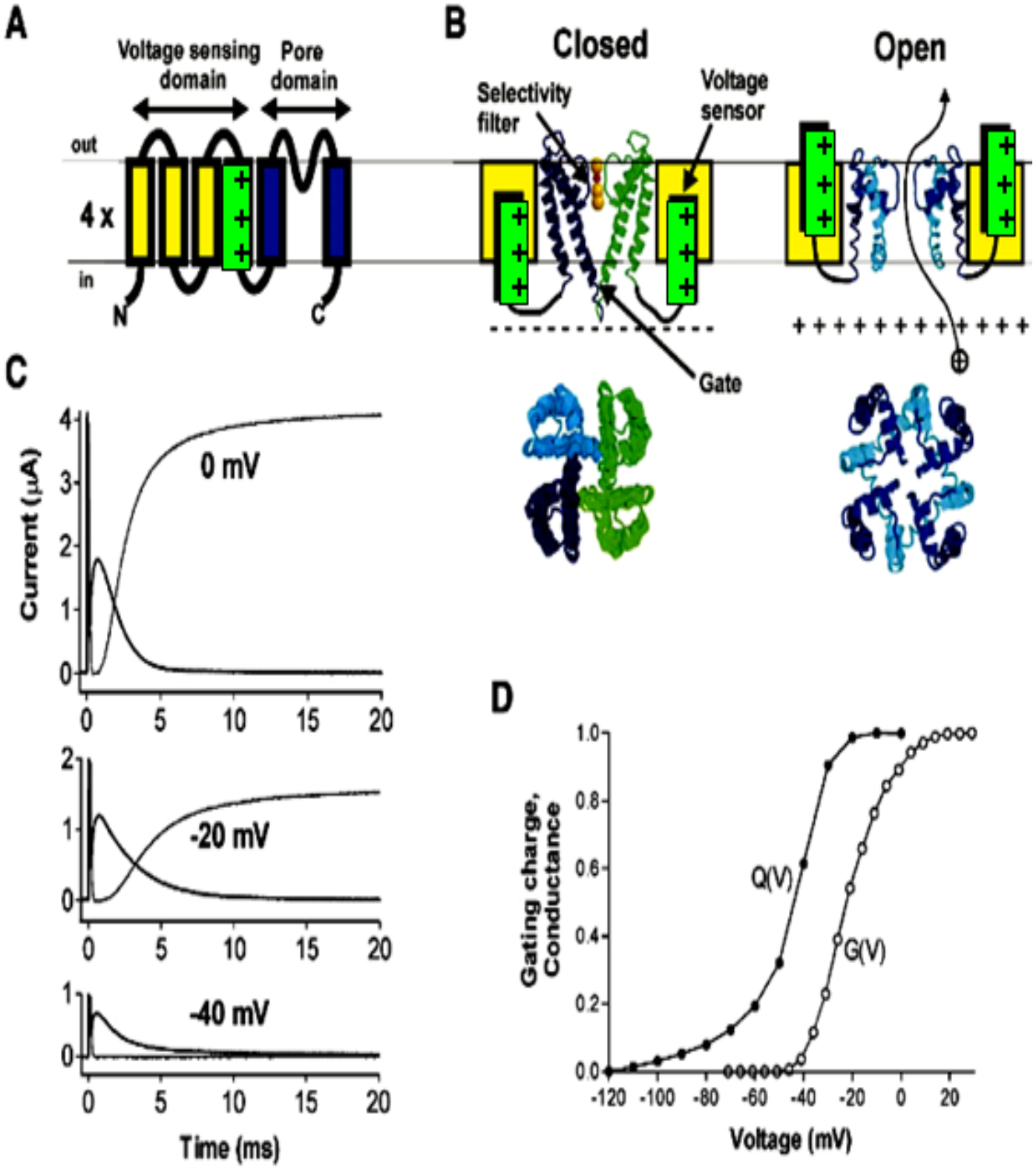
A
Voltage sensing domain
Pore domain
out
4 x
in
N
C
B
Closed
Open
Selectivity filter
Voltage sensor
Gate
C
Current (μA)
0 mV
-20 mV
-40 mV
Time (ms)
D
Gating charge, Conductance
Q(V)
G(V)
Voltage (mV)

Figure 11: Conformational and structural changes of K_v channels regulate their kinetics and functional properties.

A. *Topology of a-subunit in a 6TMchannel, showing voltage sensing domain and the pore domain. Left to right are S1 to S6 TM segments. Four such subunits make an octomeric ion channel.* ***B***. *Structural working hypothesis of voltage-gated 6TM ion channels in closed and open configurations. Pore domain of a closed (KcsA), and open channel Methanobacterium thermoautotrophicum (MthK). For clarity only two subunits are shown in the side view (upper part). Views from the extracellular side (lower part).* ***C.*** *Ion currents (thin line) and gating currents (thick line) at the voltages indicated. Voltage-clamp technique based study in Xenopus oocyte at a holding potential (-100mV) show ion currents measured from wild-type K_v channels and gating currents measured from non-conducting mutant K_v channels.* ***D.*** *Integrated gating current vs. voltage, Q (V), and conductance vs. voltage, G (V) (Elinder et al., 2007).*

A

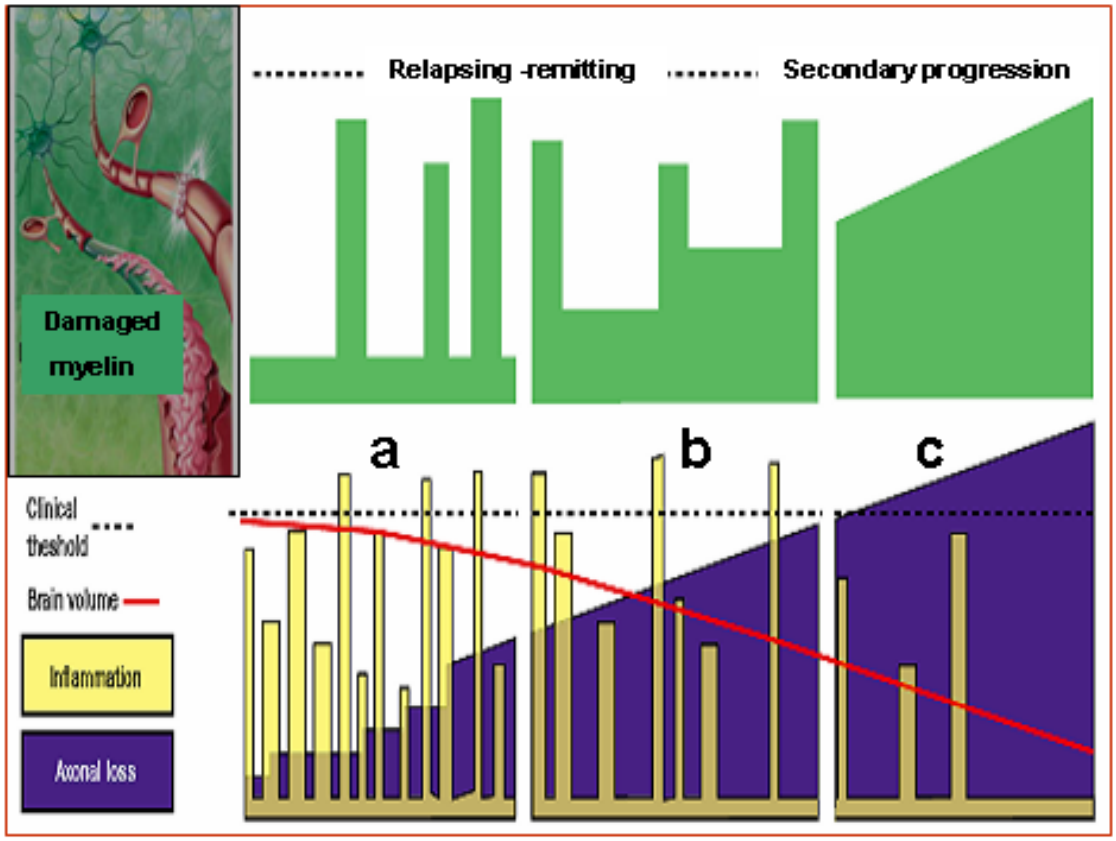
Relapsing -remitting
Secondary progression
Damaged myelin
a
b
c
Clinical theshold
Brain volume
Inflammation
Axonal loss

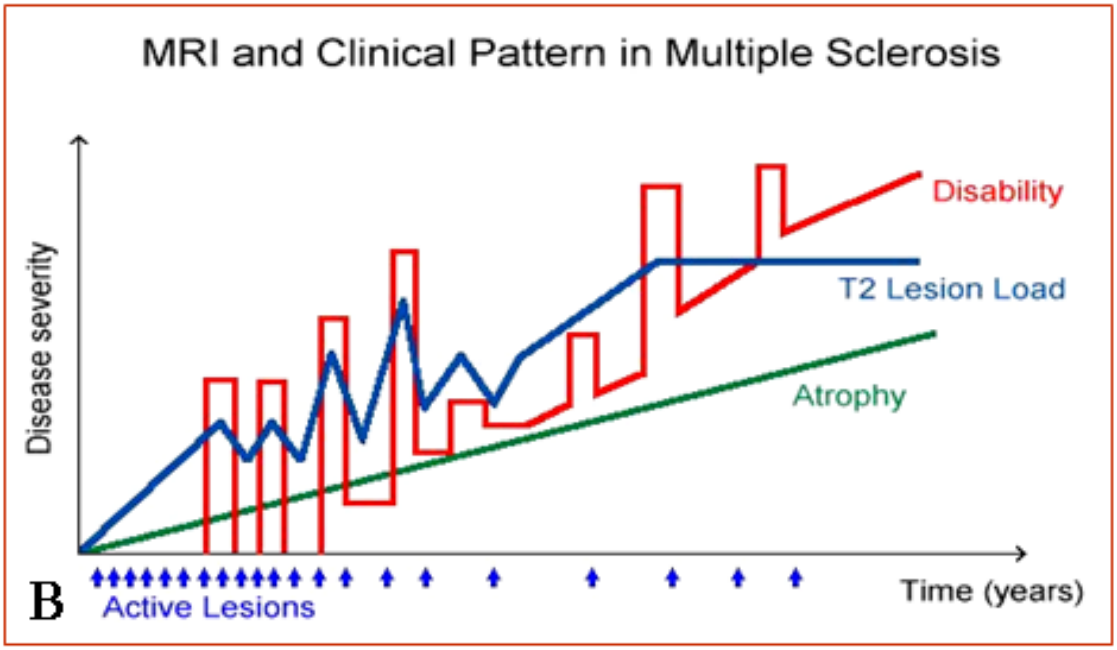
MRI and Clinical Pattern in Multiple Sclerosis
Disease severity
Disability
T2 Lesion Load
Atrophy
Time (years)
Active Lesions

B

Figure 12: MS pathogenesis, course of neurological disability and therapeutic intervention(s).

A. *MS pathogenesis during the clinical phases of relapsing remitting and secondary progressive phase involve loss of myelin or demyelination (left corner). Disease onset* ***(a)*** *involves frequent inflammation (yellow bars), along with demyelination (purple plateau region), axonal transaction plasticity and remyelination. Subsequent phase is marked by continued inflammation and persistent demyelination* ***(b)*** *but, in the last progressive phase is featured by gradual waning of inflammation, accompanied with axon degeneration and gliosis* ***(c).*** *Clinical threshold (dashed line) when immuno-therapeutic interventions are used to contain the disease progression is limited until the onset it reaches the progressive phase. Early events of axon loss at the onset continue till the late phase leading to loss of brain volume (red line).* ***B.*** *Even though axonal loss (purple) begins very early on, it is diagnosed at a much later phase when brain atrophy (green line) and disability levels (red line) of the patient are very high. This is demonstrated in the T2 lesion load (blue line) of clinical diagnosed based on MRI. Active lesions labelled on the X axis of (B) indicate the patient age at disease onset (20-40 yrs) till the terminal time point reflecting prolonged disabling survival phase of the patient (Compston and Coles, 2002)*

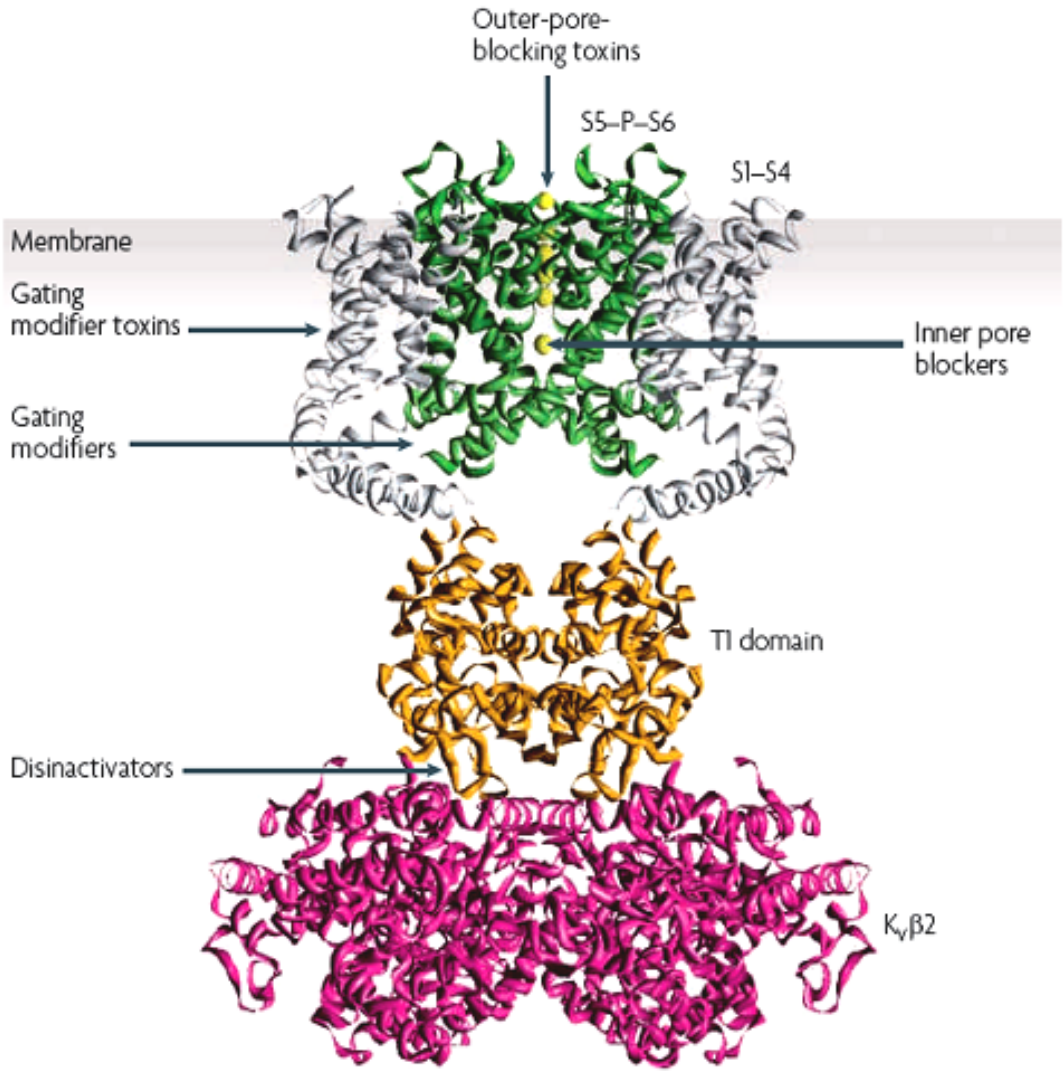
Outer-pore-
blocking toxins
S5–P–S6
S1–S4
Membrane
Gating
modifier toxins
Inner pore
blockers
Gating
modifiers
T1 domain
Disinactivators
$K_v\beta2$

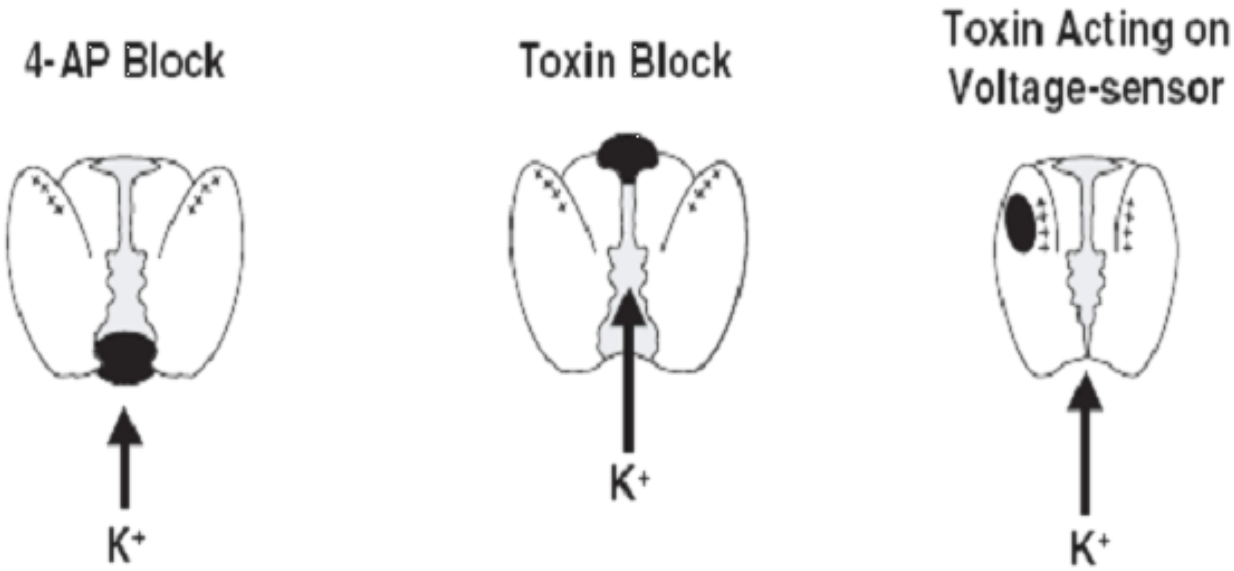
4-AP Block
Toxin Block
Toxin Acting on
Voltage-sensor
K+
K+
K+

Figure 13: K_v channel blocking strategies.

Structural illustration of K_v1.2 channel highlighting domains and sites of action for various types of blockers (Eunson et al., 2000). S5–P–S6 regions are shown in green the voltage sensor domain (S1–S4) light grey, tetramerization (T1) domain in orange and the intracellular $K_v\beta$2 subunit in magenta. Outer- and inner- pore, blocking toxins obstruct the pore domains, gating modifiers interact with S1-S4 segments, and disinactivators disrupt $\alpha\beta$ association. For clarity, only two of the four subunits are shown (Wulff et al., 2009). In the bottom panel (left) an open, non-conducting channel in which 4-AP molecule has gained access to its intracellular binding site thereby occludes the channel. An open non-conducting channel gets blocked due to toxin binding at the extracellular pore surface (bottom middle panel). Bottom right panel shows a condition when closed, non-conducting channel in which a voltage-sensor-modifying toxin molecule has partitioned into the membrane lipid bilayer binds to the voltage sensor region (at the S3 segment) inducing closure of the channel (Judge and Bever, 2006).

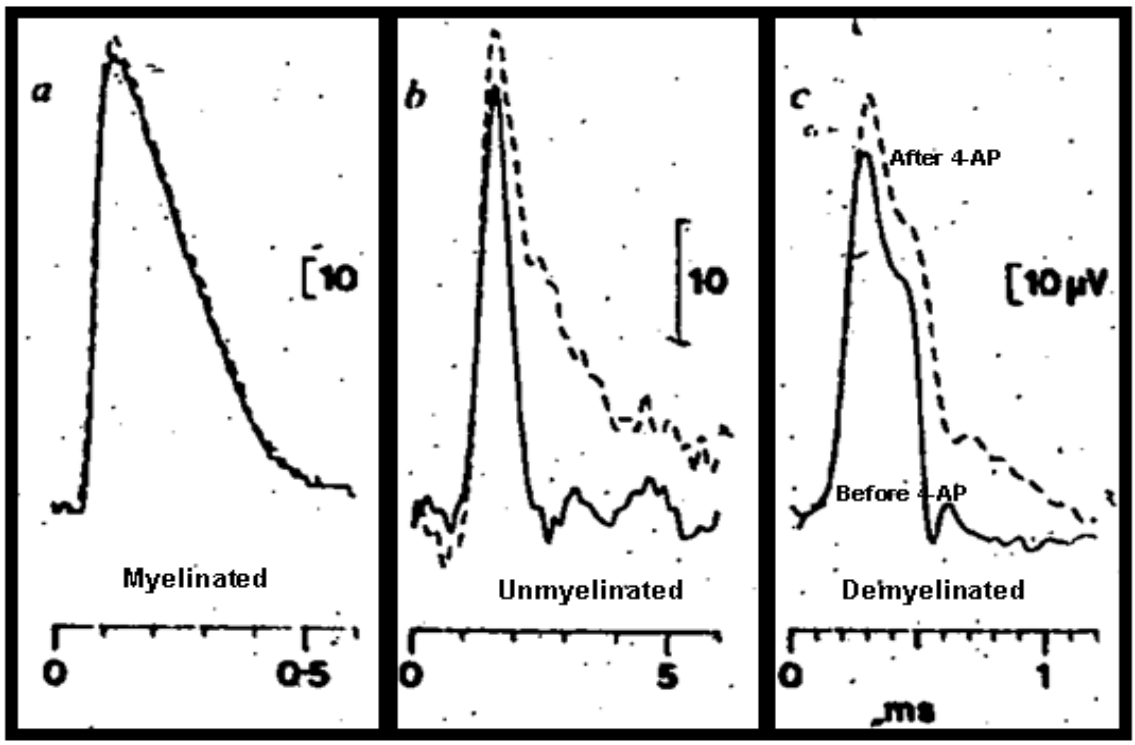
a
10
Myelinated
0
0·5
b
10
Unmyelinated
0
5
c
After 4-AP
10 μV
Before 4-AP
Demyelinated
0
1
ms

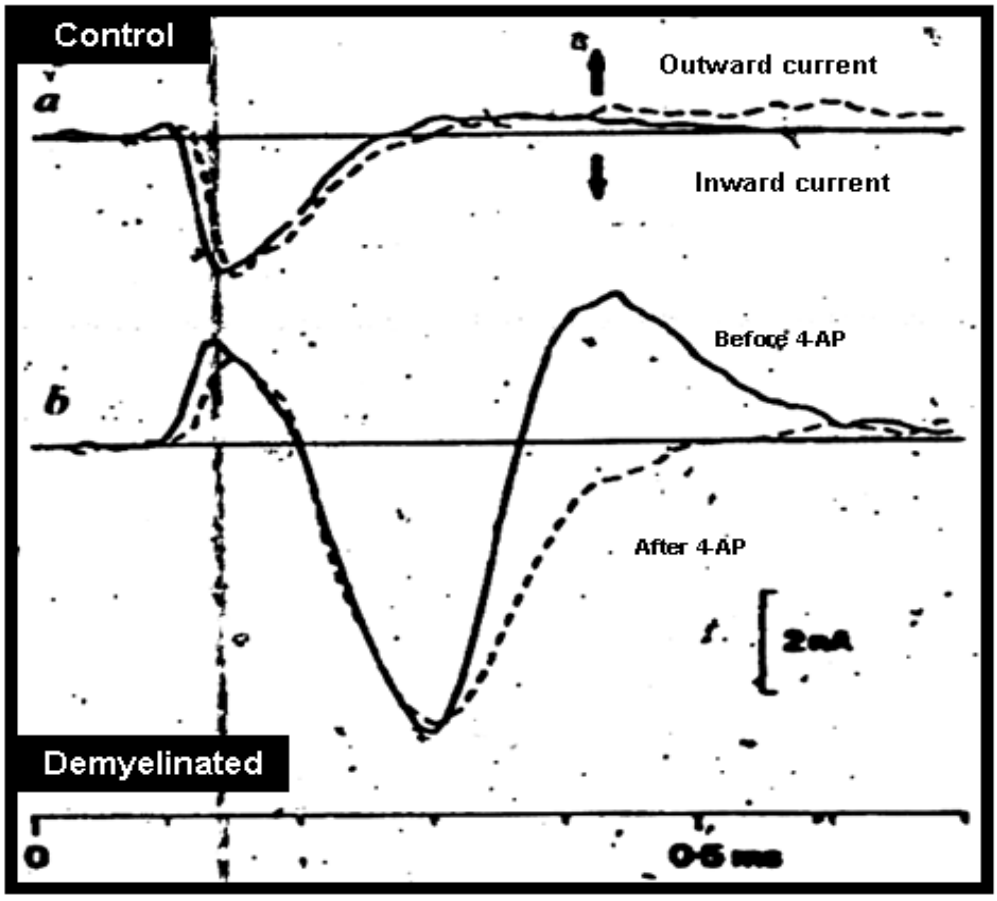
Control
a
Outward current
Inward current
b
Before 4-AP
After 4-AP
2nA
Demyelinated
0
0·5 ms

Figure 14: K_v channel blocking and restoration of conduction.

Blocking of K_v channels in demyelination has restorative effect has been identified much early on nearly two and half decades back. Effect of 4-AP (dashed line) on CAP in rat dorsal root ganglion, can distinguish the myelinated and unmyelinated components (top left and middle). It does not have any effect on a myelinated axon (top left). The unmyelinated and demyelinated (top middle and right panel) axons exhibit broadening of the CAP base indicating the presence of exposed K_v channels. (Sherratt et al., 1980)Bottom panel demonstrates the effect of 4-AP on membrane currents of two consecutive nodes 1mm apart in control and demyelinated axon. Solid lines and dashed lines represent before and after 4-AP application. Note the emergence of second hump, which disappears upon application of 4-AP (Sherratt et al., 1980).

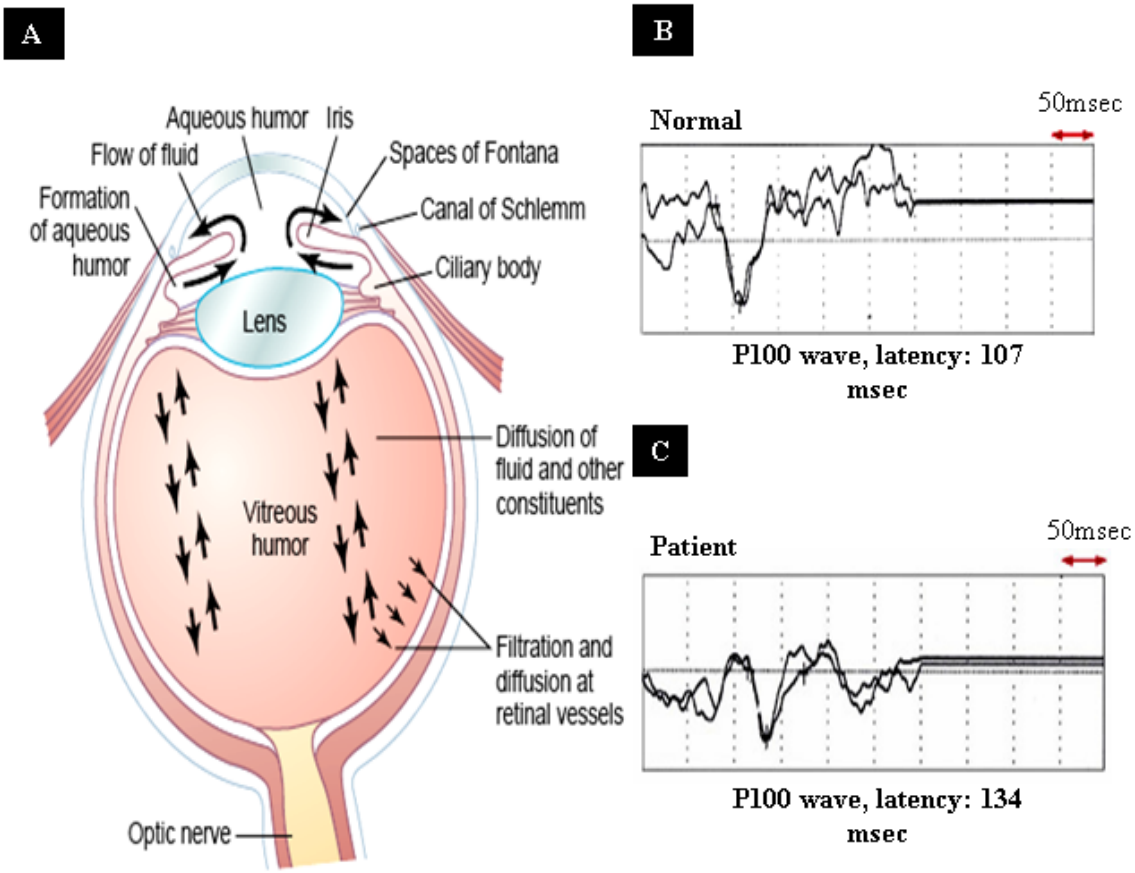
A
Aqueous humor
Iris
Flow of fluid
Spaces of Fontana
Formation of aqueous humor
Canal of Schlemm
Ciliary body
Lens
Diffusion of fluid and other constituents
Vitreous humor
Filtration and diffusion at retinal vessels
Optic nerve
B
Normal
50msec
P100 wave, latency: 107 msec
C
Patient
50msec
P100 wave, latency: 134 msec

Figure 15: Anatomy of eye and clinical relevance of ON.

A. *Organisation of eye showing various chambers, lens, retina, origin of ON and muscles involved in the visual process.* ***B****. Difference in latency is depicted in VEP recordings due to onset of demeylination in MS. A comparison of P100 wave or trace from the recording demonstrates increase in latency from 107msec of a normal case to 134msec in abnormal or affected individual (****C****). Adopted and accessed from University of Utah, School of Medicine, website on 30th November 2011, Webpage, Visual Evoked Potentials in a Patient with Multiple Sclerosis, John Rose, M.D.* *http://library.med.utah.edu/kw/ms/mml/ms_vep.html*

CHAPTER 2

MATERIALS AND METHODS

2.1. Animal husbandry, mouse strain and cuprizone treatment

Male C57BL/6J mice (8 weeks old) were acquired under import license from Harlan, UK. They were kept under controlled housing conditions (ambient temperature 27-28ºC, humidity 36%, lights on from 6.00am to 6.00pm) in certified Bio-Resource Unit (BRU) at Dublin City University and handled by trained animal technicians. The mice were provided with *ad libitum* access to water and food. The technique for oral administration of CZ was approved by the Department of Health and Children in Ireland and conformed to relevant EU regulations. The designed experiments were peer reviewed by the University's REC (Review Ethics Committee) and supervised by a consultant veterinary surgeon. These were in compliance with the European Communities Council Directive of 24th November 1986 (86/609/EEC), under the license number BE100/3609. Prior to the introduction of feeding protocol, they were ensured their health and absence of any obvious abnormality. They were acclimatized for 3-4 days under normal housing conditions at BRU facility and then grouped as 4/cage for each experimental and control conditions. The treated (T) and normal control (UT) populations were housed in separate cages. Daily monitoring sheets were maintained to record the details of their weight, feeding and drinking pattern.

Groups under treatment received Modified LabDiet® (Laboratory Rodent Diet) 5001 with CZ (5TBI – 1810588, ½" pellet). This special feed was prepared by IPS Product Supplies Limited, London, UK, by including 0.2% CZ (bis-cyclohexanone oxaldihydrazone; Sigma-Aldrich Inc., St. Louis, MO) in normal laboratory rodent diet 5001. The feed was stored at 4ºC before opening the bags and once opened they were stocked in airtight containers to avoid oxidation of the added compound. All opened bags were consumed within 4 months. Each lot of mice were administered this special diet for 8 weeks following which the experiments were conducted or samples prepared and saved at appropriate temperature

(4ºC, -20ºC) until used. All efforts were made to minimize animal suffering and reduce their number.

2.2. Determination of brain myelin content and demyelination

Homogenization of CNS tissue in a solution of low ionic strength peels off myelin from the axons and reforms vesicles of size range equivalent to the nuclei and mitochondria. Due to the high lipid content, these myelin vesicles have a low intrinsic density relative to any membrane fraction. Myelin from mouse forebrain was purified and quantitated based on this principle, employing sucrose density gradient centrifugation (Norton and Poduslo, 1973). In brief, a lethal dose of sodium pentobarbital (Euthatal, 200mg/kg. i.p.,) was used and irreversible anesthesia was invoked in these mice. Their body weight was recorded. Then the brain was quickly removed, frozen in liquid nitrogen and saved at -80ºC till used. Brain tissue was gradually thawed on ice weighed in tared dry tubes to confirm the wet weight. Then the forebrain was defined by a coronal cut bordering the anterior end of the cerebellum and posterior end of the olfactory lobe. The posterior end was extended to include the entire cerebellum and used for total brain myelin content. The weighed tissue was homogenized in 0.25M sucrose, and centrifuged for 10 min at 500 x g, 4°C. The supernatant was then centrifuged for 10 min at 10000 x g, 4°C, and the resulting pellet resuspended in 10 volumes (relative to the supernatant) of 0.25 M sucrose. The same volume of 0.88M sucrose was added delicately below, and centrifuged for 3hrs at 100000 x g, 4°C. Myelin was collected from the interface of the two sucrose layers and resedimented at 15000 x g for 30min at 4°C. Further on, residual amounts of sucrose were removed from the myelin pellet by employing osmotic shock. For this, the pellet was resuspended in 10 volumes of ice-cold deionized water and recentrifuged at 15000 x g for 30min at 4°C. This step was repeated 4 times to get rid of contaminating sucrose. The final pellet was dried and weighed (Perrot et al., 2007, Sperber et al., 2001).

2.3. Transcardial perfusion of mice and tissue fixation

In order to perform transcardial perfusion, the mice were irrevocably anaesthetized **(Section 2.2)**, to immobilize them, so that they were non-responsive to toe pinch anesthesia It was then placed on the surgical platform immediately without any delay and a cautious superficial cut was made along the ventral skin below the zyphoid process. The skin was pulled to expose the thoracic and peritoneal membranes. They were then cut below the zyphoid process to expose the diaphragm and visceral organs taking care not to lacerate any vasculature. Then both lateral aspects of the rib cage were carefully cut in a caudal to rostral direction up to 2nd rib avoiding damage to the lung, heart and mammary arteries. The thoracic organs were exposed. Dissection-pan was then oriented so that the apex of heart was at 6 o'clock and the aortic outflow at 12 o'clock position. Using thumb forcep, the right ventricular free-wall was visualized delineating the darker, blood-filled-coloration of right ventricle and the redder, muscular-coloration of left ventricle. Right atrial-chamber was lacerated with scissors and carefully (but quickly) inserted with 25 gauge hypodermic needle attached to the perfusion set. The needle was angled at 2 o'clock position. Slowly the forcep grasp was released from the right ventricular free-wall to begin perfusion by setting the pump at a rate of 1 drop (50µl) per minute. Blood and phosphate buffered saline (PBS) (0.01 M PBS containing 137 mM NaCl, 2.7 mM KCl, 10 mM Na_2HPO_4 and 2 mM KH_2PO_4, pH7.4) effluent flow from the right atria laceration was allowed to drip into the dissection pan. As the perfusion takes place, the heart and liver get blanched due to blood being replaced with buffer. Upon completion of saline perfusion, the motor was switched off and buffer replaced with the fixative.

2.3.1. Fixation, cryopreservation and sectioning

Freshly prepared 4% PBS buffered paraformaldehyde (PFA) was used for tissue fixation. During perfusion visualization of extremities for evidence of tremors resulting from the aldehyde-crosslinking within the nervous tissue and muscle indicated appropriate perfusion within the circulatory system and, thus, a good fixation was ensured. Following perfusion-fixation, the brain along with ON was isolated and the brain was allowed to be further fixed in the same fixative for 12-24 hrs at 4ºC, whereas the ON was fixed for another 45 minutes

only (room temperature). Thus overfixing of axons was avoided. The tissue was then cryoprotected by transferring into 30% sucrose and allowed to sink. It was then embedded in cryomatrix (Tissue-Tek), mounted on Leica cryostat platform and 10 or 30µm ON/brain sections in the requisite plane was obtained. They were placed on superfrost charged slides (VWR # J1800AMNZ / FisherBrand) or suspended in PBS as per the experimental requirement. The sections placed on super-frost charged slides were allowed to dry and then stored at -70ºC until used.

2.3.2. ON preparation for transmission electron microscopy (TEM)

In case of TEM samples, the transcardial perfusion was performed as described above **(Section 2.3)**, but 0.1M Sorensen's sodium phosphate buffer (0.1M $Na_2HPO_4.2H_2O$ + 0.1M $NaH_2PO_4.2H_2O$, pH7.2) containing 1.5% glutaraldehyde was used for draining the blood and care was taken to maintain the temperatures at 37ºC during the entire process. This buffer was perfused for 2-3 minutes at a rate of 3 drops (100-150µl) per minute. Then it was replaced by a freshly prepared fixative solution (2% PFA + 2% glutaraldehyde made in 0.1M Sorensen's phosphate buffer). These buffers were prepared in 13 mega ohm deionised water. A volume of 125ml fixative was perfused to drain out the blood completely which ensured adequate and ideal fixation as it was evident by the stiffening of the entire animal. Then the ON was dissected and saved in the same fixative at 4ºC until it was sent to University College of Dublin, Electron Microscopy facility, for further processing and TEM.

2.4. Brain histology

2.4.1: Luxol fast blue (LFB) staining.

The cryosections were rehydrated in PBS and cryomatrix was washed thoroughly. The sections were then passed through a series of ethanol: 70%, 90%, and 100%. Dehydrated tissue was then processed for a de-fat step by keeping it immersed in chloroform: ethanol (1:1) overnight. This was followed by a wash in 95% ethanol, and transferred in 0.1% luxol

fast blue (LFB) stain in 95% acidic ethanol (100 ml 95% ethanol + 5 ml glacial acetic acid) at 50-60ºC temperature. Time required for the stain to develop was manually monitored under light microscope to acquire the desired intensity. Excess stain was washed in 95% ethanol. Then the stain was cleared in, 0.05% lithium carbonate followed by final dehydration in 95% and 100% ethanol. Before mounting the sections with DPX mounting medium, they were dipped in xylene and allowed to dry. LFB is a sulfonated copper phthyalcyanine type of dye. It is a popularly used histo-pathological stain for demonstrating normal myelin**.** This dye is insoluble in water and hence, used as solutions of alcohol or other moderately polar liquids. It stains phospholipids, and the hydrophobic domains of protein molecules. Cryosections (30µm) were processed for LFB histology. A minimum of five animals from each T and UT group were analyzed. Mid-saggital sections were processed from a collection of serial sections. The myelinated tracts or portions after staining appear blue which can be easily distinguished under the microscope. The staining solution was applied long enough so that almost everything in the section became colored followed by a differentiation step. This “background” coloring was removed by subsequent washing in lithium carbonate. This is a preferred way of performing LFB histology, as inclusion of the “differentiation” step leaves the stain only in the myelin sheath and rules out any kind of false staining. Further care was taken to avoid any kind of discrepancy that may arise in different lots due to the processing procedure; and hence, all the sections were handled simultaneously under the same conditions.

2.4.2. Cresyl violet staining.

For cresyl violet (CV) staining the fixed tissue samples which were saved on superfrost slides were rehydrated in distilled water to get rid of the cryomatrix. They were then placed in 0.1% CV counterstain. A few drops of glacial acetic acid were added to the stain just before use and filtered on whatman paper to get rid of the crystallized precipitates. The stain was manually monitored under the microscope. When the desired intensity was achieved, it was dehydrated by passing on to ethanol series followed by a clearing step in xylene. This preparation was then mounted using DPX mounting medium. The slides were allowed to dry appropriately, cleaned with xylene and used for bright field microscopy.

2.4.3. Toluidine blue staining and TEM processing.

The PFA fixed nerve was further fixed in 1% osmium tetroxide for 2hr, and dehydrated. It was then stained with 1% toluidine blue made in 2% borate solution. The quality of fixation and gross morphology of ON was assessed on these 15µm cross-section preparations. Rest of the tissue was processed in graded ethanol, dehydrated and embedded in Epon resin. Ultra-thin sections (70nm) were cut in an ultra-microtome (Ultramicrotome, Leica Microsystems, Ireland) and contrasted with uranyl acetate and lead citrate, placed on grid, and imaged with an FEI Tecnai-12 electron microscope (Tecnai FEI, Oregon, USA). This was done under arrangements made for a service provided by University College of Dublin, Electron Microscopy Facility, Dublin, Ireland.

2.5. Double immunohistochemistry

In general double immunohistochemistry (IHC) involved: rehydration, washing off the cryomatrix, permeabilization and blocking followed by primary antibody incubation and then development of signals with flurophore-tagged secondary antibodies. When signal amplification was required, an intermediate step was included after the labeling with primary antibody wherein the samples were incubated with biotinylated secondary antibody followed by streptavidin-tagged fluorophore tertiary antibody. Alexa fluor® dyes -488, -568 or -594 (Molecular Probes, Invitrogen, Ireland) were used to develop the fluorescent signals in green or red. Permeabilization step involved incubation with the requisite concentration of Triton- X100 in PBS (PBST) or blocking buffer. Usually the blocking and washing contained 0.1% PBST, but in case of $Na_v/K_v1.2$ staining 0.3% PBST was used. Blocking was always maintained for at least an hour and, if longer blocking was required, the permeabilization was conducted as a separate step. The antibodies were usually diluted in the blocking buffer unless mentioned otherwise. A combination of monoclonal (mAb) and polyclonal antibody was used for double labeling. Usually the mAb was incubated ahead of polyclonal antibody. The primary antibodies were always incubated for 4-5 hrs at room temperature or overnight at 4ºC depending on each experiment. When the samples needed to be incubated simultaneously, for both primaries they were mixed and applied. If sequential development was required, as in case of signal amplification, the first primary

was incubated for 4-5 hrs at room temperature developed by the flurophore and then kept in second primary overnight at 4ºC. The secondary and tertiaries were never incubated for more than 45 min to minimize non-specific binding. Along with this appropriate negative control were also processed. This required omission of primary/secondary/tertiary antibody depending on the experimental requirement/ design(s). Washes were 3 x 5min in between each antibody incubation step. Finally, Vectashield (Vector Labs, Peterborough, UK) was used for mounting the tissue samples and ProLong® Gold antifade reagent (Cat. no P36930, from Molecular Probes, Invitrogen, supplied by Bio-Sciences, Dun Laoghaire, Dublin, Ireland) was used to mount the ON axon preparation. The details of antibody dilution used in this study are provided in **Table 2**. For quantitative analysis, the samples under T and UT conditions were simultaneously processed.

2.6. Microscopy and imaging

This study involved three types of imaging as described below. During imaging the exposure time was kept the same for each sample in all experiments.

Light microscopy: Bright field microscopy (Axioskop, Zeiss Germany fitted with a digital camera) was used to obtain DIC images. A single chip color CCD camera DP72 (Olympus) and Cell^F imaging software were used to analyze images and show loss of myelin following 8 weeks of CZ treatment. This entailed using the same exposure time and frame size for anterior commissure, corpus callosum and fornix imaging from LFB stained sections.

Confocal microscopy: Micrographs were obtained by EC Plan-Neofluar 10X/0.30, EC Plan-Neofluar 20X/0.50 and EC Plan-Neofluar 40X/1.30 Oil objectives, using a laser scanning microscope (AxioObserverZ1, LSM710, Carl Zeiss, Germany). Field micrographs were obtained (10 or 20X objective) in epifluorescence mode (pinhole wide open). For confocal images, the pinhole was set to 1AU and for Z-stack images the section thickness was defined and a laser scan set up accordingly. Argon and Helium/Neon lasers provided the 488 and 568nm lines for excitation; the emitted signals were sampled in a frame mode at spatial resolution of 30 nm per pixel with 1.5 µs dwell time. An appropriate and standard excitation-emission spectrum was set up, using the “smart set up” option for the Alexa dyes

from Molecular Probes used herein. Alexa® 488, 568 and 594 had their excitation set at 499, 579 and 591nm, with their corresponding emissions at 519, 603 and 618 nm. Usually images of the same pixel resolution and size were obtained in comparable frame for each experiment. 8 bit images were obtained from Zen 2008, Zeiss ObserverZ1, LSM 710. For intensity profiles, several selection tools were used to define the regions of interest (ROI). For instance "closed bezier" tool or any other appropriate tool as per the requirement was used to obtain the raw data.

Transmission Electron Microscopy: FEI Tecnai-12 electron microscope (Tecnai FEI, Oregon, USA) was used at UCD EM Facility to obtain high resolution images; 16 bit images obtained were saved with the requisite scale bar.

2.7. Scoring of demyelination

Evaluation of demyelination status for brain regions employed blinded scoring by neutral observers. Images of the same magnification were obtained and the cerebellar nuclei (located in the cerebellar marrow) i.e., the lateral cerebellar nucleus (LCN), medial cerebellar nucleus (MCN), and interpositos nucleus (IN), or hippocampus or corpus callosum, were numbered and 5 to 10 independent and blinded readers scored these regions of interest (ROIs) against the UT sample which was processed simultaneously (Groebe et al., 2009). Five UT and CZ-treated mice samples were included with three sections (30µm) per animal. The blind observers were asked to score the LFB staining intensity in between 0-5. This scoring allowed identification of demyelination. A score of five is equates to the myelin status of a mouse not treated with CZ, whereas zero is equivalent to full demyelination. So, a score of one or two meets $1/5^{th}$ (~ 20%) or $2/5^{th}$ (~40%) of fiber myelination.

2.8. Densitometric mapping of images and analysis

LFB-stained images were first converted into gray scale black and white format and then analyzed. Parallel images (30µm) corresponding to the same regions from both UT and T group were traced to define the ROIs and the intensity was measured using Zen 2008, Carl

Zeiss software. The background for each image was obtained by multiple sampling from the regions which were devoid of tissue boundary. This particular software returned the intensity signals as high numerical values for the blank regions. Lower numerical values were obtained for the defined ROI. Three such images from each sample were analyzed to get an average value. The raw data obtained was normalized for the sampled background. A comparison of absolute value obtained from both groups has been used for data interpretation here. LFB and MBP stained tissue sections were analyzed in this manner. Fluorescence images for MBP produced direct signal read outs after the threshold cut-off, unlike the bright filed images for LFB. Zen 2008 software, histogram view function displayed the distribution of pixel intensities of defined ROI in addition to the summary of values in a tabular form. Co-localization data were also obtained from this software and the values obtained as Pearson's correlation coefficient. This selection provided the information of intensity distribution within the co-localizing region. Scattergram was used to define the threshold for co-localization analysis.

Alternatively, Image J (NIH) software was employed for densitometric analysis and is specified in the subsequent section. The TEM images were analyzed using the standard methods of this software. The scale was set by following the steps "Image menu-scale-define the length". Any measurement made after this adjustment generates the result in a separate window which was copied and saved on an Excel sheet for further analysis. Free hand line and polygon tools were used here to define the ROI. This works in such a manner that larger values were obtained for high intensity signals and the background was lower relative to signal. So, it provided a direct read out of the visual impact of an image, whereas it was reverse in case of ZEN software for bright field images.

Length and area measurements were collected using either of the two softwares from pre-scaled images.

2.9. Affinity chromatographic purification of antibodies specific for K_v1 α and β subunits

Polyclonal K_v1α- and β subunit antibodies (Scott et al., 1994a, Scott et al., 1994b) were affinity purified on a 1ml column of protein A/G-sepharose fast flow (Sigma). A 1 ml column was prepared. The column bed was calibrated in methanol, washed with purified water several times (5ml volume) and then equilibrated using 20mM sodium phosphate buffer pH 7.4. The buffer was allowed to stand for 10-15 min taking care that no air bubble was trapped within. It was again washed with 5ml sodium phosphate buffer. 500µl of $K_v1.1$, 1.5 and 1.2 (RCK (rat cortex K^+ channel) 1, 2 & 5) or K_vβ antibodies to be purified was applied on to a column. The crude serum and Sepharose beads were mixed properly before allowing it to stand. It was then, allowed to settle for 10min and washed with sodium phosphate till the optical density for a 280nm fraction was less than 0.05. After re-equilibration of the column, the antibodies were eluted with 0.1M glycine pH 3. 1ml fractions were collected in each tube containing 100µl of 1M Tris HCl, pH 9 for neutralization. Absorbance was read at 280nm. Fractions containing antibody were pooled and dialyzed for 24 hours against 5 liters of PBS. The column was re-equilibrated after use with PBS. Purified antibodies $K_v1.1$ and $K_v1.6$ produced non-specific bands whereas RCK 5 / (mAb5) / ($K_v1.2$) (McNamara et al., 1993, Muniz et al., 1992) and guinea-pig β subunit antibodies showed excellent reactivity in Western blots (Lab data, C. Sidera's Thesis, 1999).

2.10. Extraction of proteins from ON

Tissue homogenization and protein extract: Mice were anaesthetized **(Section 2.2)** and the ON dissected out. A T 10 basic ULTRA-TURRAX® homogenizer was used to homogenize the nerve in 500µl of homogenizing buffer. This contained 0.32M sucrose, 20mM Tris-HCl, 2mM ethylenediamintetracetic acid (EDTA), 0.5mM ethylene glycol bis (β-aminoethyl ether)-N,N,N',N'-tetraacetic acid (EGTA), 1mM Sodium orthovanadate, 50mM Sodium pyrophosphate decahydrate, 1mM Phenylmethylsulfonyl fluoride (PMSF),

50mM sodium fluoride, and 1X protease inhibitor cocktail (Sigma# Catalogue no: S8830). The resultant homogenate was centrifuged at 1000 x g for 10 min to remove nuclei and debris. The supernatant was then recentrifuged at 45,000 x g for 1hour to pellet the crude membranes.

- The resultant **membrane** obtained was resuspended in a solublization buffer containing 20mM Tris-HCl, 2mM EDTA, 0.5mM EGTA, 1mM sodium orthovanadate, 50mM sodium pyrophosphate decahydrate, 1mM PMSF, 50mM sodium fluoride, 1X protease inhibitor and 1% Triton X-100 (Utsunomiya et al., 2008).
- For obtaining **total protein,** the first step was excluded and the pellet obtained after homogenization was solubilized by including 1% Triton-X 100 in the buffer.
- For the preparation of **cytoskeletal protein** which mostly remains in the insoluble fraction of the homogenate the dissected ON nerve was placed in a BUST buffer (Xu et al., 1996), containing 25mM phosphate buffer pH 7.2 , 1mM EGTA, 1% SDS, and 1mM PMSF and homogenized. The homogenate was allowed to stand for 10-15 min at room temperature, subjected to high speed centrifugation and the clear supernatant was used for protein quantification.

All these protein preparations were performed as per the experimental requirement and aliquots saved at -70ºC until used. A separate aliquot was saved for BCA protein quantification. BCA assay (Pierce kit) was performed as per given protocol of the manufacturer. Absorbance (562nm) was obtained using a plate reader. A representative standard curve for BCA is shown in Figure 16**.** Regression values for all the preparations were maintained above 0.9.

2.11. SDS-PAGE and western blotting

SDS-PAGE and protein transfer: Solubilised ON membrane was resolved by SDS-PAGE, using precast 12% or 4-12% NuPAGE® Novex® Bis-Tris gels from Invitrogen. Samples were prepared in NuPAGE®LDS (Lithium dodecyl sulfate) sample buffer by

heating at 95-100ºC for 5 min. The gels were run in MOPS buffer (50 mM MOPS, 50 mM Tris base, 0.1% SDS, 1 mM EDTA, pH 7.7) at 90 mV till the protein migrated into the gel, following which it was allowed to run at higher voltage (120 mV), maintaining the entire process at 4ºC. In general, the resolved proteins from the gels were then transferred onto polyvinylidine difluoride (PVDF; Millipore) membrane for 45 min at 19V in a trans-Blot SD cell (Bio-Rad). 25 mM Tris, 192 mM glycine, 10% methanol was used for transfer buffer. Use of 10% methanol provided good transfer for mid-range protein, whereas for lower kD protein, a better transfer was achieved by using 20% methanol. For immunoprecipitation experiments 60mM Dithiothreitol (DTT) was included in the sample buffer.

Blocking and antibody treatment: The PVDF membranes were blocked with 2-5% non-fat marvel milk in TBST for an hour. The membrane was cut out according to the loaded sample and incubated in separate tubes containing the requisite IgG overnight at 4ºC or 2-4 hrs at room temperature. After antibody treatment, the blots were subjected to TBST washes (15 x 3 min).

Detection of immuno-reactive bands: Proteins of interest were detected using anti-mouse secondary antibodies conjugated with horse-radish peroxidase (1:10,000; Jackson Laboratories), in combination with enhanced chemiluminescence (ECL) detection (Millipore) system. Due to the known presence of avidin in milk, 2-5% BSA fractionV blocking in TBST (0.2M NaCl, 50mM Tris-HCl, 0.5% Tween 20, pH 7.4) was used when signal amplification with biotinylated secondary was employed. After blocking with BSA these blots were treated with biotinylated secondary antibody, washed (15 x 3 min) and followed by treatment with high sensitivity streptavidin conjugated to horse-radish peroxidase (1: 80,000, Pierce Protein Research Products) for 30 minutes. Incubation with secondary and tertiary antibodies never exceeded 45-60 min in order to minimize non-specific binding. After this the blots were washed (15 x 3 min) in TBST, exposed to the ECL reagent (Millipore) for 30 seconds only and imaged in the G-box attached with a CCD camera.

Use of UC Davis/ NIH NeuroMab Facility monoclonal antibodies, in conjunction with biotinylated secondary for signal amplification produced some background. Hence the stringency of washing buffer (TBST) was increased by raising the concentration of NaCl from 100 mM to 500 mM in the washing buffer. In order to confirm the specificity of the IgGs, a preadsorption control was set up by incubating the antibody solution with excess of the peptide used for its generation. The pre-adsorbed antibody did not produce any signal. In this case rat brain, membrane preparations were used as positive control. Collectively this allowed identification and elimination of non-specific bands. Thus only specific bands within the predicted protein size range were ensured to be included for quantitation. Cases where a non-specific band was obtained due to the use of biotinylated secondary and their size coincided with the protein of interest, no primary negative control was included in each experiment to eliminate such ambiguity. Further precaution was maintained by considering the protein bands only within a linear loading range for quantification. The experimental proteins were normalized against α-tubulin, wherever suitable. Densitometric analysis was performed using ImageJ software (NIH). The molecular weights of the protein bands obtained from Western blot (below) were calculated by semi-log plot analysis or GeneTool Software from Syngene, Cambridge, UK.

2.12. Immunoprecipitation (IP), co-IP and sequential-IP

Immunoprecipitation experiments were employed to demonstrate α-subunit interaction(s) and it involved co-IP and sequential-IP from solubilized protein preparations. K_v1 polyclonal antibody (1µg antibody / 3µg of protein) for the α-subunit of interest was incubated with 45µg of solubilized ON homogenate so that the antibody bound the protein in solution. Incubation was maintained at 4ºC for 4 hrs or overnight under gentle agitation. The antibody/antigen complex was then pulled out of the sample using protein A coupled agarose beads. This physically isolated the K_v1 protein from the rest of the sample. The specificity of these antibodies was determined by setting up a preadsorption control with 1µg antibody / 3µg of glutathione- S- transferase (GST) fusion protein against which the antibody was developed.

In order to prepare the slurry, protein-A Sepharose® 4B, Fast flow beads from *Staphylococcus aureus*, aqueous ethanol suspension (from Sigma) was added to 1ml PBS for one hour and rinsed in PBS twice before use. The supernatant was removed and 400 µl of PBS with protease inhibitors was added. This slurry was stored at 4°C until used for few days. For longer storage, the beads were saved in PBS with 0.02% sodium azide at 4ºC. When precipitating, the protein complex was mixed with the slurry (70-100 µl of the beads) and maintained on ice for centrifugation at 1000 rpm, for 15 min at 4ºC. The supernatant was removed and beads washed in PBS buffer three times (each time centrifuging at 4°C). Finally, 25-50µl of 4X LDS loading buffer supplemented with 60mM DTT was added to these beads and boiled at 95-100°C for 5 minutes to denature the protein and separate it from the protein-A Sepharose. Supernatant from these IP-experiments were also included for western blot analysis. In cases where SDS-PAGE analysis was not performed immediately, samples were frozen (-20ºC) at this stage.

2.13. Quantification of K_v1 channels from ON membrane extract by immuno-fluorometric titration

Quantification of K_v1 protein using Western blot analysis remained woeful largely owing to two facts. Firstly, a large quantity (at least 15µg per well) was required for detection of K_v1 on Western blots, but the protein yield from an ON was miniscule. Secondly, individual response associated with variability in CZ treated mice had to be ruled out. Hence an immuno-fluorometric titration assay, employing chemiluminescence detection was devised to overcome these issues. Serial dilutions of GST fusion tagged peptide for $K_v1.1$, 1.2, 1.4 were used to generate a linear standard plot with regression values above 0.9; and the ON protein samples from treated and untreated conditions were quantitated against the standard value. For each experiment conducted triplicate samples were included and the averages considered for quantification. The linear range was also considered by setting up an initial experiment using varying concentrations of the analyte (ON membrane extract). The precision and accuracy of the assay was established for specificity in terms of the nature of the analyte and concentration to be measured.

Briefly, the free antigen (solubilized ON protein from treated and untreated mice) and K_v1 antibody were incubated overnight at 4ºC to form antigen-antibody complex and then these complexes were allowed to bind the antigen-coated surface (solubilized ON protein) in the assay plate. The unbound antibody-antigen complex was washed off before adding enzyme-linked (alkaline phosphatase) secondary antibody against the rabbit polyclonal primary antibody. CSPD (Disodium 3-(4-methoxyspiro 1,2-dioxetane-3,2'-(5'-chloro)tricyclo[3.3.1.13,7] decan-4-yl) phenyl phosphate) substrate was then added and antigen concentration determined by the signal strength elicited due to enzyme-substrate reaction as relative luminescence units (RLU) per second, by comparing it against the known values obtained using a standard. These readings were obtained by Gen5 software from BioTek (Bedfordshire, UK). A standard optical sensitivity and filter setting recommended by the software was used to measure the RLU. The background was eliminated by subtracting values obtained from the wells which went through all stages of washings and incubation and were devoid of samples.

Protocol details:

1. Opaque white walled 96 well plates were used to perform this luminescence assay.
2. ON homogenate (0.1µg protein/ml) diluted in PBS was used to coat the plate, overnight at 4ºC before washing (3 x 10 min) with PBS (200µl).
3. Then it was blocked with 2% skimmed milk in PBST (0.1% Tween, filtered)
4. Preincubated overnight peptide with antibody (3µg peptide/µg antibody, $K_v1.1$, 1.2 and 1.4) was serial diluted, 0.02, 0.04, 0.09, 0.18, 0.37, 0.75, 1.5, and 3µg and plated in duplicate wells to generate a standard curve (100 µl volume)
5. Correspondingly 3µg of unknown protein from ON was incubated with rabbit polyclonal $K_v1.1$, 1.2 or 1.4 antibodies overnight. The antigen-antibody complex was serial diluted and plated in duplicate wells besides the standard.
7. This was allowed to stand for 3-4 hrs at room temperature.
8. It was then washed PBST (3 x 10min) before incubation with goat anti-rabbit alkaline phosphatase antibody (1:10,000, Sigma-aldrich, A9919) for 1 hr at room temperature.

9. Washed with PBST (3 x 10 min).

10. Washed with buffer (Tropix, Aalto Bio Reagents, Dublin 14, Ireland)

11. CSPD (50µl/well) with Sapphire Substrate (Tropix reagent, Aalto Bio Reagents, Dublin 14, Ireland) was added and the luminescence checked.

The enzymatic dephosphorylation of CSPD by alkaline phosphatase leads to the metastable phenolate anion which decomposes and emits light at a maximum wave length of 477nm. The luminescent light emission was recorded using Gen 5 software attached to BioTek Luminometer, as described earlier, and the signals obtained. Six such experiments were averaged and a graphical representation from all these is presented.

2.14. Proximity Ligation Assay (PLA)

Duolink® *in situ* PLA™ Assay from Olink Bioscience, Sewden, is a PCR amplification based technique for detection, visualization and quantification of individual protein, protein modifications and protein interactions in tissue or cell samples prepared for microscopy. The target is detected using one or two primary antibodies. When two primary antibodies are used, they must have been raised in different species or modified with different haptens. In principle a pair of oligonucleotide labeled secondary antibodies (PLA probes) is expected to generate a signal only when the two PLA probes have bound to close proximity (approx. 40 nm (Yang et al., 2007b, Shafey et al., 2010) after the application of ligase enzyme. The sample locations where ligation could be achieved were further amplified by application of polymerase enzyme and then the signal from each such spot was detected by a fluorescent signal. Microscopic visualization of each fluorescent dot indicated the presence of protein interaction. In order to identify $K_v1.1$ interacting subunits a combination of the following antibodies were used:

a) $K_v1.1$ containing subunits: Polyclonal (rabbit) $K_v1.1$ raised against cytoplasmic or intracellular epitope and mAb $K_v1.1$ for extracellular epitope developed in mouse

b) $K_v1.1$-1.2 interaction: mAb $K_v1.1$ extracellular epitope (raised in mouse) and rabbit polyclonal $K_v1.2$ against cytoplasmic or intracellular epitope

Epitope	No. of residues	Peptide sequence
K_v1.1 (extracellular)	191-208	ELKDDKDFTGTIHRIDNTC
K_v1.1 (intracellular C-terminus)	416-495	HRETEGEEQAQLLHVSSPNLASDSDLSRRSSSTISK SEYMEIEEDMNNSIAHYRQANIRTGNCTTADQNC VNKSKLLTDV
K_v1.2 (intracellular C-terminus)	417-499	YHRETEGEEQAQYLQVTSCPKIPSSPDLKKSRSAS TISKSDYMEIQEGVNNSNEDFREENLKTANCTLAN TNYVNITKMLTDV
K_v1.4 (intracellular C-terminus)	589-655	PYLPSNLLKKFRSSTSSSLGDKSEYLEMEEGVKES LCGKEEKCQGKGDDSETDKNNCSNAKAVETDV

Table 1: Epitope sequences of K_v1.1, 1.2 and K_v1.4 antibodies used in PLA and fluorometric titration

Briefly, the method involved sample (placed and fixed on superfrost slide, **Section 2.3.1**) **incubation with primary antibodies** that bind to the protein(s) to be detected. Incubation timings were same as used for IHC experiments. **Hybridization of PLA probes**, i.e., secondary antibodies conjugated with oligonucleotide required their addition and incubation at room temperature. PLA probes MINUS and PLUS used here at this stage indicated the complementary oligonucleotide sequence which was expected to anneal in the presence of hybridization buffer if they were in close proximity. Ligation of these two nucleotides was achieved using a **ligase reaction.** The ligation solution contained ligase which was added next for the two hybridized oligonucleotides to form a closed circle. Then these protein interactions were subjected to **amplification**. This was done by addition of a solution, consisting of nucleotides followed by polymerase treatment. The oligonucleotide arm of one of the PLA probes acts as a template, for a rolling-circle amplification (RCA) reaction using the ligated circle as a template, generating a concatemeric (repeated sequence) product. The final step required **detection,** and for this a solution, consisting of

fluorescently labeled oligonucleotides, was added and the labeled oligonucleotides hybridized to the RCA product. The signal obtained is easily visible as a distinct fluorescent dot (excitation 598 nm /emission 634 nm) and it was analyzed by microscopy. For these experiments a negative control was used by omitting one of the primary antibodies, here to estimate the amount of background signal. A positive control using the standard specimen provided by the company was included to establish the validity of the technique employed.

2.16. Neuronal Culture as an *in vitro* system for analyzing K_v1 expression

2.16.1. Neuronal cultures

Two types of primary neurons, namely cerebellar granule neuron and hippocampal neuron were cultured. Conditioned media from astroglial primary cultures and OLN 93 cell line **(Section 2.16.3)** was tested on hippocampal neurons. This required dissection of timed pregnant mice to obtain E18 embryos which were further dissected to isolate the brain and hippocampus, and cultured on poly-D Lysine coated coverslips. Cerebellar granule cell culture was performed on (postnatal day 1) P1 pups.

2.16.2 Dissection of timed pregnant mice to obtain E18 embryos

Pregnant mice (18 days) were anesthetized **(Section 2.2),** the abdomen was wiped off with 70% ethanol and then cut open by grabbing the skin with curved forceps and cutting along the midline with scissors. Two cuts were made onto the sides and both horns of the uterus pulled out. These uteri were then placed on to a 10 cm dish containing hanks buffered salt solution (HBSS). Using the tip of a scissors the embryos (E18) were removed, decapitated, and the heads placed in a fresh dish containing HBSS. Subsequent dissection was performed under a dissecting microscope (Vicario-Abejón, 2004), as described in Figure 17.

The dissected hippocampus of E18 pups was pooled (3 of them in this case) and minced using a fine scissor. It was then dissociated in 100µl trypsin. This was achieved by placing the trypsin containing tube was placed at 37ºC for 4 minutes in water bath and allowed to dissociate on its own. The tube content was then resuspended in dissociation medium

[(BME (B1522, Invitrogen) /MEM) with 10% fetal calf serum, 0.5% glucose, 1mM sodium pyruvate, 25mM glutamate, 1% penicillin-streptomycin solution (Sigma # P4333, 10,000 units penicillin and 10 mg streptomycin/ml)] and an even suspension containing cells was obtained. These evenly suspended cells were placed in 15 ml tube each containing 5 ml of dissociation medium, centrifuged at a speed of 1000 rpm at 22ºC for 5 min. The supernatant was discarded and the cells were re-suspended in another 5 ml of dissociation medium centrifuged as described above and discarded. These cells were then plated on the desired coated surface. Following 8-10 hrs of culture in dissociation medium, it was replaced with serum free media described as neuronal culture medium (Neurobasal with B27 supplement 0.5mM glutamax and penicillin streptomycin.), which had been conditioned with OLN-93 or astroglial culture for 24 hours. These were cultured for the requisite days in vitro (DIV) and then analyzed for the presence of K_v1 ion channels **Figure 18** employing immunohistochemical staining for Kv1 and neuronal marker β-tubulin III. For cortical neuron culture, the same procedure was employed except that tissue from cortex was used for seeding the cells.

2.16.3. Culturing of OLN 93 cell line

OLN-93 cell line is a rat oligodendrocyte precursor cell line received from, Department of Pediatric Neurology, University Children's Hospital Carl Gustav Carus, University of Technology Dresden, 01307 Dresden, Germany. Growth medium consisted of high glucose DMEM medium, 5-10 % fetal bovine serum, and 1% (v/v) antibiotica/antimycotica, 5% CO_2, 95% relative humidity and 37°C temperature. It required sub-culturing every ~ three days with trypsin/EDTA (3-4 min). The cells have a doubling time of 16-18 hours **Figure 19.**

2.17. CAP recordings and pharmacological analysis

Mice were decapitated under deep anesthesia **(Section 2.2).** Brain with attached ON was extracted and immersed for 5 min in bubbled (95% O_2, 5% CO_2) ice-cold solution containing (in mM): sucrose, 75; NaCl, 85; KCl, 2.5; NaH_2PO_4, 1.25; $NaHCO_3$, 25; $CaCl_2$, 0.5; $MgCl_2$ 4; glucose, 25, pH 7.3. The meninges of ON were carefully removed and the

brain was transferred and secured with tissue glue (with ON facing up) in the recording chamber attached to the stage of the upright Olympus BX51WI microscope of the rig. The distal end of the nerve was drawn into the suction electrode for stimulation (100 μs pulse). Recordings of CAPs were made with low-impedance glass pipettes (10 μm tip diameter, 1-3 MΩ input resistance) filled with artificial cerebrospinal fluid (ACSF) which was carefully inserted into the ON at close proximity to the chiasm under stimulation (1.0-1.5 mA/0.03Hz). Recordings were made under continuous perfusion with bubbled (95% O_2, 5% CO_2) ACSF containing (in mM): NaCl, 125; KCl, 3; NaH_2PO_4, 1.25; $NaHCO_3$, 25; $CaCl_2$, 2; $MgCl_2$, 2; glucose, 25; pH 7.3 after at least 1h equilibration at 32°C. Analog signals were acquired continuously and amplified with EPC-10 USB amplifier controlled by Patchmaster 2.20 software (HEKA Instruments), digitized at 5-10 kHz and stored for off-line analysis (Clampfit 10.0; Molecular Devices, CA). For measurements of the refractory period, paired stimuli were applied at various inter-pulse intervals, and the maximum amplitude of the second response was plotted as a function of the inter-pulse interval. Peptide blockers stored at -20°C were thawed and added to the perfusion medium before use.

2.18. Reagent suppliers

DTX_K was purified in-house; TsTX-K was obtained from Peptide International. Duolink® *in situ* PLA™ Assay Kit was purchased from Olink Bioscience, Sewden. Antibodies used were sourced from different vendors listed below **(Section 2.20).** All other reagents were obtained form Sigma-Aldrich, Ireland.

2.19. Data and statistical analyses

All the data were calculated and graph generated using Microsoft Excel software and presented as means ± S.E. or S.E.M. Student's *t-test* was used to evaluate significance of changes and expressed as 'ns' $p>0.05$ (not significant), '*' $p<0.05$, '**' $p<0.01$, '***' $p< 0.001$, '***' $p< 0.0001$.

2.20. List of antibodies

Primary antibodies and Cat. No.	Monoclonal (mAb) or polyclonal (poly)	Vendor	IF Dilution	WB Dilution
K_v1.1 Cat. No.73-007	mAb (K20/78)	NeuroMab	1:10	1:10
K_v1.2 Cat. No. 73-008	mAb (K14/16)	NeuroMab	1:10	1:10
K_v1.3 Cat. No. 73-009	mAb (L23/27)	NeuroMab	1:10	1:10
K_v1.4 Cat. No. 73-010	mAb (K13/31)	NeuroMab	1:10	1:10
K_v1.5 Cat. No. 73-011	mAb (K7/45)	NeuroMab	1:10	1:10
K_v1.6 Cat. No. 73-012	mAb (K19/36)	NeuroMab	1:10	1:10
$K_v\beta$ 1.1 Cat. No. 73-018	mAb (K9/40)	NeuroMab	1:10	1:10
$K_v\beta$ 1.2 Cat. No 73-019	mAb (K47/42)	NeuroMab	1:10	1:10
K_v1.1 extracellular Cat. No 73-105	mAb (K36/15)	NeuroMab	1:10	1:10
K_v1.1 Cat. No. APC 009	poly	Alomone Labs	1 : 200	1 : 200
K_v1.2 Cat. No. APC 010	mAb	Alomone Labs	1 : 200	1 : 200
K_v1.4 Cat. No. APC 007	poly	Alomone Labs	1 : 200	1 : 200

Pan Na_v (SP19) S6936	poly	Sigma-Aldrich	1 : 50	NA
PLP Cat. No ab28486	poly	Abcam	1 : 1000	1 : 1000
CNPase Cat. No. C5922	mAb	Sigma-Aldrich	1 : 1000	1 : 1000
MBP (SMI -99P)	mAb	Abcam	1 : 1000	1 : 1000
β-tubulin III Cat. No. T2200	poly	Sigma-Aldrich	1 : 50	1 : 1000
GFAP Clone G-A-5, G3893	poly	Sigma-Aldrich	1 : 400	NA
GFAP Cat. No. G9269	poly	Sigma-Aldrich	1 : 100	1 : 1000
Anti- APC Cat. No.(Ab-7)	mAb	Millipore	1:100	1:50
Neurofilament 200 Cat. No. N5389	mAb	Sigma-Aldrich	1 : 400	1 : 500
Phosphorylated neurofilament (SMI 31)	mAb	Abcam	1 : 1000	1 : 1000
Dephosphorylated neurofilament (SMI 32)	mAb	Abcam	1 : 1000	1 : 1000
α- tubulin Cat. No.ab8227-50	poly	Abcam	1 : 1000	1 : 1000

NeuroMab -- NeuroMab Facility, UC Davis/NIH

Sigma -- Sigma-Aldrich Ireland Limited, Wicklow, Ireland

Abcam -- Abcam, Cambridge, UK

Alomone -- Alomone Labs, Ltd, Jerusalem, Israel

Millipore -- Millipore, Cork, Ireland

mAb – Monoclonal antibody

Poly – Polyclonal antibody

Table 2: List of antibodies their suppliers and indicated dilutions used in this study.

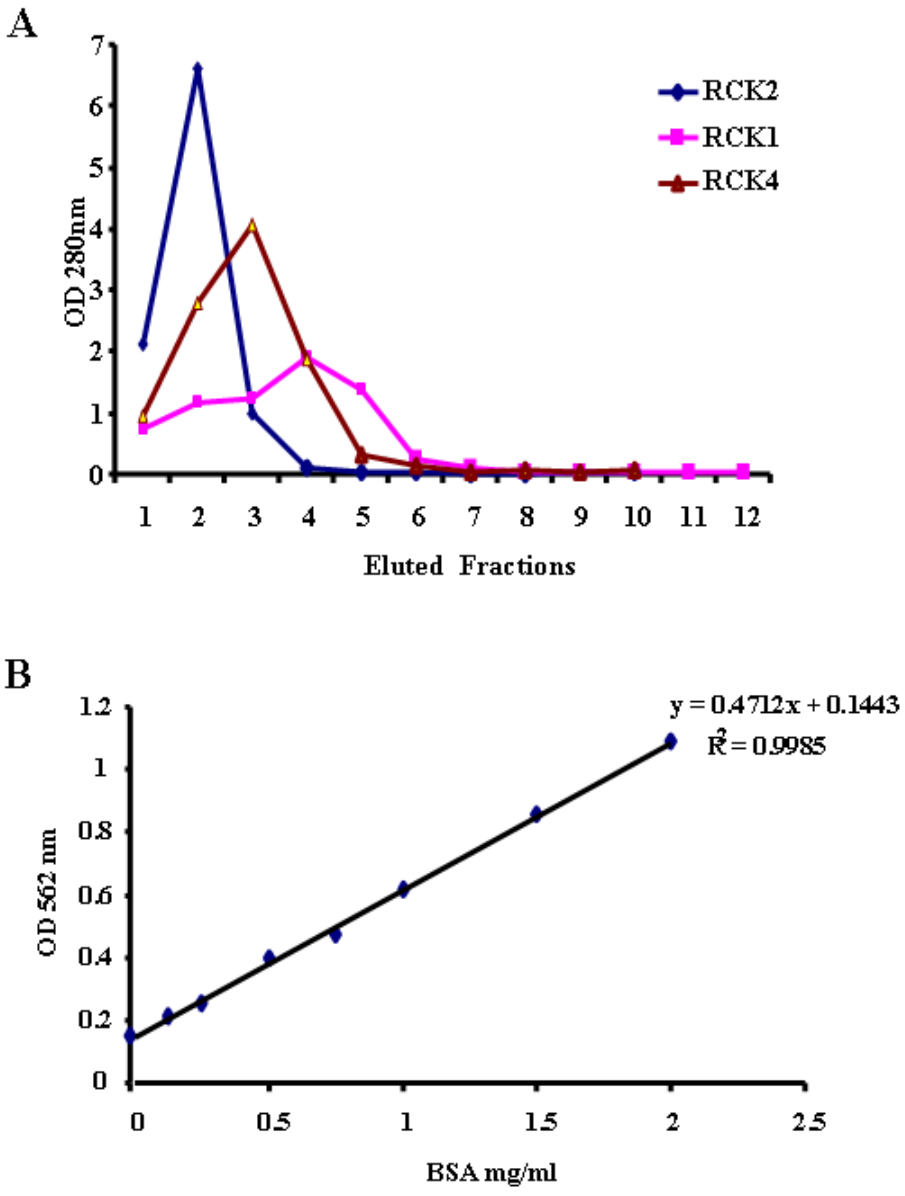

Figure 16: Representative elution profile and Bicinchoninic acid (BCA) standard curve.

A. *Protein A affinity chromatography eluate showing peak fractions that contain purified RCKs represented in the elution profile.* ***B.*** *Graph representing a typical standard curve obtained for BCA assay and the regression formula used to calculate the protein quantity.*

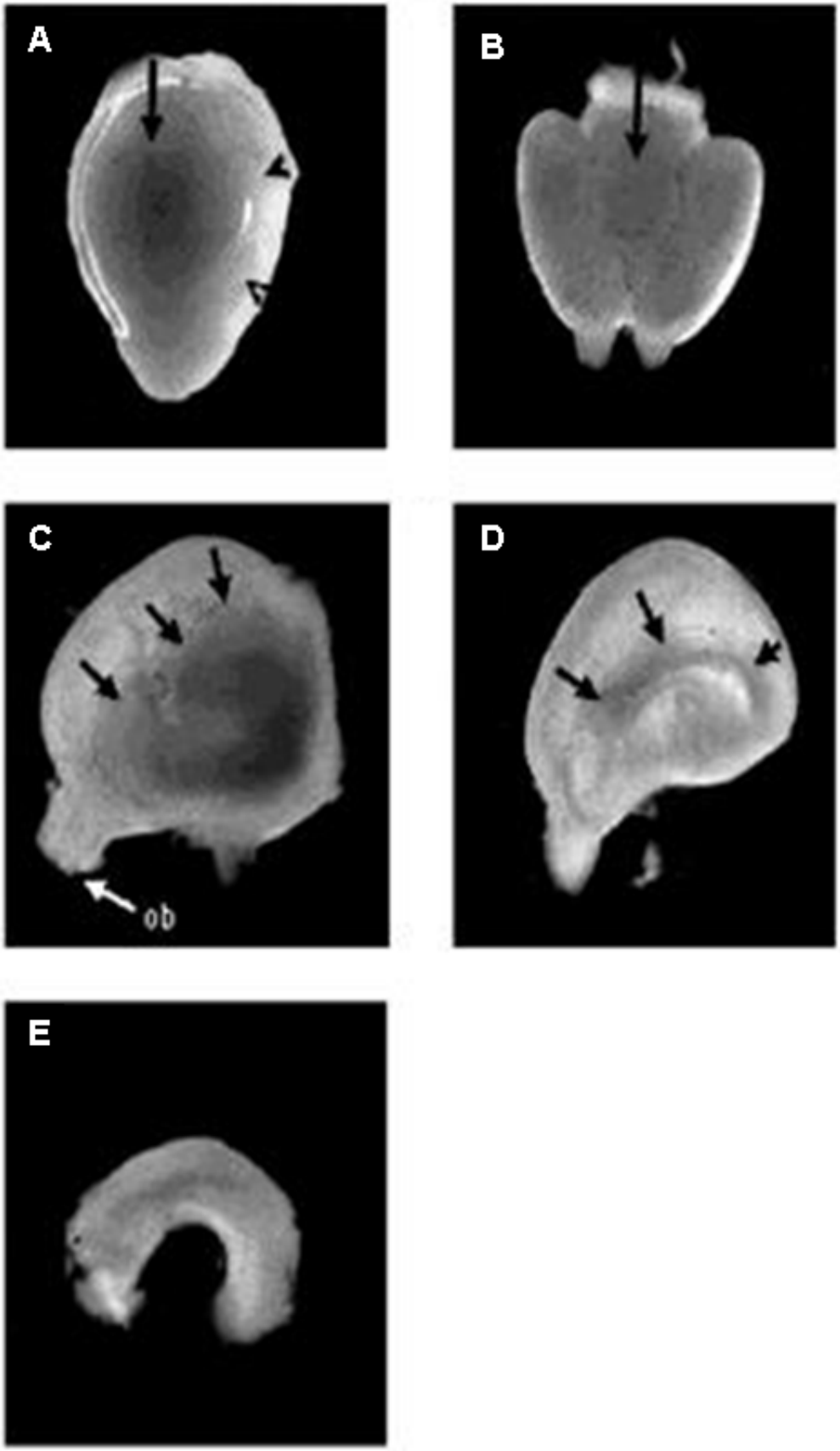
A
B
C
ob
D
E

Figure 17: Method for dissection of E18 mice embryos and isolation of hippocampus.

A. *A pair of Dumont forceps was used to grasp the embryo head firmly to remove the skin and skull with another pair of forceps. The skull was removed beginning from the lambda and continuing forward to bregma. The tissue surrounding the head (arrowheads) was also removed.* ***B.*** *Caudal parts of the CNS, such as the cerebellum, pons, and cervical portions of the spinal cord, was then removed. With the ventral aspect of the brain facing up, the two hemispheres could be separated by moving the forceps through the midline.* ***C.*** *The septum and diencephalic tissue (thalamus and hypothalamus) of one hemisphere is removed (arrows) in the next step. The olfactory bulb (ob) is indicated.* ***D****. The hippocampus is visible as a slightly thicker portion lining the curved medial edge of the cortex (arrows).* ***E****. The hippocampus was dissected out by making a longitudinal cut through the border and the cortex. This could be done from either the ventral or dorsal side. Finally, the meninges and choroid plexus surrounding the hippocampus were carefully removed [Adopted from (Vicario-Abejón, 2004)].*

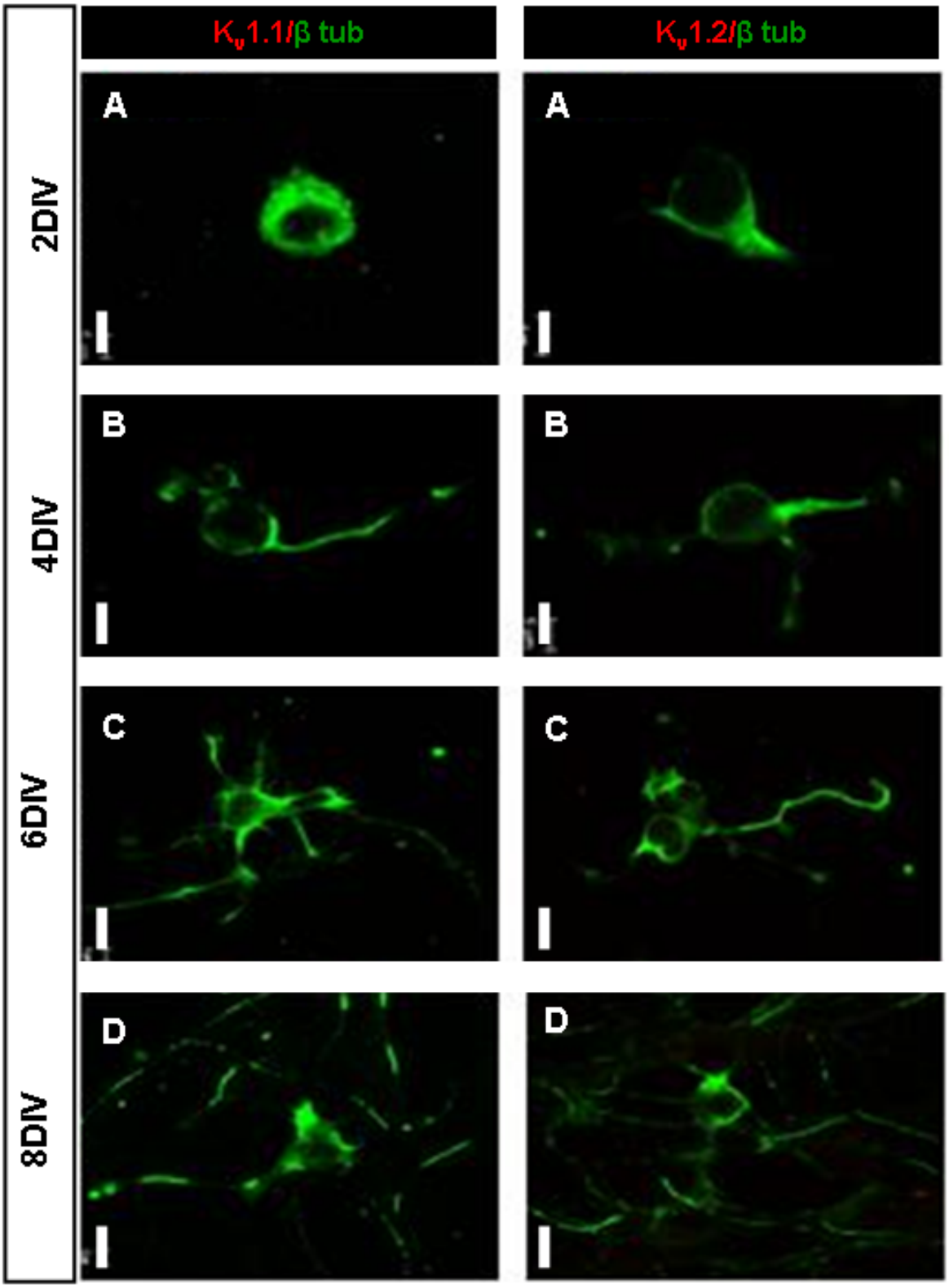
Kv1.1/β tub
Kv1.2/β tub
2DIV
4DIV
6DIV
8DIV
A
A
B
B
C
C
D
D

Figure 18: Demonstration of absence of K_v1.1 and 1.2 channels from 8 DIV hippocampal neurons.

Hippocampal neurons at 2, 4, 6 and 8 days DIV immunostained with β-tubulin III (green) and K_v1.1 or K_v1.2(red) to show the absence of these two channels until 9 DIV in culture.

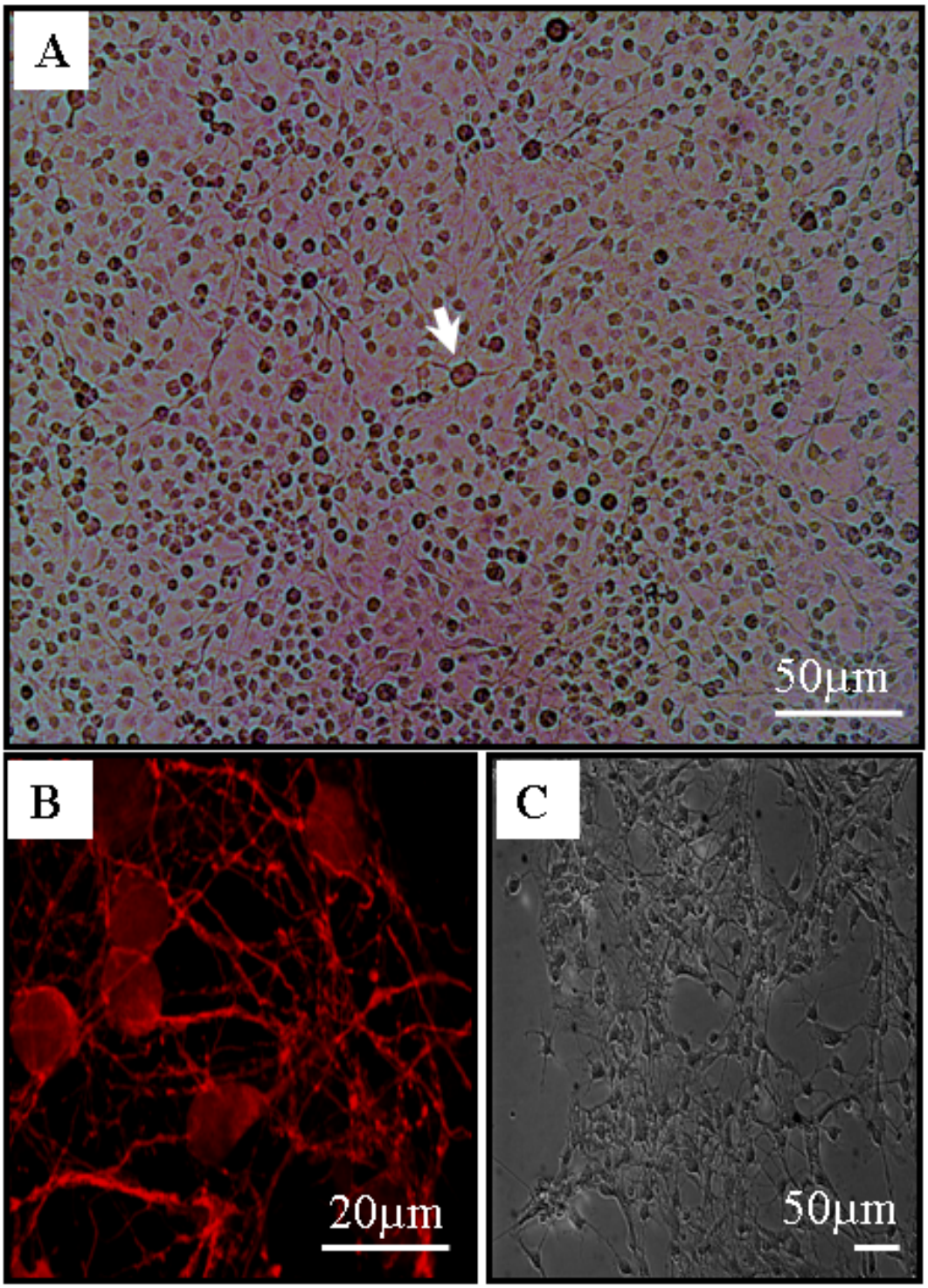
A
50μm
B
20μm
C
50μm

Figure 19: Microscopic illustration of cells in culture.

A. *OLN 93 cells after 8 days in culture. The undifferentiated cells have a small cell body. When they get differentiated, the cell body becomes large as seen in the centre of the image (white arrow). The scale bar is 50µm.* ***B****. Cerebellar grannule cell and* ***C.*** *cortical neuron culture. Left hand image shows cerebellar granule neuron cultured and stained red for a neuron specific protein β-tubulin III (scale bar 20µm). Right hand image represents a bright filed image of cortical neurons in culture (scale bar 50µm).*

CHAPTER 3

CZ INDUCED CNS MYELIN LOSS, AND ITS RELEVANCE TO MS

3.1. Introduction

CZ-induced demeylination impairs oligodendrocyte-axon association. A substantial extent of variation in myelin loss can exist within CNS regions owing to different levels of susceptibilities. Similar clinical and paraclinical heterogeneity in MS pathology is also identified because of the polygenic and multifarious nature of this disease. Such diversities are considered as manifestations of time for clinical presentation and therapeutic responses (Lassmann et al., 2001, Lucchinetti et al., 2000, Gilmore et al., 2009). MS induction is complex which stems in several factors, individual responses, and differences in demyelinating pattern between subgroups. Furthermore, there could be indiscriminate amplifying factors for myelin loss. For instance, autoimmune antibody directed against the surface components of myelin or factors that impair metabolism of myelin-supporting oligodendrocytes. Even though as a dogma demyelination is considered as loss of myelin from white matter tracts, but studies in past few years have shown that grey matter (GM) demyelination is not excluded in MS (Vercellino et al., 2009, Geurts and Barkhof, 2008). Gilmore et al., estimated significantly high levels of myelin loss from GM rather than WM in several anatomical sites (Gilmore et al., 2009). Additional complexity can arise owing to the nature of lesions which could be large, multifocal and with reactive glial scar formation (Lassmann et al., 2001). Irrespective of such facts, loss of myelin invariably affects myelinated axons, responsible for efficient saltatory conduction and important in neural co-ordination.

Inclusion of CZ in mouse diet induces CNS demyelination within weeks (Blakemore, 1973) and its withdrawal can produce nearly complete remyelination (Ludwin, 1980, Crawford et al., 2009). Even though the background for this model stems from studies of the toxic effects of this compound (Suzuki, 1969, Suzuki and Kikkawa, 1969, Venturini, 1973), in the past few years, this model has gained wide acceptance for studying demyelination and remyelination (Matsushima and Morell, 2001, Hoffmann et al., 2008, Koutsoudaki et al., 2009, Crawford et al., 2009). CZ leads to loss of myelin within 5-6 weeks of oral administration, but it is possible to study the chronic phase by continued feeding (12-13 weeks at 0.2% dose) in C57BL/6 mice (Mason et al., 2001, Hoffmann et al., 2008). The characteristics induced parallels type-III lesion features (Stidworthy et al., 2003) of MS. Mice treated with higher doses 0.5- 0.6% exhibit diffuse status spongiosus of the brain stem and midbrain (Suzuki and Kikkawa, 1969). CZ induces GM and WM (Koutsoudaki et al., 2009) lesions similar to MS characterized by degeneration of oligodendrocytes rather than by a direct attack on myelin sheet (Kipp et al., 2009).

CNS myelin loss in MS leads to sensory and motor incapacitation. Several types of studies on MS therapeutic strategies highlight a marked difference between CNS and PNS axonal features, creating a sizeable void in the present understanding (Smith et al., 2000), which continues to grow (Chomiak and Hu, 2009, Sperber et al., 2001). Even though pioneering studies (Moran and Mateu, 1983) in this field were based on peripheral nerves (Brismar and Schwarz, 1985, Sobko et al., 1998, Vabnick et al., 1999) and has significantly contributed to the understanding of mechanisms underlying demyelination, (Arroyo et al., 2001), it is imperative that CNS axon features need to be explored. A mere glimpse of the two systems provides sufficient reasoning for the existing gap.

- For instance, the distance between successive repeats of myelin membranes (i.e., between the midpoints of two consecutive MDLs differ in these two systems. Additionally, CNS and PNS myelin shrinks differentially during EM sample preparation (Hildebrand, 1974, Waxman, 2005). These differences seem to reflect varied effects of organic solvents, preservatives and fixatives on the lipid content of myelin, highlighting their compositional diversity (Siegel, 2005). This in turn could

relate to differences in the membrane dynamics owing to characteristics associated with lipid rafts which are vital for the maintenance of membrane protein topology.

- Structurally, myelinated CNS fibers lack a delimiting basal lamina. In cross sections, the string-shaped cytoplasmic domains of myelin sheath appear as inner and outer loops. In thin myelinated fibers, both loops are very small; but in large fibers, and all PNS fibers, the outer loop may include the myelinating glial cell soma.
- The paranodal loops which represent expansions of MDL at the nodal end of each myelin lamella, attach to the axon. These dense lines in internodal parts of the myelin sheath are stacked in sequence one on top of the other **(Figure 2B)**, which forms incisures of Schmidt and Lanterman in PNS but is usually found to be lacking in CNS axons (Waxman, 2005).

The main objective of this study was to develop an *in vivo* model of MS with CNS demyelination features for evaluation of concurrent changes in axonal K_v1 channels. This chapter is focused in providing a description of the induction of myelin loss from the brain, detailing specific patterns of WM and GM. Histochemical techniques like LFB/CV or toluidine blue staining, in conjunction with sucrose density gradient ultracentrifugation analysis, IHC and Brightfield or confocal **(Chapter 2)** were employed to elucidate biochemical and morphometric features.

3.2. Mild dose of 0.2% (w/w) CZ is suitable in terms of morbidity, weight loss and general behavior of mouse

The protocol for inducing demeylination involved 8 weeks oral administration of CZ by its inclusion in chow feed (rodent diet) **(Section 2.1)** to effectively produce early 'chronic phase-like' features of the disease. In this study 8 week old young adult C57BL/6 male mice were fed 0.2% CZ (w/w) diet under the experimental condition (T); the controls (UT) received the same diet devoid of this additive **(Section 2.1).**

3.2.1. CZ feeding did not introduce any behavioral abnormality

CZ-fed mice did not display any kind of gait abnormality, like splayed hind-limb or ataxia. No apparent vision associated defect could be observed. Habituation behavior was normal. However, after 3-5 weeks the group which received CZ-diet showed increased climbing activity. Occasional aggression during 4^{th} week of induction was seen in both groups. Since no actual cause accountable to such a behavior could be traced, it was assumed to be a normal aggressive demeanor of C57BL/6 mice. Furthermore, no visual sign for anxiety was noticed, except as reported by Franco- Pons et al., 2007, which indicated reduced anxiousness owing to lower rates of defecation in the treated group. In essence no major behavioral change or morbidity, mortality or motor co-ordination defect (visual assessment) appeared during the course of 8 week treatment.

3.2.2. Food intake is normal in CZ treated animals

Even though *ad lib* food and water were provided, the respective food intake for the control and CZ-treated group was 3.65 ± 0.8 and 2.7 ± 0.2 g/day (data is represented as SD). In spite of lower intake by the experimental group, differences were never significant ($p=0.10$, $n=4$) during the entire course of treatment. Minimum and maximum intake was recorded as 0.4g, and 8g in the both case. Since the average intake was within accepted limits, this could not be interpreted as loss of appetite (anorexia) due to CZ. Individual feeding pattern varied a lot displaying peak differences at the fourth week. The disparity in food intake did not exceed 2.2g. However, this difference gradually waned off in the following weeks and both of the groups displayed a similar feeding pattern.

3.2.3. Concurrent body and brain weight gain during CZ-feeding

During 8 weeks of treatment mice from both groups gained an average 10g body weight, and the increase was proportional to their feeding pattern. As described in earlier section, a corresponding discrepancy was noticed between 3^{rd} -4^{th} week of CZ feeding. They

exhibited a lower weight gain (5-7%) in between 2nd to 5th week with an increased disparity of (7-10%) during last three weeks. After 8 weeks (T1) of CZ treatment (end-point) body weight was 9.2 ±0.3 % lesser in the treated group relative to controls (n = 20). An additional week of CZ administration i.e., 9 weeks (T2) resulted in further increase in this disparity (13±0.23%). They differed significantly for T2 ($p>0.01$) but not for T1 ($p= 0.31$) **Figure 20A).** This discrepancy accounted for 50% and 30% weight gain following 8 weeks in the normal and CZ-fed mice. Overall, the experimental group exhibited lower weight gain at the end of treatment.

Does this mean that brain weight is also affected? In order to assess this briefly the wet weight of a dissected brain was recorded and compared to the corresponding body weight of that particular animal. Even though brain weight of treated group exhibited a decrease **(Figure 20B),** after normalizing them to the body weight, it revealed a non-significant (8.4 ± 0.01% g, n=8, $p=0.40$) difference. These brain weights were further co-related to myelin loss induced by CZ (described in a later section, **Section 3.3**).

3.2.4. Increased variation in body weight gain response in post 8 week CZ treatment

Variability of weight gain depends on the severity of demyelinating changes present in an individual mouse undergoing CZ treatment (Suzuki and Kikkawa, 1969, Stidworthy et al., 2003). Collectively, if the individual responses exhibit high variability their suitability for experimental use would be low. Body and brain weight scatter plot analysis provided an insight into such a deciding factor before commencing further analysis. The body wt. *vs.* brain wt. data points cluster closely **(Figure 20C)** for 8 week treated group (T1) indicating low variability. Extending the treatment to a longer period (T2, 9 week) exhibited an obvious lower clustering and reduced overlap in this analysis. This was reflected by an equal co-relation (R^2) values for the control groups after 8 or 9 weeks, but CZ-fed groups showed higher 0.21 co-relation at 8 week relative to 9 week 0.11 (n=20), indicating increased variation. On the basis of these confirming observations during the course of treatment, T1/8 week CZ-feeding was considered an appropriate time point for establishing the demyelinating features.

3.2.5. Seizure is induced during anaesthetization in the treated group

Throughout this study even though no overt behavioral symptom was exhibited during the entire course of CZ-feeding **(Section 3.2.1),** a mild seizure activity **(Supplementary, movies)** was noticed after the administration of commonly used anesthesia drugs namely, Ketamine (80-120mg/kg) / Xylazine (100mg/kg) or pentobarbital (Euthatal 200mg/kg). Most of the experimental CZ-fed mice, 15 out of 20 (~ 75%) showed an induced seizure activity. Interestingly, some (2 out of 10) mice exhibited greater extent of seizure, than the recorded video presented here. The control group which did not receive CZ had no such effect during anaesthetization. Apart from this no activity was noticed in response to startle-induced stimulations like handling, opening of the cage lid, or flashes of light. This was interesting as Hoffman group, noticed clinical seizure employing EEG/video after 12 weeks CZ-feeding and a chronic demeylination response to different types of startle-induced stimulations was concluded. The earliest response noted by that group was starting 9 weeks (0.2% CZ diet) (Hoffmann et al., 2008). Unlike Hoffman, in this study, a seizure activity was noticed after 8 weeks CZ (0.2%) feeding in spite of no obvious sign demarcating neurological deficit.

3.3. Loss of brain myelin content is eminent after 8 weeks of CZ treatment

CZ fed mice was expected to have induced CNS demeylination; hence, brain myelin loss was evaluated. Even though this can be measured in several ways, herein standard method of differential sucrose density gradient ultracentrifugation (Norton and Poduslo, 1973) was employed to obtain total myelin content and examine the myelin dry weight (Sperber et al., 2001) as a first step towards estimating the myelin loss. Mice from both groups were anesthetized, their brain dissected, and forebrain and total brain defined by coronal cuts **(Section 2.2, Figure 20D)** and weighed. Parts excluding the olfactory bulb and distal to the cerebellum was considered as total brain and forebrain defined by excluding the entire cerebellum. Myelin obtained from the interface of sucrose gradient was used for

quantification. Significant loss of myelin was observed in the treated group. The myelin content was normalized against the brain weight of each animal. This corresponded to 75.55 ± 6.76% and 55.78 ± 2.4% (p= 0.02, 0.02 n=3,) for total brain and forebrain in CZ treated group, when the control was expressed as 100 (mg dry wt)/ (wet brain wt) **(Figure 20F).** This reflects a notable reduction of 24.45± 6.7 and 44.22± 2.4% in these two parts of the brain. As is evident here, forebrain alone contributes to a larger amount of myelin loss accounting for CNS demyelination.

Biochemically, demyelinating changes may involve altered forms of protein (Kim et al., 2003), lipid (Wheeler et al., 2008, Saher et al., 2005) and carbohydrate moieties (glycolipid) (Tomlinson and Gardiner, 2008) which, in turn, would affect protein complexing/association with other protein(s). For instance, the myelinoid bodies reflect catabolic turnover resembling degraded myelin fragments formed during wallerian degeneration (Waxman, 2005) due to the acid phosphatase activity of surrounding astrocytes and microglia. Participating calpains of the degrading myelin proteins during degeneration, might be present in the floating fraction (FF) of the myelin **(Section 2.2)** obtained by sucrose density gradient ultracentrifugation. FF is highly enriched in myelinoid bodies, which can be obtained from the CNS pathological tissue (Waxman, 2005). Interestingly, similar FF was noticed in myelin preparations from CZ-treated samples. Mass spectrophotometer analysis of such fractions could be revealing but it remained beyond the scope of present interest. It had been impossible to extract the myelin content of an ON at sucrose interface, owing to its very small dimension relative to total brain. However, following observations on myelin membrane features of ON axons **(Chapter 4, Section 4.3),** it was of interest to analyze the myelin content in subsequent section 4.6, hence, 10 ONs were pooled together for such extraction. Efforts to analyze the myelin loss from cerebellum also remained unsuccessful.

3.4. Anatomically CNS demyelination features regional variation in myelin loss

The distribution, nature and extent of CZ-induced myelin loss is anatomically variable (Groebe et al., 2009, Koutsoudaki et al., 2009) as in human (Lassmann et al., 2001,

Lucchinetti et al., 2000). Hence, in order to validate the model for MS associated demeylination it was imperative to **(Section 1.17 and 1.18)** ensure a consistent and reproducible demyelinating pattern (Altmann and Boyton, 2004, Schmandt et al., 2006) of axon rich CNS tracts. Even though several morphological assays for estimating the myelination status in discrete brain regions exists, here in order to identify anatomical myelin loss Luxol Fast Blue stain (LFB) histology (Deloire-Grassin et al., 2000, Merrill, 2009) which works via an acid-base reaction was used. This allows semi-quantitative evaluation of myelin status by subjective (but observer blinded) scale. Cresyl violet (CV) and LFB stain were collectively used to define the ROIs **(Figure 20E).** Mid-saggital sections (30µm) from the brain of both groups were used. Additionally, MBP immunohistochemistry (IHC) was included to estimate GM demeylination of hippocampus. Even though these techniques suffer from several limitations due to the fact that lipid debris from degraded myelin gave a positive signal, these microscopic methods along with myelination (histological) scoring (Groebe et al., 2009) and densitometric profiling have provided ample evidence to establish CNS demeylination in cerebellum, hippocampus and corpus callosum (CC). However, the analysis of ON axo-myelin pattern had to be established using ultrastructural TEM analysis **(Chapter 4).**

3.4.1 Deep cerebellar nuclei is severely demyelinated by CZ treatment

Total brain myelin content exhibited lower loss relative to the forebrain, indicating a differential impact on parts of the brain. Cerebellum is well known to be a part of the pathological processes associated with demyelination in MS (Gilmore et al., 2009, Kutzelnigg et al., 2007) and animal models as well (Crawford et al., 2009, Groebe et al., 2009, Shields et al., 2012). So in order to gain an insight into the effect at a cellular level myelin loss in cerebellum after 8 weeks of CZ-treatment was evaluated. The rostro-caudal and medio-lateral peduncle of cerebellum identified in CV stained mid-saggital sections **(Figure 21A, B)** and parallel LFB staining were used to analyze the effect on WM and GM regions. The molecular layer (ML), granular layer (GL), pyramidal layer (PL), and WM layers of the cerebellar cortex (CCx) as well as the cerebellar marrow (CM) could be

distinguished. CM of the cerebellar peduncle containing the three deep cerebellar nuclei (DCN) namely, lateral (LCN), medial (MCN), and interpositus nucleus (IN) were assessed. The WM which is rich in myelinated axonal tracts appeared brownish red; whereas the GM with larger cellular population in ML, GL, and PL were purple in CV stained preparations **(Figure 21A, B).** LFB stained myelinated tracts were prominently blue colored structures of CM and WM tracts of the CCx folia across the entire cerebellum including the anterior to posterior lobe **(Figure 21C, D).** CZ-treatment for 8 weeks resulted in a massive and evident loss of myelin from the CM as LFB stained fibers diminished in these samples. Entire DCN in the cerebellar peduncle region and its three nuclei namely, LCN, MCN, and IN cease to stain blue due to myelin deprivation **(Figure 21 C, D, E, F**, double black arrow**)** in the treated group. Interestingly, the surrounding area of the cerebellar nuclei was not much affected. The myelin sheets in the CCx and distinct cellular layers the ML, GL and PL did not reveal any change in myelination **(Figure 21 C, D** red arrow**)**. Blinded quantitative histological scoring of LFB stain intensity in the entire cerebellum on a scale of 1-5 was performed by 10 neutral observers. According to this assessment, the myelin status in the entire cerebellum was significantly reduced **(Figure 20G) (**$p>0.001$, $n=10$).

Densitometric profiling of the above-described ROIs within the cerebellum was adopted to investigate the difference between WM and GM subdomains. The average data obtained from 5 ROIs defined in 3 images of each brain sample was normalized for the background (density of regions without tissue) **(Section 2.8).** This approach provided evidence of highly significant ($p>0.001$, $n=3$) loss of myelin in the deep cerebellar nucleus only **(Figure 20H).** Rest of the regions namely the WM of CCx (foliar structure), and GM of ML and GL also showed a minor, non-significant decrease in myelin. Thus, it is concluded that post 8 week CZ-treatment, CCx of the cerebellar folia remains resistant to WM or GM demeylination. The GL and ML are not susceptible to myelin loss as per this method, but there is a drastic deprivation of myelin from the CM depleting it from the entire DCN.

Differential demyelinating effect on the rostral or caudal cerebellar cortex of CZ mice (Stidworthy et al., 2003) may lead to varied symptoms as found in human (Gilmore et al., 2009). Herein, demeylination was assessed for the entire cerebellum. Saggital sections at

an interval of 500µm from the medial longitudinal fissure until the lateral edge i.e., 3mm away were analyzed**.** No difference in the pattern extending from the medial to lateral position was observed in the treated group. It is therefore, concluded that after 8 weeks of CZ feeding, entire cerebellar peduncle extending from i.e., latero-central to the rostro-caudal end is uniformly demyelinated.

These results established, cerebellar demeylination pattern in CZ fed animals at 8 week time point. Disparity between the WM of cerebellar folia and peduncle is similar to 5-6 week pattern (Groebe et al., 2009). GM layers like ML and GL remains unaffected as per this method of assessment. The DCN of cerebellar peduncle was extensively demyelinated. This also explains the inability to detect myelin from cerebellum, using sucrose density gradient method, possibly due to the low yield of myelin content expected from the demyelinated nuclei **(Section 3.3).**

3.4.2 Extensive forebrain demyelination due to myelin loss from axon-rich WM tracts of CC, striatum and fornix

Forebrain demyelination which accounts for 44% myelin loss **(Section 3.3)** was anatomically delineated to structures like corpus callosum (CC), hippocampal regions striatum and fornix. CC is a broad-arched band forming the most distinguishing portion on the surface of the cerebrum. If the two hemispheres are observed when they are still interconnected, the CC is on the floor of the longitudinal cerebral fissure. Functionally, this structure links the two cerebral hemispheres and allows the two sides of the brain to inter-communicate.

After CZ-treatment it was found that CC and striatum are the most demyelinated regions of forebrain. Axon tracts from the entire WM **(Figure 22A1, A2, B1, B2)** are significantly demyelinated. Both these regions portrayed different levels of myelin loss. Collective myelination score on LFB stained sections for forebrain areas including hippocampus, CC and fornix exhibit 62±0.5%, ($p>0.001$, $n=10$) myelin loss **(Figure 23E).** This method

showed higher levels of demeylination relative to sucrose density gradient **(Section 3.3).** This reflects major myelin loss from the CC **(Figure 22, Figure 23),** which is the largest WM tract of brain. Segregated scoring for CC and striatum gave 96±0.2% and 88±0.71%, ($p>0.001$, 0.001, $n=10$) reduction in myelin for these regions after 8 weeks of CZ challenge, indicating that CC is more susceptible to demyelination than striatum **(Figure 22, Figure 23 A1, B1,** white boxes 1 and 2**).** Densitometric analysis revealed differential effect on the rostro-caudal end of CC. The myelin loss from the rostral end i.e. genu of CC (gcc) was higher than the caudal end **(Figure 23A, B, C, E).** Similarly striatum junction **(Figure 23A1, A2, B1, B2, D)** showed lower susceptibility as compared to rest of the regions of this large white matter tract. This confirms varied extent of demyelination within the sub-regions of CC.

Similarly, fornix (fx) **(Figure 22, Figure 23A2, C1)** which is a prominent and compact bundle of white fiber through which the hippocampus of each cerebral hemisphere projects to the opposite hippocampal lobe, septum, anterior nucleus of the thalamus, and mammillary body portrayed greater demeylination **(Figure 23B1, B2)** relative to the entire hippocampus after 8 weeks of CZ-treatment. Even though CZ demyelination can be employed for studying the hippocampus (Koutsoudaki et al., 2009, Hoffmann et al., 2008), LFB stain estimation of hippocampal GM demyelination (Gilmore et al., 2009) was supplemented with MBP immunostaining of sections. This allowed distinct visualization of CA3, CA2 and CA1 sub-regions and all these structures were extensively demyelinated **(Figure 22C1, C2**) in this study. Most formations of the hippocampus like stratum oriens, hilus and stratum radiatum were affected. Entire alveus (rostral and caudal ALV), stratum moleculare (SLM) - the terminal layer of the medial prefrontal path were found to be demyelinated. The cortex also underwent myelin loss **(Figure 22D1, D2).** Interestingly enough even loss of myelin was obviously visible in parallelly processed MBP labeled sections. However, densitometric analysis for both LFB and MBP did not show any marked difference between the hippocampal regions of treated and untreated group. Comparison of WM tracts exhibits a greater difference. It was hereby noted that even though MBP and other myelin protein based IHC could be employed for visualization of demyelinating effect in large axonal tracts, a quantitative estimation remained elusive for GM regions,

which have larger cell populations. Herein, the possibility of obtaining signals from myelin debris cannot be ruled out and, hence, a quantitative estimation of GM demeylination based on myelin protein IHCs may remain biased. However, it is important to note that several groups have successfully employed proteolipid (PLP) IHC which is an integral membrane protein for myelin to successfully differentiate regional variability in demyelination of MS tissue and animal model as well (Gilmore et al., 2009, Groebe et al., 2009). Irrespective to all these, it was concluded that fornix, striatum and CC **(Figure 23E)** were prominently demyelinated regions of the hippocampus.

Hippocampal demyelination owing to the effects of CZ can induce seizure in response to stress-induced stimuli. Epileptiform spikes resembling patterns similar to known forms of chronic epilepsy, and electroencephalogram (EEG) from hippocampal electrode implant study, have indicated alterations owing to axonal pathology after prolonged treatment (12 weeks) (Hoffmann et al., 2008). This group considered neuronal damage secondary to CNS demyelination which might have a potential role in hippocampus induced seizures. Considering such deductions, here it implies that the GM demyelinating effects of hippocampus after 8 week of CZ feeding are subtle or small, which cannot be robustly indicated. However, it might be possible to observe a higher level of quantitative and distinguishing loss of myelin after a prolonged period of treatment if the loss becomes more extensive. On the other hand functional impact resulting in seizure **(Section 3.2.5)** was noted, even though it cannot be directly extended to any morphological alteration using myelin protein IHC. It is possible that other processes which precede myelin loss and debris removal is in place and mild effects are being induced. Such interpretations would require ultrastructural analysis of hippocampus, which remains beyond the scope of the present study. So, it can be reasonably assumed that the effect of 8 week 0.2% CZ is subtle in this region and in order to distinguish GM/WM demeylination further work is warranted. It is concluded that the entire forebrain is variously affected and CC is the most altered WM tract followed by the fornix. GM tracts appear to be demyelinated but a quantitative estimation and conclusive deduction using histochemical techniques is elusive.

3.5. Conclusion: This chapter conclusively describes the establishment of CNS demeylination employing a CZ-feeding protocol. Forebrain incurs greater loss of myelin relative to entire brain. Most of the axon rich tracts are adversely affected. Cerebellum exhibits a differential pattern, where only DCN is affected and CCx is excluded, whereas forebrain structures like CC and striatum are entirely demyelinated following 8 weeks of CZ-feeding.

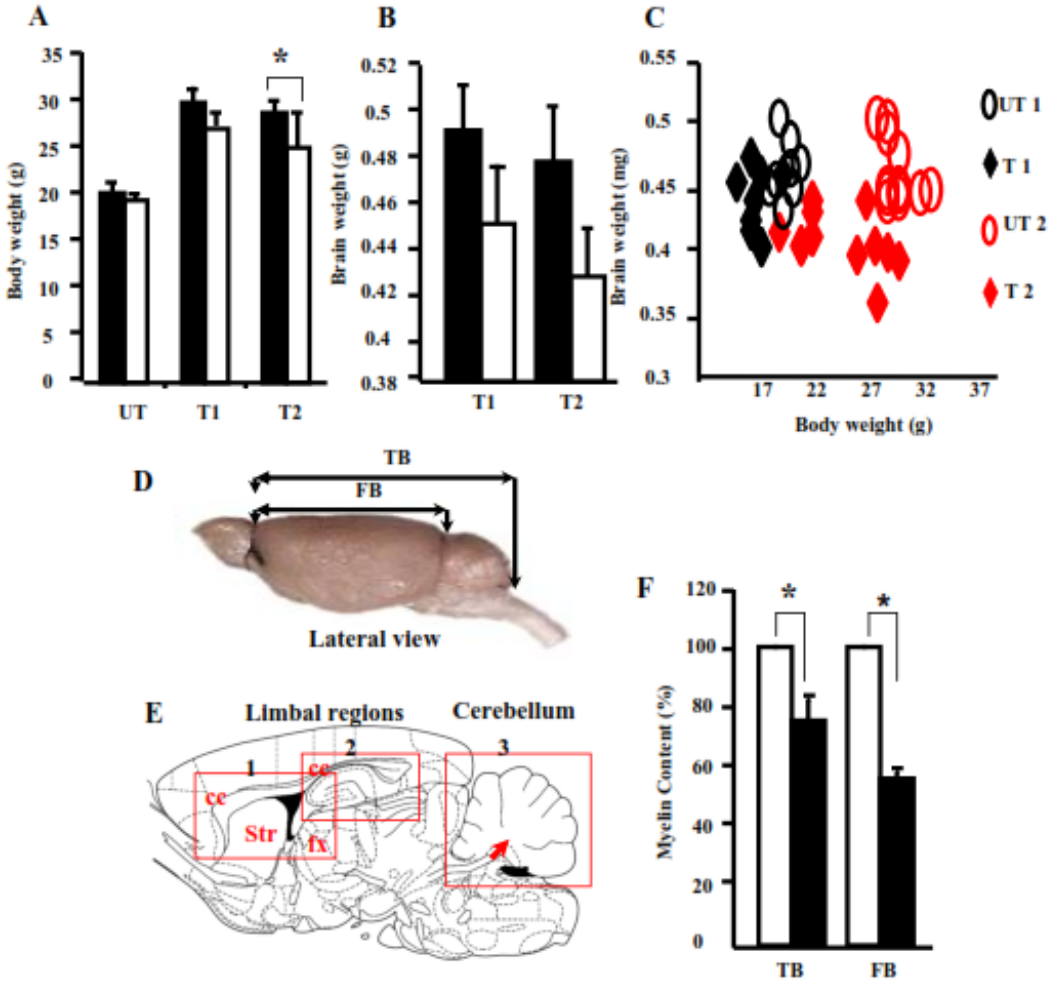

Figure 20: CZ induces demeylination, but with no apparent effect on body or brain weight.

A. *Cumulative weight gain (gms) during 8 to 9 weeks of treatment was obvious. Here UT, T1 and T2 indicate untreated and treated groups at 8 and 9 weeks, respectively.* ***B.*** *The total weight of a dissected brain showed reduction in treated groups. This was a non-significant change (p=0.4, n=20).* ***C.*** *Body weight gain correspondence to brain weight was examined during the course of treatment to note any difference in individual response. It was found that T1 animals had a synchronous response; variability sets in only at T2, shown as spread of red diamonds (n=20).* ***D.*** *Lateral view of a brain to show the regions used to delineate forebrain and total brain for myelin content quantification. The arrows pointing downwards indicate the position of incision(s). Horizontal arrows represent the brain regions used for analysis (top panel).* ***E****. Schematic mid saggital view of murine brain shows the anatomical location of the ROIs in this study. The forebrain system (box1) includes corpus callosum (cc), striatum (Str), and fornix (fx). The caudal end of corpus callosum, and hippocampus (box2) and cerebellum (box3) are marked in the boxes.* ***F.****CZ feeding induces loss of total myelin content from the brain (total) and forebrain (p=0.02 for both groups, n=3). Normalized values of myelin (mg dry wt./brain wet wt.) is represented here, □ untreated, ■ treated.*

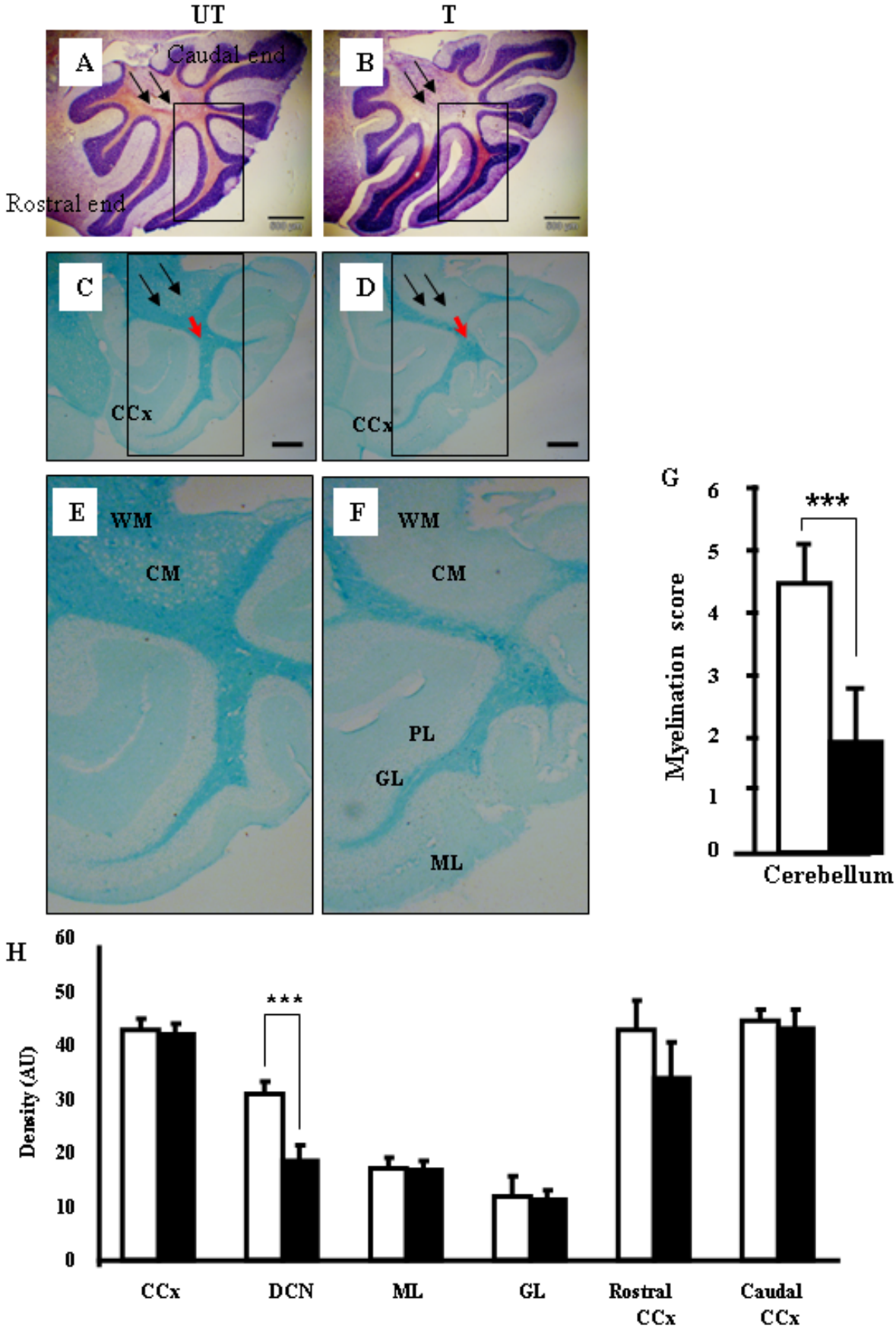
UT
T
A
Caudal end
Rostral end
B
C
CCx
D
CCx
E
WM
CM
F
WM
CM
PL
GL
ML
G
Myelination score
0
1
2
3
4
5
6
***
Cerebellum
H
Density (AU)
0
10
20
30
40
50
60
***
CCx
DCN
ML
GL
Rostral CCx
Caudal CCx

Figure 21: DCN demyelination due to CZ feeding.

A. *Cresyl Violet stained mid-saggital sections (30µm) representing the general architecture of cerebellum, black double arrows point cerebellar peduncle, marking the WM and DCN from control group.* ***B.*** *CZ-treated cerebellum stained with CV shows similar organization.* ***C.*** *Myelin specific stain for LFB highlights the WM tracts stained blue (black arrow) and GM (light blue stain) in the cerebellum of untreated control.* ***D.*** *Diminished LFB stain from DCN of CZ-treated cerebellum. Red arrows point to the myelin-rich area at the junction of cerebellar folia and boxed areas represents single folia of the cerebellum. The CCx comprising the foliar tract did not undergo demeylination after CZ feeding.* ***E.*** *The region squared in C has been enlarged to illustrate intact DCN of control brain.* ***F.*** *The region squared in D has been enlarged to show specific demeylination of cerebellar marrow. A complete loss of myelin can be noted in this region relative to the untreated group. The PL, GL and ML did not show any distinguishable effect on the myelin using LFB stain.* ***G.*** *Myelination score for the entire cerebellum including all folia extending from rostral to caudal end and CM shows a highly significant decrease after treatment ($p>0.001$, $n=10$).* ***H.*** *Histogram summarizing the prominent effect of CZ demeylination on DCN relative to other regions of cerebellum, □ untreated, ■ treated. Cerebellar cortex (CCx), Cerebellar matrix (CM), Purkinje layer (PL), granular layer (GL), Grey matter (GM) and molecular layer (ML), deep cerebellar nucleus (DCN), White matter. Scale bar, 500µm for A-D.*

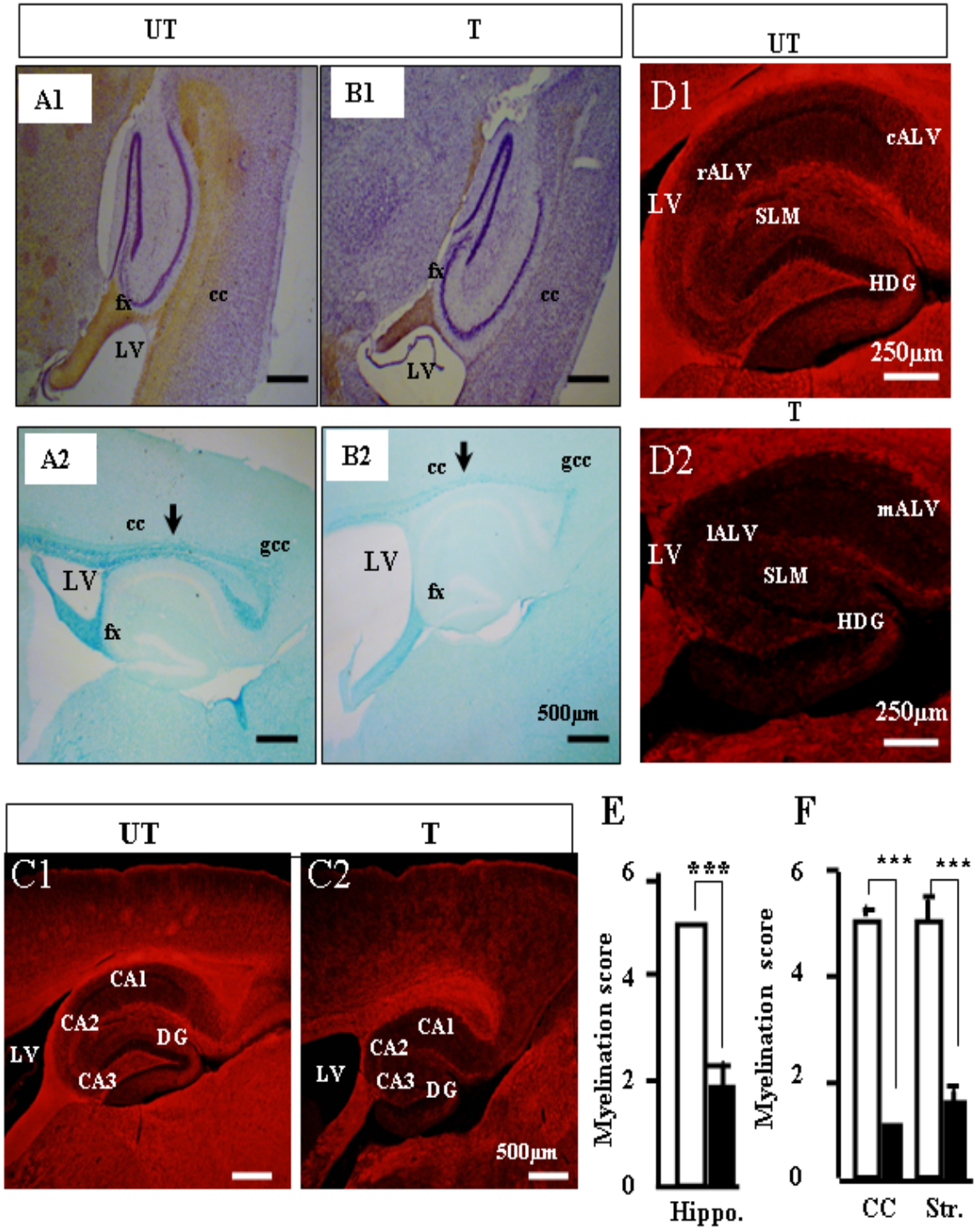
UT
T
UT
A1
B1
D1
fx
cc
LV
cALV
rALV
SLM
HDG
250μm
T
A2
B2
D2
gcc
500μm
mALV
lALV
UT
T
C1
C2
CA1
CA2
DG
CA3
E
F
Myelination score
***
Hippo.
CC
Str.

Figure 22: Forebrain demeylination.

A1. *CV stained mid-saggital sections (30µm) of untreated brain representing the general architecture of CC, striatum and fornix.* ***B1****. Similar sections from CZ-treated group showing diminished WM tracts (brown color).* ***A2.*** *Similarly these regions have been identified in LFB stained comparable sections of control.* ***B2.*** *Overall loss of myelin is obvious relative to the control group.* ***C1****. MBP stained mid-saggital section of control brain showing the myelinated tracts of forebrain, highlighting the hippocampal formations like CA1, CA2, CA3 and DG.* ***C2.*** *Similar sections from treated group show low intensity of stain for MBP in these regions and CC.* ***D1.*** *Hippocampus of untreated group sample showing the levels of MBP in ALV, SLM and HDG.* ***D2.*** *Visible loss of myelin stain within these ROIs of CZ-treated brain is evident. Scale bars 500µm (A1, A2, B1, B2, C1, C2), 250µm (D1, D2).* ***E.*** *Histogram showing significant loss of myelin from hippocampus, (p>0.001, n=5).* ***F.*** *Similar histogram represent loss of myelin from CC and striatum (p>0.001, >0.001, n=5) as well based on myelination score in 0-5 scale, □ untreated, ■ treated. Lateral ventricle (LV), fornix (fx), striatum (Str), corpus callosum (cc), dentate gyrus (DG), cornu ammonis (CA1, CA2, CA3), stratum lacunosum moleculare (SLM), rostral alveus (rALV), caudal alveus (cALV), and hilus of dentate gyrus (HDG).*

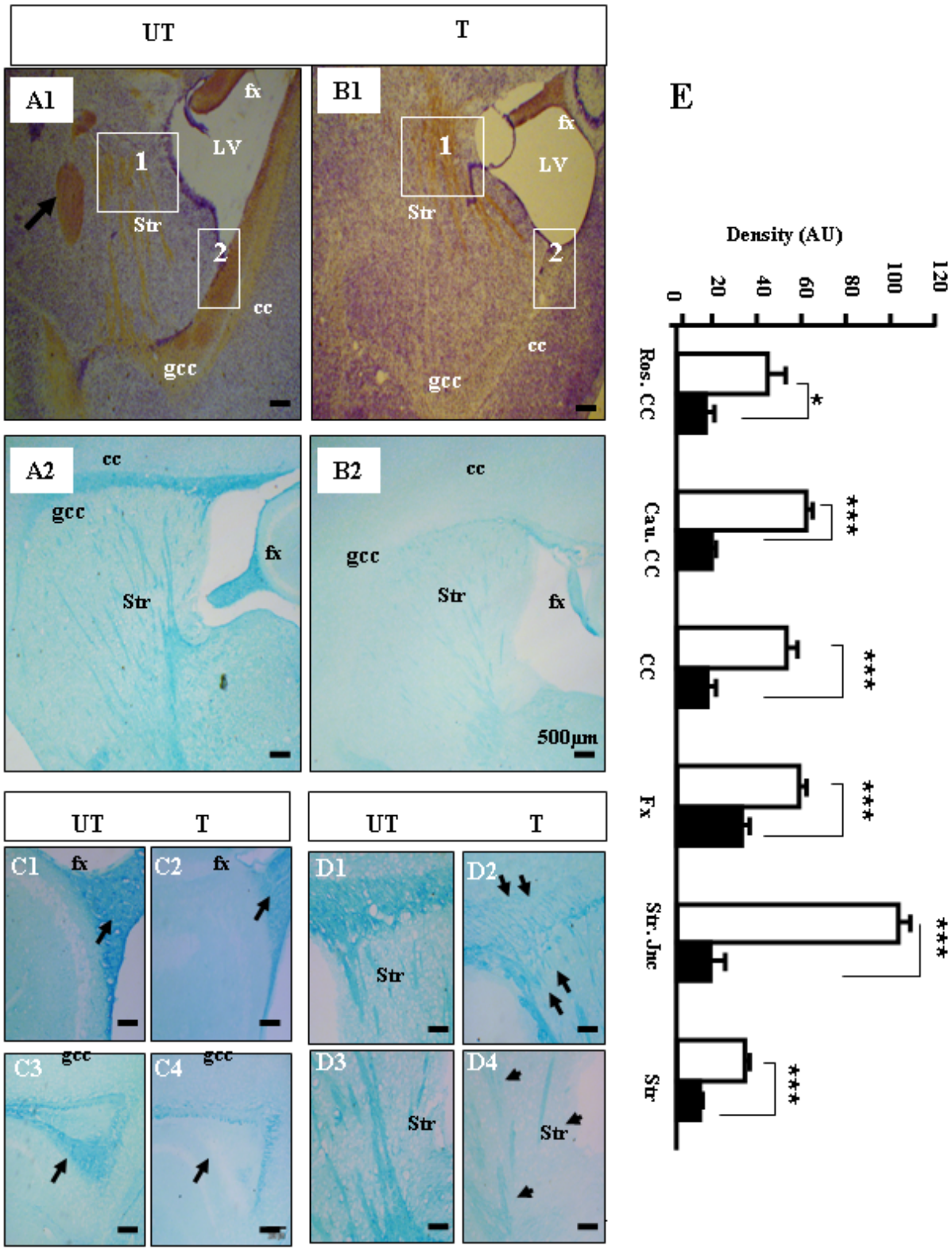
UT
T
A1
B1
fx
LV
1
2
Str
cc
gcc
A2
B2
500µm
C1
C2
C3
C4
D1
D2
D3
D4
E
Density (AU)
0
20
40
60
80
100
120
Ros. CC
Cau. CC
CC
Fx
Str. Jnc
Str
*
***

Figure 23: Hippocampus and fornix demyelination.

A1. *CV stained mid-saggital sections (30µm) representing the general overview of hippocampus and associated structures in control.* ***B1.*** *Similarly, these structures have been identified in the experimental group, where WM tracts (brown color) appear to be diminished.* ***A2.*** *LFB stained comparable sections from control group showing intact CC, striatum and fornix with prominent axon tracts (dark blue).* ***B2.*** *Note the loss of these WM axon rich tracts from the demyelinated brain. These structural details (boxed A1, B1) have been highlighted in the bottom panel (C, D).* ***C.*** *The fx (C1 and C2), gcc (C3 and C4), show marked loss of myelinated tracts. More prominent loss of gcc is noted compared to fx.* ***D.*** *Similarly, the junction of cc at the LV (D1 and D2), and striatosomes (D3 and D4) of the striatum have been highlighted to show the loss.* ***E.*** *Histogram representing differential loss of myelin as assessed by densitomeric analysis of defined ROIs, Rostral CC (Ros. CC), caudal CC (Cau CC), corpus callosum (CC), fornix (Fx), striatum junction (Str. Jnc), striatosomes (Str.) genu of corpus callosum (gcc),* □ *untreated,* ■ *treated, scale bar500µm (A1, A2, B1, B2), 100µm (C1- C4, D1-D4).*

CHAPTER 4

OPTIC NERVE DEMYELINATION LEADS TO LOSS OF MYELIN MEMBRANE PERIODICITY AND INCREASED HYPO-PHOSPHORYLATION OF NEUROFILAMENT

4.1. Introduction

Further to the convincing and reproducible evidence for CNS demeylination from WM tracts following CZ-treatment, the myelin status of ON axons was analyzed to elucidate axo-oligodendrocyte features. Clinically MS is often presented as an acute unilateral optic neuritis, a condition leading to complete or partial loss of vision (Soderstrom, 2001, Smith and Hall, 2001). Such conditions may or may not turn out to be clinically definite MS (CDMS), but with well-informed cases and emerging pharmaco-therapy, the distinction between such patients has become more important than ever (Barnett and Sutton, 2012). These suggestive cases often evidence subclinical demyelination in their brain MRI and they respond positively to the treatment resulting in reduction of development of CDMS. Neurotherapeutic intervention to contain the disease progression at such a stage can be equally important in preventing disability amongst the patients, which arise due to continued myelin loss. One of these therapeutic strategy that is expected to be detrimental is K_v channel blocking **(Section.1.16)** (Judge and Bever, 2006, Sherratt et al., 1980). Mismatched action potential propagation leads to interrupted or disrupted axon conduction resulting in cognitive and motor dysfunctions of MS. This is an infestation of myelin loss, which in turn affects K_v channels located at the JXP. Their clustered and sub-domain specific expression in an axon is dependent on the compacted nature of myelin irrespective of oligodendrocyte attachment to the axolemma (Baba et al., 1999). This morphological feature has been described for development, but it also co-relates to demyelination, when axo-myelin association is disrupted due to a reverse process. This type of attribute leads to

loss of continuity within the cable like structure of myelinated axon. If such a myelin disruption is considered as dysmyelination (disorganized myelin membrane), then it precedes demyelination (disappearance of myelin membrane) (Song et al., 2002, Sun et al., 2006) which involves loss of myelin membrane from the internodal segment. Identification of such features to make a progressive research on the lines of K_v channel blocking strategy in animal models is anticipated to prove relevant for neurotherapeutic intervention. Collectively, these facts are foreseen to augment K_v channel therapeutics, allowing an early stage intervention (Compston and Coles, 2002) rather than usually-recognized importance in late stage symptomatic relief (Judge and Bever, 2006) in MS. Unfortunately, most of the animal model studies involving role of K_v channels have been conducted on developmental stages of myelination in ON (Rasband et al., 1999b, Dangata et al., 1996, Foster et al., 1982, Roncagliolo et al., 2006) or peripheral nerves. Studies based on adult nerve features have usually been conducted on mutant models (Devaux and Gow, 2008, Griffiths et al., 1998), which are suitable for analyzing the effect induced by one particular protein. Whereas MS is a chronic CNS disease of adults, and analysis in systemic demyelinating animal models can establish global or a broad spectrum clinical bearing which has not been established so far. Research on functional aspects of ON has been equally lacking in these models and hence the understanding remains incomplete.

Anatomically, ON is an extension of the retinal ganglion cell (RGC) axons of the retina and is highly susceptible to functional blockade (Stys, 2004). During demyelination axons have an inherently low safety factor for conduction, and are predisposed to the effects of soluble factors as well **(Section 1.8)** (Smith and Hall, 2001, Waxman, 2005). As the disease progresses, profound effect can be manifested due to synergistic or collective action of several factors (Coleman, 2005, Waxman, 2005). Such a global perspective is important for an increased understanding of the development of therapeutic strategy. So, this study undertakes evaluation and analysis of demyelinating effects in such a model. The myelin content, quality, and extent in addition to changes in surrounding cellular pattern due to CZ were investigated in axons of adult ON. Additional use of TEM based ultra-structural analysis has been beneficial in establishing elaborate effects induced.

4.2.1. Cross sectional surface area of the ON increases after CZ-treatment

ON is a tiny structure relative to other regions described earlier (**Section 3.4**). So, no difference was noticed amongst the isolated nerve from both groups. It had a uniform appearance which measured 2.2 mm long and was lodged in between the optic foramen and chiasma. The distal (distal to mid body axis, i.e., close to the optic foramen) and proximal end (proximal to mid body line correspondingly close to the chiasma) width (diameter) was 250 and 500µm. Microscopic investigation of CV stained 30µm radial cryosections from both ends did not display any drastic change in morphology. The entire nerve exhibited no significant change in appearance **(Figure 24A).** Average cross sectional area was analyzed on slide mounted cryosections and was found to be 49.2 ± 7.7 and 68.0 ± 7.6 mm^2, n = 5, p = 0.13, ranging between 15 to 69 mm^2 and 56 to 83 mm^2 for control and treated group in these preparations **(Figure 24D).** The wide range of cross-sectional area in the untreated group signified that the nerve was more slender at one end relative to the experimental group. An estimation of nerve diameter at both ends, namely proximal and distal showed that proximal end is relatively swollen after CZ-treatment. The average perimeter was 813.3 ± 76.1 and 927 ± 41.9 µm, n = 5, p = 0.28 ranging in between 460 to 960 µm and 860 to 1000 µm for untreated and treated ON **(Figure 24C).** This corresponded to 38.3% and 13.9% increase in average area, and perimeter of ON when the CV stained cross sections were assessed; thus indicating swelling of the nerves at one end.

4.2.2. Inter-fascicular cells of ON re-orientate in between the axons of CZ-treated group

Light microscopic examination of mid-nerve cross sections (5µm) stained with toluidine blue was used to reveal the fascicular organization of ON. The inter-fascicular space appeared larger in the treated group **(Figure 24B).** The ON axons were uniformly spread within these fascicles. Axonal counts in the untreated and treated groups were 310.3 ± 13.2 *vs.* 272.4 ± 19.1 per μm^2; p = 0.15, which was indicative of a minor non-significant decrease **(Figure 24E).** Intercalated cells in between the fascicular space within the nerve

appeared to re-orientate themselves. This was more noticeable in longitudinal sections, with cells exhibiting various types of nuclear and cellular morphology **(Figure 24H-I).** Even though the identity of these cells was not established in this study, they could be oligodendrocytes, astrocytes, microglia and NG2-glia as they are the main inter-fascicular cells of ON (Butt et al., 2004). All these cells perform varied functions; hence, this observation could only be an indication of a consequential effect of CZ on ON cells. However, the exact nature of these changes remains unknown in this study. It would not be surprising, if they are astrocytes as shown in a recent study (Skripuletz et al., 2013), even though not established here as this was beyond the main objective.

4.3. Influence of CZ on myelin proteins of ON

Myelinated axons are one of the most complicated biological structures owing to the intimate association **(Section 1.1)** between the axon and glia (Nave, 2010b, Nave, 2010a, Rash, 2010). Lipid-enriched myelin contains large amounts of proteins like, proteolipid protein (PLP) and myelin basic protein (MBP) (Siegel, 2005, Nadon et al., 1997). An array of such protein maintain the integrity of myelinated axons (Baumann and Pham-Dinh, 2001, Nave, 2010a). Some of the major myelin proteins, namely myelin basic protein (MBP), proteolipid protein (PLP) and 2',3'-Cyclic-nucleotide 3'-phosphodiesterase (CNPase) were assayed herein from the homogenates of ON, and further analyzed by confocal microscopy to elucidate the axo-myelin morphological features.

4.3.1. Myelin proteins are marginally decreased in homogenate of ON

Whole nerve homogenates were assayed for MBP which is an intercalating peripheral protein present in between the myelin membranes. The normally phosphorylated form of MBP is hypo-phosphorylated in MS brain (Kim et al., 2003). It is a complex protein, transcribed from multiple transcription sites. Here five isoforms of MBP varying size ~14, ~17.2, ~17.3, ~18 and ~21 kD were detected from ON homogenate under denaturing conditions using SDS-PAGE. The most prominent form was ~18kD **(Figure 25A)** band

hence, this was considered as a representative for quantitative evaluation. CNPase was identified as a doublet of ~46-48kD and PLP as ~30kD band on these blots **(Figure 25A).** In spite of established robust CNS demeylination of these mice **(Section 3.3, 3.4),** surprisingly there was no apparent difference between the myelin proteins of ON. However normalizing the quantity relative to the tubulin band (~55kd) was indicative of varying levels of non-significant loss (n = 3). Nevertheless it was always found to have a considerable amount of variability in between sample preparations. This could not be overcome by use of antibodies against house-keeping proteins as a loading control. Even though tubulin is regularly used as a control, surprisingly here, quantities of tubulin exhibited 40-43% variation between untreated and treated groups, indicating that such proteins are affected following CZ-treatment. Then, it was further questioned whether this variability is specific to ON or other tissues as well. Evaluation using retinal protein did not show such variation for tubulin; which remained within acceptable limits of 0.70-0.73% in equal amounts of BCA quantified protein for both groups. Thus, evaluation of myelin proteins using this method remained unreliable.

4.3.2. Altered expression of myelin proteins in CZ-treated axons indicated structural changes

To investigate the above observations, ON axons were labeled for IHC analysis; their microscopic evaluation provided some insight into the effects induced after CZ-treatment. Confocal microscopy was performed for 10µm thick ON longitudinal sections fluorescently labeled with Alexa Fluor® for MBP and NF **(Figure 25B1-C2),** CNPase and PLP/DM20 in order to identify the axons. Interestingly, all the myelin proteins in these preparations revealed three different types of structural changes in axo-myelin association. Firstly, NF positive axons **(Figure 25C1, C2)** overlapped with MBP-labeled myelin sheaths in both groups **(Figure 25 B1, B2),** indicating none of the axons are completely devoid of myelin **(Figure 25B)**. Secondly, the fluorescence intensity for MBP did not vary amongst the treated and untreated groups, but structural disruption of the myelin layer marked by vacuolization was noticed in both MBP and CNPase **(Figure 25 D1, D2, E1, E2)** labeled

axons. The axon-myelin (MBP) associations appeared disrupted in the treated group **(Figure 25 D1, D2).** This effect was more prominent when they were labeled with CNPase. It exhibited a loss of emerging processes radiating out of the soma of the oligodendrocytes in treated group, whereas these remained intact in the control groups **(Figure 25E1, E2).** This observation was indicative of loss of CNPase, as it is readily affected by CZ-induced demeylination (Carey and Freeman, 1983). Lastly, use of PLP/DM20 specific antibody to reveal axo-myelin association indicated widespread loss of compact myelin. Untreated group myelin appeared as uniform and regular structure whereas in the treated group axons they acquired a striated sheet like structure**.** Collectively these results provide evidences of ON myelin proteins being adversely influenced due to CZ, so that there is disruptive loss of axo-myelin.

4.3.3. Glial astrocyte fibrillary protein indicate hypertrophy in treated ON

It was evident from the above-described observations that the cells surrounding axons are differently affected by CZ-treatment. Astrocytes are one of the cell type which occupy 30% of space in ON (Perge et al., 2009) and they have numerous projections which anchor neurons to their blood supply (Rash, 2010). So, specific labeling of astrocytes with glial fibrillary acid protein (GFAP) was employed to analyze their association with axons; and this displayed two interesting features. Firstly, the shape of astrocyte was changed in the treated group. The astrocytes changed their shape. The control ON astrocytes possessed a few (4-5) short processes **(Figure 26A1, A2)** whereas in CZ-treated samples they were hypertrophic and multipolar. It had acquired profusely branched processes in the experimental group. Even though astrocytosis would involve both hypertrophy and hyperplasia, herein an increase in astrocyte branching and area was easily observable **(Figure 26B1, B2).** Each process of the astrocyte has several sub-branches after treatment **(Figure 26B2).** A representative electron micrograph is presented here (n = 3), which shows the marked appearance of processes invaginating in between the axon clusters, indicating typical astrocyte activity **(Figure 26C)**. An analysis of the signal from the two groups exhibited 10% increase in average fluorescence per mm^2 following CZ treatment. It was 39.23 ± 5.43 for control and 59.19 ± 2.06 (AU/mm^2) for the treated samples, n = 35, p

= 0.03 **(Figure 26D).** These cells regulate the external chemical environment of neurons by removing excess ions, notably K^+, and, also, recycle neurotransmitters released during synaptic transmission (Adelman and Fitzhugh, 1975). Overall, these observations indicate an increased astrocyte activity in the ON metabolism during CZ-induced demyelination.

4.4. Ultrastructural changes in ON after CZ administration

4.4.1. Axon and myelin

The susceptible axo-myelin interactions (Chomiak and Hu, 2009, Piaton et al., 2010, Trapp and Nave, 2008) undergo subtle structural changes during injury or disease, which influence the myelinated axon(s) and/or its surrounding(s), capable of inducing functional deficits (Devaux and Gow, 2008, Moran and Mateu, 1983, Sun et al., 2006, Song et al., 2002, Nave, 2010b). So the myelin structure, and its surroundings within the nerve, was further evaluated by employing transmission electron microscopy (TEM). Usually ultra-structural CNS response to CZ involves induction of status spongiosus, characteristically affecting the myelin sheaths and glial cells (Suzuki and Kikkawa, 1969) of the brain. Herein, for the first time, ON features in CZ-induced demeylination was explored to assess the extent of effect on myelin. Several parameters like myelin sheath thickness, fiber-and axon-caliber and "g" ratio were evaluated to establish the axo-myelin status after CZ-treatment.

4.4.1.1. Most of the axons remain myelinated after CZ treatment

TEM images of myelin sheaths were assessed in longitudinal and cross sections for both the groups. They appeared to have similar myelin membrane profiles at 5µm scale. At higher magnifications, different types of membrane-associated changes were noticed (described in subsequent sections 4.4.1.2, 4.4.13, and 4.5). Virtually all axons appeared to be myelinated 96.8 ± 5.06 %, n = 1525 in the control group. The treated group also showed

similar profile 95.2 ± 4.23 %, n = 1289 **(Figure 27A, B**). The minor unmyelinated population of axons noticed in both groups 3.2 *vs.* 4.7% was as expected attributed by the small diameter cross sectional profiles of the nodes of Ranvier. Average fiber thickness (di+do) defined as the total diameter including the axolemma bound inner diameter (di) and the thickness of the myelin membrane bound to the outer diameter of the myelin sheath (do) was 1.16 ± 0.04 and 0.96 ± 0.03 µm for control and experimental group **(Figure 28C)**. These measurements were manually obtained using ImgaeJ (NIH) by drawing lines between the delimiting membranes. They range between 0.36-3.70 µm for control and 0.10-3.50 µm for the treated sample; on the other hand "di" was 0.27-3 µm and 0.13-3 µm for control and treated group **(Figure 28C).** Individual axons of treated mice appeared less annular. Their profiles could not be considered as exactly round in shape **(Figure 27B).** In order to get the reliable values herein, the less annular axons were sampled twice or thrice along their radial axis passing through the centre of these profiles and the average for each axon was considered as a representative measurement. These analyses were conducted on TEM images from three sets of experiment.

4.4.1.2. Loss of myelin thickness is eminent

As the myelin sheath gets thicker it occupies an increasing proportion of the surrounding volume which, in turn, alters its resistance and capacitance, thereby, changing the axon function. Myelin thickness was measured as (do-di) from the TEM 500nm images. Average myelin thickness for untreated group was 0.26 ± 0.01µm, n=1087 and 0.16 ± 0.08µm for the treated group, n = 805, p > 0.001 **(**Figure **27E).** Their range (0.01- 1 µm) was same for both the groups.

For the untreated group the peak average frequency (21.48 ± 1.49 to 22.96 ± 2.68%) of myelin thickness was between 0.2-0.3µm. The second (13.01 ± 1.8%) and third (12.80 ± 2.15%) most frequent myelin thickness were 0.1-0.4 and 0.4-0.5 µm. The remainder accounting for the thickest and thinnest myelin layers was found to be in a narrow frequency range of (8.6 ± 1.08 to 6.55 ± 1.04%). Some of them were also categorized as the

least frequent (1-2 %) **(Figure 28A).** None of the axons exceeded myelin thickness of 1.3µm in these preparations. Similarly, for the treated group peak average frequency was between 35.24 ± 2.00 to 37.08 ± 2.66% for myelin thickness range 0.01-0.1 µm. The second most prevalent thickness was 0.2µm, with a frequency of 13.69 ± 1.87%. The remaining had a thickness of 0.4-0.5µm, and was within a frequency range of 3.34 ± 2.05 to 1.44 ± 0.69% respectively **(Figure 28A).** This frequency analysis indicates an increasing trend for low myelin thickness in the treated axons signifying loss of myelin from the internodal segments.

So, according to this parameter for measuring myelin 4.7% axons were accounted to be devoid of myelin membrane in the treated group relative to 2.2% in the untreated group. This was in fair correspondence to the measurements described in the above paragraph where myelinated axons were accounted on the basis of visual assessment of electron micrographs **(Section 4.4.1).** The myelin membranes had a remarkable difference in their morphology. Apart from the usual myelinated axons, some circular and rounded profiles were observed in the treated group which could not be classified as axon, since they lacked the regular myelin membrane stacks. These cross sections had a central cytoskeleton and a surrounding thick membranous layer which was not distinctly multi-layered, as expected for a myelinated axon **(Figure 29E, F).** Several layers of membrane appeared to be fused along the axon radius **(Figure 29F).** This pattern possibly reflected a minor type of induced effect which remains unexplained here. Axons with this type of myelin pattern were not found in controls. These analyses were conducted on TEM images from three sets of experiment.

4.4.1.3. Alterations in "g" ratio and myelination index indicate loss of myelin

Further on, in order to evaluate the structure-function co-relate in CZ-treated ON axons, "g" ratio was analyzed. Rushton's view (Rushton, 1951) that "g" ratio (the ratio of the inner axonal diameter to the total outer diameter) is a reliable way for assessing axonal myelination, is a parameter which is widely accepted and used. The ratio becomes unstable

during demyelination and the changes reflected loss of myelin. An increase in the "g" ratio implies a relative reduction in the thickness of the myelin sheath, as fiber diameter approaches that of axon diameter (Beuche and Friede, 1985). CNS and PNS are differentially susceptible to such changes (Chomiak and Hu, 2009, Perrot et al., 2007). Here in this study, the average "g" ratio for untreated and treated group was assessed as 0.779 ± 0.008, n = 1087 and 0.827 ± 0.01, n = 805, p > 0.001, respectively **(Figure 27A).** They ranged in between 0.3 - 1.1 for both groups**,** whereas, the average myelination index (do/di) exhibited a decrease in the experimental group **(Figure 27B)**. Collectively, these results indicate that demyelination of ON axons take place here owing to CZ-treatment.

4.5. Loss of myelin membrane periodicity due to collapse of IPL is a major effect induced by CZ

Even though both groups appeared to exhibit similar axon cross section profiles at low magnification **(Section 4.2.1)** the membrane structure varied. Untreated group axons had compact myelin with distinct periodicity, whereas the treated group exhibited several intra-myelinic changes. Vacuolization in between the myelin membranes was a prominent effect noticed after CZ administration. This intra-myelinic change was due to disruption of myelin layer **(Figure 29A, B)** and loss of regular membrane stacked structure owing to interruptions in the compacted myelin **(Figure 29C, Figure 30A, B)**, rendering it loose at several places in radial and longitudinal sections and yielding a vacuolated appearance **(Figure 29C, D, E)** of IPL. They are formed due to the apposition of external myelin plasma membranes surfaces **(Figure 29A, B).** The myelin vacuoles were lodged in between the successive membranes, which were always found between the IPL. Interestingly, these vacuoles were not continuous to the extracellular space. Small diameter axons appear to have lesser disruptions. A single axon in its radial section could exhibit 1-10 such disruptions, indicating varied impact on each of them. The extent of such interruptions could be mild, where it generates a single gap between the successive myelin layers **(Figure 29B),** or have several large vacuoles such that the stack like structure of myelin falls apart **(Figure 29C, Figure 30A, B).** In cases of even more extensive breakdown, these membranes could invaginate inside the axoplasm **(Figure 29D).** Even

though unexpected, yet such disruptions were present in some control samples as well, but the effect was much higher in the treated samples. In order to examine the periodicity of intact stretches of myelin in both groups, a detailed densitometry was performed. A representative scan across the myelin sheath is shown **(Figure 30).** Even though the disruption is not apparent in these remaining stretches of myelin sheath **(Figure 30A, B)** loss of compactness was evident **(Figure 30D).** Linear densitometric scan profiles along these portions of myelin sheath in the treated group exhibit reduced height or amplitude of the crest and trough which are representations of MDL and IPL **(Figure 30C, D).** Collectively, these structural evidences prove the presence of non-uniform, faltering myelin covering in CZ-treated axons, which may appear intact, but has resulted in loss of its periodicity and compaction.

4.6. Decreased PLP/DM20 ratio; a jeopardizing factor for loss of periodicity

Glia to axon signaling requires intimate cellular interaction at a global and local level as well (Perrot et al., 2007, Nave, 2010b, Nave, 2010a); and lipophilins are one of the important implicating factors. Specifically, the proteolipid (PLP) and it's variant DM20, which are integral hydrophobic components of CNS myelin sheaths. They bestow essential compaction of myelin lamellae required for efficient saltatory conduction. The electron microscopic data established that myelin membrane looses its uniformity **(Figure 29, Figure 30)** due to the collapse of the intraperiod line (IPL), leading to clustered major dense line (MDL) and thus, creating intra-myelinic vacuoles **(Figure 30B).**

Cross-sectional view of a single axon illustrates such regions, which indicates extensive myelin disruption. The intact stretches of these sheaths also show a loss in their periodicity, which were pronounced in the densitograms **(Figure 30D).** It was noted that the lipophilin group specific proteolipid protein (PLP) and its variant, DM20 are structural constituents of the myelin sheath, which maintains the integrity of IPL. Hence, these were analyzed in purified myelin obtained by sucrose density gradient centrifugation and detected with Western blotting. Use of SMI99 antibody allowed detection of both PLP and DM20 as it identifies epitopes corresponding to amino acids 109-128 which are common to both. A

minor ~42kD contaminating band was not included in the analysis or interpretation because its molecular weight does not correspond to any protein from the lipophilin group. The three specific bands separated correspond to the expected protein sizes of PLP ~30kD, DM20 ~26kD and a small ~10kD band **(Figure 31A).** DM20 is an alternative spliced variant of PLP transcript and they together form the transmembrane protein of myelin which holds them together like a zipper and maintains compact myelin. ~10kD band is often referred to as a degradation product of PLP (Macklin et al., 1987, Nave et al., 1987). Normally, PLP and DM20 are expected to be present in equal proportions, a disproportionate increase or decrease leads to altered myelin compaction. Here, in the treated samples, the level of DM20 increased whereas PLP decreased in the total lipophilin pool, relative to the untreated samples **(Figure 31B, C).** Expressing these two proteins as % of the total lipophilin pool, which would contribute to maintaining the periodicity of myelin membrane, showed lower ratios (PLP/DM20) for the experimental samples (n = 3), relative to the control group in ON, total brain and forebrain **(Figure 31).** This was a consistent pattern observed in ON and total or forebrain myelin.

4.7. CZ influences cytoskeletal organization of axon and surrounding glia

Demyelination exerts an adverse impact on the axon. Cytoskeleton changes are often suggestive of the pathological state and mechanism(s) involved which, in turn, might affect trafficking of proteins, axon diameter and axon-myelin associated functions. An impact on the NF cytoskeleton is a widely accepted aspect of disease progression in MS (Trapp et al., 1998, Schirmer et al., 2011, Dziedzic et al., 2010, Salzer et al., 2010, Trapp and Stys, 2009). Herein, on the basis of ultrastructural TEM analysis, the axonal NF and cytoskeleton of surrounding cells were found to be affected in the CZ treated group.

4.7.1. Axonal neurofilament gets disorganized following CZ-treatment

Axon cytoskeleton cross sections of untreated control group appeared as a discretely organized association of microtubules and NF in transmission electron micrographs. At high magnification (100nm, scale bar) the axoskeleton represented the typical NF and

microtubule interaction. Microtubules (25nm) were representative of typical round hollow structures and the NF (10nm) is a solid globular structure with several filamentous processes or arms attached to the microtubule in axon cross sections **(Figure 32C).** These collectively form a distinguished network in control which was lacking in the experimental group **(Figure 32D).** They appear as long organized, but trailing structure in longitudinal sections **(Figure 32B**). This discrete and uniform organization was prevalent in untreated group only. The treated group axon exhibit intermittent stretches of organized and disorganized cytoskeleton **(Figure 32A).** Loss of such association or network was more evident in the cross-sections **(Figure 32C, D).** It was interesting to note that this kind of assembly was better maintained in relatively small diameter axons. This axoplasmic randomness caused due to cytoskeletal disorganization was measured by calculating the particle density within the defined ROIs of an axon. According to this analysis the untreated group exhibited low density when expressed as particles/nm^2. The treated group exhibited 29% increase ($n = 60$, $p > 0.001$) indicating disorganization of the cytoskeleton **(Figure 32D).** The impairment of the NF was a localized event as noticed in longitudinal sections of ON axon **(Figure 32A).** Herein, loss of NF arm has been indicative of hypo-phosphorylation of neurofilament leading to disorganization of axo-cytoskeleton.

4.8. Increased hypophosphorylation of NF is a liable factor for axoskeleton disorganization

These changes might lead to loss of axon rigidity which is essential for uniform propagation of action potentials and trafficking of proteins as well. NF plays a vital role in maintaining an uncompromising structure. It is mostly implicated with their radial growth (Xu et al., 1993). The subunit composition (NFH and NFM) of NF specify axon diameter (Xu et al., 1996). The relatively higher proportions of phosphorylated form NFH renders them more rigid and it is a phosphorylation dependent phenomenon. Loss of myelin protein like MAG (myelin associated glycoprotein) results in reduced axon caliber, owing to decreased NF phosphorylation. This in turn reduces spacing between cytoskeleton (Yin et al., 1998, Garcia et al., 2003) and loss of rigidity. Such studies have indicated that myelin and NF phosphorylation collectively maintain a healthy and normal axon diameter essential

for efficient action potential propagation. Ample evidence has been gathered so far in the present study, which has implied a role of NF phosphorylation.

NF represented as NF200 (NFH) was easy to detect on western blots and it did not exhibit any change in quantity **(Figure 33A)**. So, it was hypothesized that the phosphorylation of NF is perturbed with respect to the total pool in ON cytoskeleton. De-phosphorylation of NF in axons and hyper-phosphorylation in neurons are indicators of disturbed axon transport and neuron damage in MS (Schirmer et al., 2011, Trapp et al., 1998, Pitt et al., 2000). Hence, in order to further characterize the divergent features of axon induced by CZ demyelination in MS pathology use of SMI antibodies were employed. SMI 31 (SMI® Monoclonal Inc. or Steinberger product from Covance) is an antibody which extensively reacts with the phosphorylated epitope of neurofilament both heavy (NFH) and medium (NFM) (Tsuda et al., 2000). It was used herein to distinguish the relative state of C-terminal region, as SMI 31 recognizes the phosphorylated form of a highly conserved consensus phosphorylation site KSP (Lysine-Serine-Proline) repeats of the NF arm. On the other hand SMI 32 recognizes the less phosphorylated NF (Tsuda et al., 2000).

Cytoskeletal protein preparation from ON was resolved by SDS-PAGE, followed by Western blotting and detection of phospho- NF (p-NF) and dephospho-NF (dp-NF) bands. This showed a decrease in the p-NF and increase in dp-NF following treatment. The total pool of NF cytoskeleton was assessed by combined use of both antibodies SMI31 and SMI32 as described by Tsuda (Tsuda et al., 2000). SMI 31 labeled bands (~200, 168 kD) indicated the quantity of p-NF and SMI 32 labeled bands (~200kD) indicated the quantity of dp-NF **(Figure 33A).** The sum of these two signals was considered as the total pool and percentage values for p- and dp-NF was calculated as:

$$\% \text{ of total p-NF} = 31/(31+32)*100;$$
$$\% \text{ of total dp-NF} = 32/(31+32)*100.$$

p-NF levels were low ($p > 0.01$, $n = 3$) **(Figure 33B),** whereas dp-NF was increased ($p > 0.001$, $n = 3$) **(Figure 33C)** after CZ-treatment in ON axons. The p-NF/ dp-NF ratio in the

total pool of NF cytoskeleton was expected to reveal the impact on maintenance of axon diameter. When this was expressed as % of the total NF pool it was found to be highly altered owing to increase in dp-NF levels **(Figure 33D).**

4.9. Increased dp-NF is a hallmark of large diameter CZ-treated axons

The observed hypophosphorylation of NF in electron micrographs were further established by fluorescence labeling of ON axons with p-NF (SMI31) and dp-NF (SMI32).

The % frequency of p-NF and dp-NF positive axons in both control and treated samples were detected in confocal micrographs. The axon diameter from both groups of ON follow same pattern, where they fall within this broad range. p-NF positive axons are within diameter 0.2-2.24µm in both groups. But, the majority of these are in a range of 0.2 to 1.8µm. Occurrence of very large diameter axon is infrequent. This is an observation similar to that noted in **Section 4.4.1.2.** Control ON represents higher level of dp-NF in small diameter axons, which is assumed to be immature. The mid range axons which is expected to be mature have an intermediate level of p- and dp-NF **(Figure 34A).** This pattern is shifted to the right in treated ON, indicating increase in dp-NF of large diameter axons **(Figure 34B).** This was further indicated by the medial distribution of p-NF (2.39 and 2.50) and dp-NF (3.15 and 8.91) in UT and T samples. The shift in the indicated pattern has been highlighted by the shaded portion in the graph **(Figure 34).** These observations collectively indicate that NF phosphorylation is perturbed by CZ-treatment and in affects the axon diameters, increasing hypophosphorylation mostly in the larger axons**.**

4.10. Organization of inter-axonal cytoskeleton indicate activity of surrounding cells

Some prominent cytoskeletal changes were also observed in the surroundings of myelinated axon. The micro-filaments were found to be well organized as striations packed around the myelinated axons in treated group in electron micrographs **(Figure 35A,** box**)**. This organization is typical for astrocytes and is remarkably different from axon cytoskeleton **(Figure 35B)** shown in **(Figure 35C, D).** A globose structure attached to the myelin

layer of axons was also noticed. They were present in both groups and represented a decrease after CZ-treatment (Fig. 30C, D) n= 1525, 1289. At several occasions these cells with profuse micro-tubular elements had some membrane enclosed organelles embedded in between them. These organelles have stacks of horizontally organized membrane and looked very similar to mitochondria **(Figure 37F)**. However, the shape appeared to be distinctly different from the mitochondria found in the axons, which could be easily identified due to its presence in the myelin, enveloped axon and a typical textbook appearance **(Figure 37A, B).**

4.11. CZ induced change in nuclear morphology was indicated by altered chromatin pattern

Apart from all these another obvious and interesting observation was evident from these TEM micrographs. Treated ON had alterations in the nuclear organization of cells intercalated in between myelinated axons. Two types of cells were observed which differed in the electron density of their cytoplasm. One type of cell had a denser material relative to the other. The electron dense cells were smaller in size with respect to the translucent cells **(Figure 36A).** Their corresponding nuclear size also differed; the smaller ones had tinier nuclei (yellow arrow) relative to the larger ones (white arrow) **(Figure 36A).** The nuclei of translucent cells exhibit more dispersed pattern of chromatin **(Figure 36C1, C2)** and the electron dense cells had more compacted look. **(Figure 36B1, B2).** Similar cells were found in both groups, which were indicative of presence of two different types of cells. They differed in their chromatin distribution after CZ-treatment. They appeared to be differently organized in the treated group, with an apparent perinuclear scattering of the chromatin in the translucent cells **(Figure 36C2, B2).** These morphological changes observed in the nuclei after CZ-treatment collectively indicate an induced effect, which might have a transcriptional role. This observation remained beyond the main objective of the study, hence it their involvement in any functional aspect was not investigated.

4.12. Loss of mitochondrial inner membrane integrity in ON axon

CZ is a copper chelator and is expected to have an effect on the mitochondria and consequential supply of energy (ATP). On the other hand increased energy demand needed for electrical conduction in viable demyelinated axons, combined with reduced axonal ATP production, leads to a state of virtual hypoxia in chronic lesions of MS (Trapp and Stys, 2009). Herein, for the first time evidences for morphological changes in demyelinated ON axon after CZ-treatment is being presented. The general appearance of mitochondria indicates that they are 250nm to 150µm long or oblong structure in the longitudinal sections of ON axon. Cross sectional view of an axon exhibit the presence of as many as 1-3 mitochondria, which were spherical in shape and their diameter was 400-500nm. This was true for both groups. They were mostly located on the periphery of axoplasm and in close proximity to the axolemma. In some cases, they were found to be centrally located. In these cross sections, the inner membrane appeared intact, but the cristae were blemished. Even though it was not possible to analyze the exact distance at which these mitochondria were interspersed within an axon, as a 3D reconstruction of nerve would be needed, it was evident from these TEM micrographs that they were in close proximity (1µm or even less).

The inner and outer membrane could be easily distinguished in these preparations, rendering it a double membrane bound structure. The outer and inner membranes of 20 out of 25 mitochondria examined became wavy **(Figure 37B,** black arrow head) after CZ-treatment. Many cristae show club-shaped dilatation, with accumulation of moderately dense homogeneous material **(Figure 37B,** red arrow heads**),** whereas in other areas, there is almost complete loss of cristae, accounting $3/4^{th}$ membrane span of a single mitochondria. Such expanse of mitochondria are bordered only by single membranes, which appear to be protruding outward **(Figure 37B, D** black arrow head) from the regular contours**.** This feature has been highlighted in the outline trace generated for such an electron micrograph **(Figure 37D**, black arrow) Thus morphologic evidence favors the altered permeability of mitochondrial membranes (Suzuki, 1969). The average

membrane density per unit area (nm^2) was 192.19 ± 1.28 and 173.83 ± 1.78 for control and treated group, n = 25, p > 0.001 **(Figure 37E**). This was analyzed by defining the mitochondria as a ROI and then calculating the length of traced line per unit area using ImageJ software. This reflected an apparent loss of cristae from the mitochondria. Interestingly, no obvious difference could be distinguished for the mitochondria of surrounding cells in samples from both groups. However, some elongated and profuse membrane stacked structures were observed in both groups **(Figure 37F)**. Collectively, these observations here in the ON axons provide direct evidence for loss of inner membrane integrity of axonal mitochondria.

4.13. Conclusion

This chapter conclusively provides evidence for ON demyelination, marked by an increase in "g" ratio and loss of myelin membrane periodicity in axons after 8 weeks of CZ-feeding. Differential increase in DM20 and a corresponding decrease of PLP alters their ratio in the entire lipophilin pool, which is a possible cause of the described myelin disruption. Additionally, increase in hypo-phosphorylation of NF indicates an impact on the axons, due to referred myelin loss. Alterations in the surrounding cells are indicative of induced impact on the delicate balance of neuron-glia association following CZ treatment.

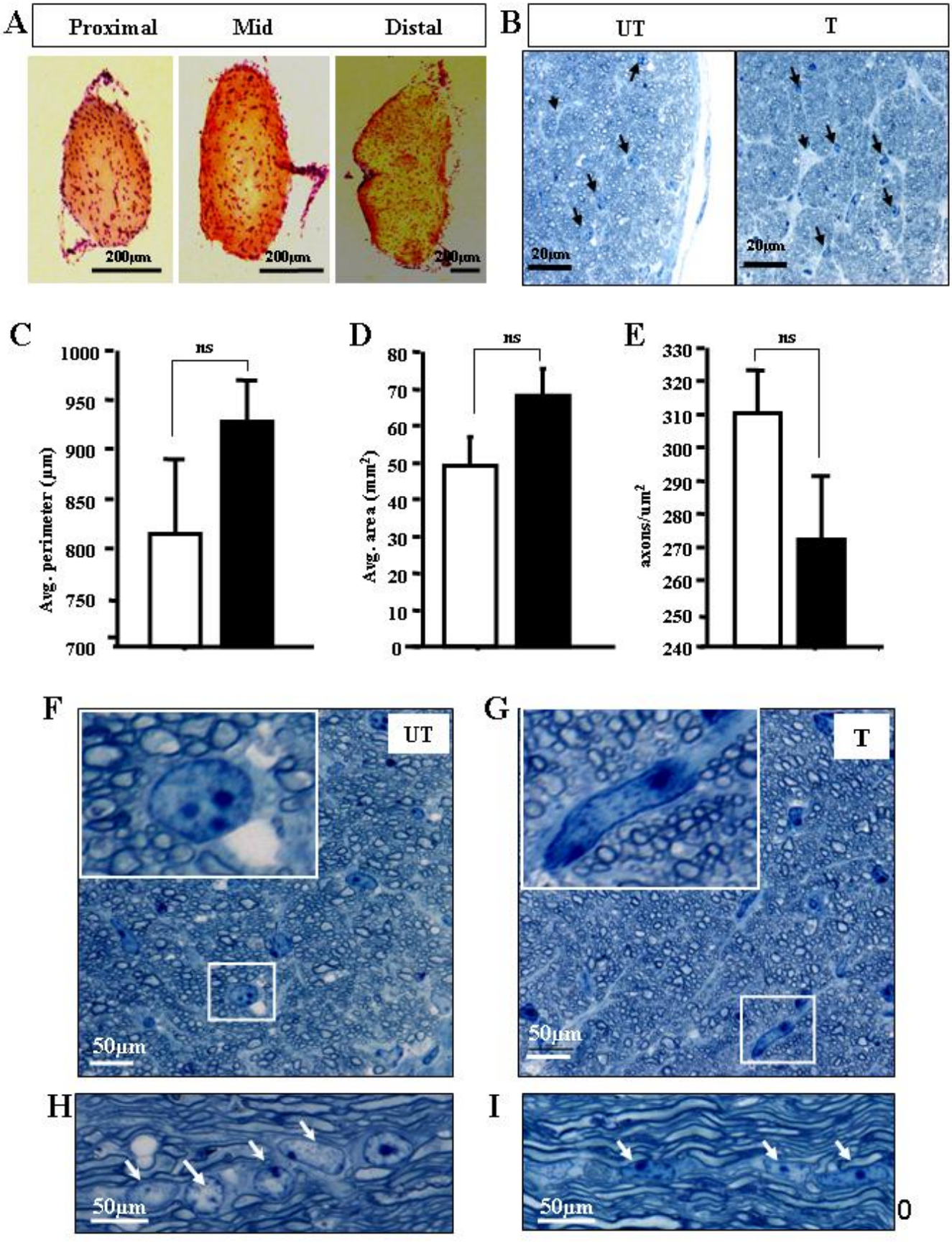
A
Proximal
Mid
Distal
200µm
200µm
200µm
B
UT
T
20µm
20µm
C
ns
Avg. perimeter (µm)
1000
950
900
850
800
750
700
D
ns
Avg. area (mm²)
80
70
60
50
40
30
20
10
0
E
ns
axons/um²
330
320
310
300
290
280
270
260
250
240
F
UT
50µm
G
T
50µm
H
50µm
I
50µm

Figure 24: ON morphometrics before and after CZ treatment.

***A**. CV stained ON cross sections (30µm), from the distal (facing eye ball), medial and proximal end (facing chiasma) showing the general profile of nerve.* ***B.** Toluidine blue stained cross sections of ON from control (left) and treated (right) group showing an increase in interfascicular space (black arrows) following CZ treatment.* ***C.** Histogram showing an increase in average cross-sectional nerve perimeter (µm).* ***D**. Histogram showing a non-significant increase in the average cross sectional area (mm^2) of the nerve and* ***E.** decrease in the number of myelinated axons/μm^2 □ untreated, ■ treated.* ***F.** The glial cells within the fascicle remain randomly oriented in untreated (UT) group (left). The white box shows the broad view of a cell which has been expanded and represented in the inset to show the shape of this cell (left).* ***G**. Glial cells get realigned longitudinally in between the inter-fascicular space of the treated ON. The cell in white box is an expanded view of the same cell (inset top left).* ***H.** Longitudinal section of optic nerve exhibits sequestered and realigned cells in between the fascicles (pointed by white arrows) in untreated group.* ***I**. Similar cells in treated group ON highlighting the marked change in the shape of some of these streaming cells.*

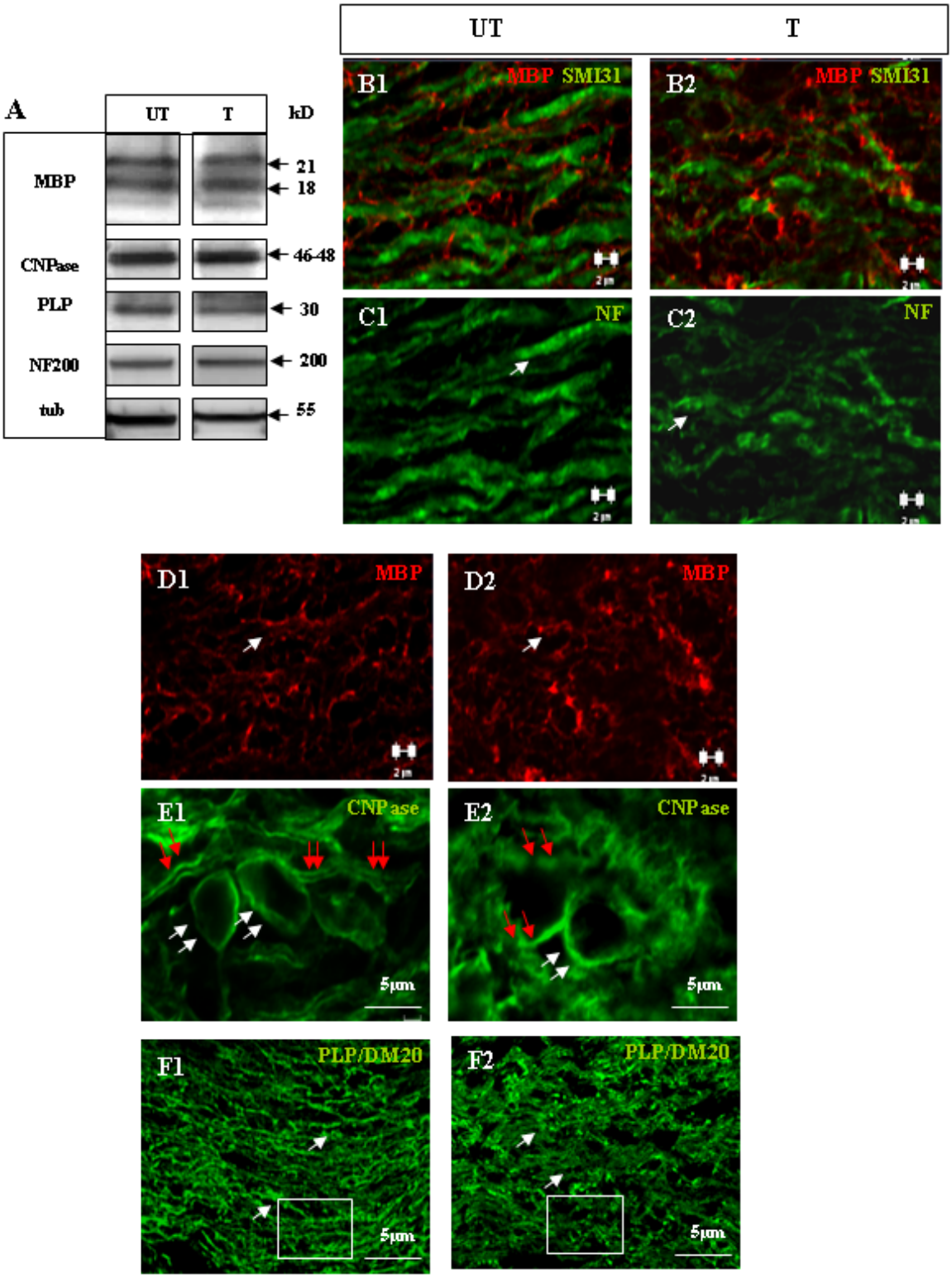
A
UT
T
kD
MBP
CNPase
PLP
NF200
tub
21
18
46-48
30
200
55
UT
T
B1
MBP SMI31
B2
MBP SMI31
C1
NF
C2
NF
D1
MBP
D2
MBP
E1
CNPase
E2
CNPase
5µm
F1
PLP/DM20
F2
PLP/DM20
5µm

Figure 25: ON axons and expression pattern of myelin proteins.

A. *Myelin proteins MBP (~21, 18kD), CNPase (~46-48kD), PLP (~30kD), NF200 (~200kD), tubulin (~55kD) were detected on western blots from ON homogenate.* ***B-F.*** *Representative IHC panels show myelinated (UT) and demyelinated (T) ON axons from 10µm thick cryosections labeled for various myelin proteins.* ***B.*** *Axons double labeled for MBP (red) and NF (green), show the axo-myelin pattern in control* ***B1****, and CZ-treated nerve B2.* ***C.*** *Axons labeled for axonal protein NF (C1, C2). The NF labeling for CZ-treated axons have a creased appearance (C2) relative to controls (C1) (white arrow).* ***D.*** *MBP stained myelin protein showing the structure of the same axons (D1, D2). They have a vacuolated appearance in treated axons (white arrow).* ***E.*** *This effect is more prominent when the axons are labeled with CNPase (green) (E1, E2). They show marked disruption of double layered myelin which surrounds the axon longitudinally along its axis (red double arrow). This can be distinguished from the somatic formation (white double arrow).* ***F.*** *PLP/DM20 (green) stained sections (F1, F2) show a difference in the morphology of myelin layers, it bears a more striated appearance in the treated group****.*** *The boxed regions in* ***F*** *show the change. Scale bar is 2µm and 5µm for B, C and D, E, F respectively.*

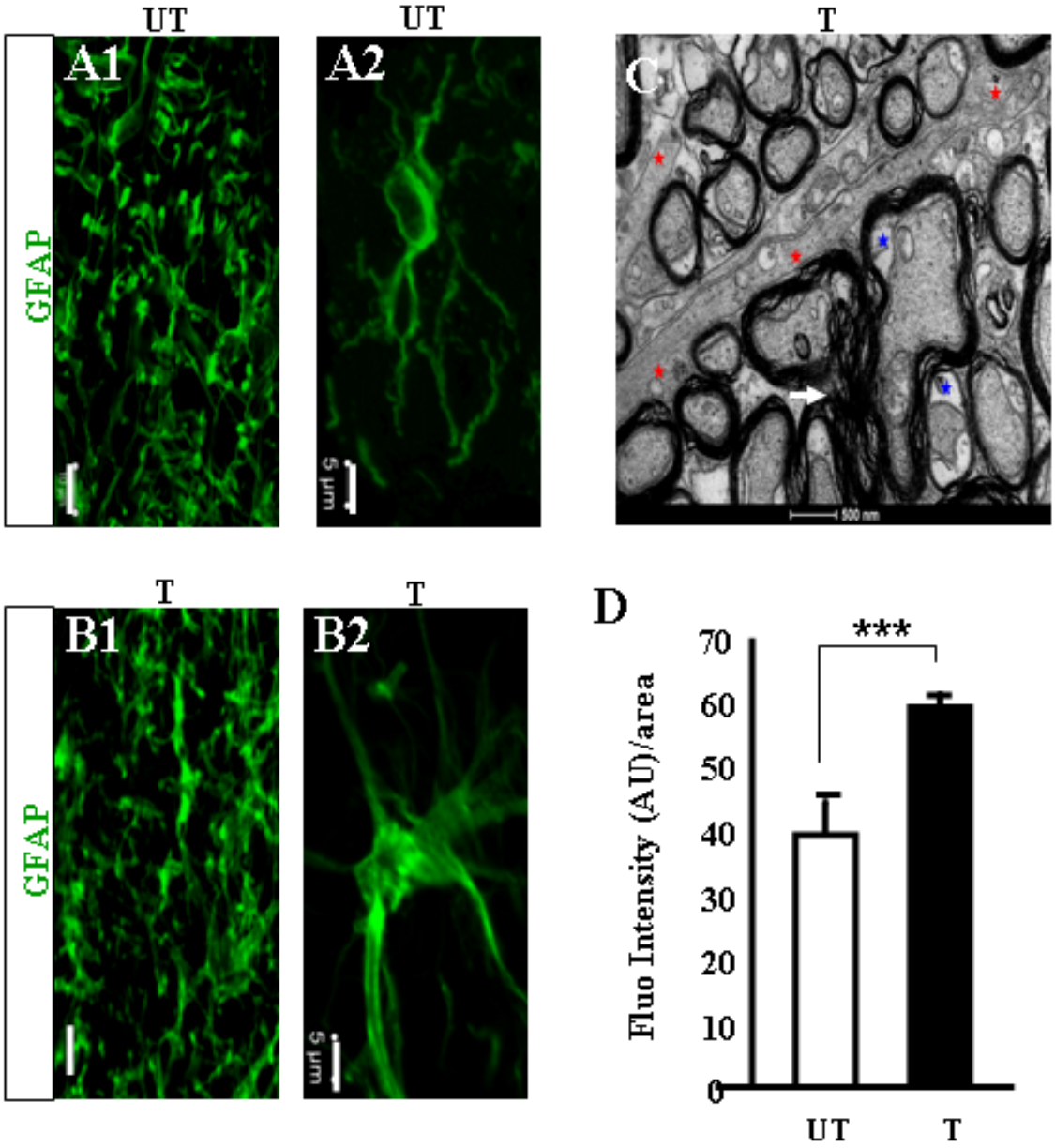
UT
UT
T
A1
A2
C
GFAP
T
T
B1
B2
GFAP
D
***
70
60
50
40
30
20
10
0
Fluo Intensity (AU)/area
UT
T

Figure 26: Astrocytic reaction to CZ-treatment.

A. *Longitudinal sections of control ON labeled with GFAP (10µm, A1). An individual GFAP-positive cell shows the normal morphology of an astrocyte which has few processes, scale bar 5µm (A2).* ***B.*** *Similar section from treated ON displays labeling for GFAP; scale bar 10µm (B1). An astrocyte from the experimental ON show profusely branched processes emerging out of the cell soma, scale bar 5µm (B2). Astrocyte shape in CZ–treated ON differs in morphology owing to several processes which emerge from their soma.* ***C.*** *Representative electron micrograph shows streaming inter-axonal glial processes signifying activity of these cells upon CZ-treatment. Red star marks the invading cytoplasmic strands of the glial processes in between axons. Demyelination of axon is indicated by appearance of large axo-myelinic space (blue star) and a mass of deranged myelin membranes (white arrow), scale bar 500nm.* ***D.*** *Histogram showing an increase in GFAP fluorescence signals represented as AU/unit area (μm^2), ($p=0.03$, $n=35$), □ untreated, ■ treated.*

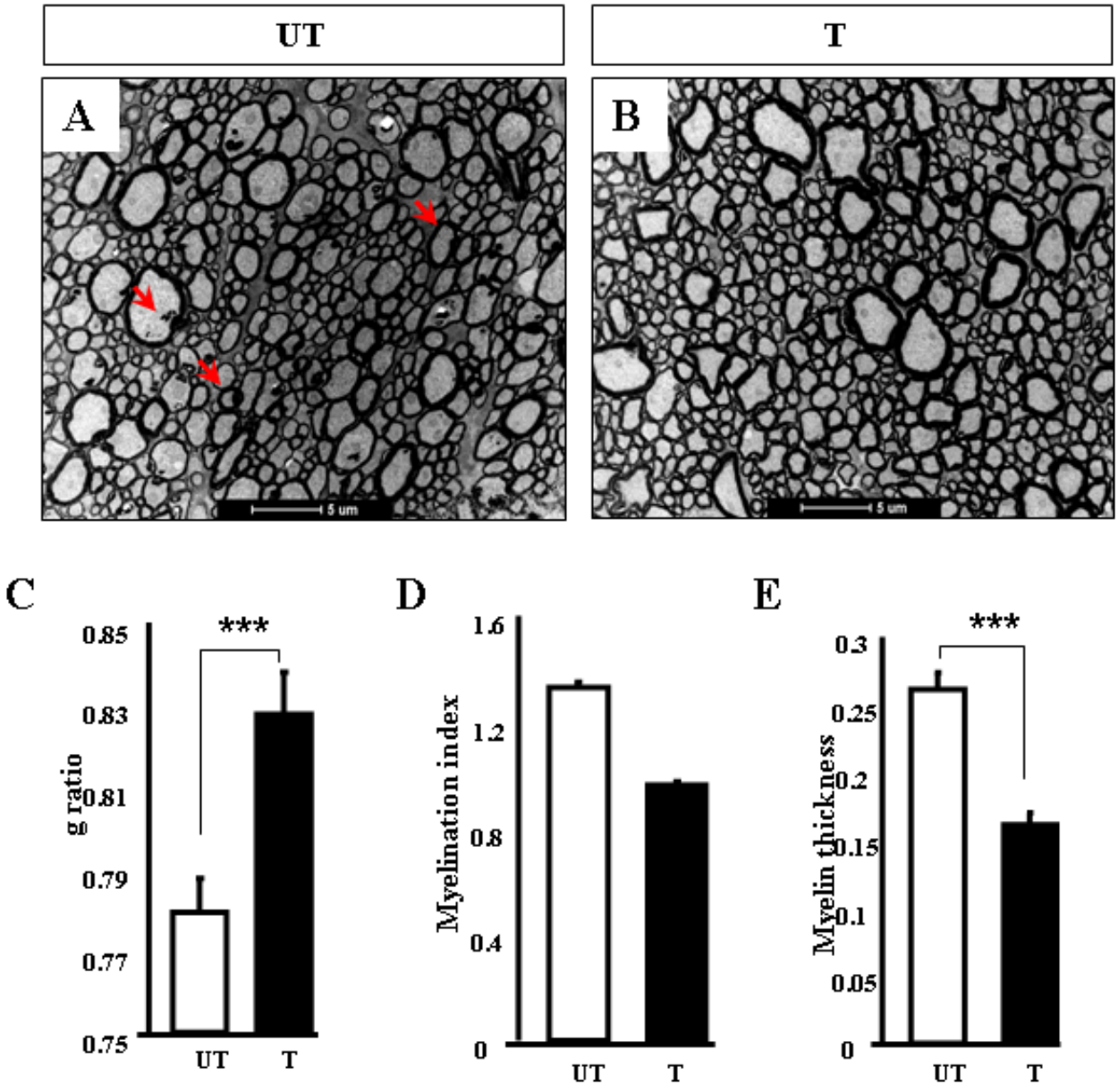
UT
T
A
B
5 um
5 um
C
***
0.85
0.83
0.81
0.79
0.77
0.75
g ratio
UT
T
D
1.6
1.2
0.8
0.4
0
Myelination index
UT
T
E
***
0.3
0.25
0.2
0.15
0.1
0.05
0
Myelin thickness
UT
T

Figure 27: Ultrastructural myelin loss from ON axons due to CZ.

***A**. Cross sectional view of ON from control group, showing rounded and smooth profiles of normal myelinated axon (red arrow). **B**. Cross-sectional view of ON from experimental group exhibit, a prominent presence of myelinated axons (scale bar 5µm) but with less annular profiles. **C.** The "g" (di/do) ratio increased after CZ-treatment (n=1087, 805, p>0.001). **D.** Whereas there was a slight decrease in myelination index (do/di), it did not read significance (p=ns). **E**. Average myelin thickness was also lower after treatment (p>0.001) (□ untreated, ■ treated).*

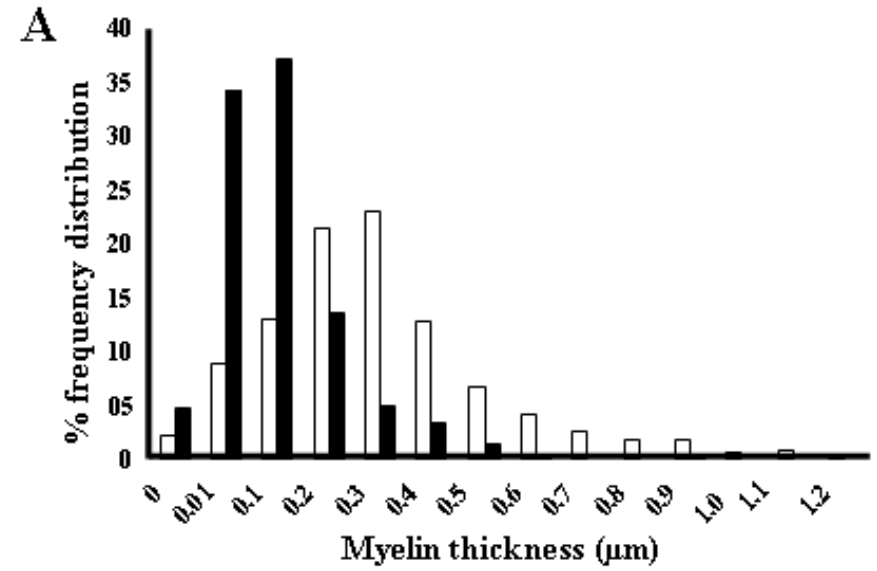
A
% frequency distribution
40
35
30
25
20
15
10
05
0
0
0.01
0.1
0.2
0.3
0.4
0.5
0.6
0.7
0.8
0.9
1.0
1.1
1.2
Myelin thickness (µm)

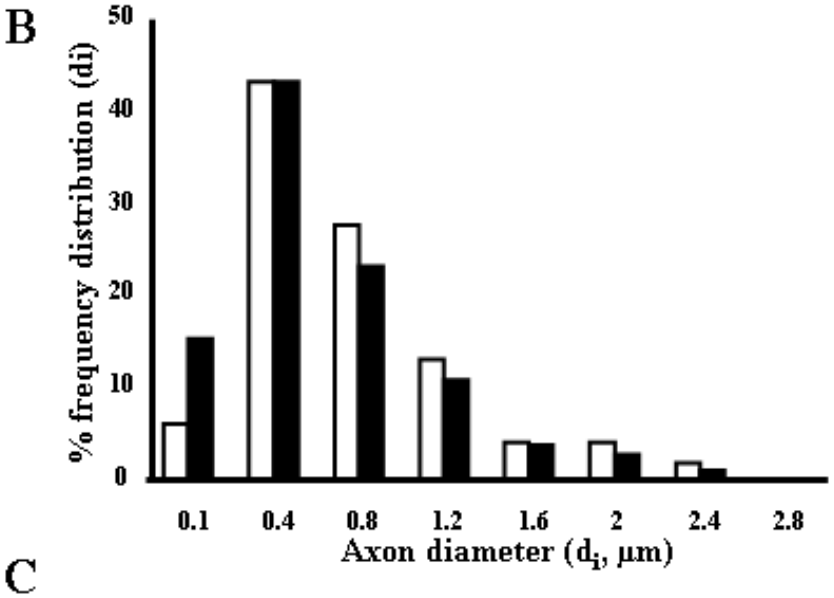
B
% frequency distribution (di)
50
40
30
20
10
0
0.1
0.4
0.8
1.2
1.6
2
2.4
2.8
Axon diameter (di, µm)

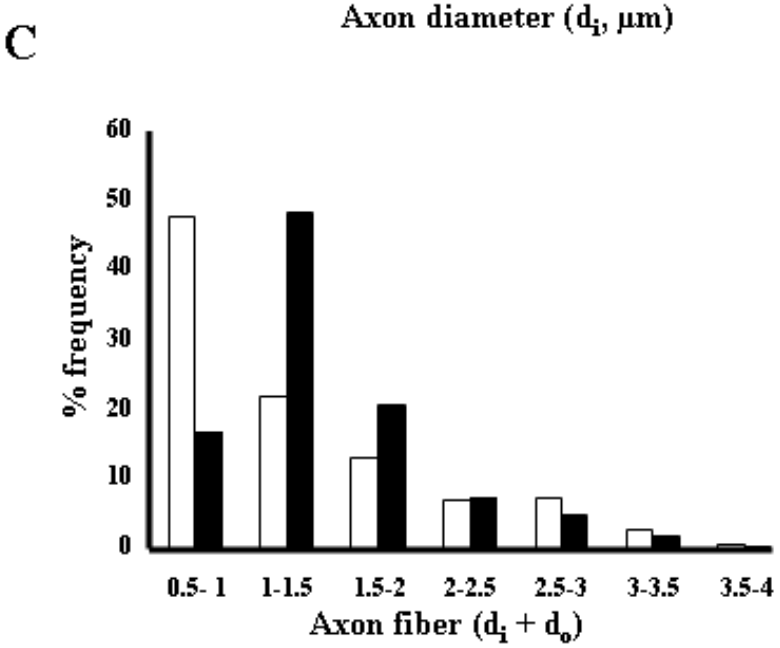
C
% frequency
60
50
40
30
20
10
0
0.5- 1
1-1.5
1.5-2
2-2.5
2.5-3
3-3.5
3.5-4
Axon fiber (di + do)

Figure 28: Morphometric changes in ON axons after CZ treatment.

A. *Frequency distribution of myelin thickness in both groups show a shift towards reduced number of myelin membrane.* ***B.*** *Frequency distribution of axolemma bound axon diameter (di) remains comparable in both groups.* ***C.*** *Axon diameter, including the axolemma delimiting axon (di) width and myelin membrane thickness (do), was analyzed from random fields selected across the entire nerve cross-section show a shift towards increase in mid-range axons and decrease in large diameter axons,* □ *untreated,* ■ *treated, n= 1525, 1289.*

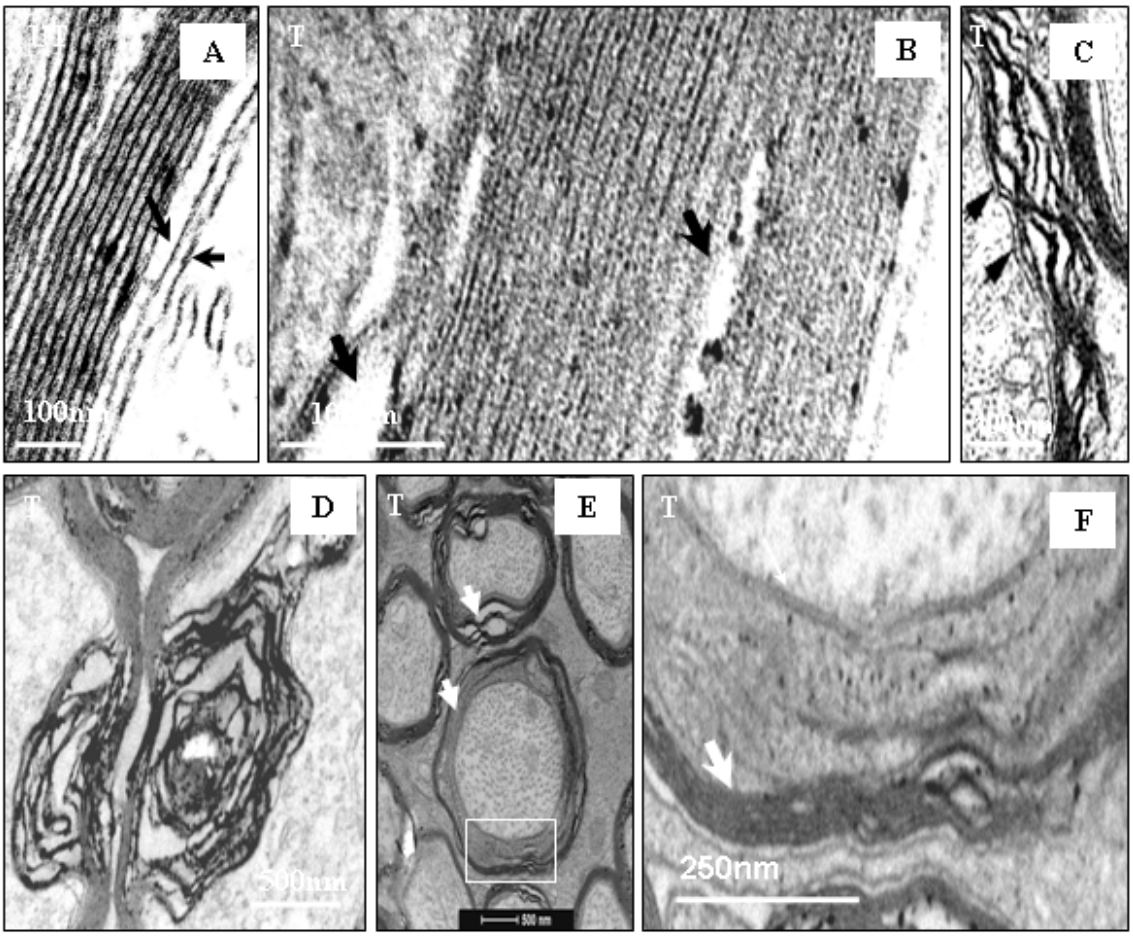
A
B
C
D
E
F
250nm

Figure 29: Altered myelin sheath morphology in CZ-treated axons.

A. *Organization of myelin membrane stacks in the ON axons of control group, showing a normal spacing between the axolemma and myelin membrane (black arrow) in a healthy myelinated axon; scale bar 100nm. Arrow pointing left shows the adaxonal membrane and the one pointing downwards indicate and intact sub-myelinic periaxonal space.* ***B.*** *Myelin membrane disruption and changes induced after CZ-treatment. The change could be subtle, so that it separates one layer from the other in inter-myelinic membrane stack (black arrow, center) creating a localized bifurcation within myelin or in between the adaxonal membrane and axolemma so as it increases the submyelinic-periaxonal space locally (black arrow left bottom) scale bar 100nm.* ***C.*** *Several membranes might collapse leading to loss of IPL and creating space or gap between the axons, scale bar 250nm.* ***D.*** *Severe cases of demyelination exhibit the collapse of myelin membrane which can be accompanied by an invaginating membranous structure formation, so, that it squeezes the axoplasm and occupies the majority of axonal space; scale bar 500nm.* ***E.*** *An axon showing deviant membrane organization in the treated group which has fused stacks (white box), 500nm.* ***F.*** *Boxed region from F has been expanded to show this aberrant feature which arises after CZ-treatment. Scale bar, 250nm. These images represent the patterns noted through 3 sets of experiment.*

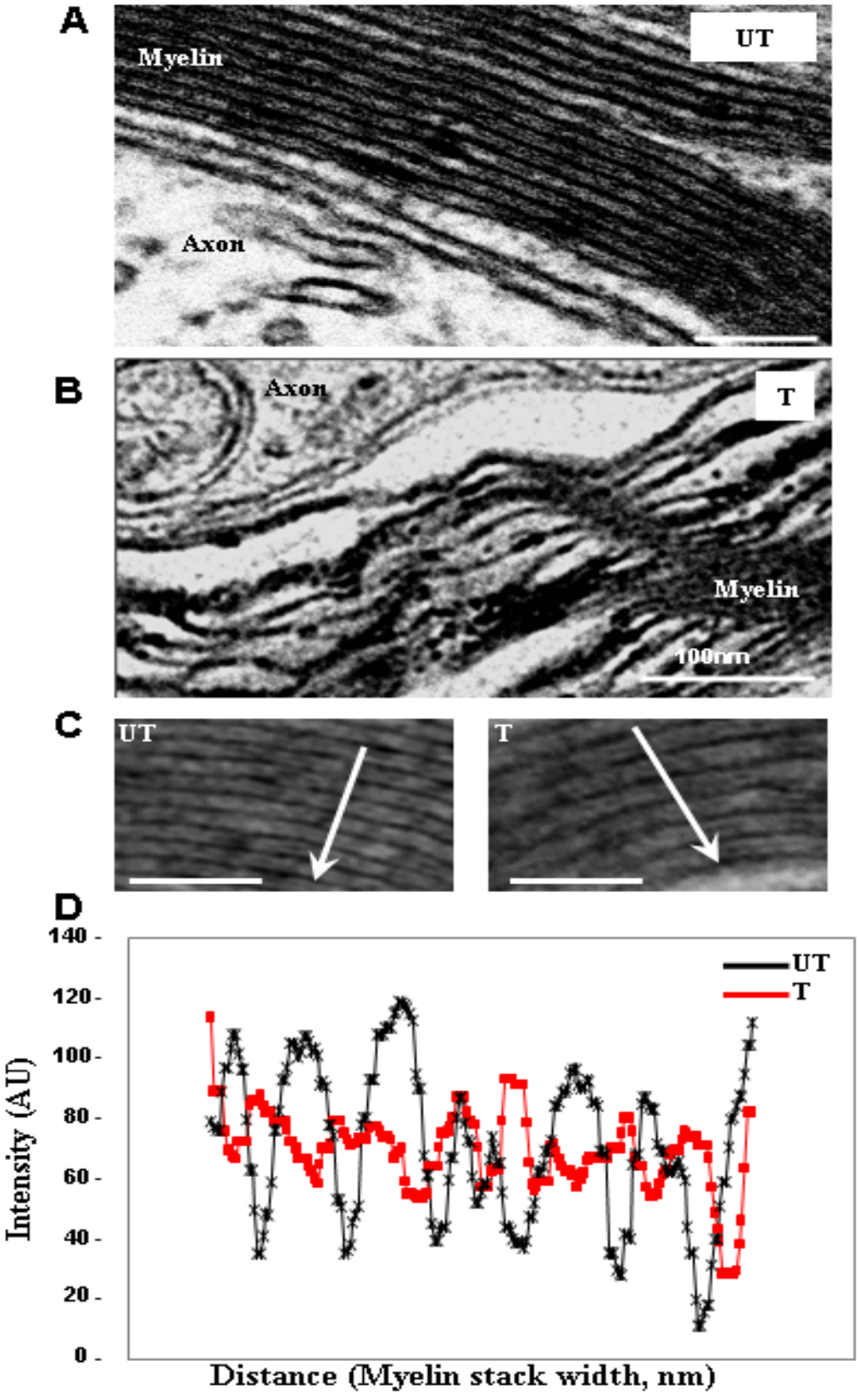
A
Myelin
UT
Axon
B
Axon
T
Myelin
100nm
C
UT
T
D
140
120
100
80
60
40
20
0
Intensity (AU)
UT
T
Distance (Myelin stack width, nm)

Figure 30: Loss of membrane periodicity and decreased levels of PLP in ON from CZ-fed mice.

A. *high magnification electron micrograph of intact myelin membrane spans of ON axons from control* ***(A)*** *and (****B****) CZ-treated group.* ***C.*** *Densitometric scans profiling the myelin diameter from untreated (A) showing normal lamellar pattern of IPL (intraperiod line) and MDL (major dense line) represented by the crests (downward arrow) and troughs.* ***D.*** *Loss of periodicity in treated axons within intact stretches of myelin is noted by irregular crests (downward arrow) and troughs. Images in A and B represent myelin from 3 sets of experiment.*

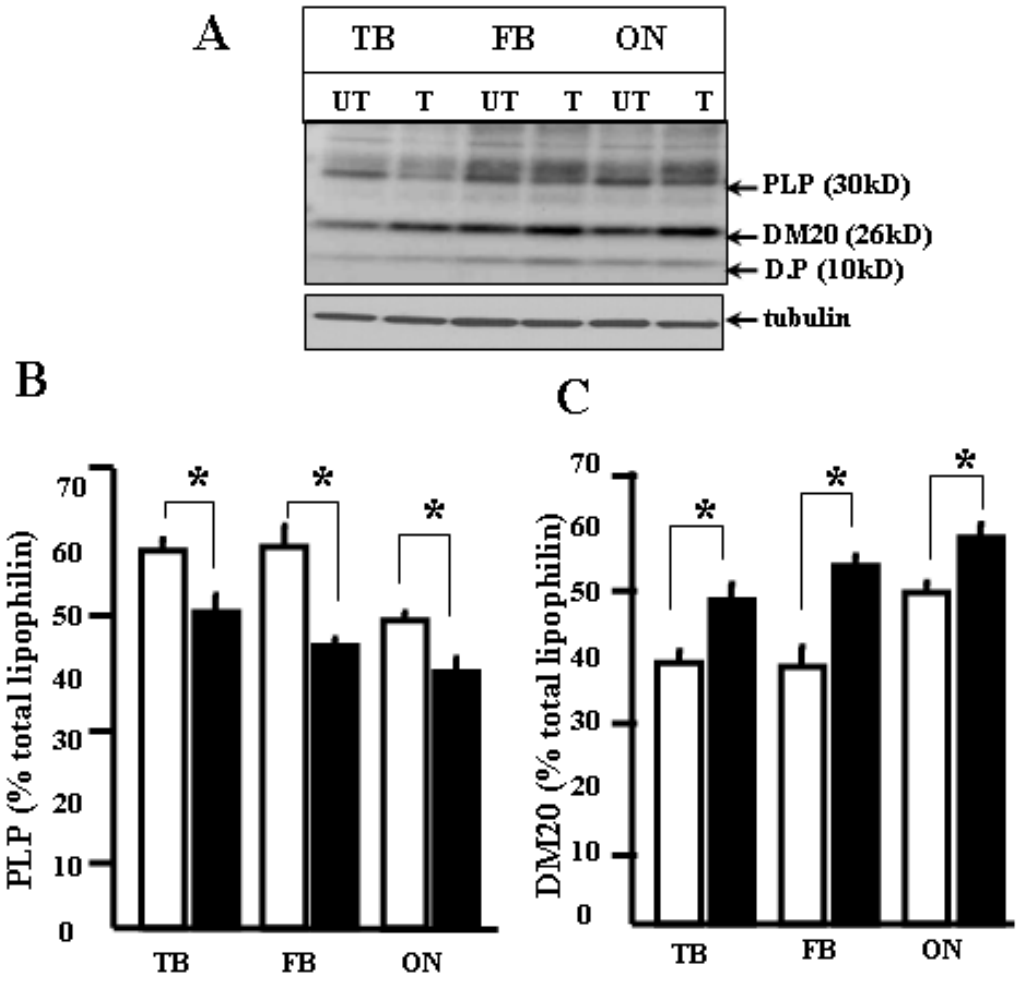
A
TB
FB
ON
UT
T
UT
T
UT
T
PLP (30kD)
DM20 (26kD)
D.P (10kD)
tubulin
B
PLP (% total lipophilin)
70
60
50
40
30
20
10
0
*
*
*
TB
FB
ON
C
DM20 (% total lipophilin)
70
60
50
40
30
20
10
0
*
*
*
TB
FB
ON

Figure 31: Altered ratio of PLP/DM20 in ON of CZ-fed mice.

A. *Western blot analysis PLP (proteolipid protein) and its splice variant DM20 from density gradient purified form of myelin reveal differential levels of these two proteins in total brain (TB), forebrain (FB) and ON samples from both groups (control, UT and experiment T). DM20 increases after. PLP and DM20 were identified as ~30kD and ~26kD proteins; the ~10kd band indicates a degradation product (D.P) of PLP (Lees and Bizzozero, 1992).* ***B***. *Histogram showing decrease in PLP following CZ- treatment compared to the control.* ***C.*** *DM20 levels showed an increasing trend in the treated group. The values are plotted as % of total (PLP+DM20) (p=0.03, 0.01, 0.03, n=3, □ untreated, ■ treated).*

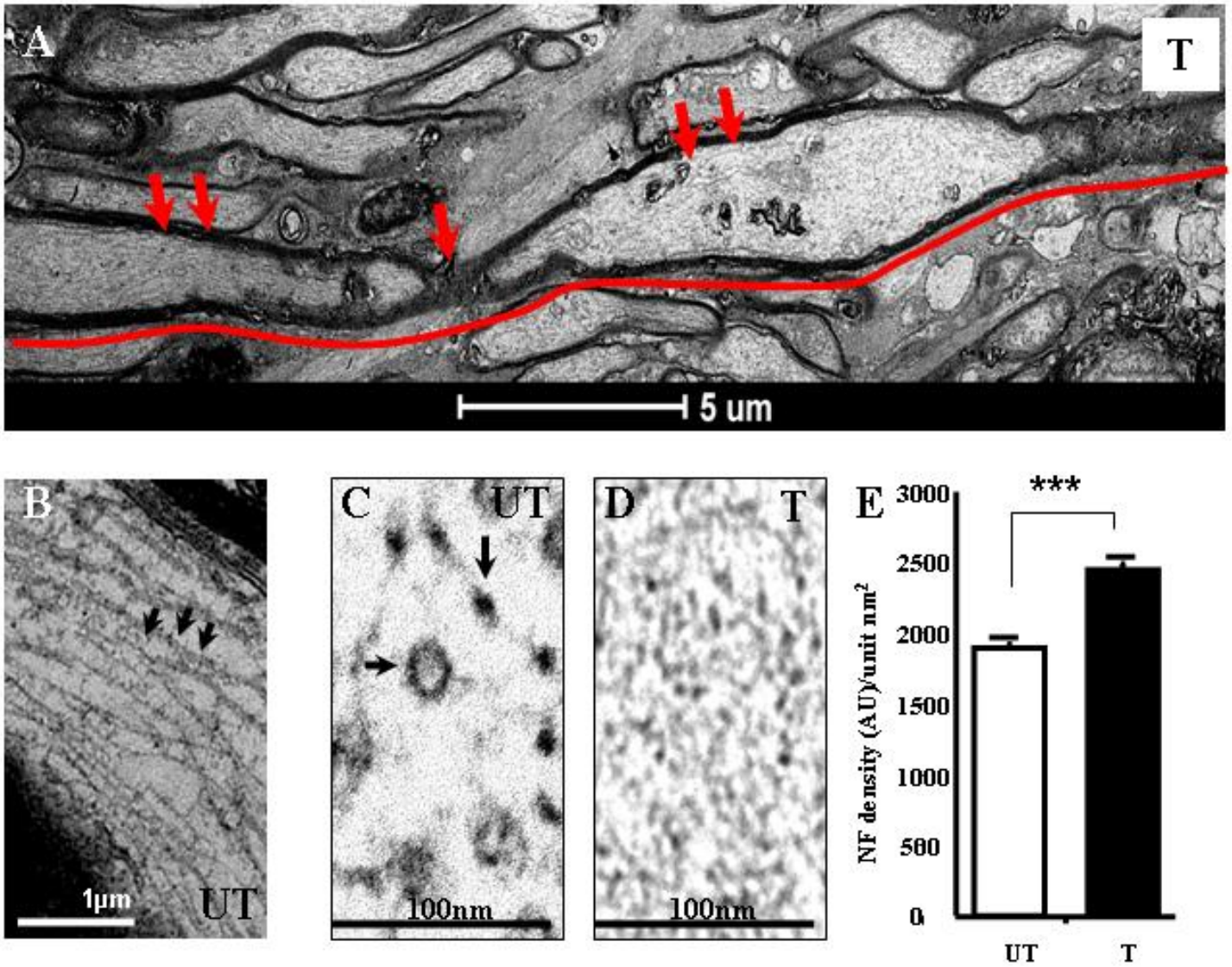
A
T
5 um
B
1µm
UT
C
UT
100nm
D
T
100nm
E
***
NF density (AU)/unit nm²
3000
2500
2000
1500
1000
500
0
UT
T

Figure 32: Organization of axonal cytoskeleton in CZ-treated ON.

A. *A representative 25µm long axon exhibits irregular width and disorganized cytoskeleton in treated ON. Red color double arrows show intermittent increase in axon width of the same axon is shown in longitudinal section. Such axons are interspersed in between cells with prominent cytoskeleton which is different in organization, scale bar 5µm.* ***B.*** *The NF cytoskeleton is discretely organized in the untreated group and helps in maintaining the axon caliber as seen in longitudinal section, scale bar 1µm.* ***C.*** *The interaction between microtubule (black arrow pointing right) and the extended arms NF (black arrow pointing down) form a nexus essential for maintaining a rigid structure.* ***D.*** *Such an organization is lacking in treated axons and hence leads to a random form of cytoskeleton marked by the increased particle density.* ***E.*** *Histogram showing increased particle density in treated axons ($p>0.001$, $n=60$, □ untreated, ■ treated). Scale bar 100nm for C and D.*

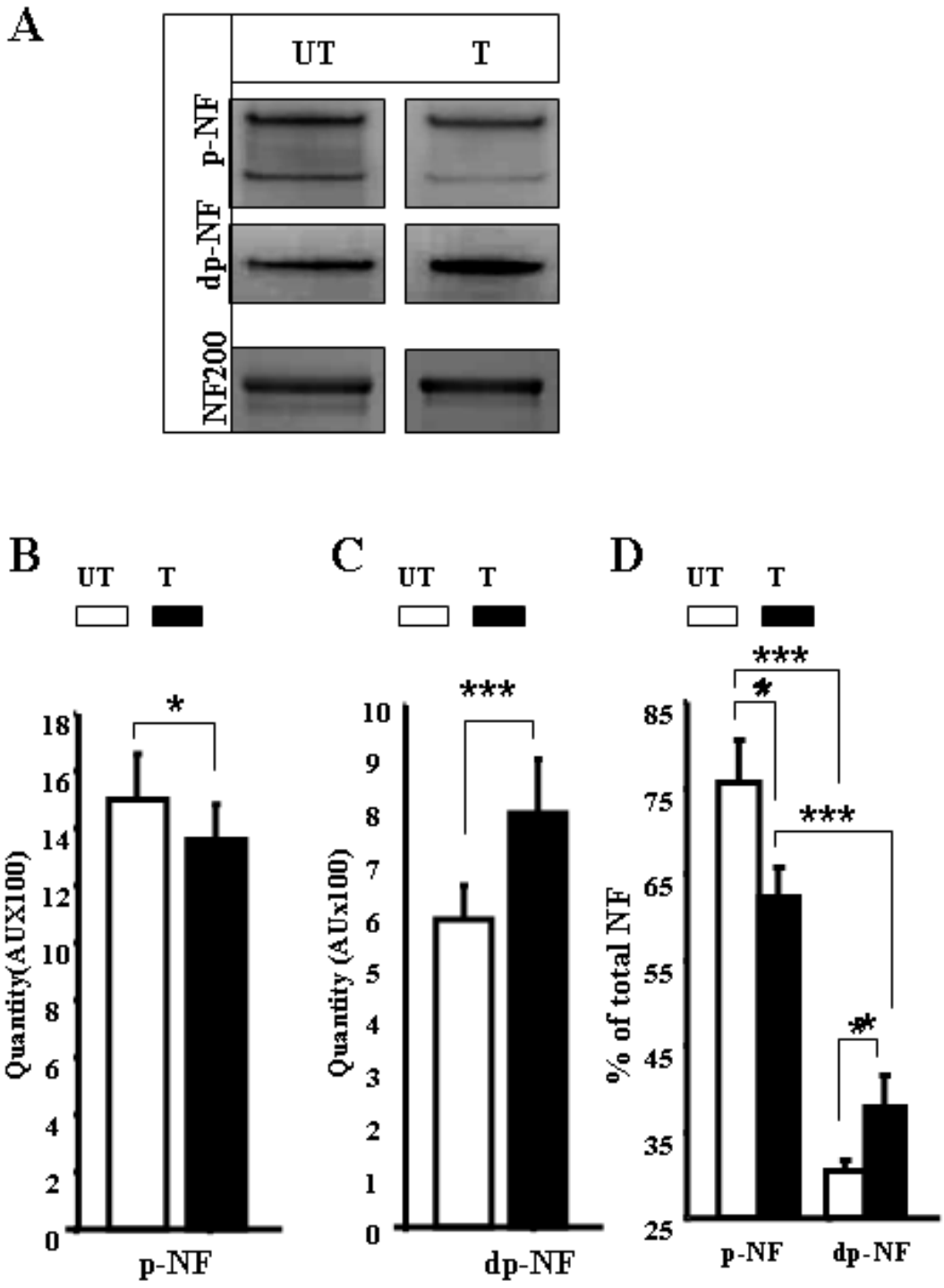
A
UT
T
p-NF
dp-NF
NF200
B
UT
T
*
Quantity(AUX100)
18
16
14
12
10
8
6
4
2
0
p-NF
C
UT
T
***
Quantity (AUx100)
10
9
8
7
6
5
4
3
2
1
0
dp-NF
D
UT
T
***
*
***
**
% of total NF
85
75
65
55
45
35
25
p-NF
dp-NF

Figure 33: CZ perturbs NF phosphorylation in ON axons.

A. *Differential levels of p- and dp-NF detected in ON after demyelination using Western blot analysis. There is a loss in smaller size p-NF (~168kD) relative to the larger one (~200kD). Correspondingly there is an increase in the dp-NF (~200kD) in the treated ON. No change was noted for NF200.* ***B.*** *Histogram representing significant decrease in the quantity (arbitrary unit (AU) x 100) of p-NF (p>0.01, n=3)* ***(C)*** *and an increase in dp-NF (p>0.001, n=3).* ***D.*** *This accords much larger difference in the levels of p-NF and dp-NF in the total pool of NF after CZ treatment (p>0.001, n=3).* □ *untreated,* ■ *treated.*

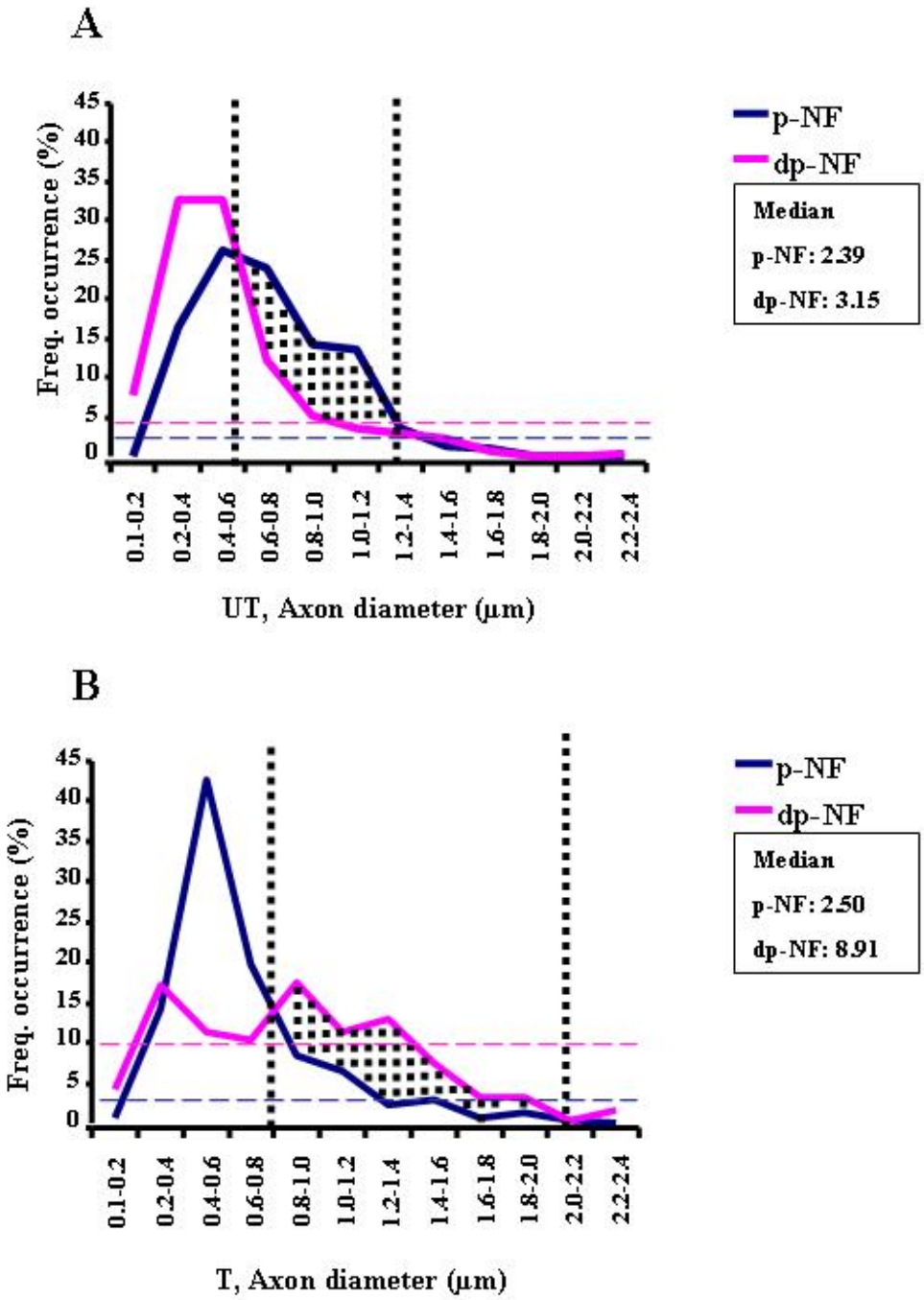
A
Freq. occurrence (%)
45
40
35
30
25
20
15
10
5
0
0.1-0.2
0.2-0.4
0.4-0.6
0.6-0.8
0.8-1.0
1.0-1.2
1.2-1.4
1.4-1.6
1.6-1.8
1.8-2.0
2.0-2.2
2.2-2.4
UT, Axon diameter (µm)
p-NF
dp-NF
Median
p-NF: 2.39
dp-NF: 3.15
B
Freq. occurrence (%)
T, Axon diameter (µm)
p-NF
dp-NF
Median
p-NF: 2.50
dp-NF: 8.91

Figure 34: p-NF and dp-NF represents varying diameters of axons in ON.

A. *A comparison of axon diameters labeled with p-NF and dp-NF indicate the threshold (dashed vertical line), when p-NF exceeds dp-NF. This trend is true for axons between 0.4 to 1.4µm diameter (shaded portion).* ***B.*** *Whereas for the treated group the trend is reversed (dashed lines) as there is an increase in dp-NF labeled axons showing a shift (shaded portion) favoring large diameter axons (0.6 to 2.2µm). The median of frequency occurrence of dp-NF positive axons show an increase (box, A and B) following CZ-treatment (n = 235, 286), UT = untreated, T = treated, dp-NF = dephosphorylated NF and p-NF = phosphorylated NF.*

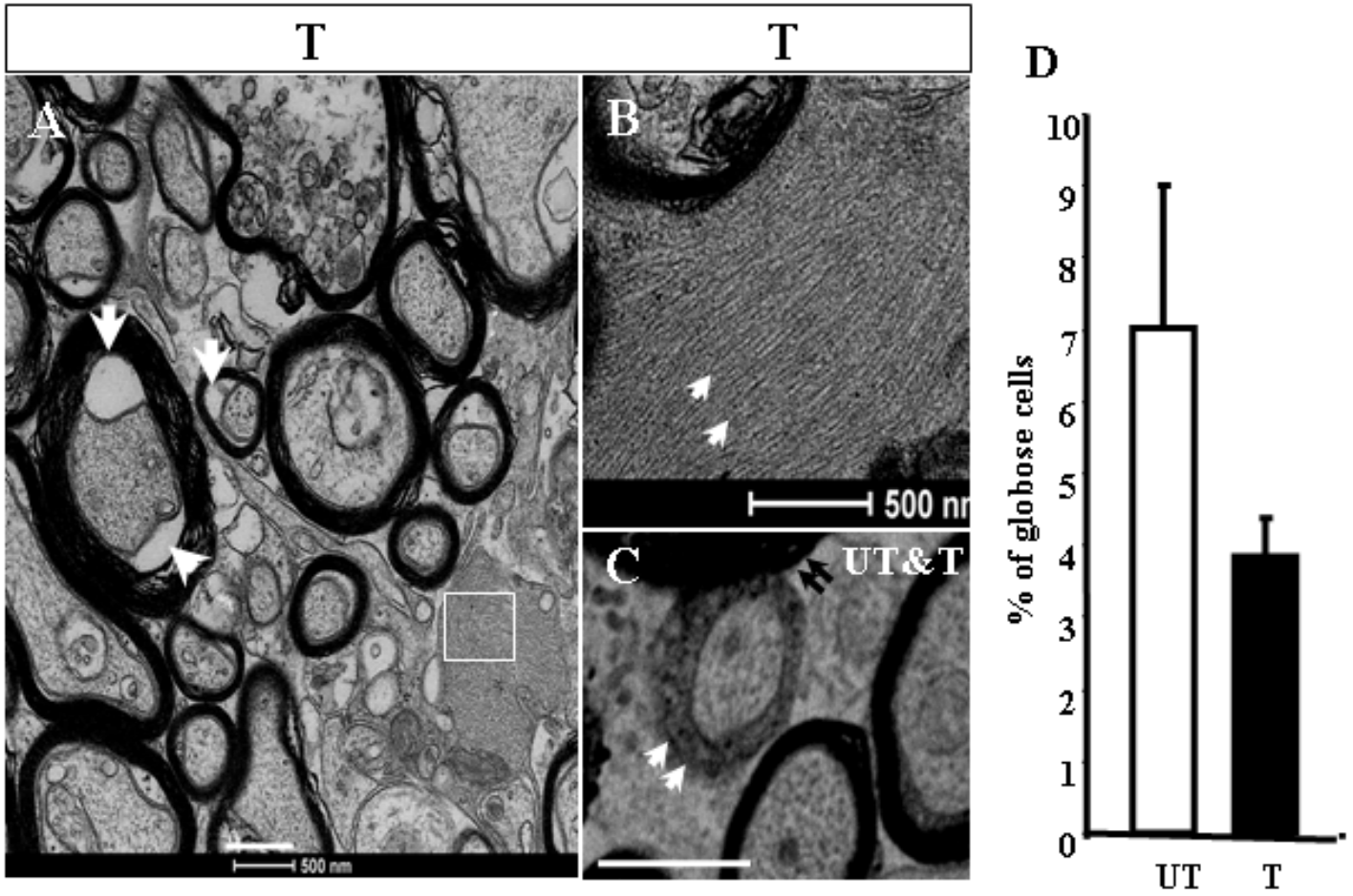
T
T
A
B
C
UT&T
500 nm
500 nm
D
% of globose cells
10
9
8
7
6
5
4
3
2
1
0
UT
T

Figure 35: Inter-axonal organization after CZ treatment.

A. *Representative visuals fields from TEM cross sections of treated ON section showing various types of streaming processes in between the myelinated axons. These inter-axonal spaces are filled with various types of membranous structures. The white arrow points the collapse of axolemma and formation of wider submyelinic periaxonal space. The axon on top (12 o'clock position) and middle shows the vacuolization of axoplasm. Right bottom corner is a well organized micro-tubular cytoskeleton of an intercalating cell (white box).* ***B****. This has been highlighted (double white arrow) in (****B****) to show the difference in organization of cytoskeleton relative to axons (refer Fig. 27).* ***C****. Occasional globose structures (white double arrow) were observed, which remained lodged on the outer periphery of myelinated axons (black double arrow) of treated axons only.* ***D****. Such cells were found to be reduced (non-significant) after CZ treatment,* □ *untreated,* ■ *treated groups, n = 1525, 1289, p = ns*

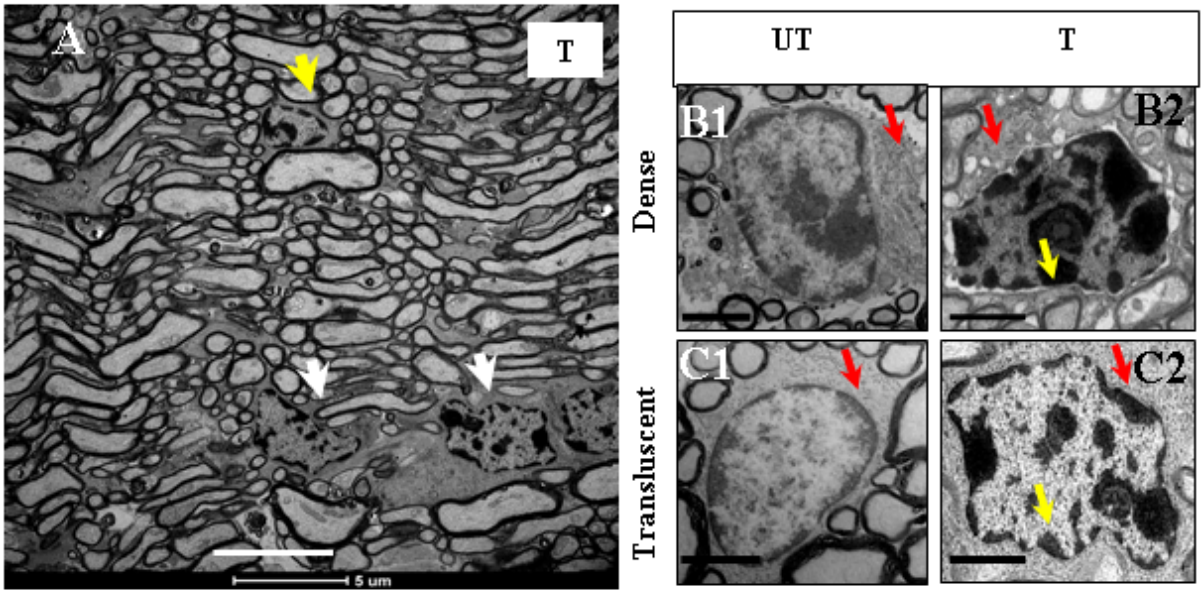
A
T
5 um
UT
T
Dense
Translucent
B1
B2
C1
C2

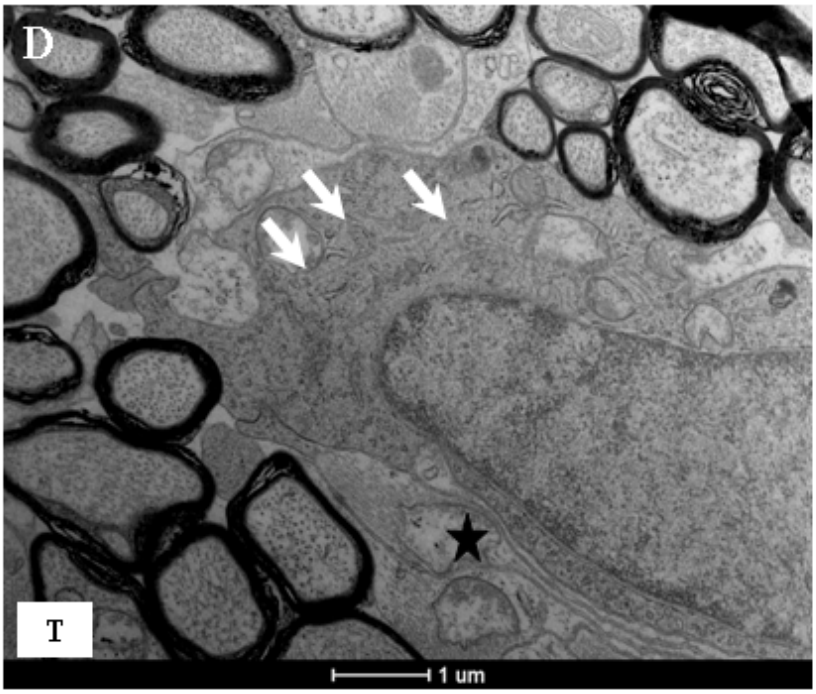
D
T
1 um

Figure 36: Nuclear morphology of inter-fascicular cells change after CZ treatment.

A. *Representative image form treated ON showing two types of cells, one surrounded with electron dense (yellow arrow) and the other with electron translucent (white arrow) material, scale bar 1µm. They differ in their nuclear size.* ***B.*** *Electron dense cells and* ***C.*** *electron translucent cells of ON. Both these cells have different nuclear morphology owing to the scattered distribution of chromatin material in the perinuclear region (dark blobs) (B2, C2). Red arrows indicate electron dense material and yellow arrows show the perinuclear distribution of chromatin in treated group.* ***D.*** *Eminent hypertrophic processes of the intercalating cells exhibit invaginating processes (white arrow) with membrane filled subcellular structures. These cells have distinct nucleus with a marked perinuclear margin (black star). The scale bars are 1 µm (A and D), 5µm and 2µm for B and C panel respectively,* □ *untreated,* ■ *treated.*

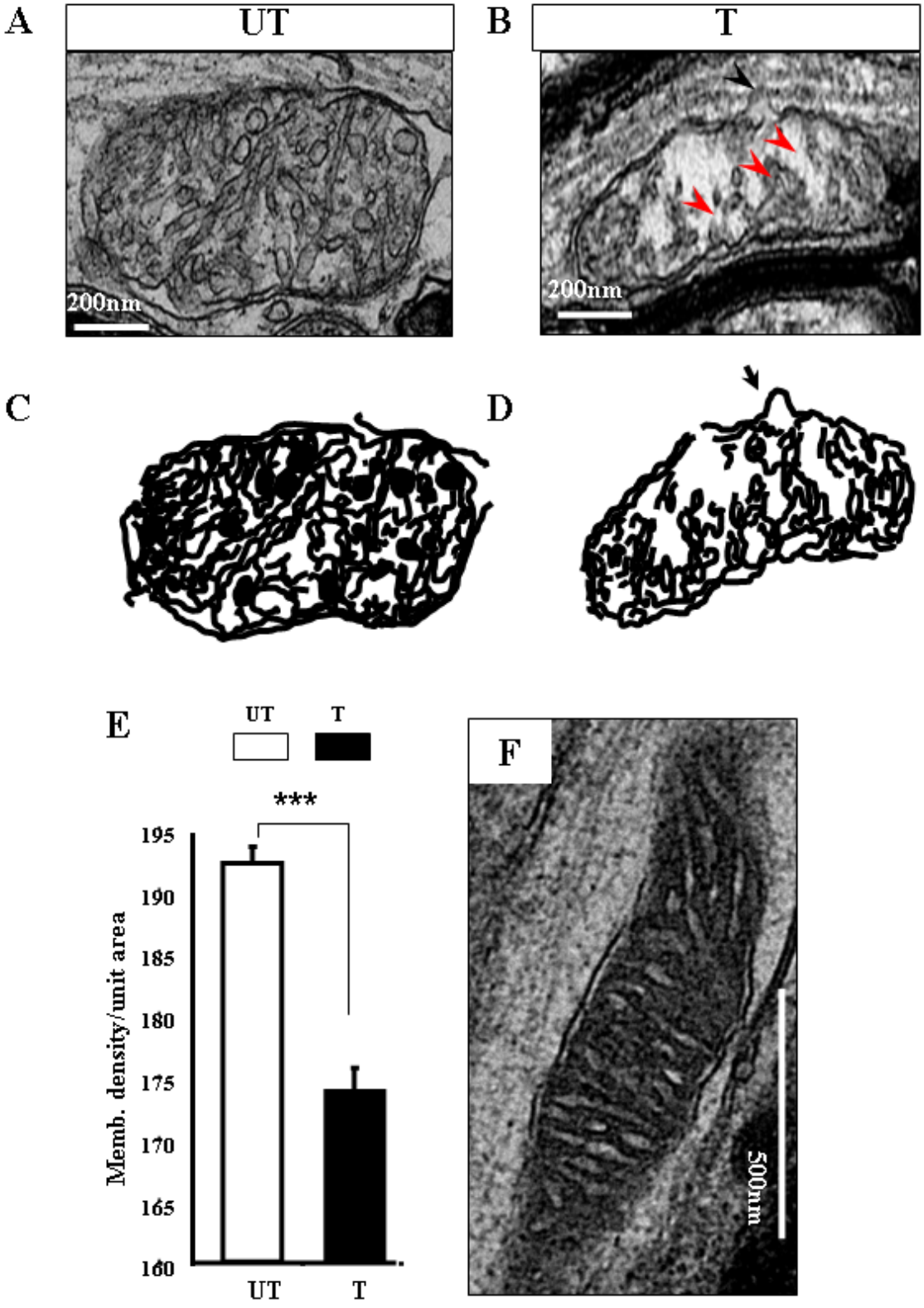
A
UT
200nm
B
T
200nm
C
D
E
UT
T
***
Memb. density/unit area
195
190
185
180
175
170
165
160
UT
T
F
500nm

Figure 37: Evident partial loss of inner membrane of mitochondria and organized cristae in CZ treated axons.

A. *Representative electron-micrograph of untreated control mitochondria from axon exhibit intact inner and outer membranes (scale bar 200nm).* ***B.*** *The treated group show eminent loss of inner membrane (scale bar 200nm). Black arrowhead points to the wavy outline of these membranes* ***C.*** *Outlined trace of control mitochondria* ***(A)*** *highlights the perfect membrane integrity.* ***D.*** *Similar outlined trace of mitochondria from experimental group (B) shows disruption, black arrow points to the single membrane span.* ***E.*** *Histogram plot showing loss of inner membrane density (represented as membrane density/nm^2) of mitochondria following CZ treatment ($p > 0.001$, $n = 25$, □ untreated, ■ treated).* ***F.*** *Membrane stacked structure of the mitochondria from the surrounding cell differ in morphology (scale bar 500nm).*

CHAPTER 5

CZ INDUCES ALTERED EXPRESSION OF K_v1 CHANNELS IN OPTIC NERVE AXONS

5.1. Introduction

K_v channels are well known therapeutic targets for neurons, cardiac and immune T cells (Judge and Bever, 2006). Neuronal K_v1 channels could be of synaptic or axonal origin with different functional attributes like neuro-transmission (Caleo, 2009, Michaelevski et al., 2007, Wang et al., 1994), or mediating action potential propagation (Mert, 2006, Debanne, 2004). Axonal K_v1 channels are usually present as a paired cluster apposing each other on the longitudinal axis, often described as punctate expression. These specialized compartments or sub-domains are known as JXP of an axon (Rasband, 2004). They flank Na_v rich unmyelinated part the focal node. Myelin concealed JXPs (Chiu and Ritchie, 1980, Rasband et al., 1999b) maintain subcellular segregation of K_v channels from nodal Na_v, which is the basis of action potential propagation. This is essentially true for saltatory mode of fast conduction **(Section 1.2).** Disease conditions leading to demyelination result in compromised axon architecture of the surviving axons due to several types of local and/or global changes associated with it (Hu et al., 2008, Arroyo et al., 2002, Baba et al., 1999, Bitsch et al., 2000, Cerda and Trimmer, 2010, Rash, 2010, Gubitosi-Klug et al., 2005). The underlying effects rendered by such surviving/spared axon(s) in addition to those of the affected ones together contribute to neurological deficits. In case of MS although demyelination and axon loss are marked at the onset (Compston and Coles, 2002), the subsequent malfunctioning of surviving axons following disease inception is of prime importance in the development of a therapy. Unfortunately, these events which affect the nervous system are detected late in clinical assessments. The major contributors of axonal

conduction deficits (Lasiene et al., 2008) include depletion of myelin and consequential effect induced on other structural elements of axons. Such changes in turn may be associated with altered activity of ion channels which play important roles (Nashmi and Fehlings, 2001) in neuronal co-ordination.

5.2. K_v1 channels as a therapeutic target in multiple sclerosis

It has been theorized that exposure of K_v channels as a result of demyelination would induce a reduced safety factor (Waxman, 2005) (the ratio of available current to an axon divided by the current sufficient for axon membrane to attain excitation threshold) of action potential propagation across demyelinated region of the axon **(Section 1.12).** Low safety factor means lower probability of an action potential to traverse the axon (Nashmi and Fehlings, 2001). Although this theory was originally conceived on the basis of electrophysiological studies and nodal features of Na_v channels, it is important to note that efficient AP propagation is equally dependent on the JXP K_v1 channels of a myelinated axon. The roles of these channels are further highlighted by pharmacological studies involving K_v channel blockers on animal nerve preparations (Gordon et al., 1988). Investigations of neuron function using 4-aminopyridine (4-AP) a blocker of rapidly activating K_v channel has established its relevance as a therapeutic agent in MS and injury where demeylination is an eminent feature. Several preliminary clinical trials of K_v channels inhibitors have demonstrated therapeutic benefit in MS (Stefoski et al., 1987) and spinal cord injury (Nashmi and Fehlings, 2001) although it induces epileptogenic activity due to off-site action.

This study for the first time presents JXP K_v1 expression analysis of ON axons in CZ-treated mice. The use of a murine model for sub-chronic CZ-induced CNS demyelination to establish the relevance of K_v channels in axons was anticipated to be revealing, since little is known about K_v1 channel associated deficits in this type of system(s).

5.3. Multiple K_v1 α-subunits are present in the ON axons

5.3.1. $K_v1.1$, 1.2 and 1.4 are the major K_v1 α-subunits in the ON of both groups

In order to detect the expression of CNS axolemmal K_v1 channels from mice, detergent solubilized ON membrane protein from both untreated control and treated samples were resolved in SDS-PAGE gels under denaturing conditions and probed with antibodies for the six major $K_v1.x$ channels on PVDF membranes **(Figure 38)**. Of all the six α-subunits $K_v1.1$- 1.6, signal was obtained only for three namely $K_v1.1$, 1.2 and 1.4. $K_v1.3$, 1.5 and 1.6 remained undetected in this type of analysis. The molecular weight for $K_v1.1$ and $K_v1.2$ bands were always higher than ~60kD in the solubilized membrane extract. Even though both were detected within a similar range, $K_v1.2$ tended to be of a larger size as broad and fuzzy bands. These corresponded to ~65kD for $K_v1.1$ and ~70kD for $K_v1.2$ **(Figure 38A)**. The broad $K_v1.2$ signal could be resolved into three bands of ~77, 71, and 68kD size respectively, but it was impossible to achieve such a resolution for $K_v1.1$ in these preparations **(Figure 38B).** The higher molecular weight of $K_v1.2$ obtained from the membranes of ON were similar to bovine brain membrane (Scott et al., 1990) and human CNS (Coleman et al., 1999). The densitometric quantification of $K_v1.1$ on Western blots from 15µg of ON protein showed a minor, but non-significant increase (29.37 ± 2.13%, $p = 0.39$, $n = 3$), whereas $K_v1.2$ exhibited a decrease (3.8 ± 1.02%, $p = 0.85$, $n = 3$) in the CZ treated samples. This indicated some kind of dysregulation of K_v1 channels following CZ treatment, but remained inconclusive, possibly owing to variation induced due to individual response.

5.3.2. Molecular weight of $K_v1.4$ in ON protein is larger relative to $K_v1.1$ and 1.2

Unlike $K_v1.1$ and 1.2, $K_v1.4$ signal from ON of CZ-treated and untreated group was always obtained as a doublet of much larger size corresponding to ~94 and 86kD in Western blot analysis. These were similar to human CNS membranes (Coleman et al., 1999). They were sharp bands in comparison to $K_v1.1$ and 1.2 **(Figure 38A)**. This is because the mouse $K_v1.4$, from brain and cardiac tissue has two distinct mRNA species, ~ 3.5 kb and ~ 4.5 kb

in length (Wymore et al., 1996, Jang et al., 2008). These mRNA differ in the 3' non-coding region corresponding to potential polyadenylation determinants, located ~ 0.2 kb and ~ 1.2 kb downstream of the coding region (Jang et al., 2008, Wymore et al., 1996, Wymore et al., 1994). Study in *Xenopus* oocytes has indicated differential levels of $K_v1.4$ current owing to the expression of these two forms. Here in this study an quantitation of these two protein bands, which is anticipated to correspond to the two different proteins translated from the said transcripts, indicated 8.7 ± 0.03%, p = 0.01, n = 3 higher levels of the ~94kD band in the experimental CZ treated group. Collectively, these two bands for $K_v1.4$ correspond to a non-significant 4.33 ± 2.08%, p = 0.51, n = 3 increase following treatment. These observations **(Section 5.3.1 and 5.3.2)** proved that $K_v1.1$, 1.2 and 1.4 are the major membrane associated K_v1 channels present in the ON.

5.3.3. Dysregulation of $K_v1.1$, 1.2 and 1.4 α-subunits of ON after CZ-treatment

Neurons and their networks undergo a process of homeostatic plasticity that stabilizes neuronal output by integrating activity levels with network and cellular properties to counter perturbations. The excitability of an individual neuron is governed by the extent of commonality at the most fundamental and basic level, and yet little is known about these processes (Ransdell et al., 2012). Dysregulation of ion channels is one of the factors, which regulate such processes. Demeylination associated deficits in function are known to result due to several components **(Section. 1.9)**. Herein the relative level of K_v1 channels localized on the JXP **(see below)** of ON axons was examined employing a sensitive detection system for the homogenates.

5.3.4. $K_v1.1$ and 1.4 is up-regulated, whereas $K_v1.2$ is down-regulated

Western blot analysis indicates a dysregulation of K_v1 channels in ON after CZ-treatment, but they could not be reliably evaluated for an individual nerve owing to their low protein yield. Hence, the expression level in nerve homogenate was further explored by combining two sensitive detection systems like ELISA (Enzyme linked immunosorbent assay) and

CSPD chemiluminescence. This permitted investigation of samples from individual nerves, using very less amounts (3µg) of ON protein. Known quantities of Glutathione- S-transferase (GST) fusion peptide corresponding to sequence from K_v1.1, 1.2 and 1.4 **(Table 1)** were used to generate a standard curve, against which the unknown samples i.e., ON homogenate from CZ-treated and untreated control mice were compared. This strategy allowed evaluation of the relative levels of K_v1.1, 1.2 and 1.4 α-subunits against a known standard and expression as relative luminescence unit (RLU). This methodology allowed assay of the relative levels of K_v1.1 and 1.2 in a nerve. K_v1.1 exhibited a significant 54.04 ± 0.12% ($p > 0.001$, $n = 6$) increase **(Figure 39A)** whereas K_v1.2 represented 45.35 ± 0.01% ($p > 0.001$, $n = 6$) decrease **(Figure 39B)** in CZ-treated nerve. Interestingly, K_v1.4 also exhibited an increase of 62.53 ± 0.29% ($p > 0.001$, $n = 6$) **(Figure 39C)** in the treated samples. The peptides used in this experiment corresponded to C-terminus **(Table 1)** such that only mature forms of these proteins were detected herein. Hence, these observations are indicative of the changes in the mature form of α-subunits which are possibly the membrane pool. The greater difference observed here relative to western blot, could be due to the detection of non-axolemmal contaminating pool in those samples. Negative controls for background elimination arising due to protein coating, buffer salts and washes were included in these experiments. The samples were quantified in serially-diluted range of concentrations and the average difference between treated and untreated sample was considered for evaluation. The experiments also allowed estimation of the relative levels of all three K_vs in untreated and treated groups. Their normal levels (K_v1.2>1.1>1.4) in ON, shifted in the CZ-treated group (K_v1.1>1.2>1.4) which was indicative of predominance of K_v1.1 after demyelination. This in turn might signify an anticipated change in the α-subunit associations of ON, specifically K_v1.1 and 1.2.

5.4. K_v1.1 and 1.2 are the major K_v channel constituents of ON axons and they attain disparate expression after CZ treatment

K_v channels regulate a variety of neuronal properties, including action potential amplitude and duration, frequency of firing, neurotransmitter release, and resting membrane potential (Hille, 2001). Their precise location is a determining factor for such an attribute. JXP

localization is vital for saltatory conduction in myelinated axons. Herein, following induction of demeylination by CZ, there was a loss of compact myelin which is an important regulator for expression, of K_v1 channels (Baba et al., 1999). Hence, immuno-labeling experiments were performed using 10µm longitudinal cryosections of ON. $K_v1.1$ and 1.2 specific antibodies visualized apposing punctate structures of axons on the longitudinal axis in the control group as expected. A broad view micrograph shows several such structures which appear as elongated dots **(Figure 40A,** red box) representing the JXP location of these channels. Similar pattern was observed in CZ-treated ON **(Figure 40B,** red box)**.** Most of the JXPs showed intense labeling of $K_v1.1$ and 1.2. All $K_v1.1$-labeled JXPs overlapped with 1.2 positive JXPs in the untreated group thereby, exhibiting 100% overlap whereas, experimental group axons showed only 96% overlap **(Figure 40B).** Even though one would expect $K_v1.1$ and 1.2 to exhibit an absolute co-localization, these JXPs had relatively greater $K_v1.2$ signal in controls than the experiment. Accordingly $K_v1.1$ signal appeared higher in the experimental group than the controls. Further analysis **(Section 5.10),** showed an array of JXP pattern in the treated group, indicating CZ induced disparity.

5.5. CZ induces two types of alterations in the expression of JXP $K_v1.1$ and 1.2

CZ-induced heterogeneity in the expression of JXP $K_v1.1$ and 1.2 was eminent and it could be classified as two distinct categories.

- **Internodal K_v1:** Firstly, several JXPs appeared elongated such that labeling of $K_v1.1$ and 1.2 spread along the entire length of internodes. Some axons had lost demarcated JXPs and it appeared as smeared, elongated structure along the axon. Apparently, these represent the most affected axon following due to CZ and have lost their typical punctate identity **(Figure 40B (white box) C, D).** This kind of exclusive feature has never been reported before, specifically CNS featuring axons of ON with defined demyelinating pattern

.

- **Elongated JXP:** Secondly, the remaining JXPs showed loss of paired punctate labeling in these micrographs. Even though it was a visible feature, yet in order to avoid any ambiguity that might arise owing to visualization of JXPs on these micrographs, this was analyzed in affiliation to the nodal labeling with pan Na_v (described in a later, **section 5.11**)

5.6. Associated α-subunits in K_v1 channels of ON

Unlike nodal Na_v channels, which are single chain proteins, the functional axolemmal K_v1 channels are formed by the assembly of four subunits into a tetrameric protein which spans the membrane and collectively forms the domains essential for the flow of K^+. Even though one might assume a huge number of combinations of subunits, owing to the oligomerisation often being restricted within the same Shaker subfamily (Shamotienko et al., 1997), K_v1 channels are tailored in this way only to a limited set of combinations explaining the basis for fine-tuning of neuronal function by regulating K^+ conductance along the membrane (Shamotienko et al., 1997, Akhtar et al., 2002). For instance, $K_v1.1$ exerts a more dominant influence on K_v1 channel activation, with lowered voltage threshold for activation; this is shifted negatively upon increase in the number of $K_v1.1$ subunits relative to $K_v1.2$ in a tetramer. Thus, depending upon the numbers of these subunits in a tetramer their biophysical and pharmacological profile might differ (Bostock et al., 1981, Sokolov et al., 2007, Akhtar et al., 2002, Al-Sabi et al., 2010). Interestingly $K_v1.1$ shows higher sensitivity to 4-AP relative to its known obligate associate $K_v1.2$ in expression systems (Scott et al., 1994b)**.** Since MS demeylination also leads to an increase in 4-AP sensitivity as indicated by the therapeutic benefit rendered by similar compounds (Dunn and Blight, 2011), an apparent role of $K_v1.1$ α-subunit is anticipated.

5.6.1. $K_v1.2$ α-subunit associate with $K_v1.1$ to form hetero-oligomers

In order to investigate the possible associations of $K_v1.1$ and 1.2 in JXP of ON, co-IP experiments were performed. ON homogenate was briefly incubated with polyclonal antibody against $K_v1.x$ **(Section 2.12)** and then the complexes were pulled down using

protein-A Sepharose beads and probed for other K_v1.x α-subunit(s) (Shamotienko et al., 1997). Combinations of α-subunit specific antibodies were used to decipher the associations **(Figure 41A).** K_v1.2 antibody could pull down K_v1.1 α-subunits from both treated and untreated samples. Reciprocal IP using K_v1.1 specific antibodies yielded K_v1.2 signals. This indicated that these two subunits co-associate in ON.

5.6.2. ON homogenate has self-assembled homo-oligomers of K_v1.1

On the basis of the noted up-regulation of K_v1.1 protein **(Section 5.3.4)**, an effect exerted mainly due to this particular channel is anticipated, so the possibility of its homo-oligomeric association was explored by employing a sequential-immunoprecipitation (seq-IP) (Shamotienko et al., 1997). This involved three stages of IP, namely IP-1, IP-2 and IP-3 **(Figure 41A).** Since the content of K_v1.4 is the lowest in ON, the first IP was conducted to precipitate all possible oligomers of K_v1.4 (K_v1.4-1.2, 1.4-1.1, 14-1.4). These combinations were not confirmed, but it was ensured that the resulting supernatant did not contain any remaining K_v1.4 signal, implying that all these possible oligomeric associations (if present) are eliminated in this step. Second step (IP-2) involved precipitation of K_v1.2 containing oligomers (1.2-1.2, 1.2-1.1) and, finally, and the last step IP-3 employed precipitation with K_v1.1 antibody. Signals were obtained in each stage of seq-IP, reconfirming the presence of all these three α-subunits. Interestingly, K_v1.4 precipitation detected a doublet band, similar to that obtained from membrane extract. On the other hand, K_v1.2 precipitation yielded a broad band (~60-70kD). This possibly indicated the presence of various types of oligomeric associations even though that remains to be confirmed. Since it was of interest to investigate homo-oligomeric association of K_v1.1, the supernatant was subjected to the last IP-3 to further precipitate proteins with polyclonal Kv1.1 IgG and this allowed detection of two low molecular weight bands of ~55 and 50kD **(Figure 41B).** K_v1.1 protein of this size was not detected in the membrane extract.

So, it was reasoned that these bands corresponded to the cytoplasmic protein, probably of Golgi origin, because, nerve homogenate had to be used in these experiments (n=2) as they required larger amounts of protein (45µg). Use of lower amount of protein did not yield any

band at the end stage. Alternative explanation may stem the fact that, these bands represent free peptides from the axoplasmic protein pool or a form of membrane protein which has not undergone post-translational changes. In a pioneering study, on *in vitro* assembly of K_v1.1 transcript it has been shown that ~55kD band corresponds to K_v1.1 protein in absence of microsomal membranes, whereas it acquires high molecular weight in their presence (Babila et al., 1994). Taken together, ~50kD band is apparently an unglycosylated form of K_v1.1, but the ~55kD peptide corresponds to a glycosylated form (Manganas et al., 2001). In a separate study on the hydrodynamic nature of K_v1.1 protein it has been indicated that such a heterogeneity underlies the heterogeneous pattern of oligomer association under a given condition (Shen et al., 1993) which is expected to vary greatly in a neuronal environment compared to any *in vitro* expression system. It was anticipated, that if a minor population of K_v1.1 homo-oligomeric axolemmal form is present in the ON, it would remain undetected here in these experiments, but lead to the fine tuning of nerve function.

Herein, there is a possibility of existence of other homo-oligomers for K_v1.2 and 1.4, but it has remained unexplored in the present study, partly because it was not of relevance to establish their identity and partly because of the paucity of protein due to low yield from ON.

5.6.3. *In situ* localization of K_v1.1 and 1.2 interacting subunits in ON axons

In-spite of extensive evidence supporting the formation of K_v1.1-1.2 hetero-oligomers in the nervous system, the conclusive existence of these complexes in their native environment has not been demonstrated. For myelinated axons, such interpretations have remained difficult owing to the myelin concealed location of JXP and expression of these two α-subunits within a micro-domain. So PLA was adopted herein to decipher the *in situ* localization of K_v1.1 and1.2 interacting subunits if in close proximity, <16nm (Trifilieff et al., 2011). Localization of K_v1.1 containing α-subunit was detected using two specific antibodies one directed against the extracellular epitope (mAb) and the other for an internal

intracellular epitope (rabbit polyclonal) **(Table 1, 2)** to yield fluorescent signals **(Figure 42A).** Similar to the patterns observed using IHC and described in the paragraph above, the JXPs from CZ-treated nerve represented various types of patterns. This allowed detection of $K_v1.1$ signal only and, interestingly, this corresponds to elongated JXP signals. Many of them acquired a much more elongated and smeared appearance, but their exact identity could not be established in the present study. Probably these were the much extended internodal expressed $K_v1.1$ observed in treated group. Collectively, these indicated a wide distribution of $K_v1.1$ along the JXP which tend to spread out to the internode **(Figure 42B1).** Whereas detection of $K_v1.1$-1.2 interacting subunits using antibodies directed against $K_v1.1$ extracellular (mAb) and $K_v1.2$ intracellular epitope (rabbit polyclonal), showed that $K_v1.1$-1.2 interacting subunits remain in close proximity to the nodal gap **(Figure 42B2)** in the treated group samples. This is the first demonstration of such an *in situ* interaction between the two channels of JXPs in ON axon.

5.7. Minority of $K_v1.2$ expressing JXP co-localize with $K_v1.4$

Even though the exact role of $K_v1.4$ in MS or demeylination is not established (Wulff et al., 2009), a prominent and consistent $K_v1.4$ signal was obtained from the ON homogenate using Western blot analysis **(Section 5.3.2);** hence, it was further investigated by IHC analysis. Longitudinal sections (10µm) were treated with antibodies for $K_v1.2$ and 1.4 because; Rasband group reported the presence of $K_v1.4$ on 1.2 positive JXP. (Ogawa et al., 2010) Surprisingly, very little $K_v1.4$ signal was found on the usual punctate JXP **(**Figure 43**A, B)** structure described in above paragraph. Microscopically, it appeared as fuzzy background. The number of $K_v1.2^{+ve}$ JXPs that were also $K_v1.4^{+ve}$ represented a minor population. Only 18.6 ± 1.8% vs. 9.2 ± 1.2% ($p > 0.001$, n = 1161, 892) JXPs showed such an overlap in the untreated control and treated groups. The remainder did not show any overlap and were found to be either $K_v1.2^{+ve}$ of $K_v1.4^{+ve}$. For the JXPs which did not overlap $K_v1.4$ exhibited a decrease and the $K_v1.2$ showed a corresponding increase in CZ-treated ON **(**Figure 43**C)** but these changes were non-significant.

5.8. Area and length of surviving JXPs co-labelled with K_v1.1/1.2 increases after CZ treatment

The alterations in JXP expression pattern of K_v1.1/1.2 label were so prevalent that sometimes it was difficult to account for the entire internodal length, even though it was visibly a prominent feature. So morphometric analysis of the surviving JXPs was performed. This included all of those which appeared as a single lone unit or a paired apposing structure along the axons. Area and length were measured manually for each JXP by outlining the ROIs. K_v1.1 and 1.2 co-labeled images exhibiting yellow signal signifying the overlap of these two fluorescence namely red (K_v1.1) and green.(K_v1.2) The border of these ROIs was defined by setting a threshold where yellow signal diminished and red/green or ceased/emerged. The average JXP area before and after CZ-treatment was 10.31 ± 0.81 and 12.46 ± 1.06 µm^2, (p = 0.06, n = 46, 42) **(Figure 44B).** The area range was 3.43 to 26.78 µm^2 before and 2.76 to 40µm^2 after treatment **(Figure 44A).** A binned frequency distribution of these JXP areas is represented in **Figure 44 A**. The K_v1.1/1.2 labeled JXPs of the experimental group occupied larger axon area relative to the untreated. This indicated spread of K_v1 channels into a wider space along the internodal length of the axon after treatment.

Based on the same defined ROI, their length was assessed from the point of peak signal intensity close to the nodal gap till the other end which extends into the internode. The average JXP length increased from 4.0 ± 0.32 to 5.90 ± 0.35 µm (p > 0.001, n = 46, 42) after treatment **(Figure 44D).** Binning of these length measures **(Figure 44C)** to evaluate the trend did not prove conclusive. Considering the increase in area, it was expected that the length changes would be proportionate, but that was not the case; apparently, the axon diameter is a contributing factor here. Taken together, these measurements indicate a widespread increase in the internodal expression of K_v1.1 and 1.2 following CZ-treatment.

5.9. Inter-JXP length increases in the treated group

Edges of JXP adjoining the node exhibited variations, which appeared as extensions beyond their restricted domain. This was evident due to the different shapes they acquired following CZ treatment **(Figure 45).** These could be normal blunt ended **(Figure 45 A1, B1)** or pointed cone like **(Figure 45A2, A3).** Sometimes the cone like JXPs tended to fuse from the apposing ends and loose their characteristic punctate structure in the treated group **(Figure 45B2, B3).** It was worth noting that these features lead to merging of adjoining JXPs. This could be further highlighted on an intensity profile, where the distance between the two peak intensities of the apposing JXPs varied **(Figure 45C).** This parameter was analyzed in $K_v1.2$ labeled JXPs. The frequency distribution of these inter-JXP length distributions indicated a shift towards the longer length in the treated group, indicating an increasing trend in the nodal gap after CZ treatment **(Figure 45D).**

5.10. Co-localization of $K_v1.1/1.2$ within unaffected surviving axons exhibit a relative decrease of $K_v1.2$ intense JXPs

It was interesting to note that these surviving axons exhibit varied morphological features; so the possibility of differential role that could be acquired by two α-subunits on these axons was examined on the basis of their levels of expression. The extent of $K_v1.1/1.2$ labeling on these surviving JXP showed dissimilarity **(Figure 40, Figure 42, Figure 46C, D).** $K_v1.1$ fluorescence extended much longer on the JXP in the internode relative to $K_v1.2$ in the treated group **(Figure 42C, D, Figure 46A).** The collective mean intensity/area (µm2) of the defined JXPs (ROI, as described in earlier section), for both $K_v1.1$ and 1.2 showed a non-significant decrease in the treated group **(Figure 46B)**, indicating a spreading of the signal away from the JXP. The number of $K_v1.1^{+ve}$ and $K_v1.2^{+ve}$ JXPs and their corresponding intensity plots provided a trend for the two. Prediction based on extended linear regression (R^2) co-efficient for $K_v1.1$ was ascending whereas $K_v1.2$ showed a marked descends in the treated group. Taken together, it reflects a change in the pattern of expression of these two α-subunit on the surviving JXP of treated

group, where $K_v1.2$ appears to be down-regulated mostly extending towards the nodal end of JXP in majority of these axons**.** This observation further supports the feature noted by the area and length measurements.

Since $K_v1.1$ and 1.2 exhibited a differential labelling on the JXPs **(Figure 47 Fig. 35, 41A, C, D),** the extent of their overlap was further examined, by analysing the correlation coefficient (Pearson's). This allowed information regarding intensity distribution within the co-localising region (LSM 710/ConfoCor3 user manual, page 4-170, 10/2008). R^2 for untreated was 0.145 and 0.176 for the treated group indicating a tighter co-relation in the experimental group **(Figure 46F).** The average co-relation co-efficient (Rr) for these JXPs showed an increase in the treated group ($p > 0.001$, $n = 92, 96$) **(Figure 46D).** This was further reflected by the average overlap co-efficiency of these two channels, namely $K_v1.1$ and 1.2 **(Figure 46E)** which showed a significant increase ($p > 0.001$, $n = 93,115$).

5.11. Minor nodal disruption is accompanied by changes in JXP

The nodes are complementary structures required for efficient action potential propagation besides the JXPs. Herein labeling of focal nodes using pan-Na_v antibody exhibited multiple effects due to CZ induced demeylination. In the micrographs of Na_v labeled ON axons from both groups these appeared to be of varied shapes and sizes **(Figure 48A).** Briefly, the normal or intact nodes could be described as compact and focal spots with a visible delimiting boundary. The nodes that were affected appeared as smeared or elongated. Some of them also appeared as doublets **(Figure 48. 43B).** Whether, these doublets were an induced feature or a mere co-incidence of two closely apposed nodes was a question. However, these doublets were less frequent in the untreated nerves. So, it was assumed as an induced effect for analysis here, considering the fact that such nodal proximity will create interference with the trains action potentials propagation (Waxman, 2005). Even though most of the nodes remained intact, small proportions were affected as per these morphological parameters **(Figure 48 C, D).** It was interesting to note that a minority of the nodes exhibited elongated shape in the untreated group as well, which could be referred

as oblong shape rather than an absolute spherical or rounded shape. Taking that into consideration and accounting them as normal revealed that 21 ± 3.04 % ($p > 0.001$, n = 712, 635) of the nodes are affected due to CZ-treatment. This observation indicated that Na_v is dislocated from its focal node following CZ-treatment. These collectively indicate an induced effect on the nodal Na_v.

Analysis of these features of the node in affiliation with the JXPs was anticipated to be revealing as they collectively form the structural units for maintenance of effective action potential propagation along an axon. Herein a composite morphological element comprising of two intact and apposing JXPs flanking a focal node was considered as a structural unit for impulse conduction. These units in control samples are being referred as "intact JXP" for the sake of description here. They were assessed on the basis of double immuno- labeling for $Na_v/K_v1.2$. Those which maintained such a feature in the treated nerve was categorized as "spared" or "surviving" units **(Figure 49).** It was interesting to note that there is a significant decrease in such units after CZ-treatment **(Figure 49D, F).** The effects were multifarious and they were indicated by a) absence of adjoining JXP which would normally flank the other side of the node, b) disparate JXPs flanking a node c) the JXP appears fragmented as two or more interlinked segments **(Figure 49C).** All these structural changes are bound to produce a designated effect on the propagation of action potential and summon an impact on the safety factor of these axons, resulting in impedance mismatch. One would expect that the hemi-nodes are present in a normal condition as well, but the described alterations were very frequent in the treated group, so it is accepted as a CZ induced effect here. The treated group exhibit 60.53 ± 9.62% average decrease, ($p = 0.02$, n = 157, 102) of such functional units. Subsequently, an analysis of the signal intensity of these nodes, indicated a significant increase in the average absolute intensity relative to the controls (253.28 ± 24.23 vs. 353.65 ± 34.44 AU) in the treated group ($p > 0.001$, n = 40, 46). Collectively, these indicate an accompanied displacement of nodal Na_v channels.

5.12. Cellular profiles exhibit K_v1.1, 1.2 and Na_v signals after CZ treatment

CZ-treatment induced expression of these ion channels in some cellular profiles which remain intercalated in between the axons. Na_v, K_v1.1 and 1.2 all were found in such type of cells. Na_v expressed was most prominent **(Figure 50A, B).** Since these were located on the cells, it was expected that they will not have a direct impact on the electrophysiological property of an axon; hence it was not considered in this study. Even though the precise identity of these cells expressing K_v1.1 and 1.2 was not established here, it is anticipated that these are proliferating microglial cells induced by CZ treatment (Pott et al., 2009, Groebe et al., 2009, Hiremath et al., 1998) which express K_v1.1 and 1.2 (Li et al., 2008, Wu et al., 2009) **(Figure 50C, D).**

5.13. K_v1.4 is of glial origin

K_v1.4 had a limited expression on the JXPs, but the microscopic signal obtained appeared fuzzier and a co-labelling of axons with CNPase, indicated their presence of cells. These clusters of spotty signal surrounded a nucleus **(Figure 51).** The cells were further identified as oligodendrocytes which surround the axons, employing staining for Adenomatous polyposis coli a marker of oligodendrocyte and propidium iodide to label the nuclei. This allowed confirmation of their identity. Thus, it is concluded that majority of K_v1.4 signal obtained from ON homogenate is of glial origin.

5.14. Abnormal electro-responsiveness and conductivity of ON from CZ-treated mice

The functional impacts of these changes in ON were assessed by CAP recordings from the central stump of semi-dissected ON at physiological temperature **(Figure 52A).** In controls, stimulation of the distal end of the nerve evoked synchronous CAPs, whose amplitude could be graded by varying the stimulus strength **(Figure 52C)**; the threshold stimulus ranged between 0.36 and 0.44 mA (0.39 ± 0.2; n = 6) with responses saturating at

intensities between 0.9 and 1.2 mA (0.96 ± 0.4, n = 6) **(Figure 52C1, C2)**. Uniform conduction of normal axons was evident from synchronous monophasic CAPs, evoked by a single or paired pulse stimuli, with absolute refractory phases of control nerve ranging between 2.0 and 2.6 ms (2.38 ± 0.2 ms, n=6) **(Figure 52B, D1, D2).** Analysis of the effects of TEA (10mM) or 4-AP (1mM) on sub-maximal CAPs in the control nerves showed an increase in their amplitude with stabilization of their blocking effect 15-20 min after application. **Figure 52 (E, F)** illustrates representative CAPs before and in the presence of TEA or 4-AP. The effect of TEA in controls was subtle and slow, but failed to reach statistical significance (n=4, P=0.061). In contrast, 4-AP that caused a more prominent increase of CAP amplitude (67.2 ± 5.2%; n=5; $p<0.005$), which declined during the 10 min washout (not shown). Notably, neither TEA nor 4-AP affected the 50% refractory phase of CAPs (5.3 ± 0.3ms and 5.4 ± 0.2ms; p=0.21 and p=0.48) in controls, with only 4-AP reducing the threshold stimulus intensity (3.3 ± 0.4; p=0.038) for eliciting CAPs. Unlike the controls, CAPs of ON from CZ-treated mice revealed a complex shape, with an early synchronized fast phase followed by a protracted late component **(Figure 52C1)**, reflecting altered excitability and conductive properties of the demyelinated axons. Furthermore, the minimal stimulus intensity required for eliciting CAPs in the demyelinated ON was elevated (range: 0.42 and 0.62mA, mean: 0.58 ± 0.3; n=5) with the absolute refractory phase prolonged (range: 2.8 and 3.6 ms; mean: 3.0 ± 0.2, n=5) **(Figure 52D).** Similar to controls, blockade of K^+ channels with TEA (10mM) or 4-AP (1mM) in demyelinated nerves increased CAP amplitude, with the effects of both blockers reaching statistical significant (58.4 ± 21.2% and 114.2 ± 21.7%, respectively, n=5 in each group; $p<0.005$) **(Figure 52E, F).** As observed with the controls, refractory time for 50% recovery of CAPs (7.7 ± 0.3ms and 7.5 ± 0.2ms) remained unaltered under both treatments while the threshold stimulus intensity was significantly reduced (0.47 ± 0.1mA and 0.46 ± 0.1mA; n=5 in each group; $p<0.05$) (not shown).

5.15. Differential contribution of $K_v1.1$ and $K_v1.2$ to CAP in demyelinated ON

The relative contributions of $K_v1.1$- and 1.2-containing channels in ON to tuning the electrogenic properties of these axons were evaluated. Blockade of $K_v1.1$ and 1.2 subunits of normal ON with DTX_K (100nM) or TsTX-K (100nM) revealed little change in the characteristics of CAPs, with both amplitude and activation threshold remaining relatively unaltered (amplitude increase: 15 ± 7.2%, n=5; 10.3 ± 5.8%, p>0.05; n=6, respectively) **(Figure 53A, B, C, D).** At the specified concentrations, DTX_K is known to block completely $K_v1.1$-containing channels (IC_{50} of 2.5nM) (Robertson et al., 1996, Wang et al., 1999) while TsTX-K abolishes K^+ currents mediated by $K_v1.2$ channels (IC_{50} of 0.55nM) (Hopkins, 1998). Because of the presence of both subunits in mouse ON JXPs, ineffectiveness of such toxin blockers in myelinated axons is likely to be due to poor accessibility of K^+ channels. Such an interpretation also accords with the toxins' failure to change the refractory time in control ON (n=5; p>0.05) **(Figure 53E).** In stark contrast, in demyelinated nerves, the same concentrations of DTX_K and TsTX-K caused significant augmentation of the CAP amplitude (74.3 ± 5.4%, n=5; 32.2 ± 4.2%, n=5; respectively, P<0.05) with the late asynchronous component being especially sensitive **(Figure 53A, B)**. Concurrently, both current thresholds (72.5% decrease with DTX_K; or TsTX-K 22.8%; P<0.05) and 50% refractory time period were notably reduced, albeit the latter reached statistical significance only in DTX_K-treated samples (61.3 ± 7.1%, n=4 vs. 13.2 ± 3.1%) **(Figure 53C-E)**. Of note, blockade of $K_V1.2$ subunits with TsTX-K after the effect of DTX_K reached a plateau did not produce additional changes in the threshold or the peak amplitude of CAPs (n=4; P=0.11 and P=0.091, respectively). The quantitatively different effects of these blockers were unexpected given that the presence of one toxin-sensitive subunit renders the hetero-tetrameric channels susceptible to toxins (Akhtar et al., 2002, Hopkins, 1998), and suggests that enhanced K^+ conductance in demyelinated axons could be mediated largely through JXP tetrameric K_v1 channels possessing higher numbers of $K_v1.1$ than 1.2, or even an unusual homo-tetrameric form $K_v(1.1)_4$.

5.16. Conclusion

Thus, this chapter demonstrates evidences for dysregulation of JXP K_v1 channels. Preferential and ectopic emergence of $K_v1.1$ channels on the axons following CZ treatment is indicated by fluorescence microscopy studies. This has been further supported by the higher blocking effect obtained by DTX_K in CAP recordings. The fluorescence signal for K_v1 and Na_v channels obtained in the cells of unidentified origin following CZ feeding remains an interesting and intriguing observation, which might be of relevance in the progression of demyelination.

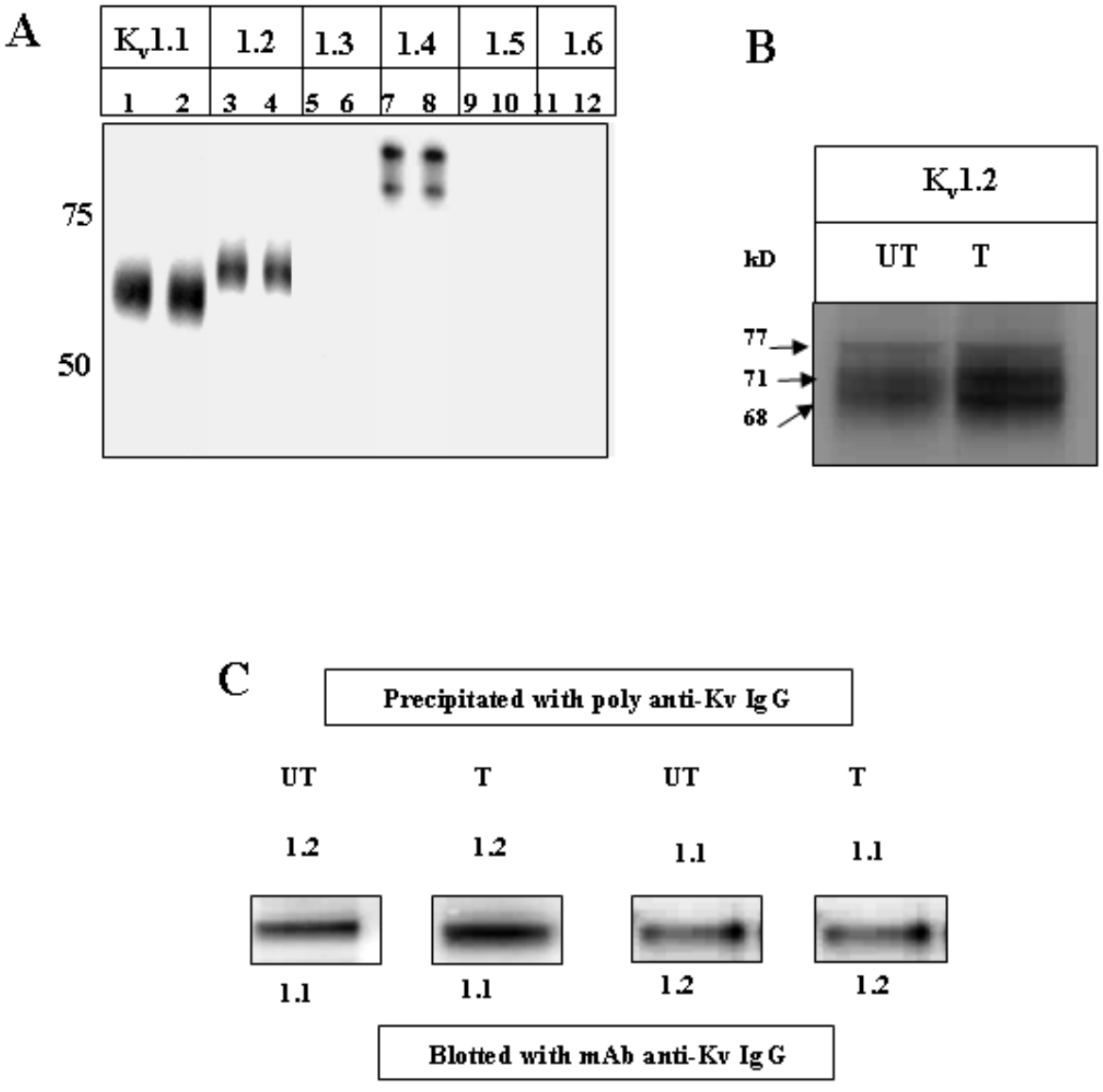
A
Kv1.1
1.2
1.3
1.4
1.5
1.6
1 2 3 4 5 6 7 8 9 10 11 12
75
50
B
Kv1.2
kD
UT
T
77
71
68
C
Precipitated with poly anti-Kv Ig G
UT
T
UT
T
1.2
1.2
1.1
1.1
1.1
1.1
1.2
1.2
Blotted with mAb anti-Kv Ig G

Figure 38: Expression of K_v1 α-subunits in ON.

***A**. Identification of K_v1 α-subunits in detergent-solubilised nerve membrane extract of ON, using Western blot analysis. Lanes: 1, 3, 5, 7, 9 and 11 untreated control; 2, 4, 6, 8, 10 and 12, CZ-treated samples. Mouse monoclonal IgGs for $K_v1.1$-1.6 were used for probing as indicated on top. Lane: 1, 2, $K_v1.1$; 3, 4, $K_V1.2$; 5, 6, $K_v1.3$; 7, 8, $K_V1.4$; 9, 10 $K_V1.5$ and 11, 12, $K_V1.6$. The positions of markers shown on the left side are marked as Mr ~ 50 and ~75. These indicate the presence of $K_V1.1$, 1.2 and 1.4 but absence of $K_V1.3$, 1.5 and 1.6 α-subunits in the ON of both groups (15µg membrane protein). **B**. The right hand panel shows resolution of $K_v1.2$ band into three bands corresponding to sizes ~68, 71 and 77kD, when freshly prepared, non-frozen ON protein, maintained with protease inhibitors at 4ºC was used. **C.** Co-IP of ON $K_v1.2$ α-subunit from detergent solubilized nerve homogenate (25µg of nerve protein); indicate its association with $K_v1.1$. They were precipitated using polyclonal IgG and probed with mAb antibody for each subunit. This was confirmed by reciprocal co-IP of both subunits. The polyclonal antibody is indicated on top and mAb at the bottom of each band in this panel.*

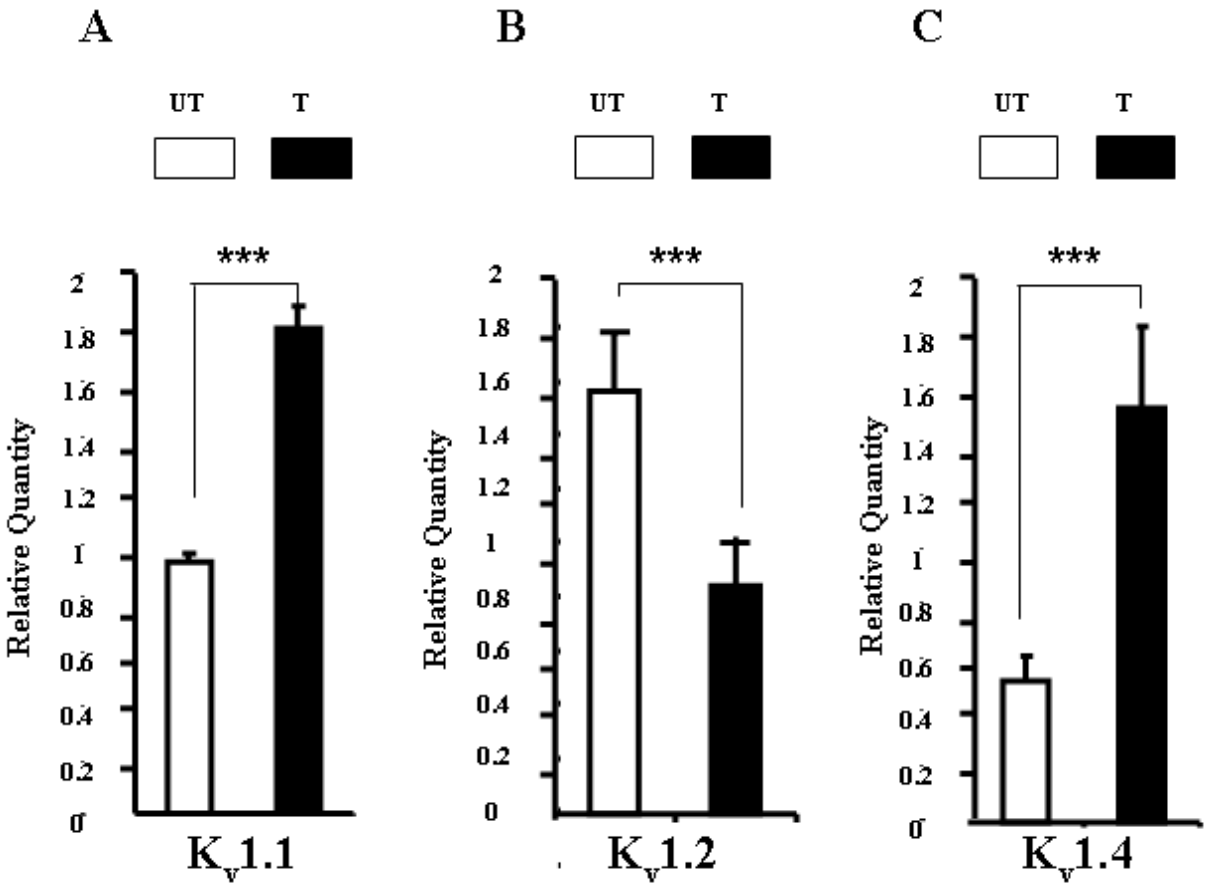
A
B
C
UT
T
***
Relative Quantity
2
1.8
1.6
1.4
1.2
1
0.8
0.6
0.4
0.2
0
$K_v1.1$
$K_v1.2$
$K_v1.4$

Figure 39: Dysregulation of K_v1 channels following CZ treatment.

ELISA based quantification of K_v1 channels show a significant increase in $K_v1.1$ ***(A)*** *and 1.4* ***(C)*** *(n=6, p>0.001 and>0.001), and a decrease in $K_v1.2$* ***(B)*** *(n=6, p>0.001). The signal has been quantified as RLU (Relative luminescence intensity) and the relative values of untreated control and treated sample against the known standard has been presented here as histogram, □ untreated, ■ treated.*

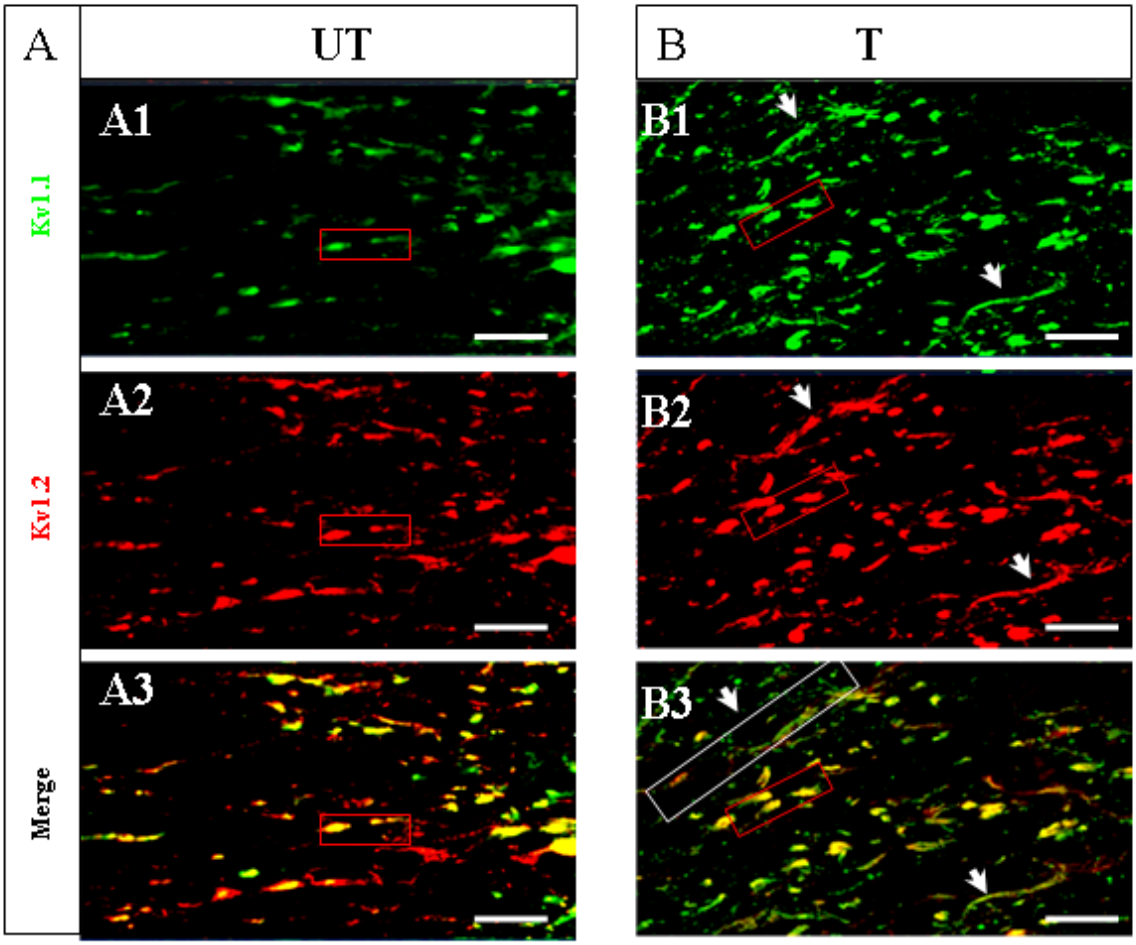

Elongated internodal expression of K_v1 channels in demyelinated axon

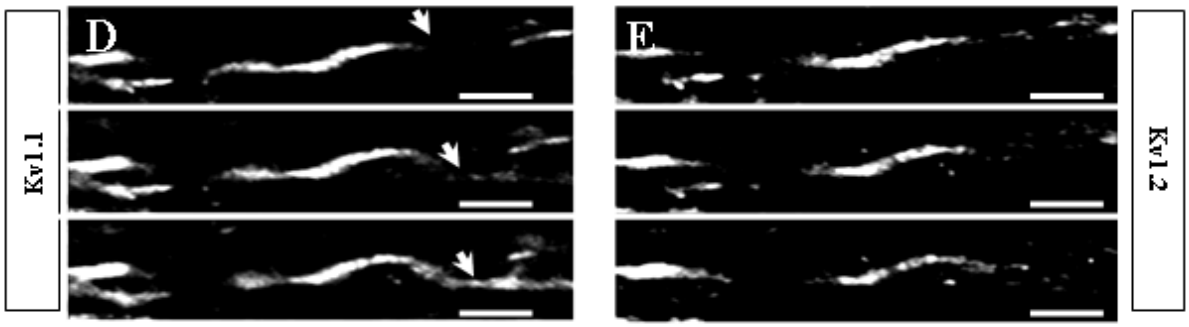

Figure 40: Altered expression of JXP K_v1 channels after CZ treatment.

***A**. Normally JXP K_v1 channels are expressed as paired punctate structure on the axon axis (red box). Both $K_v1.1$ (A1, green) and 1.2 (A2 red) normally co-localise (A3, yellow). The extents of red labelling appear to be more in untreated axons (A3). **B.** After CZ-treatment apart from normal appearing punctate JXP structure (red box), these channels gain internodal prominence (white box, white arrow). The levels of green labelling ($K_v1.1$) also seem to increase after treatment. **D**. A confocal Z-stack image represented in gray scale shows elongated internodal expression of $K_v1.1\alpha$-subunits after CZ treatment. **E**. Same axon shows the labelling for $K_v1.2$ α-subunit. Note a more extended internodal distribution of $K_v1.1$ (left) relative to $K_v1.2$ (right), indicating gain of axonal expression by this particular subunit. Scale bar 10µm, □ untreated, ■ treated.*

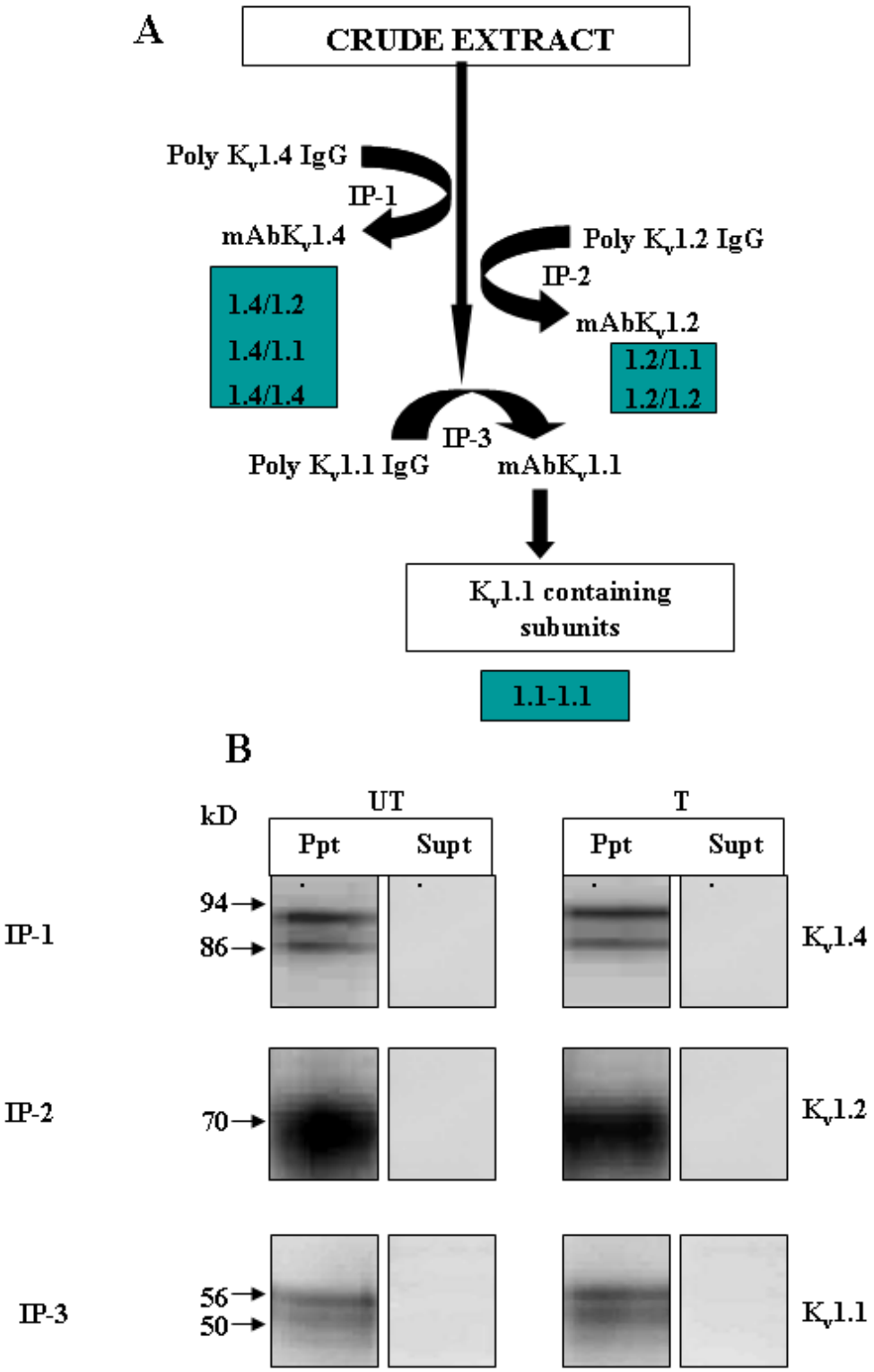
A
CRUDE EXTRACT
Poly Kv1.4 IgG
IP-1
mAbKv1.4
1.4/1.2
1.4/1.1
1.4/1.4
Poly Kv1.2 IgG
IP-2
mAbKv1.2
1.2/1.1
1.2/1.2
IP-3
Poly Kv1.1 IgG
mAbKv1.1
Kv1.1 containing subunits
1.1-1.1
B
kD
UT
T
Ppt
Supt
Ppt
Supt
94
86
IP-1
Kv1.4
70
IP-2
Kv1.2
56
50
IP-3
Kv1.1

Figure 41: $K_v1.1$ homo-oligomers identified in ON homogenate of both groups.

A. *Generalized scheme of multi-stage immunoprecipitation of $K_v1.1$ homo-oligomer in a detergent solubilized crude extract of ON. IP-1, IP-2 and IP-3 indicate the three immunoprecipitation steps involved. The blue boxes show the elimination of all possible combination of $K_v1.x$ oligomers at that particular step.* ***B.*** *An aliquot (45µg protein suspended in 750µl) of solubilized extract was precipitated with different polyclonal anti $K_v1.x$ antibodies (5µg/ml) in the sequence illustrated* ***(A)****. The resultant pellets (ppt) from each step (IP-1, IP-2 and IP-3) were subjected to SDS-PAGE and blotted with the anti-$K_v1.x$ (mAb) as indicated in A. The supernatant (supt) obtained at each step was also subjected to the same probing step in order to ensure that the supernatant is devoid of any associated oligomer (indicated as blue box in A) in that particular step. The marker position is indicated on the left of each panel. UT and T indicate the untreated and treated ON samples used for these experiments.*

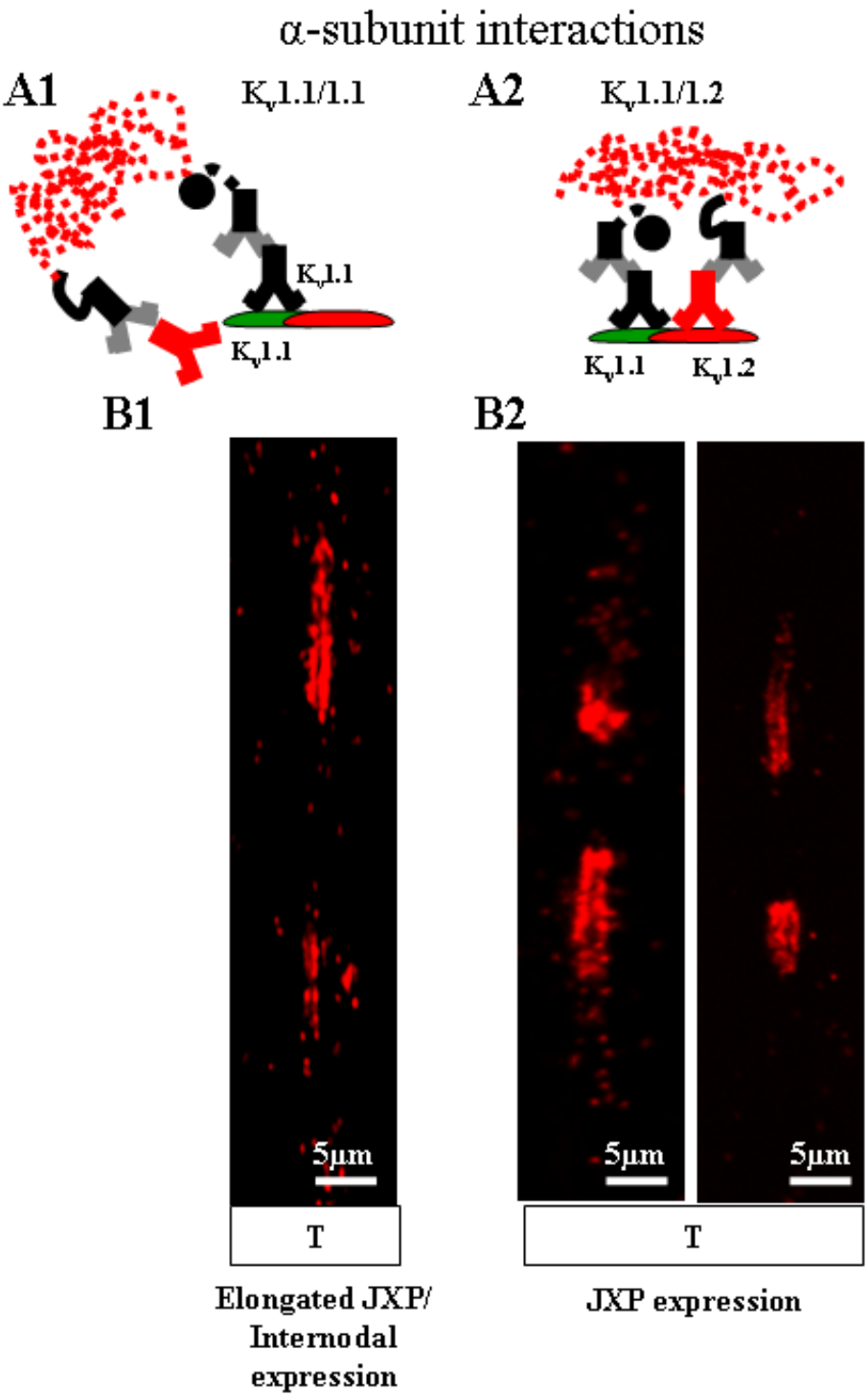
α-subunit interactions
A1
K_v1.1/1.1
K_v1.1
K_v1.1
A2
K_v1.1/1.2
K_v1.1
K_v1.2
B1
B2
5µm
5µm
5µm
T
T
Elongated JXP/ Internodal expression
JXP expression

Figure 42: Demonstration of in situ interaction of K_v1.1-1.2 α-subunits in JXPs after CZ treatment unveils their disparate patterns.

A. *Schematic diagram to show the use of two antibodies directed against different epitopes of the same K_v1.1* ***(A1)*** *of different proteins like K_v1.1 and 1.2* ***(A2)*** *in generation of PLA fluorescent signals. The black and red antibodies are directed against two different epitopes. Grey symbolizes the secondary antibody and the red flocculent structure is amplified signal after ligation of the PLA probes.* ***B.*** *First panel shows the elongated JXP feature of an axon following CZ treatment and prevalence of K_v1.1 in such axons. Next panel* ***(B2)*** *demonstrates two different shapes of JXP after CZ treatment. Note the aggregated K_v1.1/1.2 cluster near the nodal gap, whereas channels lacking K_v1.2a-subunit in them tend to extend much longer into the internode, Scale bar 5µm.*

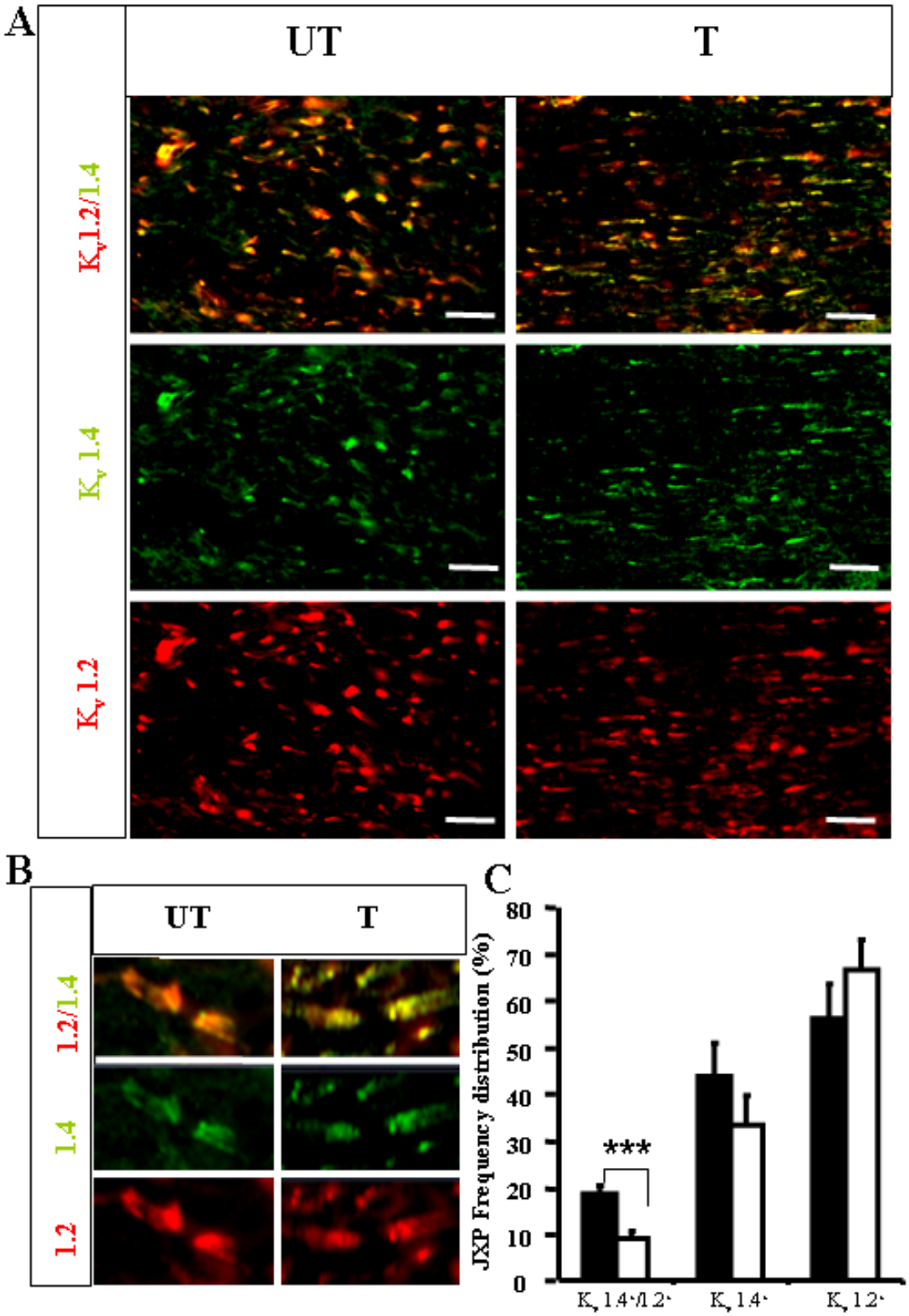
A
UT
T
Kv1.2/1.4
Kv 1.4
Kv 1.2
B
UT
T
1.2/1.4
1.4
1.2
C
JXP Frequency distribution (%)
80
70
60
50
40
30
20
10
0
***
Kv 1.4+1.2+
Kv 1.4+
Kv 1.2+

Figure 43: JXPs expressing $K_v1.4$ is not as prominent as $K_v1.2$.

A. *Broad view of $K_v1.2$ (red)/1.4(green) labeled axons from control group (left panel). There is an evident reduction in $K_v1.2/1.4$ co-labeled JXPs after CZ treatment (right panel), Scale bar 10µm.* ***B.*** *A $K_v1.2^{+ve}$ JXP overlaps with $K_v1.4^{+ve}$ signals in control. This is shown as an inset (bottom left) using co-labeling for both a-subunits in untreated and treated samples.* ***C.*** *Histogram representing different levels of overlap in the JXPs of both groups. $K_v1.2/1.4$ overlap decreases following CZ treatment ($p>0.001$, $n=1161, 892$), □ untreated, ■ treated.*

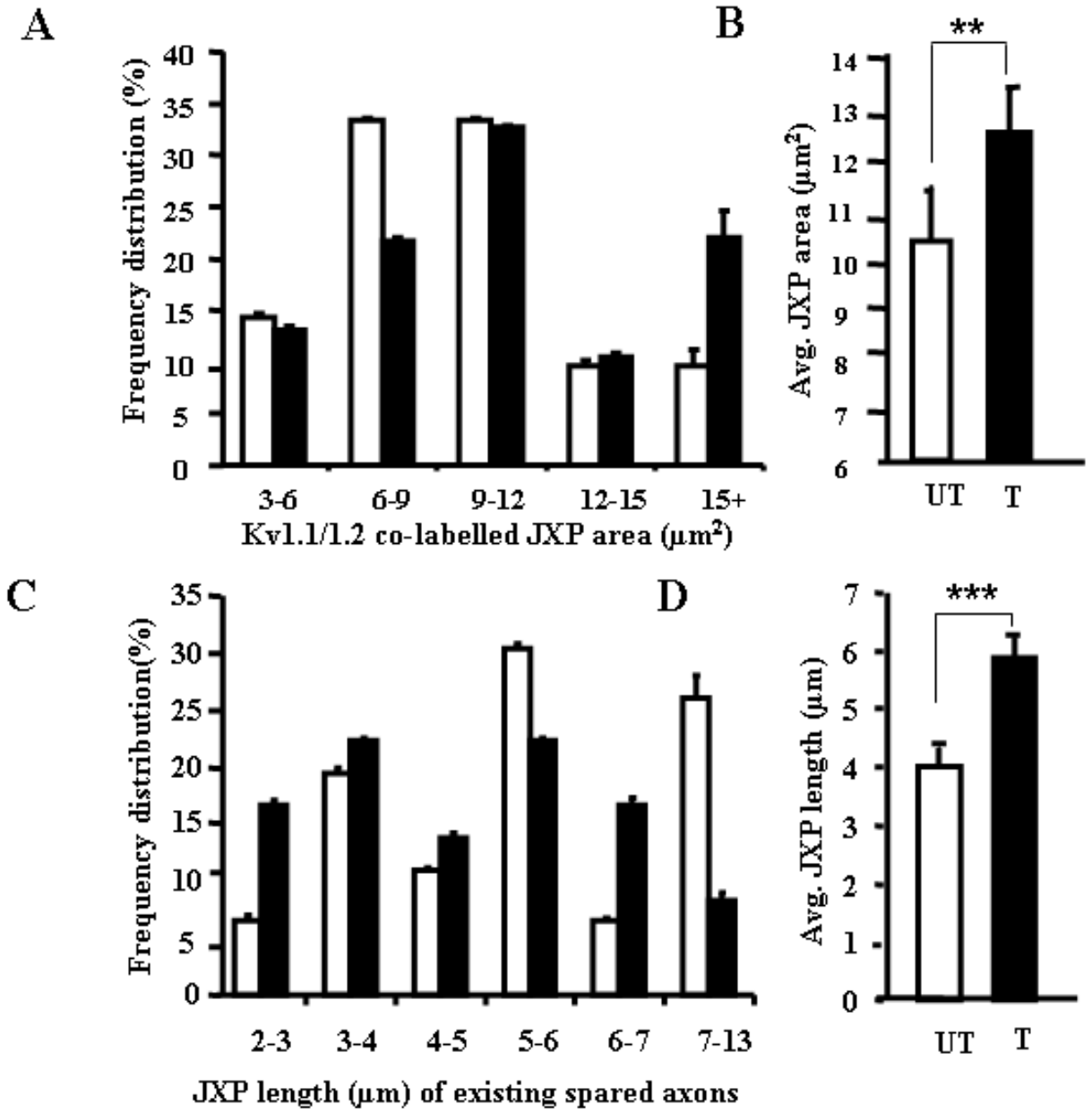
A
B
C
D
Frequency distribution (%)
Kv1.1/1.2 co-labelled JXP area (µm²)
3-6
6-9
9-12
12-15
15+
Avg. JXP area (µm²)
**
UT
T
Frequency distribution(%)
JXP length (µm) of existing spared axons
2-3
3-4
4-5
5-6
6-7
7-13
Avg. JXP length (µm)
***

Figure 44: CZ treatment induces variation in JXP length and area

A. *Frequency distribution of area occupied by K_v1.1/1.2 co-labeled JXPs.* ***B***. *Average JXP area of treated group increases relative to control (p>0.001, n=46, 42).* ***C***. *Frequency distribution of JXP length of surviving axons.* ***D***. *Increase in average JXP length is eminent following CZ treatment, (p>0.001, n=46, 42),* □ *untreated,* ■ *treated.*

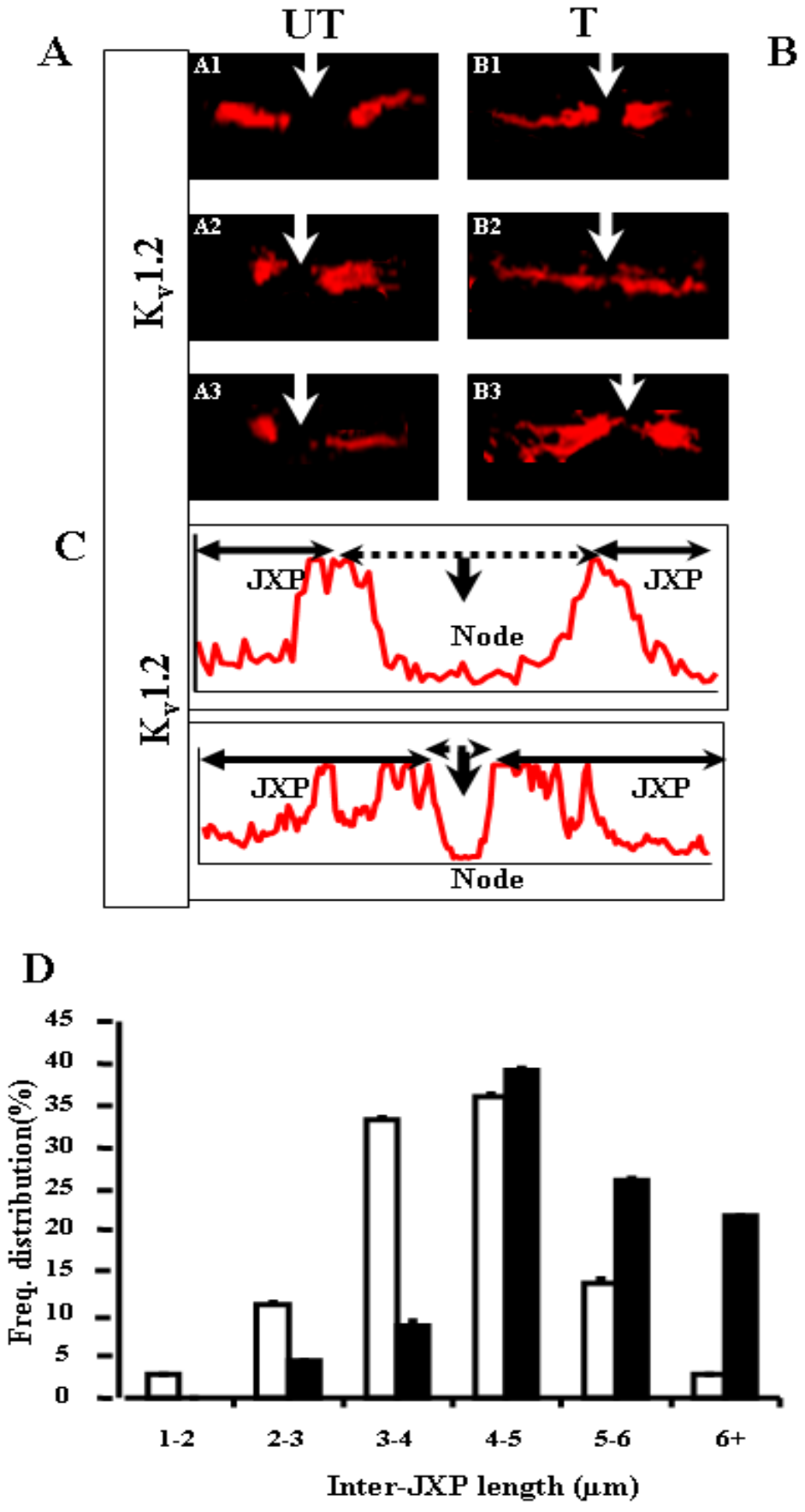
A
UT
T
B
A1
B1
A2
B2
A3
B3
$K_v1.2$
C
JXP
Node
JXP
$K_v1.2$
JXP
Node
JXP
D
Freq. distribution(%)
45
40
35
30
25
20
15
10
5
0
1-2
2-3
3-4
4-5
5-6
6+
Inter-JXP length (µm)

Figure 45: Inter-JXP length increases in the treated group.

A. *Representative images of $K_v1.2$ labeled (red) JXPs from control group showing different shapes (A1-A3).* ***B.*** *Similar images of $K_v1.2$ labeled (red) JXPs from treated group show the deviation from normal pattern. Note the disparity of two apposing JXP (B1), fusion of such JXPs along the nodal gap (B2) and emergence of extended JXP protruding towards the node. The white arrows indicate the position of node in between the two adjoining JXPs. (Scale bar 5µm).* ***C.*** *Intensity profiles have been shown in the bottom panel to highlight such digression.* ***D****. Representative frequency distribution showing the difference between both samples. There is an increase in inter-JXP length after CZ treatment, (n = 120, 109),* □ *untreated,* ■ *treated.*

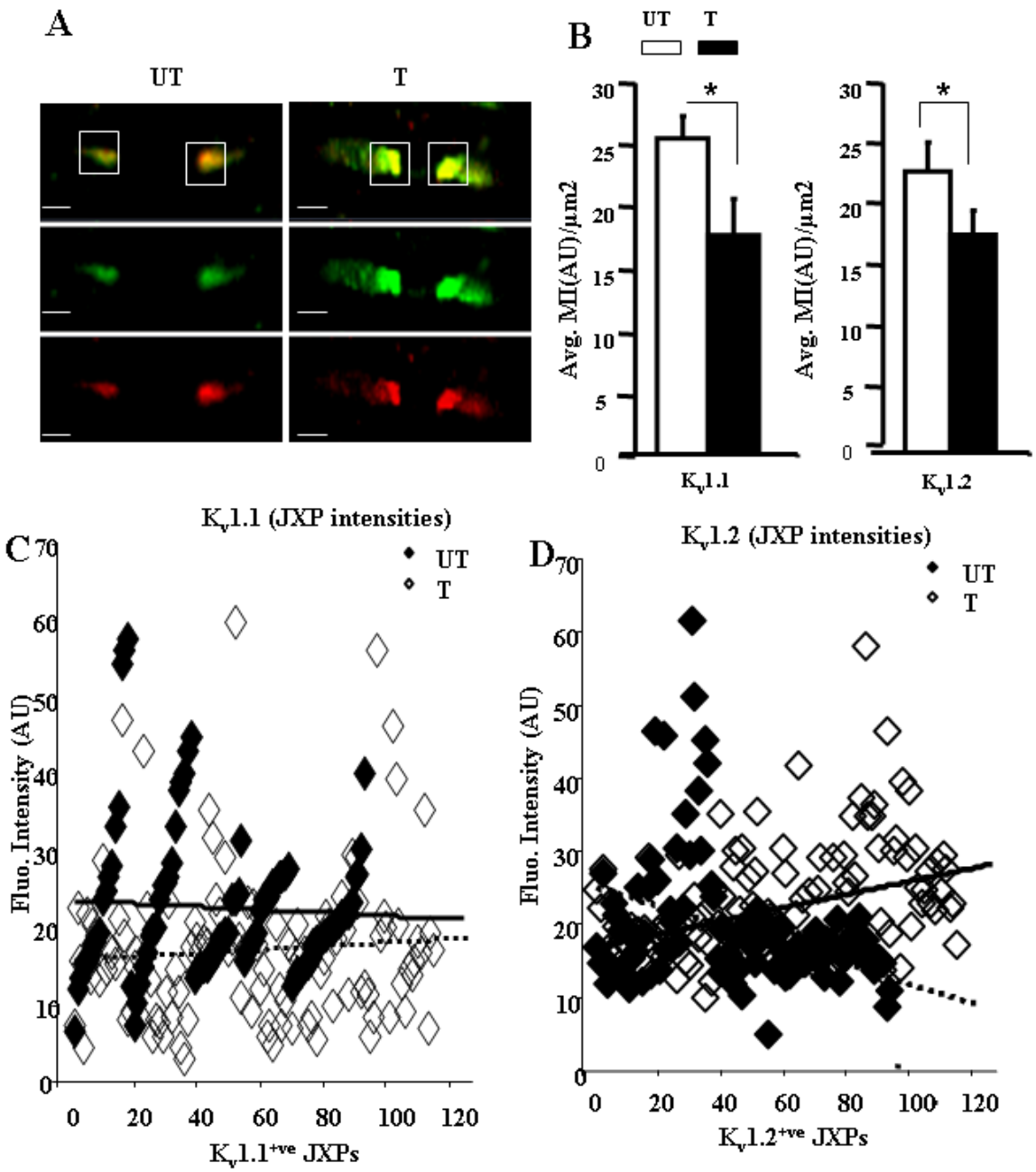
A
UT
T
B
UT
T
Avg. MI(AU)/µm2
*
K_v1.1
K_v1.2
C
K_v1.1 (JXP intensities)
UT
T
Fluo. Intensity (AU)
K_v1.1^{+ve} JXPs
D
K_v1.2 (JXP intensities)
UT
T
Fluo. Intensity (AU)
K_v1.2^{+ve} JXPs

Figure 46: Differential expression intensities of K_v1.1 and 1.2 in the surviving JXPs exhibit discordant effect induced on these α-subunits by CZ.

A. *Intact JXPs of untreated control and treated ON axons exhibit differential intensity of K_v1.1 (green) and 1.2(red) labelling proximal to the node. K_v1.1 tends to spread out into the internode after CZ treatment relative to the control group. Scale bar 5µm.* ***B.*** *Both of these a-subunits represent decreased levels of mean intensity (arbitrary units) (MI)/µm2 on these types of JXPs.(p=0.02 for K_v1.1, p=0.07 for K_v1.2, n=99, 123)* ***C.*** *Representative scatter plot shows the ascending intensity pattern of $K_v1.1^{+ve}$ JXP in control relative to the treated nerve (n=99, 123).* ***D.*** *Representative scatter plot showing the descending intensity pattern of $K_v1.2^{+ve}$ in JXPs of treated nerve (n=99, 123). The block and empty squares on these plots represent treated and untreated JXPs. Dashed and solid lines represent the untreated and treated trend-lines, □ untreated, ■ treated. Scale bar5µm.*

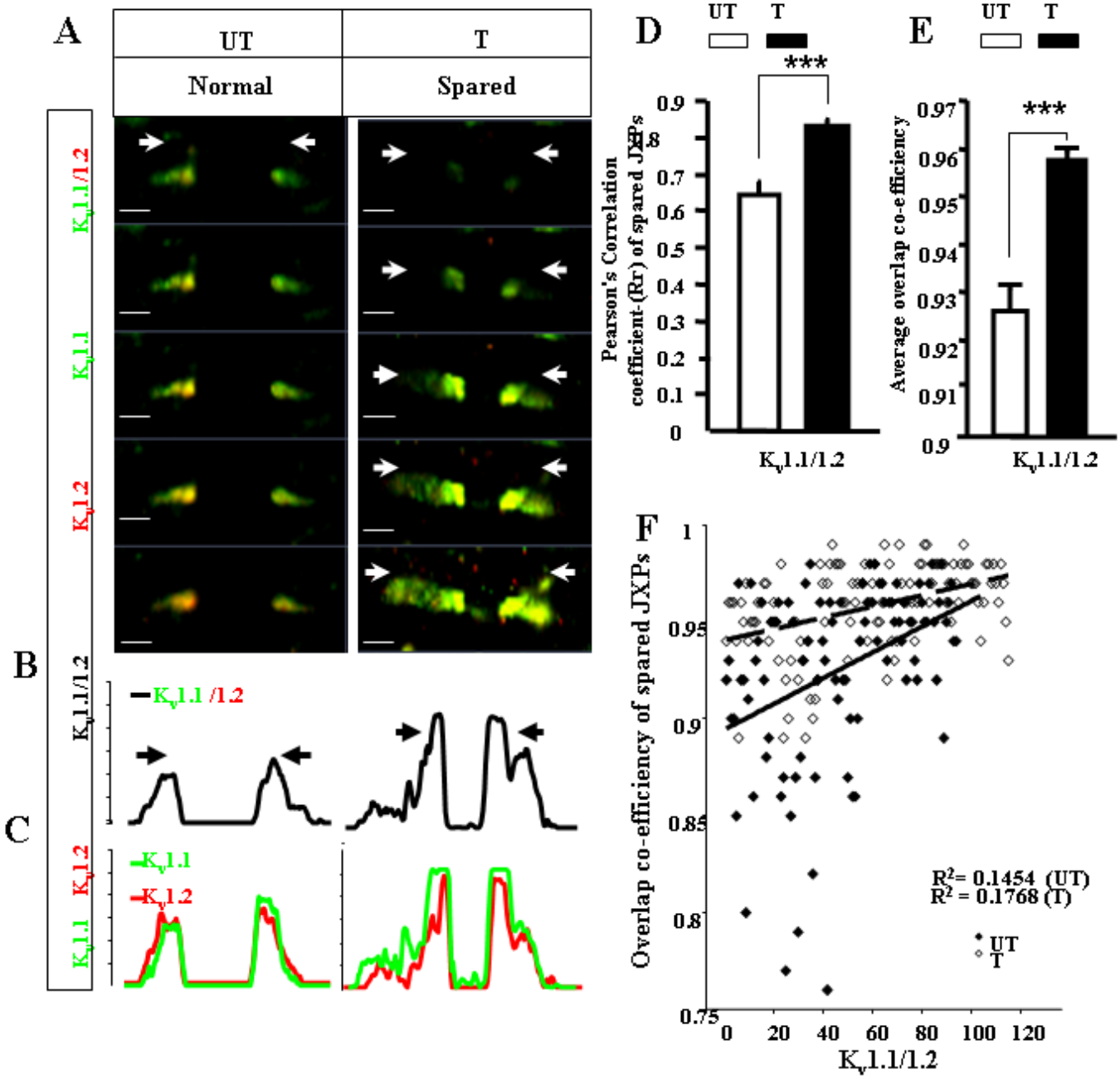
A
UT
T
Normal
Spared
Kv1.1/1.2
Kv1.1
Kv1.2
B
C
Kv1.1 /1.2
Kv1.1
Kv1.2
D
UT
T
***
Pearson's Correlation coefficient-(Rr) of spared JXPs
0.9
0.8
0.7
0.6
0.5
0.4
0.3
0.2
0.1
0
Kv1.1/1.2
E
UT
T
***
Average overlap co-efficiency
0.97
0.96
0.95
0.94
0.93
0.92
0.91
0.9
Kv1.1/1.2
F
Overlap co-efficiency of spared JXPs
1
0.95
0.9
0.85
0.8
0.75
0
20
40
60
80
100
120
Kv1.1/1.2
R2= 0.1454 (UT)
R2 = 0.1768 (T)
UT
T

Figure 47: Co- localization efficiency of K_v1.1/1.2 is high in the intact JXPs.

A. *Z-stack representation of K_v1.1 and 1.2 co-labeled JXP of control and experimental group axons, showing intense labeling close to the nodal gap, but it extends into the internode to a greater extent indicating that these channels occupy larger area after CZ treatment. White arrows point towards the nodal end. Scale bar 2µm.* ***B.*** *Co-label intensity profiles of these axons show the higher levels of these channels proximal to the nodal gap in treated condition (black top panel).* ***C****. The bottom profile shows segregated levels of K_v1.1 (green) and 1.2 (red) which contribute to the overlapped signal intensity. Note the intensity is higher proximal to the node and is more extended in the treated group(right) relative to the controls (left)* ***D.*** *Pearson's co-relation co-efficient (Rr) of surviving JXPs represented as an average indicate an increase of signal in these surviving JXPs following CZ treatment ($p>0.001$, $n=92, 96$).* ***E.*** *Similarly there is an average increase in overlap co-efficiency of K_v1.1/1.2 signals following CZ treatment ($p>0.001$, $n=93, 115$).* ***F.*** *Scatter plot of overlap co-efficiency indicate a higher co-relation in the treated samples. Dashed and solid lines represent the treated and untreated trend-lines, □ untreated, ■ treated.*

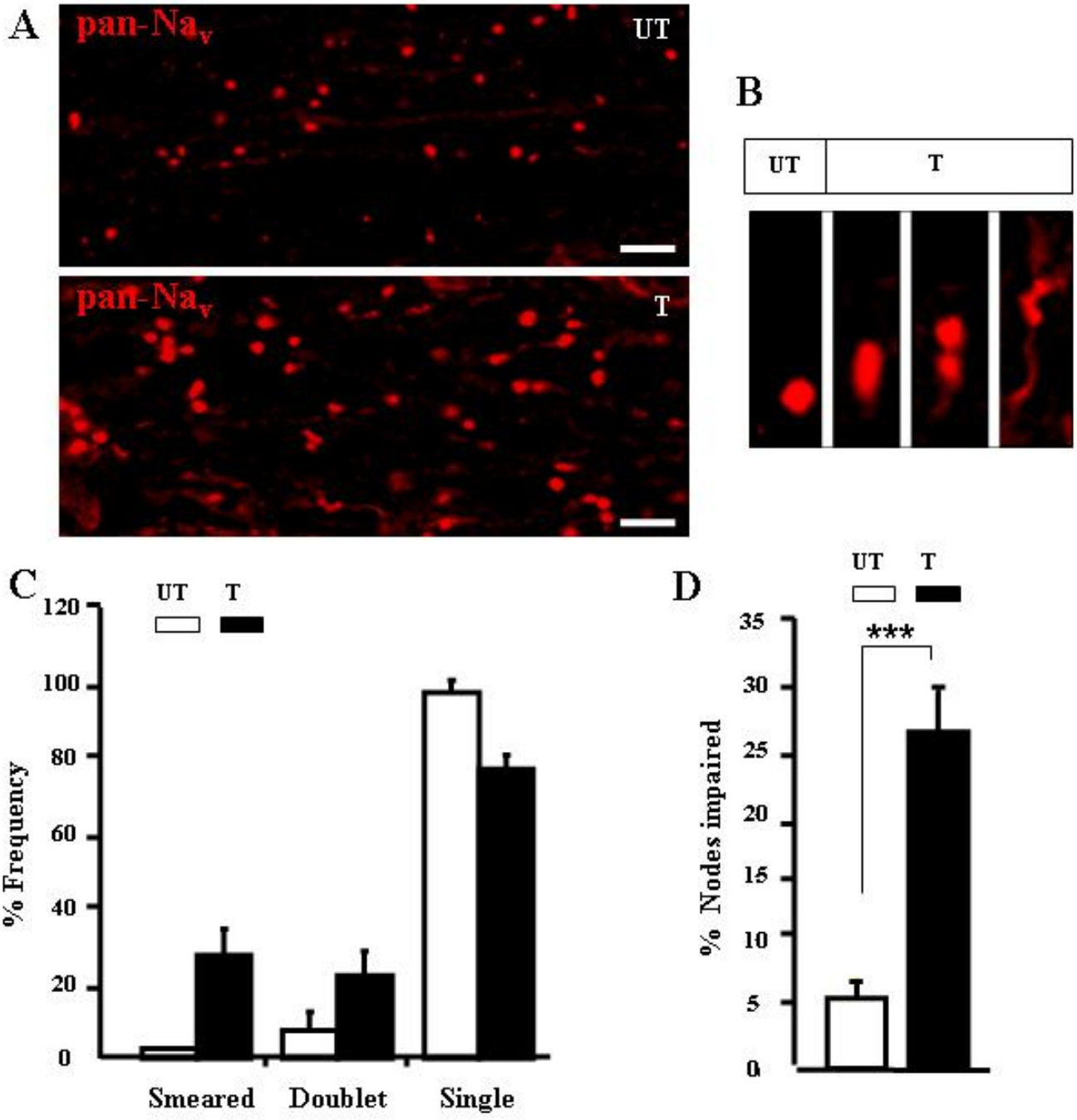
A
pan-Na$_v$
UT
pan-Na$_v$
T
B
UT
T
C
UT
T
120
100
80
60
40
20
0
% Frequency
Smeared
Doublet
Single
D
UT
T
***
35
30
25
20
15
10
5
0
% Nodes impaired

Figure 48: Na_v channels are dislocated from the node in treated group.

A. *pan Na_v labeled nodes of the experimental group (bottom panel) show a deviation from the normal compact and intense labeling in untreated control (top panel) sample (scale bar 2µm).* ***B.*** *Collectively, on the basis of morphology the nodes were grouped to represent three eminent patterns, smeared or oblong (B3), doublet (B3), and elongated (B4) in the treated group, whereas the untreated group has an intact delimited node (B1).* ***C.*** *These impaired nodes were accounted herein and it exhibits an increase in treated group of axons (n = 712, 635).* ***D****. Smearing is the most common effect and it is represented as a significant increase following CZ treatment, (p > 0.001, n = 712, 635), □ untreated, ■ treated.*

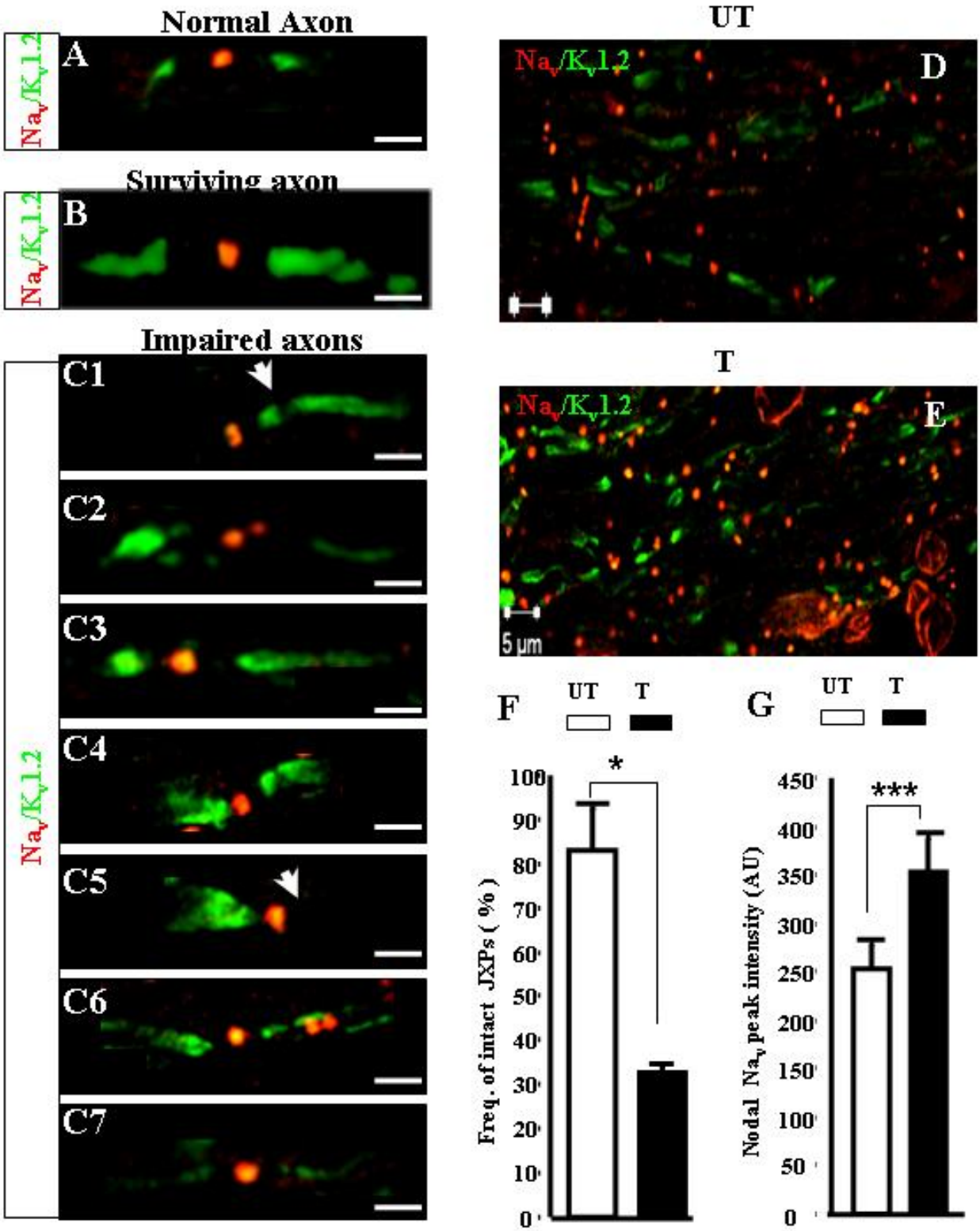
Normal Axon
A
Nav/Kv1.2
Surviving axon
B
Impaired axons
C1
C2
C3
C4
C5
C6
C7
UT
D
T
E
5 µm
F
UT
T
Freq. of intact JXPs (%)
100
90
80
70
60
50
40
30
20
10
0
*
G
Nodal Nav peak intensity (AU)
450
400
350
300
250
200
150
100
50
0
***

Figure 49: Surviving JXPs show unique labelling of nodal Na_v and $K_v1.2$.

A. *The intact JXPs from control group show uniform labeling of $K_v1.2$ (green) adjoining the nodes (pan-Na_v, red) which are equidistantly placed.* ***B.*** *The non-affected axons show a similar pattern in the treated groups as well.* ***C.*** *The impaired axons exhibit an array of pattern (C1-C7). They might appear heminodal (C1, C5), display disparate JXPs adjacent to the node (C3, C6), appear fragmented JXP (C4, C6) or be elongated (C7) following CZ treatment.* ***D.*** *Broad view of such untreated ON labeled with Na_v/$K_v1.2$.* ***E.*** *Broad view of treated ON showing Na_v/$K_v1.2$ labeling.* ***F.*** *Such intact JXP show a decrease in frequency of occurrence ($p=0.02$, $n= 157, 102$).* ***G.*** *Overall there is an increase in the peak intensity of Na_v labeling in the axons of treated samples, ($p>0.001$, $n=40, 46$), □ untreated, ■ treated.*

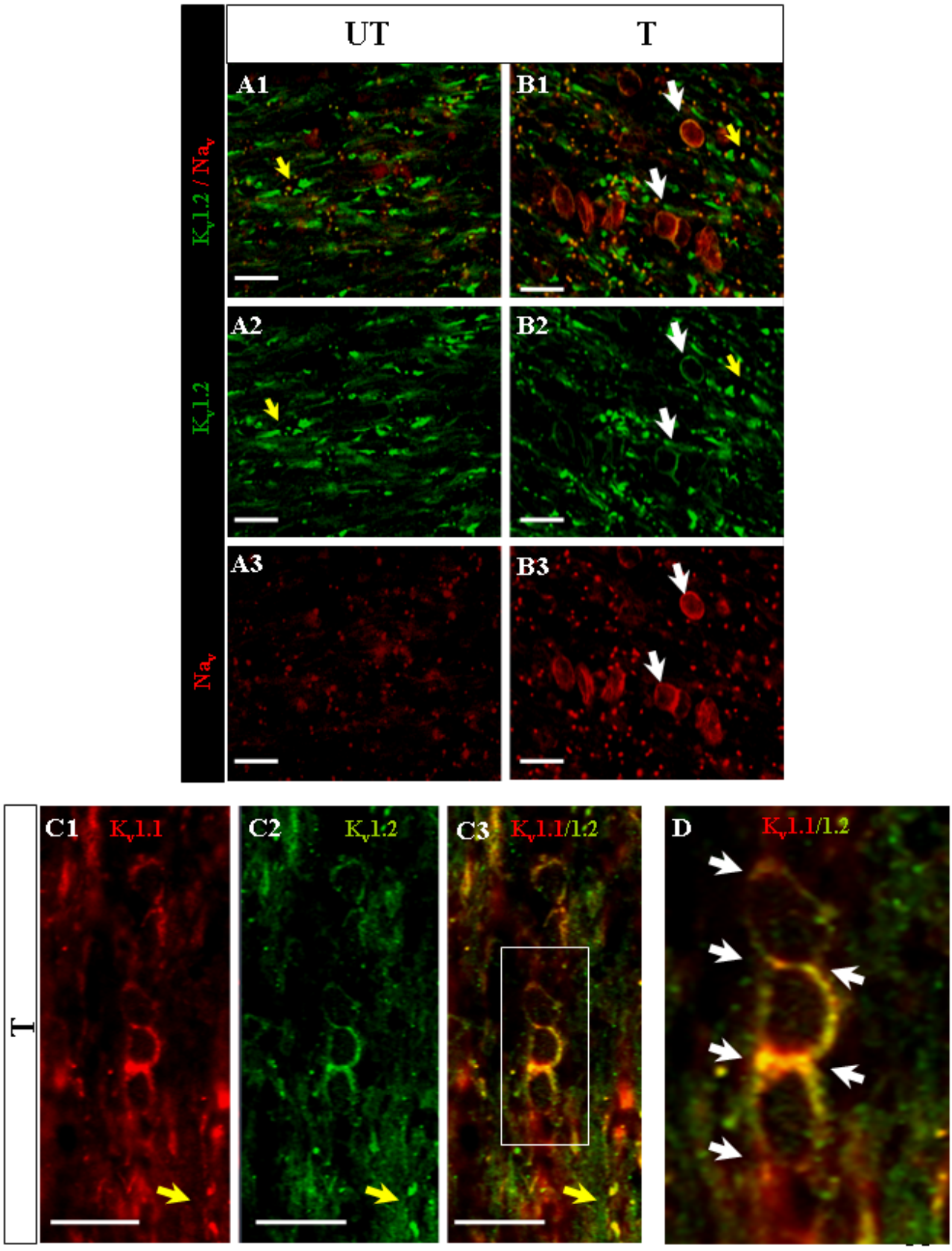
UT
T
A1
B1
A2
B2
A3
B3
$K_v1.2$ / Na_v
$K_v1.2$
Na_v
T
C1 $K_v1.1$
C2 $K_v1.2$
C3 $K_v1.1/1.2$
D $K_v1.1/1.2$

Figure 50: Ion channel expression in cells after CZ treatment.

A. *Broad view of $K_v1.2$ (green, A2) and Na_v (red, A3) colabeled axons from untreated control.* ***B.*** *Broad view of $K_v1.2$ (green, B2) and Na_v (red, B3) colabeled axons from treated group.* ***C.*** *The treated group nerve cells expressing $K_v1.2$ also co-localize with $K_v1.1$ (white box) in addition to their usual JXP location (yellow arrow).* ***F.*** *The boxed cells in C have been expanded to show all these three cells which have co-localised $K_v1.1$ and 1.2. White arrows point the junction of these cells, which are distinct from typical JXP of an axon, Scale bar10µm.*

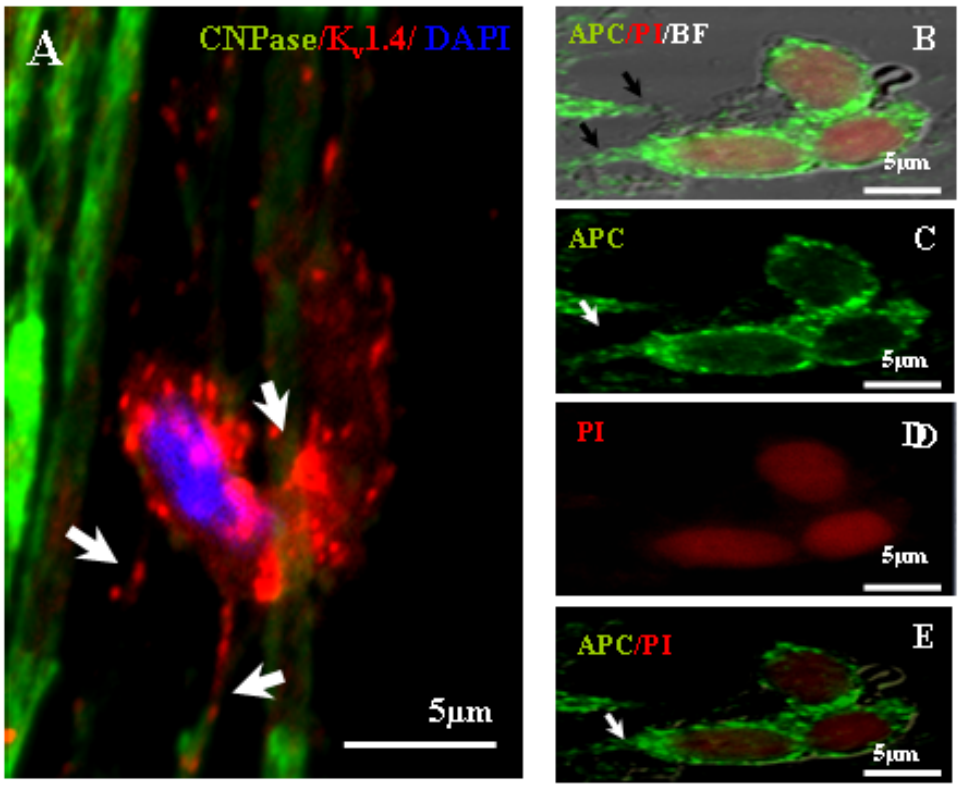
A
CNPase/Kv1.4/ DAPI
5µm
APC/PI/BF
B
5µm
APC
C
5µm
PI
D
5µm
APC/PI
E
5µm

Figure 51: K_v1.4 is expressed in APC positive cells.

A. *Cell bodies enwrapping CNPase positive axons (green) express K_v1.4 (red) indicating glial origin of K_v1.4 channels in ON. The white arrows point to the processes of these cell bodies which is CNPase positive. Panel on the right represents that the axon intercalating cells are APC positive oligodendrocyte.* ***B.*** *Merged image showing a APC positive cell (green) with prominent nuclear localisation (red) of propidium iodide (PI) and its processes in gray (bright field, BF). Black arrows point towards the processes of oligodendrocytes.* ***C.*** *APC positive cell (white arrow points to the emerging process of this cell).* ***D.*** *Corresponding nuclei of those cells confirmed using nuclear PI stain.* ***E****. APC and PI stains overlap, this indicates the cellular origin of APC signals. Scale bar 5µm.*

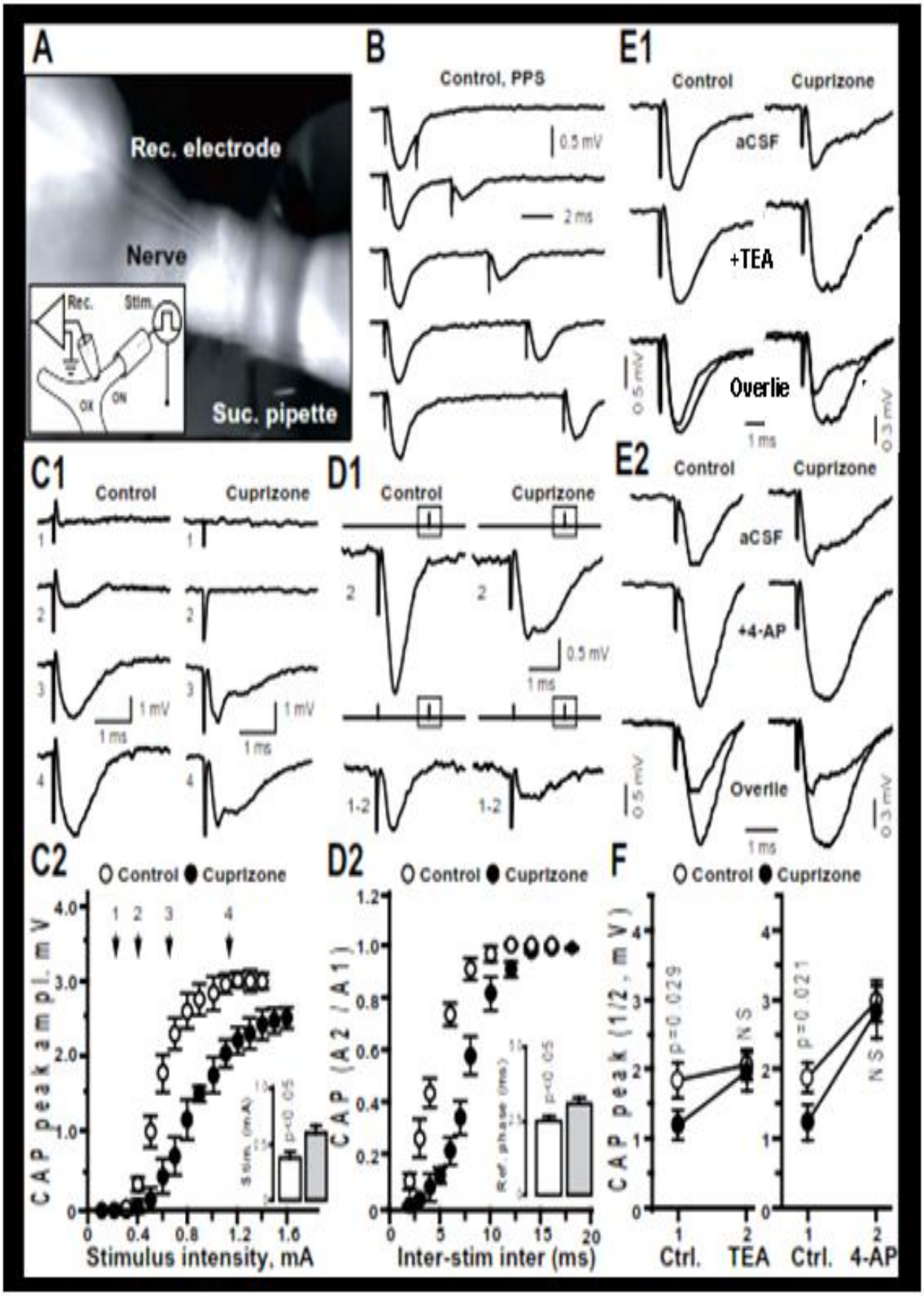
A
Rec. electrode
Nerve
Rec.
Stim.
OX
ON
Suc. pipette
B
Control, PPS
0.5 mV
2 ms
E1
Control
Cuprizone
aCSF
+TEA
Overlie
0.5 mV
1 ms
0.3 mV
C1
Control
Cuprizone
1 mV
1 ms
D1
Control
Cuprizone
0.5 mV
1 ms
E2
Control
Cuprizone
aCSF
+4-AP
Overlie
0.5 mV
1 ms
0.3 mV
C2
Control
Cuprizone
CAP peak ampl. mV
Stimulus intensity, mA
D2
Control
Cuprizone
CAP (A2 / A1)
Inter-stim inter (ms)
F
Control
Cuprizone
CAP peak (1/2, mV)
p=0.029
NS
p=0.021
NS
Ctrl.
TEA
Ctrl.
4-AP

Figure 52: Demyelination lowers the excitability and disrupts conductive synchronicity of ON axons.

A. *Low magnification view of ON showing attached stimulation and recording electrodes. Inset illustrates the experimental set-up for CAPs recordings. Rec. - recording electrode; Suc. - suction pipette used for stimulation; OX – optic chiasm.* ***B.*** *Typical CAPs evoked in control ON by paired-pulse stimulation (PPS) at varying inter-pulse intervals. Note the time dependent recovery of the second CAP from the refractory phase following the first CAP.* ***C.*** *Graded synchronous CAPs recorded from control animals (C1, left) contrasting with bi-component CAPs derived from experimental ON (C1, right) activated from higher stimulus threshold (1-4). (C2) Stimulus-response relation of CAPs in controls and experimental ON showing higher activation threshold and lower amplitude of evoked CAPs in demyelinated ON. Inset illustrates the differences in the stimulus threshold for eliciting CAPs: controls (white bar, n=6) and experimental (grey bar, n=5).* ***D1****. Representative sub-maximal single pulse (in-boxed) induced CAP (top, 2) and CAP pre-conditioned by a stimulus (bottom, 1-2) from control and experimental ON; inter-pulse interval - 3 ms (above schematics illustrate stimulation paradigms).* ***D2****. A summary plot of the relation of inter-stimulus interval with refractory phase (50% recovery); inset is a summary histogram of ½ of refractory time of sub-maximal CAPs (A2-A1). Note faster recovery of the second response from the refractory phase in controls than that in demyelinated axons (white bar vs. grey bar). (E1 and E2) Representative recordings of the effect of TEA and 4-AP on CAPs: control (left) and demyelinated (right) ON. Note the enhancement of the CAP amplitude in demyelinated ON caused by TEA and 4-AP that is also reflected in summary plots (F). NS – not significant, □ untreated, ■ treated.*

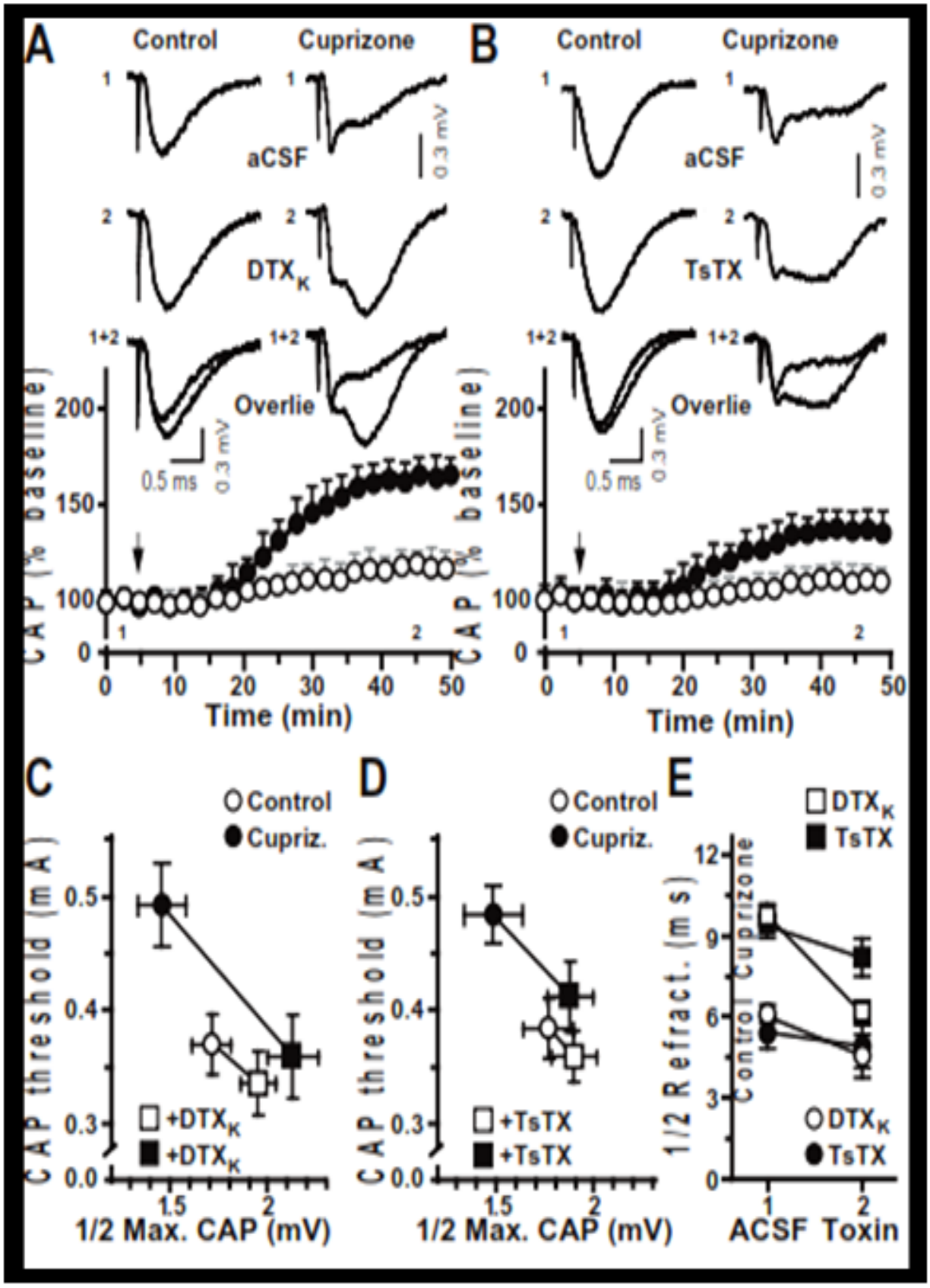

Dr. Saak. Ovsepian

Figure 53: K_v1.1 and 1.2 subunits exhibit differential role in K+ channels for regulating excitation and conduction in demyelinated ON.

Representative CAP recordings (A, B upper) demonstrating the effects of DTX_K and TsTX-K in control (A) and demyelinated (B) ON: before (1) and 40 min after presentation of the toxins to the nerves. (A, B lower) Time course of the effects of DTX_K and TsTX-K on evoked CAPs (sub-maximal) of control (white circles, n=5; n=6) and experimental (black circles, n=5; n=5) ON. Arrows point to the start of the application of toxins. Note a slight increase of the CAPs by these toxin blockers in controls (A, B lower, white circles) compared to much stronger enhancement of CAPs in demyelinated ON by TsTX-K (B) and especially DTX_K (A). (C, D and E) Summary plots demonstrating the effects of DTX_K and TsTX-K on the relation of the threshold stimulus and CAP amplitude (sub-maximal) (C and D, respectively) and 50% CAP recovery from refractory phase (E). Note the more potent effects of DTX_K on CAP stimulus threshold, amplitude and recovery from refractory phase (E).

CHAPTER 6

DISCUSSION AND FUTURE WORK

Demyelination can be induced for several reasons, but studying MS-associated chronic CNS demeylination (Compston and Coles, 2002) has remained a major challenge for the development of therapeutics. Most of the basic information available in this field has entailed studies based on PNS nerve with acute demeylination (Brismar and Schwarz, 1985), hypomyelination (Wang et al., 1995, Rasband et al., 1999b, Westenbroek et al., 1992, Peretz et al., 2000) or transgenic animal models (Smart et al., 1998, Chiu et al., 1999, Ogawa et al., 2010). 4-AP, a broad-spectrum K_v channel blocker produces beneficial effects in MS, but with epileptogenic side-effects. Altered expression and of these channels in spinal cord axon injury (Nashmi and Fehlings, 2001), are less responsive to the benefits of this type of drug (Smith et al., 2000, Judge and Bever, 2006). Whereas ON, a CNS tissue of clinical interest remains susceptible to 4-AP benefits (Kocsis et al., 1986, Foster et al., 1982). This indicates an apparent dissimilarity in axon K_v1 channels present in different types of systems. *In vitro* studies show that this kind of differential sensitivity to pharmacology could be rendered due to variation in α-subunit composition of tetrameric K_v1 channels in JXPs (Akhtar et al., 2002, Al-Sabi et al., 2011, Al-Sabi et al., 2010) . This thesis here presents data pertaining K_v1 associated features in CZ-induced sub-chronic demyelinating ON which provides a better insight into the structure and function of CNS axons.

6.1. Development of animal model for studying MS like demyelination

MS is a demyelinating disease which involves factors triggering cascade of events. This results in engagement of the immune system, acute injury of axons and glia, recovery of function and structural repair, post-inflammatory gliosis, and neuro-degeneration. The sequential involvement of these processes underlies the clinical course characterized by episodes with recovery, persistent deficits, and secondary progression. It is almost impossible to replicate such diversified complicating disease features in an animal model

(Hartmut and Kurschus, 2006, Schmandt et al., 2006, Ransohoff, 2012). Herein use of 8 week CZ- induced demyelination model, which can be considered as a time point at the confluence of acute (Crawford et al., 2009, Kipp et al., 2009) and chronic demyelination (Ludwin, 1980, Matsushima and Morell, 2001, Hoffmann et al., 2008) has provided us with a preliminary view of several phenomenon of neurotherapeutic relevance involving axon and glia. The observations presented here may not be a direct co-relate for RRPMS (a clinical complicating factor), even though elements for remyelination cannot be ruled out for the said time point in this study. An inclusion of extended and detailed time course would further elaborate these facts and establish the importance. Specific seizure induction upon anesthetization was indicative of features associated to demyelination, which was of extraneous interest here. Investigation of this response in view of changes induced in hippocampus might prove advantageous. Even though it is widely accepted that MS is a complex neurodegenerative disease and thought to arise through autoimmunity against antigens of the CNS. Interestingly, this hypothesis fails to explain why genetic and environmental risk factors linked to the disease in one population tend to be unimportant in others. Several such pertinent questions are indicative of the fact that despite great advances in documenting the cellular and molecular mechanisms underlying MS pathophysiology, the autoimmunity framework has been unable to develop a comprehensive explanation of the etiology of the disease. Last decade has witnessed several new frameworks for understanding MS (Fischer et al., 2013, Lassmann et al., 2007, Nair et al., 2008, Trapp and Stys, 2009, Corthals, 2011) as a dysfunction of the homeostasis of lipids which collapses during acute-phase inflammatory response and triggers, trauma, or stress, starting a feedback loop of increased oxidative stress (Dutta et al., 2006, Waxman, 2006, Mahad et al., 2008). Inflammatory response, and proliferation of cyto-toxic cells that cross the blood brain barrier and both catabolize myelin and prevent remyelination (Huterer et al., 1995, Corthals, 2011) are parts of the entire process. So, unlike other popular immune models for studying MS CZ-induced demyelination used herein allowed a better understanding of this disease as a chronic metabolic disorder (Ransohoff, 2012), with several neurotherapeutic implications. This will further permit exploration of axon associated changes in view of, astrocytosis (Groebe et al., 2009, Norkute et al., 2009, Pott et al., 2009), activation of

microglia (Pott et al., 2009, Groebe et al., 2009, Howell et al., 2010), oxidative stress, axon-oligodendrocyte association (Fischer et al., 2013), and seizure (Hoffmann et al., 2008).

6.2. Peripheral *vs.* Central nerve, relevance to MS like demyelination

Even though a lot is known about demyelination from studies involving peripheral nerves (Brismar and Schwarz, 1985, Zhou et al., 1998, Shields et al., 2000), an extrapolation from PNS to CNS cannot be made (Chomiak and Hu, 2009, Waxman, 2005) hence, these are of lesser relevance to MS due to the CNS nature of this disease (Compston and Coles, 2002). There could be various reasons for it (Susuki and Rasband, 2008). For instance, response to energy deficiency (hypoxia) has differential effect on these two systems, a) PNS can remain unaffected till 30 min of hypoxia exposure, CNS cannot, b) PNS recovers after reoxygenation, but CNS fails due to continued increase in Ca^{2+} load. c) CNS axons like ON are devoid of synaptic machinery, hence the interpretation is easier, d) CNS is critically dependent on energy supply, and oxidative metabolism for maintenance of excitability (Stys, 1998). These might render profound symptomatic effect, because partially demyelinated axons conduct impulses at reduced velocity—explaining the characteristic delays in conduction of evoked potentials. Demyelinated axons can discharge spontaneously and show increased mechanical sensitivity—accounting for the flashes of light on eye movement (phosphenes) and electrical sensation running down the spine or limbs on neck flexion (Lhermitte's symptom and sign) (Compston and Coles, 2002). Thus, the use of ON here brings forth a better picture of the happenings in CNS axon which is of an impinging concurrence to MS associated features.

6.3. Nature of myelin loss from WM tracts of CNS due to CZ-treatment implications for MS axonopathy

The exact nature of demyelination in MS is complex and heterogeneous in nature (Gilmore et al., 2009, Lassmann et al., 2001, Lucchinetti et al., 2000). Even though no animal model can ever produce all the characteristics, herein use of a moderate dose of CZ to induce demyelination (Hiremath et al., 1998, Matsushima and Morell, 2001) has prompted multiple features similar to MS, but with a lower immune-response (Matsushima and Morell, 2001) and associated implications. Based on the increased body wt. variation

induced it was assumed that if severe systemic effects were present, it would be mild here. This was evident due to continued weight gain in both groups denoted absence of any prominent adverse effect (Franco-Pons et al., 2007). Even though 5-6 weeks CZ-treatment induces demeylination (Matsushima and Morell, 2001), and continued feeding for 12 week (Hoffmann et al., 2008, Sun et al., 2006), is sufficient to advance it to a chronic level, present protocol was expected to yield an intermediate effect between the two phases. Possible, mild seizure was indicative of such events (Hoffmann et al., 2008). Early therapeutic intervention (Jagust, 2013) i.e., before the onset of chronic phase is anticipated to be of great significance in MS. Hence, the observations, pertaining to myelin disruption, changes in surrounding glial cells, neurofilament, JXP K_v1 and nodal Na_v channels in ON are of special interest as it represents a phase of demyelination, which emphasizes the interdependence of all these facets. Even though these aspects have been studied in different systems earlier, this study has provided a global approach to MS axonopathy. Higher susceptibility of WM rich forebrain tracts like CC, and CM are indicative of repugnant effect on axons. Thus CZ-induced demyelination was considered suitable to analyze axon features in view of preferential and robust CNS demyelination and distinguished WM pattern similar to Type III lesions (Kipp et al., 2009).

6.4. Featured changes induced were disruption of myelin periodicity and increase in dp-NF

CNS demyelination of ON herein was characterized by the demonstration of reduction in myelin sheaths, its compactness and periodicity. For the first time, this type of pattern has been described for ON which establishes an early diagnostic clinical relevance employing non-invasive methods (Sun et al., 2006) for this model. Electron microscopic analysis highlighted a reduction in the myelin thickness and a corresponding increase in “g” ratio (Chomiak and Hu, 2009) indicating radial loss of myelin and possible paranodal demyelination. Even though no pronounced phenotypic effect was observed in this nerve, ultrastructural analysis revealed several changes in axo-myelin structure and surrounding cells. Collapse of IPL and subsequent localized aggregation of MDL was evident, which was suggestive of interrupted radial insulation of the nerve. Does this relate to an experimental evidence for potassium-accumulation and a subsequent decrease in myelin

resistance that might lead to functional excitation block with varying patterns of altered spike trains (Brazhe et al., 2011) would be of great clinical relevance for ON. Proteomic ally myelin proteins like CNPase, MBP also exhibited disruption. Relative levels of lipophilins like PLP and DM20 (Griffiths et al., 1998) are one of the complicating factors involved in maintenance of myelin periodicity and surprisingly this was found to be altered due to an increase in DM20 level in their total pool. Why is it so, remains to be deciphered? All these support the observed axial loss of myelin following CZ feeding. So, it is understood that there is no or very less amount of denuded axons. This type of myelin thinning is anticipated to result in decreased insulation and, thus, interrupt the propagation of action potentials.

Neurofilament has been variously implicated in MS associated demyelination (Salzer et al., 2010, Lunn et al., 2002, Schirmer et al., 2011). Herein NF cytoskeleton was found to be disorganized, which corresponded to its reduced phosphorylation. This imparted an induced change in the proportions of the two forms (p-NF and dp-NF) in axons, with larger diameter axons accumulating more dp-NF. Thus, an imbalance could be noted within the pool of axons in ON. The small diameter axons exhibit resilience to such changes. This is possibly due to the excessive energy demand levied on thick axons relative to the thinner one (Perge et al., 2009) hence rendered more susceptible. A lower impact on small diameter axon highlights their importance in reducing the capacitative load, and favoring more effective propagation of action potentials in demyelination (Smith and McDonald, 1999, Shrager, 1993). The fore mentioned changes in axons can be attributed to metabolic challenge induced in oligodendrocytes due to CZ-treatment resulting in the loss of myelin integrity and glial trophic support. Thus, it differs from immune models where demyelination is due to T cell attack on myelin specific proteins (Schmandt et al., 2006).

Additionally, mitochondrial injury also a recognized major effector mechanism for demyelination (Khan et al., 2010, Dutta et al., 2006, Mahad et al., 2009, Mahad et al., 2008, Stys, 2004, Trapp and Nave, 2008), was noticed in this study. Interestingly, none of the animal models employed has ever been reported to have such induced changes. Even though this was not the main focus of this study, it further strengthens the relevance with

MS related mechanisms which are of great scientific interest. Changes in nuclear morphology might also be of alternative significance associated with impaired mitochondrial transport in damaged axons (Kim et al., 2010).

6.5. Ectopic axonal K_v1 channels and over expression of $K_v1.1$ is accompanied with loss functional units of JXP (K_v-Na-K_v)

Myelin integrity appears to be mandatory for targeting K^+ channels to JXPs (Rasband and Shrager, 2000, Rasband et al., 1999a). On the other hand, nodal clustering of Na^+ channels does not require myelination but their more widespread appearance along the axon during demyelination suggests a stabilizing influence of axo-glial signaling on nodal Na^+ channel clusters (Coman et al., 2006, Poliak et al., 2001). Unlike Na^+ channel aggregation, the formation of compact myelin is required for initiation and maintenance of K^+ channel clusters in ON irrespective of oligodendrocyte presence (Baba et al., 1999). Here, microscopic examination of JXPs displayed varied distribution patterns of K_v1 channels. Most of them exhibited elongation with the expression of ectopic K^+ channels in the nodal and inter-nodal segments. Notably, the treated group showed proteomic increase of $K_v1.1$ and 1.4 but reduced $K_v1.2$. $K_v1.1$ and 1.2 were the major JXP channels, whereas $K_v1.4$ was mostly of glial origin, which localized with some $K_v1.2^{+ve}$ JXPs. $K_v1.4$ was not considered for functional analysis, even though its elevated levels reaffirmed a feature similar to chronic spinal cord injury (Edwards et al., 2002). Elongated internodal expression of $K_v1.1$ was noted, in PLA and IHC signals. Normally $K_v1.1$ in higher quantities in the residual/spared JXP decreased relative to controls, which was at par in both groups. The number of $K_v1.1^{+ve}$ JXPs exhibited an increasing trend, whereas $K_v1.2^{+ve}$ JXPs showed a decrease in treated nerve. These spared JXPs exhibited higher co-efficiency of $K_v1.1/1.2$. Thus, indicating an unexpected pliancy of $K_v1.1$ in maintenance of a normal JXP feature. The unaffected axons were confirmed on the basis of a defined functional unit for action potential propagation, which was marked by the presence of two intact JXPs flanking a node. Such functional units were found to be decreased in the treated group. What leads to such a change remains unknown here, even though several in vitro studies have attributed varying causes (Connors et al., 2008, Allen et al., 1998). The basis for such a preferential

increase of localized $K_v1.1$ expression in CZ-treated axon remains to be deciphered, but this observation is suggestive of some deviant mechanism triggered by demyelination.

6.6. Augmented K^+ conductance susceptible to $K_v1.1$ selective DTX_k warrants a more in-depth study

Altered K_v1 expression accords with the physiological data highlighting an augmented K^+ conductance susceptible to DTX_K ($K_v1.1$-selective) that proved more effective in restoring CAPs in demyelinated ON than TsTX-K ($K_v1.2$-selective). The electrophysiological data demonstrated that K_v1 channel blockers partially restored the CAPs and shortened the refractive phase in demyelinated ON. Unlike control which were responsive to 4-AP only CZ-treated axons were pliable to the effects of both TEA and 4-AP. Interestingly, this is in contrast to sciatic nerve where CAPs are insensitive to these blockers prior to and after their demyelination (Bostock et al., 1981). While improved conductivity of ON by 4-AP accords with its beneficial effects in MS clinical trials (Judge and Bever, 2006, Stefoski et al., 1987), the broad spectrum action with pro-convulsive effects hinder its widespread use for MS therapy. Similar electrophysiological experiments with DTX_K as a K_v1 channel blocker in demyelinated nerves proved it more effective in restoring CAPs than TsTX-K. Because the relative strengths of K^+ and Na^+ currents in axons is a primary determinant of successful propagation of action potentials (Bostock et al., 1981), the enhanced impact of DTX_K-sensitive K^+ currents on CAPs and enrichment of demyelinated axons with $K_v1.1$ suggests appearance of channels containing heteromers or homo-tetrameric $K_v1.1$ channels. Unlike other studies (Allen et al., 2006, Velumian et al., 2010, Devaux et al., 2002, Alberts et al., 2002) where the whole nerve CAP has three peaks, here, in this study single peak was obtained. This is possible because of the insertion of sharp recording electrode very close to the stimulating electrode. Such a method is expected to lead to variation owing to the depth of electrode insertion. Herein the electrode was allowed to penetrate till $1/3^{rd}$ deep into the nerve, so that a comparable account has been achieved from both groups. A detailed account on the basis of ultrastructural analysis and whole nerve recording is warranted for revealing the consolidated effect.

Further on, electrophysiological assessment of a suspected role of $K_v1.1$ α-subunit in K_v1 channels, appearing on the axolemma of JXPs following demeylination, using recombinant expression of $K_v(1.1)_4$ channels reveals a lower activation threshold and faster kinetics than $K_v(1.2)_4$ or $K_v1.1/1.2$-containing hetero-tetramers (unpublished lab observation). Even though there has been a study which explains the emergence of K_v1 channels on membrane surface (Zhu et al., 2007). What leads to such change during disease progression remains unknown. The noted presence of $K_v1.1$ homomer in both experiment and control ON here, directs to the question that do these isoforms alter their micro domains (O'Connell and Tamkun, 2005) during demyelination, so that a functional effect can be noted. If yes, what kicks in this change? $K_v1.1$ otherwise has a strong ER retention sequence (Zhu et al., 2003), due to which it is not easily expressed as a homomeric surface protein. Is there any chaperone like protein (Schulte et al., 2006) which plays a vital role in their ectopic presence? These collectively provide an additional and important insight into demyelination-associated changes in the locations and subunit compositions of K_v1 channels of ON.

6.7. Expression of ion-channel proteins on cells of unknown identity

Axon injury and subsequent dysfunction is an integral component of MS associated neurological disability (Schirmer et al., 2011, Howell et al., 2010, Trapp et al., 1998) . Interestingly, this is an induced effect and various types of cells can be involved with mechanisms for demyelination. Herein observed emergence of K_v1 and Na_v channels in some cell of unestablished identity remained an intriguing feature. Possible identity as an oligodendrocyte, astrocyte or microglia (Butt et al., 2004) will be indicative of features relevant to the stage of disease progression (Nair et al., 2008). Little is known on these lines and whether these can be of any therapeutic relevance are questions of interest which remains to be exploited for regenerative stem cell therapy (Franklin and Ffrench-Constant, 2008). Very few studies (Jukkola et al., 2012, Edwards et al., 2002), have explored these options. Even though the present study establishes ameliorative effect of $K_v1.1$ on axon conduction, their presence on other type of cells might have an important bearing of disease progression or regeneration. This study shows the presence of $K_v1.4$ on oligodendroglia cells here. Previous studies have noted their up regulation in astrocytes (Jukkola et al.,

2012), or both astrocyte and oligodendrocyte (Edwards et al., 2002) suggesting possible neuroprotective role of these cells. Glial cells express all transcripts of the six K_v1 genes ($K_v1.1$-1.6), but do not express all proteins (Schmidt et al., 1999). So what leads to the emergence of such proteins in the cells in a disease state? Are these cells proliferative in nature (Chittajallu et al., 2002)? What is the origin of these cells? Do they signify neurodengeneration (Koeberle et al., 2010) or neuroprotection (Jukkola et al., 2012)? Astrocytes are the major intercalating cells found in ON (Perge et al., 2009). Such questions are very pertinent and even though not covered under this study an answer to them in view of the existing K_v channel blocking therapy would prove to be a step ahead in the direction of holistic approach towards the development of MS therapeutics.

Their role in regulation of de- and remyelination in MS have been suggested and this proposition has entailed several roles contemplating to be either beneficial or detrimental for disease progression. A recent study (Skripuletz et al., 2013) on this model showed that their ablation was associated with failure of damaged myelin removal and a consecutive delay in remyelination. It is important to note that similar to Skripultz et al an ultrastructural change in myelin structure has been noted in the present study. The noted changes in the morphology of astrocyte in this study is supportive of the fact that these cells have an important role in the surrounding environment of the axons, which is of great importance to understanding regenerative processes in MS (Skripuletz et al., 2013). So, employing this model with the said effect would prove beneficial in further strengthening the role of axonal K_v1 channels in view of de- and re-myelination both.

6.8. Present scenario for treatment of MS and issues

Clinicians treating MS aim to reduce the frequency of demyelinating attacks, and limit the lasting effects, of relapses, relieve symptoms, prevent disability arising from disease progression, and promote tissue repair (Compston and Coles, 2002, Trapp and Nave, 2008). The present course of treatment for patients include strategies like,

a) Interferons for reduction of relapse rates: Since permanent disability can be caused by incomplete recovery from episodes, relapse frequency is bound to correlate with accumulation of disability during the RRPMS. Successful use of the beta interferons: beta-1a (Avonex, Biogen, and Rebif, Ares-Serono), and beta-1b (Betaferon and Betaseron, Schering) reduce such relapses and accumulation of disability. But such reductions fail to have any impact on continuing secondary progression.

b) Corticosteroids for prevention of disability attributable to relapse: Corticosteroids, is used to inhibit transcription of proinflammatory cytokines, such as interleukin-1, interleukin-2, tumour necrosis factor-α and proinflammatory enzymes, including collagenase, elastase, and plasminogen activator. These anti-inflammatory effects have long been used for acute treatment of MS. All trials to date have indicated reduction of relapses and hence short-term morbidity, but not the ensuing permanent deficits.

c) Symptomatic management of fixed neurological deficits:

- The spasticity and sphincter dysfunction is treated by baclofen, which acts on spinal cord GABA-$_B$ receptors to suppress reflex arcs released from higher inhibitory control; or tizanidine, which acts through spinal cord α_2 receptors to modulate presynaptic release of excitatory amino acids.
- Bladder symptoms are most easily inhibited by anti-cholinergics.
- Paroxysmal attacks respond well to membrane-stabilizing drugs—typically carbamazepine. None of the pharmacological treatment show beneficial effect on the tremor of MS.
- Fatigue cannot be satisfactorily treated (Compston and Coles, 2002).

Two non-specific potassium K^+ channel blocking drugs, 4-aminopyridine (4-AP) and 3,4-diaminopyridine (3,4-DAP), have been tested as a symptomatic treatment in patients with MS based on the clinical rationale that neurologic function could be improved by overcoming conduction block in demyelinated axons present in MS lesions. Although 4-AP, in particular, produces clear neurologic benefits in some. Dalfampridine/fampridine (4-AP) is in phase II and III placebo- controlled clinical trials. These trials, with extended-release dalfampridine show an average 25% increase in the walking speed in more than one-third of the patients who received the drug and met the prescribed criteria for consistent responders. The safety profile of dalfampridine is also being reviewed, with a focus on the

risk for epileptic seizures as an adverse effect (Goodman and Hyland, 2010, Judge and Bever, 2006).

d) Immunotherapeutic strategies for improved treatment of disease activity:

Two approaches are adopted to reduce the activation and proliferation of auto reactive T cells. One is to suppress immune activity non-specifically and has acceptable safety profiles. Past attempts (with cyclophosphamide, cyclosporin, lymphoid irradiation, cladribine) have shown evidence for efficacy but with major side-effects; examples of this legacy are paclitaxel, teriflunomide, and autologous bone marrow transplantation. The second strategy is to assume that the specific interaction between MBP, T cells, and antigen presenting cells is the pivotal event driving MS. Several drugs have been designed to manipulate this interaction (Compston and Coles, 2002).

6.9. Indicated axonopathy and prevention of disability acquired through progression

The relationship between progression and relapse has been emphasized by a small, uncontrolled study of patients with secondary progressive MS. They were treated with a short pulse of Campath-1H (a monoclonal antibody that depletes T cells and modulates their activity). Half of the patients continued to have progression of disability; displayed continued cerebral atrophy, and loss of spectroscopic markers of axons, despite the absence of cerebral inflammatory activity. A similar dissociation between effective suppression of new lesions and continued cerebral atrophy in progressive patients was seen in a trial of the lympho cytotoxic drug cladribine, a purine nucleoside analogue resistant to the action of adenosine deaminase (Coles et al., 1999).

Thus, there are a lot of compelling evidences which has led to the conclusion that immunomodulatory drugs are of little use once axonal degeneration has reached a critical threshold and clinical progression is established. It follows that there might be an opportunity, early in the disease course; to suppress those components of the inflammatory processes that initiate the cascade leading to delayed progression. The immunotherapies prove inadequate in reducing relapse frequency, and also to prevent transition to the secondary progressive phase of the illness. Thus, the essential question involving current

immunotherapies therapies for MS is —whether an early anti-inflammatory therapy reduce the proportion of patients who ever enter the secondary progressive phase, or usefully affect the slope of that progression? These are being addressed in trial designs. However, time seems to have been lost, and possibly several years will pass before an answer is available. But, since the result cannot be prejudged, parallel strategies for limiting the effect of progression are needed. All these indicate our limited understanding of the pathogenesis of MS and the usefulness of existing therapies (Compston and Coles, 2002)

This thesis in view of the given therapeutic approach (es) for MS has sought out to explore the option of employing K_v1 blocking strategy for amelioration of disability. Even though it is considered for symptomatic treatment, with the provided background of how the diseases progresses and axon-glia and all accompanying features gradually get affected advancing towards the later phase and neurological disability acquires prominence. It is imperative that containing neurological disability should be the prime approach, but in lack of the appropriate intervention, it is worthwhile to establish specific blocking of K_v1 channels and get rid of the epileptogenic effect, which arises due to the presently available blcokers. Even though it would be premature to judge whether the strategy is right or wrong, development of blockers for $K_v1.1$ homomer will prove fruitful in providing relief to the patients with minimal side effects, specifically when the most used immunotherapeutic results are disappointing. Further continuation on the directions obtained in this pilot study would be rewarding.

BIBLIOGRAPHY

ADELMAN, W. J., JR. & FITZHUGH, R. (1975) Solutions of the Hodgkin-Huxley equations modified for potassium accumulation in a periaxonal space. *Fed Proc,* 34**,** 1322-9.

AKHTAR, S., SHAMOTIENKO, O., PAPAKOSTA, M., ALI, F. & DOLLY, J. O. (2002) Characteristics of brain Kv1 channels tailored to mimic native counterparts by tandem linkage of alpha subunits: implications for K+ channelopathies. *J Biol Chem,* 277**,** 16376-82.

AL-SABI, A., KAZA, S., LE BERRE, M., O'HARA, L., BODEKER, M., WANG, J. & DOLLY, J. O. (2011) Position-dependent attenuation by Kv1.6 of N-type inactivation of Kv1.4-containing channels. *Biochem J*.

AL-SABI, A., SHAMOTIENKO, O., DHOCHARTAIGH, S. N., MUNIYAPPA, N., LE BERRE, M., SHABAN, H., WANG, J., SACK, J. T. & DOLLY, J. O. (2010) Arrangement of Kv1 alpha subunits dictates sensitivity to tetraethylammonium. *J Gen Physiol,* 136**,** 273-82.

ALBERTS, B., JOHNSON, A., LEWIS, J., RAFF, M., ROBERTS, K. & WALTER, P. (2002) *Molecular Biology of the Cell.,* Garland Science, New York.

ALLEN, L., ANDERSON, S., WENDER, R., MEAKIN, P., RANSOM, B. R., RAY, D. E. & BROWN, A. M. (2006) Fructose supports energy metabolism of some, but not all, axons in adult mouse optic nerve. *J Neurophysiol,* 95**,** 1917-25.

ALLEN, M. L., KOH, D. S. & TEMPEL, B. L. (1998) Cyclic AMP regulates potassium channel expression in C6 glioma by destabilizing Kv1.1 mRNA. *Proc Natl Acad Sci U S A,* 95**,** 7693-8.

ALTMANN, D. M. & BOYTON, R. J. (2004) Models of multiple sclerosis. *Drug Discov Today,* 1**,** 405-410.

ARROYO, E. J. & SCHERER, S. S. (2000) On the molecular architecture of myelinated fibers. *Histochem Cell Biol,* 113**,** 1-18.

ARROYO, E. J., XU, T., GRINSPAN, J., LAMBERT, S., LEVINSON, S. R., BROPHY, P. J., PELES, E. & SCHERER, S. S. (2002) Genetic dysmyelination alters the molecular architecture of the nodal region. *J Neurosci,* 22**,** 1726-37.

ARROYO, E. J., XU, T., POLIAK, S., WATSON, M., PELES, E. & SCHERER, S. S. (2001) Internodal specializations of myelinated axons in the central nervous system. *Cell Tissue Res,* 305**,** 53-66.

BABA, H., AKITA, H., ISHIBASHI, T., INOUE, Y., NAKAHIRA, K. & IKENAKA, K. (1999) Completion of myelin compaction, but not the attachment of oligodendroglial processes triggers K(+) channel clustering. *J Neurosci Res,* 58**,** 752-64.

BABILA, T., MOSCUCCI, A., WANG, H., WEAVER, F. E. & KOREN, G. (1994) Assembly of mammalian voltage-gated potassium channels: evidence for an important role of the first transmembrane segment. *Neuron,* 12**,** 615-26.

BARNETT, M. H. & SUTTON, I. (2012) Neuromyelitis optica: not a multiple sclerosis variant. *Curr Opin Neurol.*

BAUMANN, N. & PHAM-DINH, D. (2001) Biology of oligodendrocyte and myelin in the mammalian central nervous system. *Physiol Rev,* 81**,** 871-927.

BENETTI, F., VENTURA, M., SALMINI, B., CEOLA, S., CARBONERA, D., MAMMI, S., ZITOLO, A., D'ANGELO, P., URSO, E., MAFFIA, M., SALVATO, B. & SPISNI, E. (2010) Cuprizone neurotoxicity, copper deficiency and neurodegeneration. *Neurotoxicology,* 31**,** 509-17.

BERTHOLD, C. H. & RYDMARK, M. (1995) Morphology of normal peripheral axons. In "The Axon". **,** 13–48.

BEZANILLA, F. (2000) The voltage sensor in voltage-dependent ion channels. *Physiol Rev,* 80**,** 555-92.

BEZANILLA, F. (2006) The action potential: from voltage-gated conductances to molecular structures. *Biol Res,* 39**,** 425-35.

BEZANILLA, F. (2008) Ion channels: from conductance to structure. *Neuron,* 60**,** 456-68.

BEZANILLA, F., PEROZO, E., PAPAZIAN, D. M. & STEFANI, E. (1991) Molecular basis of gating charge immobilization in Shaker potassium channels. *Science,* 254**,** 679-83.

BINDER, D. K. & STEINHAUSER, C. (2006) Functional changes in astroglial cells in epilepsy. *Glia,* 54**,** 358-68.

BITSCH, A., SCHUCHARDT, J., BUNKOWSKI, S., KUHLMANN, T. & BRUCK, W. (2000) Acute axonal injury in multiple sclerosis. Correlation with demyelination and inflammation. *Brain,* 123 (Pt 6)**,** 1174-83.

BLACK, J. A., RENGANATHAN, M. & WAXMAN, S. G. (2002) Sodium channel Na(v)1.6 is expressed along nonmyelinated axons and it contributes to conduction. *Brain Res Mol Brain Res,* 105**,** 19-28.

BLAKEMORE, W. F. (1973) Demyelination of the superior cerebellar peduncle in the mouse induced by cuprizone. *J Neurol Sci,* 20**,** 63-72.

BOSTOCK, H., SEARS, T. A. & SHERRATT, R. M. (1981) The effects of 4-aminopyridine and tetraethylammonium ions on normal and demyelinated mammalian nerve fibres. *J Physiol,* 313**,** 301-15.

BOSTOCK, H., SHERRATT, R. M. & SEARS, T. A. (1978) Overcoming conduction failure in demyelinated nerve fibres by prolonging action potentials. *Nature,* 274**,** 385-7.

BRAZHE, A. R., MAKSIMOV, G. V., MOSEKILDE, E. & SOSNOVTSEVA, O. V. (2011) Excitation block in a nerve fibre model owing to potassium-dependent changes in myelin resistance. *Interface Focus,* 1**,** 86-100.

BRISMAR, T. & SCHWARZ, J. R. (1985) Potassium permeability in rat myelinated nerve fibres. *Acta Physiol Scand,* 124**,** 141-8.

BUTT, A. M., PUGH, M., HUBBARD, P. & JAMES, G. (2004) Functions of optic nerve glia: axoglial signalling in physiology and pathology. *Eye (Lond),* 18**,** 1110-21.

CALEO, M. (2009) Epilepsy: synapses stuck in childhood. *Nat Med,* 15**,** 1126-7.

CAMPBELL, G. R., ZIABREVA, I., REEVE, A. K., KRISHNAN, K. J., REYNOLDS, R., HOWELL, O., LASSMANN, H., TURNBULL, D. M. & MAHAD, D. J. (2011) Mitochondrial DNA deletions and neurodegeneration in multiple sclerosis. *Ann Neurol,* 69**,** 481-92.

CAREY, E. M. & FREEMAN, N. M. (1983) Biochemical changes in Cuprizone-induced spongiform encephalopathy. I. Changes in the activities of 2',3'-cyclic nucleotide 3'-phosphohydrolase, oligodendroglial ceramide galactosyl transferase, and the

hydrolysis of the alkenyl group of alkenyl, acyl-glycerophospholipids by plasmalogenase in different regions of the brain. *Neurochem Res,* 8**,** 1029-44.
CERDA, O. & TRIMMER, J. S. (2010) Analysis and functional implications of phosphorylation of neuronal voltage-gated potassium channels. *Neurosci Lett,* 486**,** 60-7.
CHARAND, K. X. (2012) Action Potentials.
CHITTAJALLU, R., CHEN, Y., WANG, H., YUAN, X., GHIANI, C. A., HECKMAN, T., MCBAIN, C. J. & GALLO, V. (2002) Regulation of Kv1 subunit expression in oligodendrocyte progenitor cells and their role in G1/S phase progression of the cell cycle. *Proc Natl Acad Sci U S A,* 99**,** 2350-5.
CHIU, S. Y. & RITCHIE, J. M. (1980) Potassium channels in nodal and internodal axonal membrane of mammalian myelinated fibres. *Nature,* 284**,** 170-1.
CHIU, S. Y. & RITCHIE, J. M. (1981) Evidence for the presence of potassium channels in the paranodal region of acutely demyelinated mammalian single nerve fibres. *J Physiol,* 313**,** 415-37.
CHIU, S. Y., ZHOU, L., ZHANG, C. L. & MESSING, A. (1999) Analysis of potassium channel functions in mammalian axons by gene knockouts. *J Neurocytol,* 28**,** 349-64.
CHOMIAK, T. & HU, B. (2009) What is the optimal value of the g-ratio for myelinated fibers in the rat CNS? A theoretical approach. *PLoS One,* 4**,** e7754.
COLEMAN, M. (2005) Axon degeneration mechanisms: commonality amid diversity. *Nat Rev Neurosci,* 6**,** 889-98.
COLEMAN, S. K., NEWCOMBE, J., PRYKE, J. & DOLLY, J. O. (1999) Subunit composition of Kv1 channels in human CNS. *J Neurochem,* 73**,** 849-58.
COLES, A. J., WING, M. G., MOLYNEUX, P., PAOLILLO, A., DAVIE, C. M., HALE, G., MILLER, D., WALDMANN, H. & COMPSTON, A. (1999) Monoclonal antibody treatment exposes three mechanisms underlying the clinical course of multiple sclerosis. *Ann Neurol,* 46**,** 296-304.
COMA, M., VICENTE, R., BUSQUETS, S., CARBO, N., TAMKUN, M. M., LOPEZ-SORIANO, F. J., ARGILES, J. M. & FELIPE, A. (2003) Impaired voltage-gated K+ channel expression in brain during experimental cancer cachexia. *FEBS Lett,* 536**,** 45-50.
COMAN, I., AIGROT, M. S., SEILHEAN, D., REYNOLDS, R., GIRAULT, J. A., ZALC, B. & LUBETZKI, C. (2006) Nodal, paranodal and juxtaparanodal axonal proteins during demyelination and remyelination in multiple sclerosis. *Brain,* 129**,** 3186-95.
COMPSTON, A. & COLES, A. (2002) Multiple sclerosis. *Lancet,* 359**,** 1221-31.
CONNORS, E. C., BALLIF, B. A. & MORIELLI, A. D. (2008) Homeostatic regulation of Kv1.2 potassium channel trafficking by cyclic AMP. *J Biol Chem,* 283**,** 3445-53.
CORTHALS, A. P. (2011) Multiple sclerosis is not a disease of the immune system. *Q Rev Biol,* 86**,** 287-321.
CRANER, M. J., NEWCOMBE, J., BLACK, J. A., HARTLE, C., CUZNER, M. L. & WAXMAN, S. G. (2004) Molecular changes in neurons in multiple sclerosis: altered axonal expression of Nav1.2 and Nav1.6 sodium channels and Na+/Ca2+ exchanger. *Proc Natl Acad Sci U S A,* 101**,** 8168-73.

CRAWFORD, D. K., MANGIARDI, M., XIA, X., LOPEZ-VALDES, H. E. & TIWARI-WOODRUFF, S. K. (2009) Functional recovery of callosal axons following demyelination: a critical window. *Neuroscience,* 164**,** 1407-21.

DAI, X. Q., KOLIC, J., MARCHI, P., SIPIONE, S. & MACDONALD, P. E. (2009) SUMOylation regulates Kv2.1 and modulates pancreatic beta-cell excitability. *J Cell Sci,* 122**,** 775-9.

DANGATA, Y. Y., FINDLATER, G. S. & KAUFMAN, M. H. (1996) Postnatal development of the optic nerve in (C57BL x CBA)F1 hybrid mice: general changes in morphometric parameters. *J Anat,* 189 (Pt 1)**,** 117-25.

DEBANNE, D. (2004) Information processing in the axon. *Nat Rev Neurosci,* 5**,** 304-16.

DELOIRE-GRASSIN, M. S., BROCHET, B., QUESSON, B., DELALANDE, C., DOUSSET, V., CANIONI, P. & PETRY, K. G. (2000) In vivo evaluation of remyelination in rat brain by magnetization transfer imaging. *J Neurol Sci,* 178**,** 10-6.

DEVAUX, J., GOLA, M., JACQUET, G. & CREST, M. (2002) Effects of K+ channel blockers on developing rat myelinated CNS axons: identification of four types of K+ channels. *J Neurophysiol,* 87**,** 1376-85.

DEVAUX, J. & GOW, A. (2008) Tight junctions potentiate the insulative properties of small CNS myelinated axons. *J Cell Biol,* 183**,** 909-21.

DOLLY, J. O. & PARCEJ, D. N. (1996) Molecular properties of voltage-gated K+ channels. *J Bioenerg Biomembr,* 28**,** 231-53.

DUNN, J. & BLIGHT, A. (2011) Dalfampridine: a brief review of its mechansim of action and efficay as a treatment ti improve walking in patients with multiple sclerosis. . *Current Medical Research and Opinion,* 27**,** 1415-1423.

DUTTA, R., MCDONOUGH, J., YIN, X., PETERSON, J., CHANG, A., TORRES, T., GUDZ, T., MACKLIN, W. B., LEWIS, D. A., FOX, R. J., RUDICK, R., MIRNICS, K. & TRAPP, B. D. (2006) Mitochondrial dysfunction as a cause of axonal degeneration in multiple sclerosis patients. *Ann Neurol,* 59**,** 478-89.

DUTTA, R. & TRAPP, B. D. (2010) Mechanisms of neuronal dysfunction and degeneration in multiple sclerosis. *Prog Neurobiol,* 93**,** 1-12.

DUTTA, R. & TRAPP, B. D. (2011) Mechanisms of neuronal dysfunction and degeneration in multiple sclerosis. *Prog Neurobiol,* 93**,** 1-12.

DZIEDZIC, T., METZ, I., DALLENGA, T., KONIG, F. B., MULLER, S., STADELMANN, C. & BRUCK, W. (2010) Wallerian degeneration: a major component of early axonal pathology in multiple sclerosis. *Brain Pathol,* 20**,** 976-85.

EDGAR, J. M., MCLAUGHLIN, M., YOOL, D., ZHANG, S. C., FOWLER, J. H., MONTAGUE, P., BARRIE, J. A., MCCULLOCH, M. C., DUNCAN, I. D., GARBERN, J., NAVE, K. A. & GRIFFITHS, I. R. (2004) Oligodendroglial modulation of fast axonal transport in a mouse model of hereditary spastic paraplegia. *J Cell Biol,* 166**,** 121-31.

EDWARDS, L., NASHMI, R., JONES, O., BACKX, P., ACKERLEY, C., BECKER, L. & FEHLINGS, M. G. (2002) Upregulation of Kv 1.4 protein and gene expression after chronic spinal cord injury. *J Comp Neurol,* 443**,** 154-67.

ELINDER, F., NILSSON, J. & ARHEM, P. (2007) On the opening of voltage-gated ion channels. *Physiol Behav,* 92**,** 1-7.

EUNSON, L. H., REA, R., ZUBERI, S. M., YOUROUKOS, S., PANAYIOTOPOULOS, C. P., LIGUORI, R., AVONI, P., MCWILLIAM, R. C., STEPHENSON, J. B., HANNA, M. G., KULLMANN, D. M. & SPAUSCHUS, A. (2000) Clinical, genetic, and expression studies of mutations in the potassium channel gene KCNA1 reveal new phenotypic variability. *Ann Neurol,* 48**,** 647-56.

FAIRLESS, R., WILLIAMS, S. K., HOFFMANN, D. B., STOJIC, A., HOCHMEISTER, S., SCHMITZ, F., STORCH, M. K. & DIEM, R. (2012) Preclinical retinal neurodegeneration in a model of multiple sclerosis. *J Neurosci,* 32**,** 5585-97.

FERGUSON, B., MATYSZAK, M. K., ESIRI, M. M. & PERRY, V. H. (1997) Axonal damage in acute multiple sclerosis lesions. *Brain,* 120 (Pt 3)**,** 393-9.

FISCHER, M. T., WIMMER, I., HOFTBERGER, R., GERLACH, S., HAIDER, L., ZRZAVY, T., HAMETNER, S., MAHAD, D., BINDER, C. J., KRUMBHOLZ, M., BAUER, J., BRADL, M. & LASSMANN, H. (2013) Disease-specific molecular events in cortical multiple sclerosis lesions. *Brain*.

FLEMING, B. (2012) Ion Channels. http://www.arts.uwaterloo.ca/~bfleming/psych261/lec4se21.

FOSTER, R. E., CONNORS, B. W. & WAXMAN, S. G. (1982) Rat optic nerve: electrophysiological, pharmacological and anatomical studies during development. *Brain Res,* 255**,** 371-86.

FRANCO-PONS, N., TORRENTE, M., COLOMINA, M. T. & VILELLA, E. (2007) Behavioral deficits in the cuprizone-induced murine model of demyelination/remyelination. *Toxicol Lett,* 169**,** 205-13.

FRANKLIN, R. J. & FFRENCH-CONSTANT, C. (2008) Remyelination in the CNS: from biology to therapy. *Nat Rev Neurosci,* 9**,** 839-55.

GARCIA, M. L., LOBSIGER, C. S., SHAH, S. B., DEERINCK, T. J., CRUM, J., YOUNG, D., WARD, C. M., CRAWFORD, T. O., GOTOW, T., UCHIYAMA, Y., ELLISMAN, M. H., CALCUTT, N. A. & CLEVELAND, D. W. (2003) NF-M is an essential target for the myelin-directed "outside-in" signaling cascade that mediates radial axonal growth. *J Cell Biol,* 163**,** 1011-20.

GEURTS, J. J. & BARKHOF, F. (2008) Grey matter pathology in multiple sclerosis. *Lancet Neurol,* 7**,** 841-51.

GILMORE, C. P., DONALDSON, I., BO, L., OWENS, T., LOWE, J. & EVANGELOU, N. (2009) Regional variations in the extent and pattern of grey matter demyelination in multiple sclerosis: a comparison between the cerebral cortex, cerebellar cortex, deep grey matter nuclei and the spinal cord. *J Neurol Neurosurg Psychiatry,* 80**,** 182-7.

GOODMAN, A. D. & HYLAND, M. (2010) Dalfampridine in multiple sclerosis. *Drugs Today (Barc),* 46**,** 635-9.

GORDON, T. R., KOCSIS, J. D. & WAXMAN, S. G. (1988) Evidence for the presence of two types of potassium channels in the rat optic nerve. *Brain Res,* 447**,** 1-9.

GRIFFITHS, I., KLUGMANN, M., ANDERSON, T., YOOL, D., THOMSON, C., SCHWAB, M. H., SCHNEIDER, A., ZIMMERMANN, F., MCCULLOCH, M., NADON, N. & NAVE, K. A. (1998) Axonal swellings and degeneration in mice lacking the major proteolipid of myelin. *Science,* 280**,** 1610-3.

GROEBE, A., CLARNER, T., BAUMGARTNER, W., DANG, J., BEYER, C. & KIPP, M. (2009) Cuprizone treatment induces distinct demyelination, astrocytosis, and

microglia cell invasion or proliferation in the mouse cerebellum. *Cerebellum,* 8**,** 163-74.

GUAZZO, E. P. (2005) A technique for producing demyelination of the rat optic nerves. *J Clin Neurosci,* 12**,** 54-8.

GUBITOSI-KLUG, R. A., MANCUSO, D. J. & GROSS, R. W. (2005) The human Kv1.1 channel is palmitoylated, modulating voltage sensing: Identification of a palmitoylation consensus sequence. *Proc Natl Acad Sci U S A,* 102**,** 5964-8.

GULBIS, J. M., ZHOU, M., MANN, S. & MACKINNON, R. (2000) Structure of the cytoplasmic beta subunit-T1 assembly of voltage-dependent K+ channels. *Science,* 289**,** 123-7.

GUTMAN, G. A., CHANDY, K. G., ADELMAN, J. P., AIYAR, J., BAYLISS, D. A., CLAPHAM, D. E., COVARRIUBIAS, M., DESIR, G. V., FURUICHI, K., GANETZKY, B., GARCIA, M. L., GRISSMER, S., JAN, L. Y., KARSCHIN, A., KIM, D., KUPERSCHMIDT, S., KURACHI, Y., LAZDUNSKI, M., LESAGE, F., LESTER, H. A., MCKINNON, D., NICHOLS, C. G., O'KELLY, I., ROBBINS, J., ROBERTSON, G. A., RUDY, B., SANGUINETTI, M., SEINO, S., STUEHMER, W., TAMKUN, M. M., VANDENBERG, C. A., WEI, A., WULFF, H. & WYMORE, R. S. (2003) International Union of Pharmacology. XLI. Compendium of voltage-gated ion channels: potassium channels. *Pharmacol Rev,* 55**,** 583-6.

GUTMAN, G. A., CHANDY, K. G., GRISSMER, S., LAZDUNSKI, M., MCKINNON, D., PARDO, L. A., ROBERTSON, G. A., RUDY, B., SANGUINETTI, M. C., STUHMER, W. & WANG, X. (2005) International Union of Pharmacology. LIII. Nomenclature and molecular relationships of voltage-gated potassium channels. *Pharmacol Rev,* 57**,** 473-508.

HAIDER, L., FISCHER, M. T., FRISCHER, J. M., BAUER, J., HOFTBERGER, R., BOTOND, G., ESTERBAUER, H., BINDER, C. J., WITZTUM, J. L. & LASSMANN, H. (2011) Oxidative damage in multiple sclerosis lesions. *Brain*.

HARTMUT, W. & KURSCHUS, F. C. (2006) Animal models of multiple sclerosis. *Drug Discov Today,* 3**,** 359-367.

HILDEBRAND, C. (1974) Embedding of myelinated nerve tissue in water-soluble resorcinol-formaldehyde resins for light and electron microscopy. *Stain Technol,* 49**,** 281-95.

HILLE, B. (2001) Ion Channels of Excitable Membranes.

HIRANO, A. & LLENA, J. F. (1995) *Morphology of central nervous system axons,* New York, Oxford University Press, .

HIREMATH, M. M., SAITO, Y., KNAPP, G. W., TING, J. P., SUZUKI, K. & MATSUSHIMA, G. K. (1998) Microglial/macrophage accumulation during cuprizone-induced demyelination in C57BL/6 mice. *J Neuroimmunol,* 92**,** 38-49.

HOFFMANN, K., LINDNER, M., GROTICKE, I., STANGEL, M. & LOSCHER, W. (2008) Epileptic seizures and hippocampal damage after cuprizone-induced demyelination in C57BL/6 mice. *Exp Neurol,* 210**,** 308-21.

HOOPENGARDNER, B., BHALLA, T., STABER, C. & REENAN, R. (2003) Nervous system targets of RNA editing identified by comparative genomics. *Science,* 301**,** 832-6.

HOPKINS, W. F. (1998) Toxin and subunit specificity of blocking affinity of three peptide toxins for heteromultimeric, voltage-gated potassium channels expressed in Xenopus oocytes. *J Pharmacol Exp Ther,* 285**,** 1051-60.

HOWELL, O. W., RUNDLE, J. L., GARG, A., KOMADA, M., BROPHY, P. J. & REYNOLDS, R. (2010) Activated microglia mediate axoglial disruption that contributes to axonal injury in multiple sclerosis. *J Neuropathol Exp Neurol,* 69**,** 1017-33.

HU, C. L., ZENG, X. M., ZHOU, M. H., SHI, Y. T., CAO, H. & MEI, Y. A. (2008) Kv 1.1 is associated with neuronal apoptosis and modulated by protein kinase C in the rat cerebellar granule cell. *J Neurochem,* 106**,** 1125-37.

HUTERER, S. J., TOURTELLOTTE, W. W. & WHERRETT, J. R. (1995) Alterations in the activity of phospholipases A2 in postmortem white matter from patients with multiple sclerosis. *Neurochem Res,* 20**,** 1335-43.

ISACOFF, E. Y., JAN, Y. N. & JAN, L. Y. (1990) Evidence for the formation of heteromultimeric potassium channels in Xenopus oocytes. *Nature,* 345**,** 530-4.

JAGUST, W. (2013) Vulnerable neural systems and the borderland of brain aging and neurodegeneration. *Neuron,* 77**,** 219-34.

JAN, L. Y. & JAN, Y. N. (1992) Structural elements involved in specific K+ channel functions. *Annu Rev Physiol,* 54**,** 537-55.

JANG, G. M., TANAKA, B. S., GUTMAN, G. A., GOLDIN, A. L. & SEMLER, B. L. (2008) Alternative polyadenylation signals in the 3' non-coding region of a voltage-gated potassium channel gene are major determinants of mRNA isoform expression. *Gene,* 408**,** 133-45.

JIANG, Y., LEE, A., CHEN, J., RUTA, V., CADENE, M., CHAIT, B. T. & MACKINNON, R. (2003a) X-ray structure of a voltage-dependent K+ channel. *Nature,* 423**,** 33-41.

JIANG, Y., RUTA, V., CHEN, J., LEE, A. & MACKINNON, R. (2003b) The principle of gating charge movement in a voltage-dependent K+ channel. *Nature,* 423**,** 42-8.

JUDGE, S. I. & BEVER, C. T., JR. (2006) Potassium channel blockers in multiple sclerosis: neuronal Kv channels and effects of symptomatic treatment. *Pharmacol Ther,* 111**,** 224-59.

JUKKOLA, P., LOVETT-RACKE, A. E., ZAMVIL, S. S. & GU, C. (2012) K(+) channel alterations in the progression of experimental autoimmune encephalomyelitis. *Neurobiol Dis*.

KAMB, A., IVERSON, L. E. & TANOUYE, M. A. (1987) Molecular characterization of Shaker, a Drosophila gene that encodes a potassium channel. *Cell,* 50**,** 405-13.

KANDEL, E. R., SCHWARTZ, J. H. & JESSEL, T. M. (1991) Principles of Neural Science.

KAZARINOVA-NOYES, K. & SHRAGER, P. (2002) Molecular constituents of the node of Ranvier. *Mol Neurobiol,* 26**,** 167-82.

KEYNES, R. D. & ELINDER, F. (1999) The screw-helical voltage gating of ion channels. *Proc Biol Sci,* 266**,** 843-52.

KHAN, O., TSELIS, A. & LISAK, R. (2010) Getting to grips with myelin injury in progressive multiple sclerosis. *Brain,* 133**,** 2845-8.

KIM, J. K., MASTRONARDI, F. G., WOOD, D. D., LUBMAN, D. M., ZAND, R. & MOSCARELLO, M. A. (2003) Multiple sclerosis: an important role for post-

translational modifications of myelin basic protein in pathogenesis. *Mol Cell Proteomics,* 2**,** 453-62.

KIM, J. Y., SHEN, S., DIETZ, K., HE, Y., HOWELL, O., REYNOLDS, R. & CASACCIA, P. (2010) HDAC1 nuclear export induced by pathological conditions is essential for the onset of axonal damage. *Nat Neurosci,* 13**,** 180-9.

KIPP, M., CLARNER, T., DANG, J., COPRAY, S. & BEYER, C. (2009) The cuprizone animal model: new insights into an old story. *Acta Neuropathol,* 118**,** 723-36.

KIRYU-SEO, S., OHNO, N., KIDD, G. J., KOMURO, H. & TRAPP, B. D. (2010) Demyelination increases axonal stationary mitochondrial size and the speed of axonal mitochondrial transport. *J Neurosci,* 30**,** 6658-66.

KOCSIS, J. D., GORDON, T. R. & WAXMAN, S. G. (1986) Mammalian optic nerve fibers display two pharmacologically distinct potassium channels. *Brain Res,* 383**,** 357-61.

KOEBERLE, P. D., WANG, Y. & SCHLICHTER, L. C. (2010) Kv1.1 and Kv1.3 channels contribute to the degeneration of retinal ganglion cells after optic nerve transection in vivo. *Cell Death Differ,* 17**,** 134-44.

KOLES, Z. J. & RASMINSKY, M. (1972) A computer simulation of conduction in demyelinated nerve fibres. *J Physiol,* 227**,** 351-64.

KORNEK, B., STORCH, M. K., BAUER, J., DJAMSHIDIAN, A., WEISSERT, R., WALLSTROEM, E., STEFFERL, A., ZIMPRICH, F., OLSSON, T., LININGTON, C., SCHMIDBAUER, M. & LASSMANN, H. (2001) Distribution of a calcium channel subunit in dystrophic axons in multiple sclerosis and experimental autoimmune encephalomyelitis. *Brain,* 124**,** 1114-24.

KOUTSOUDAKI, P. N., SKRIPULETZ, T., GUDI, V., MOHARREGH-KHIABANI, D., HILDEBRANDT, H., TREBST, C. & STANGEL, M. (2009) Demyelination of the hippocampus is prominent in the cuprizone model. *Neurosci Lett,* 451**,** 83-8.

KUHLMANN, T., LINGFELD, G., BITSCH, A., SCHUCHARDT, J. & BRUCK, W. (2002) Acute axonal damage in multiple sclerosis is most extensive in early disease stages and decreases over time. *Brain,* 125**,** 2202-12.

KUTZELNIGG, A., FABER-ROD, J. C., BAUER, J., LUCCHINETTI, C. F., SORENSEN, P. S., LAURSEN, H., STADELMANN, C., BRUCK, W., RAUSCHKA, H., SCHMIDBAUER, M. & LASSMANN, H. (2007) Widespread demyelination in the cerebellar cortex in multiple sclerosis. *Brain Pathol,* 17**,** 38-44.

LASIENE , J., SHUPE L, PERLMUTTER S & P, H. (2008) No evidence for chronic demyelination in spared axons after spinal cord injury in a mouse. *Journal of Neuroscience,* 28**,** 3887-96.

LASSMANN, H., BRUCK, W. & LUCCHINETTI, C. (2001) Heterogeneity of multiple sclerosis pathogenesis: implications for diagnosis and therapy. *Trends Mol Med,* 7**,** 115-21.

LASSMANN, H., BRUCK, W. & LUCCHINETTI, C. F. (2007) The immunopathology of multiple sclerosis: an overview. *Brain Pathol,* 17**,** 210-8.

LEES, M. B. & BIZZOZERO, O. A. (1992) *Structure and acylation of proteolipid protein,* Boca Raton, FL, CRC Press, Inc. .

LI, F., LU, J., WU, C. Y., KAUR, C., SIVAKUMAR, V., SUN, J., LI, S. & LING, E. A. (2008) Expression of Kv1.2 in microglia and its putative roles in modulating

production of proinflammatory cytokines and reactive oxygen species. *J Neurochem,* 106**,** 2093-105.

LI, Y., UM, S. Y. & MCDONALD, T. V. (2006) Voltage-gated potassium channels: regulation by accessory subunits. *Neuroscientist,* 12**,** 199-210.

LONG, S. B., CAMPBELL, E. B. & MACKINNON, R. (2005a) Crystal structure of a mammalian voltage-dependent Shaker family K+ channel. *Science,* 309**,** 897-903.

LONG, S. B., CAMPBELL, E. B. & MACKINNON, R. (2005b) Voltage sensor of Kv1.2: structural basis of electromechanical coupling. *Science,* 309**,** 903-8.

LU, Q., PEEVEY, J., JOW, F., MONAGHAN, M. M., MENDOZA, G., ZHANG, H., WU, J., KIM, C. Y., BICKSLER, J., GREENBLATT, L., LIN, S. S., CHILDERS, W. & BOWLBY, M. R. (2008) Disruption of Kv1.1 N-type inactivation by novel small molecule inhibitors (disinactivators). *Bioorg Med Chem,* 16**,** 3067-75.

LUCCHINETTI, C., BRUCK, W., PARISI, J., SCHEITHAUER, B., RODRIGUEZ, M. & LASSMANN, H. (2000) Heterogeneity of multiple sclerosis lesions: implications for the pathogenesis of demyelination. *Ann Neurol,* 47**,** 707-17.

LUDWIN, S. K. (1980) Chronic demyelination inhibits remyelination in the central nervous system. An analysis of contributing factors. *Lab Invest,* 43**,** 382-7.

LUNN, M. P., CRAWFORD, T. O., HUGHES, R. A., GRIFFIN, J. W. & SHEIKH, K. A. (2002) Anti-myelin-associated glycoprotein antibodies alter neurofilament spacing. *Brain,* 125**,** 904-11.

MACKLIN, W. B., CAMPAGNONI, C. W., DEININGER, P. L. & GARDINIER, M. V. (1987) Structure and expression of the mouse myelin proteolipid protein gene. *J Neurosci Res,* 18**,** 383-94.

MAHAD, D., ZIABREVA, I., LASSMANN, H. & TURNBULL, D. (2008) Mitochondrial defects in acute multiple sclerosis lesions. *Brain,* 131**,** 1722-35.

MAHAD, D. J., ZIABREVA, I., CAMPBELL, G., LAX, N., WHITE, K., HANSON, P. S., LASSMANN, H. & TURNBULL, D. M. (2009) Mitochondrial changes within axons in multiple sclerosis. *Brain,* 132**,** 1161-74.

MANGANAS, L. N., AKHTAR, S., ANTONUCCI, D. E., CAMPOMANES, C. R., DOLLY, J. O. & TRIMMER, J. S. (2001) Episodic ataxia type-1 mutations in the Kv1.1 potassium channel display distinct folding and intracellular trafficking properties. *J Biol Chem,* 276**,** 49427-34.

MARTIN, R., MCFARLAND, H. F. & MCFARLIN, D. E. (1992) Immunological aspects of demyelinating diseases. *Annu Rev Immunol,* 10**,** 153-87.

MASON, J. L., LANGAMAN, C., MORELL, P., SUZUKI, K. & MATSUSHIMA, G. K. (2001) Episodic demyelination and subsequent remyelination within the murine central nervous system: changes in axonal calibre. *Neuropathol Appl Neurobiol,* 27**,** 50-8.

MATSUSHIMA, G. K. & MORELL, P. (2001) The neurotoxicant, cuprizone, as a model to study demyelination and remyelination in the central nervous system. *Brain Pathol,* 11**,** 107-16.

MCCORMACK, K., CONNOR, J. X., ZHOU, L., HO, L. L., GANETZKY, B., CHIU, S. Y. & MESSING, A. (2002) Genetic analysis of the mammalian K+ channel beta subunit Kvbeta 2 (Kcnab2). *J Biol Chem,* 277**,** 13219-28.

MCDONALD, W. I. & SEARS, T. A. (1970) The effects of experimental demyelination on conduction in the central nervous system. *Brain,* 93**,** 583-98.

MCKEOWN, L., SWANTON, L., ROBINSON, P. & JONES, O. T. (2008) Surface expression and distribution of voltage-gated potassium channels in neurons (Review). *Mol Membr Biol,* 25**,** 332-43.
MCNAMARA, N. M., MUNIZ, Z. M., WILKIN, G. P. & DOLLY, J. O. (1993) Prominent location of a K+ channel containing the alpha subunit Kv 1.2 in the basket cell nerve terminals of rat cerebellum. *Neuroscience,* 57**,** 1039-45.
MEISTER, M. & BERRY, M. J., 2ND (1999) The neural code of the retina. *Neuron,* 22**,** 435-50.
MERRILL, J. E. (2009) In vitro and in vivo pharmacological models to assess demyelination and remyelination. *Neuropsychopharmacology,* 34**,** 55-73.
MERT, T. (2006) Kv1 channels in signal conduction of myelinated nerve fibers. *Rev Neurosci,* 17**,** 369-74.
MICHAELEVSKI, I., KORNGREEN, A. & LOTAN, I. (2007) Interaction of syntaxin with a single Kv1.1 channel: a possible mechanism for modulating neuronal excitability. *Pflugers Arch,* 454**,** 477-94.
MORAN, O. & MATEU, L. (1983) Loosening of paranodal myelin by repetitive propagation of action potentials. *Nature,* 304**,** 344-5.
MUNIZ, Z. M., PARCEJ, D. N. & DOLLY, J. O. (1992) Characterization of monoclonal antibodies against voltage-dependent K+ channels raised using alpha-dendrotoxin acceptors purified from bovine brain. *Biochemistry,* 31**,** 12297-303.
NADON, N. L., MILLER, S., DRAEGER, K. & SALVAGGIO, M. (1997) Myelin proteolipid DM20: evidence for function independent of myelination. *Int J Dev Neurosci,* 15**,** 285-93.
NAIR, A., FREDERICK, T. J. & MILLER, S. D. (2008) Astrocytes in multiple sclerosis: a product of their environment. *Cell Mol Life Sci,* 65**,** 2702-20.
NASHMI, R. & FEHLINGS, M. G. (2001) Mechanisms of axonal dysfunction after spinal cord injury: with an emphasis on the role of voltage-gated potassium channels. *Brain Res Brain Res Rev,* 38**,** 165-91.
NAVE, K. A. (2010a) Myelination and support of axonal integrity by glia. *Nature,* 468**,** 244-52.
NAVE, K. A. (2010b) Myelination and the trophic support of long axons. *Nat Rev Neurosci,* 11**,** 275-83.
NAVE, K. A., LAI, C., BLOOM, F. E. & MILNER, R. J. (1987) Splice site selection in the proteolipid protein (PLP) gene transcript and primary structure of the DM-20 protein of central nervous system myelin. *Proc Natl Acad Sci U S A,* 84**,** 5665-9.
NORKUTE, A., HIEBLE, A., BRAUN, A., JOHANN, S., CLARNER, T., BAUMGARTNER, W., BEYER, C. & KIPP, M. (2009) Cuprizone treatment induces demyelination and astrocytosis in the mouse hippocampus. *J Neurosci Res,* 87**,** 1343-55.
NORTON, W. T. & PODUSLO, S. E. (1973) Myelination in rat brain: method of myelin isolation. *J Neurochem,* 21**,** 749-57.
O'CONNELL, K. M. & TAMKUN, M. M. (2005) Targeting of voltage-gated potassium channel isoforms to distinct cell surface microdomains. *J Cell Sci,* 118**,** 2155-66.
OGAWA, Y., OSES-PRIETO, J., KIM, M. Y., HORRESH, I., PELES, E., BURLINGAME, A. L., TRIMMER, J. S., MEIJER, D. & RASBAND, M. N.

(2010) ADAM22, a Kv1 channel-interacting protein, recruits membrane-associated guanylate kinases to juxtaparanodes of myelinated axons. *J Neurosci,* 30**,** 1038-48.

ORLOVA, E. V., PAPAKOSTA, M., BOOY, F. P., VAN HEEL, M. & DOLLY, J. O. (2003) Voltage-gated K+ channel from mammalian brain: 3D structure at 18A of the complete (alpha)4(beta)4 complex. *J Mol Biol,* 326**,** 1005-12.

PAPAZIAN, D. M., SCHWARZ, T. L., TEMPEL, B. L., JAN, Y. N. & JAN, L. Y. (1987) Cloning of genomic and complementary DNA from Shaker, a putative potassium channel gene from Drosophila. *Science,* 237**,** 749-53.

PARCEJ, D. N., SCOTT, V. E. & DOLLY, J. O. (1992) Oligomeric properties of alpha-dendrotoxin-sensitive potassium ion channels purified from bovine brain. *Biochemistry,* 31**,** 11084-8.

PARK, K. S., YANG, J. W., SEIKEL, E. & TRIMMER, J. S. (2008) Potassium channel phosphorylation in excitable cells: providing dynamic functional variability to a diverse family of ion channels. *Physiology (Bethesda),* 23**,** 49-57.

PASQUINI, L. A., CALATAYUD, C. A., BERTONE UNA, A. L., MILLET, V., PASQUINI, J. M. & SOTO, E. F. (2007) The neurotoxic effect of cuprizone on oligodendrocytes depends on the presence of pro-inflammatory cytokines secreted by microglia. *Neurochem Res,* 32**,** 279-92.

PATTEN, C. D., CAPRINI, M., PLANELLS-CASES, R. & MONTAL, M. (1999) Structural and functional modularity of voltage-gated potassium channels. *FEBS Lett,* 463**,** 375-81.

PELES, E. & SALZER, J. L. (2000) Molecular domains of myelinated axons. *Curr Opin Neurobiol,* 10**,** 558-65.

PERETZ, A., GIL-HENN, H., SOBKO, A., SHINDER, V., ATTALI, B. & ELSON, A. (2000) Hypomyelination and increased activity of voltage-gated K(+) channels in mice lacking protein tyrosine phosphatase epsilon. *Embo J,* 19**,** 4036-45.

PERGE, J. A., KOCH, K., MILLER, R., STERLING, P. & BALASUBRAMANIAN, V. (2009) How the optic nerve allocates space, energy capacity, and information. *J Neurosci,* 29**,** 7917-28.

PERROT, R., LONCHAMPT, P., PETERSON, A. C. & EYER, J. (2007) Axonal neurofilaments control multiple fiber properties but do not influence structure or spacing of nodes of Ranvier. *J Neurosci,* 27**,** 9573-84.

PIATON, G., GOULD, R. M. & LUBETZKI, C. (2010) Axon-oligodendrocyte interactions during developmental myelination, demyelination and repair. *J Neurochem,* 114**,** 1243-60.

PINTO, L. H. & KLUMPP, D. J. (1998) Localization of potassium channels in the retina. *Prog Retin Eye Res,* 17**,** 207-30.

PITT, D., WERNER, P. & RAINE, C. S. (2000) Glutamate excitotoxicity in a model of multiple sclerosis. *Nat Med,* 6**,** 67-70.

PLANT, L. D., DOWDELL, E. J., DEMENTIEVA, I. S., MARKS, J. D. & GOLDSTEIN, S. A. (2011) SUMO modification of cell surface Kv2.1 potassium channels regulates the activity of rat hippocampal neurons. *J Gen Physiol,* 137**,** 441-54.

POLIAK, S., GOLLAN, L., SALOMON, D., BERGLUND, E. O., OHARA, R., RANSCHT, B. & PELES, E. (2001) Localization of Caspr2 in myelinated nerves depends on axon-glia interactions and the generation of barriers along the axon. *J Neurosci,* 21**,** 7568-75.

PONGS, O. (1992) Molecular biology of voltage-dependent potassium channels. *Physiol Rev,* 72**,** S69-88.

PONGS, O., KECSKEMETHY, N., MULLER, R., KRAH-JENTGENS, I., BAUMANN, A., KILTZ, H. H., CANAL, I., LLAMAZARES, S. & FERRUS, A. (1988) Shaker encodes a family of putative potassium channel proteins in the nervous system of Drosophila. *Embo J,* 7**,** 1087-96.

POTT, F., GINGELE, S., CLARNER, T., DANG, J., BAUMGARTNER, W., BEYER, C. & KIPP, M. (2009) Cuprizone effect on myelination, astrogliosis and microglia attraction in the mouse basal ganglia. *Brain Res,* 1305**,** 137-49.

PRINEAS, J. W. & WRIGHT, R. G. (1978) Macrophages, lymphocytes, and plasma cells in the perivascular compartment in chronic multiple sclerosis. *Lab Invest,* 38**,** 409-21.

PUGLIATTI, M., ROSATI, G., CARTON, H., RIISE, T., DRULOVIC, J., VECSEI, L. & MILANOV, I. (2006) The epidemiology of multiple sclerosis in Europe. *Eur J Neurol,* 13**,** 700-22.

RANSDELL, J. L., NAIR, S. S. & SCHULZ, D. J. (2012) Rapid homeostatic plasticity of intrinsic excitability in a central pattern generator network stabilizes functional neural network output. *J Neurosci,* 32**,** 9649-58.

RANSOHOFF, R. M. (2012) Animal models of multiple sclerosis: the good, the bad and the bottom line. *Nat Neurosci,* 15**,** 1074-7.

RASBAND, M. N. (2004) It's "juxta" potassium channel! *J Neurosci Res,* 76**,** 749-57.

RASBAND, M. N., PELES, E., TRIMMER, J. S., LEVINSON, S. R., LUX, S. E. & SHRAGER, P. (1999a) Dependence of nodal sodium channel clustering on paranodal axoglial contact in the developing CNS. *J Neurosci,* 19**,** 7516-28.

RASBAND, M. N. & SHRAGER, P. (2000) Ion channel sequestration in central nervous system axons. *J Physiol,* 525 Pt 1**,** 63-73.

RASBAND, M. N., TRIMMER, J. S., PELES, E., LEVINSON, S. R. & SHRAGER, P. (1999b) K+ channel distribution and clustering in developing and hypomyelinated axons of the optic nerve. *J Neurocytol,* 28**,** 319-31.

RASH, J. E. (2010) Molecular disruptions of the panglial syncytium block potassium siphoning and axonal saltatory conduction: pertinence to neuromyelitis optica and other demyelinating diseases of the central nervous system. *Neuroscience,* 168**,** 982-1008.

RETTIG, J., HEINEMANN, S. H., WUNDER, F., LORRA, C., PARCEJ, D. N., DOLLY, J. O. & PONGS, O. (1994) Inactivation properties of voltage-gated K+ channels altered by presence of beta-subunit. *Nature,* 369**,** 289-94.

ROBERTSON, B., OWEN, D., STOW, J., BUTLER, C. & NEWLAND, C. (1996) Novel effects of dendrotoxin homologues on subtypes of mammalian Kv1 potassium channels expressed in Xenopus oocytes. *FEBS Lett,* 383**,** 26-30.

RONCAGLIOLO, M., SCHLAGETER, C., LEON, C., COUVE, E., BONANSCO, C. & EGUIBAR, J. R. (2006) Developmental impairment of compound action potential in the optic nerve of myelin mutant taiep rats. *Brain Res,* 1067**,** 78-84.

ROSENBLUTH, J. (1995) *Glial membranes and axonal junctions. In "Neuroglia"* Oxford University Press, New York.

RUPPERSBERG, J. P., FRANK, R., PONGS, O. & STOCKER, M. (1991) Cloned neuronal IK(A) channels reopen during recovery from inactivation. *Nature,* 353**,** 657-60.

RUSHTON, W. A. (1951) A theory of the effects of fibre size in medullated nerve. *J Physiol,* 115**,** 101-22.

RUSHTON, W. A. H. (1937) Initiation of the propagated disturbance. *Proc. R.Soc..Lond. Series B,* 124**,** 210-243.

SAHER, G., BRUGGER, B., LAPPE-SIEFKE, C., MOBIUS, W., TOZAWA, R., WEHR, M. C., WIELAND, F., ISHIBASHI, S. & NAVE, K. A. (2005) High cholesterol level is essential for myelin membrane growth. *Nat Neurosci,* 8**,** 468-75.

SALZER, J., SVENNINGSSON, A. & SUNDSTROM, P. (2010) Neurofilament light as a prognostic marker in multiple sclerosis. *Mult Scler,* 16**,** 287-92.

SCHIRMER, L., ANTEL, J. P., BRUCK, W. & STADELMANN, C. (2011) Axonal loss and neurofilament phosphorylation changes accompany lesion development and clinical progression in multiple sclerosis. *Brain Pathol,* 21**,** 428-40.

SCHMANDT, T., GOBRAU, G., KISCHLAT, T. & OPTIZ, T. (2006) Animal models for cell and gene therapy in myelin disease. *Drug Discov Today,* 3**,** 349-358.

SCHMIDT, K., EULITZ, D., VEH, R. W., KETTENMANN, H. & KIRCHHOFF, F. (1999) Heterogeneous expression of voltage-gated potassium channels of the shaker family (Kv1) in oligodendrocyte progenitors. *Brain Res,* 843**,** 145-60.

SCHNAPP, B. & MUGNAINI, E. (1978) Membrane architecture of myelinated fibres as seen by freeze-fracture. In "Physiology and Pathobiology of Axons" 83-123.

SCHULTE, U., THUMFART, J. O., KLOCKER, N., SAILER, C. A., BILDL, W., BINIOSSEK, M., DEHN, D., DELLER, T., EBLE, S., ABBASS, K., WANGLER, T., KNAUS, H. G. & FAKLER, B. (2006) The epilepsy-linked Lgi1 protein assembles into presynaptic Kv1 channels and inhibits inactivation by Kvbeta1. *Neuron,* 49**,** 697-706.

SCOTT, V. E., MUNIZ, Z. M., SEWING, S., LICHTINGHAGEN, R., PARCEJ, D. N., PONGS, O. & DOLLY, J. O. (1994a) Antibodies specific for distinct Kv subunits unveil a heterooligomeric basis for subtypes of alpha-dendrotoxin-sensitive K+ channels in bovine brain. *Biochemistry,* 33**,** 1617-23.

SCOTT, V. E., PARCEJ, D. N., KEEN, J. N., FINDLAY, J. B. & DOLLY, J. O. (1990) Alpha-dendrotoxin acceptor from bovine brain is a K+ channel protein. Evidence from the N-terminal sequence of its larger subunit. *J Biol Chem,* 265**,** 20094-7.

SCOTT, V. E., RETTIG, J., PARCEJ, D. N., KEEN, J. N., FINDLAY, J. B., PONGS, O. & DOLLY, J. O. (1994b) Primary structure of a beta subunit of alpha-dendrotoxin-sensitive K+ channels from bovine brain. *Proc Natl Acad Sci U S A,* 91**,** 1637-41.

SHAFEY, D., BOYER, J. G., BHANOT, K. & KOTHARY, R. (2010) Identification of novel interacting protein partners of SMN using tandem affinity purification. *J Proteome Res,* 9**,** 1659-69.

SHAMOTIENKO, O., AKHTAR, S., SIDERA, C., MEUNIER, F. A., INK, B., WEIR, M. & DOLLY, J. O. (1999) Recreation of neuronal Kv1 channel oligomers by expression in mammalian cells using Semliki Forest virus. *Biochemistry,* 38**,** 16766-76.

SHAMOTIENKO, O. G., PARCEJ, D. N. & DOLLY, J. O. (1997) Subunit combinations defined for K+ channel Kv1 subtypes in synaptic membranes from bovine brain. *Biochemistry,* 36**,** 8195-201.

SHEN, N. V., CHEN, X., BOYER, M. M. & PFAFFINGER, P. J. (1993) Deletion analysis of K+ channel assembly. *Neuron,* 11**,** 67-76.

SHERRATT, R. M., BOSTOCK, H. & SEARS, T. A. (1980) Effects of 4-aminopyridine on normal and demyelinated mammalian nerve fibres. *Nature,* 283**,** 570-2.

SHI, G., NAKAHIRA, K., HAMMOND, S., RHODES, K. J., SCHECHTER, L. E. & TRIMMER, J. S. (1996) Beta subunits promote K+ channel surface expression through effects early in biosynthesis. *Neuron,* 16**,** 843-52.

SHIELDS, S. A., BLAKEMORE, W. F. & FRANKLIN, R. J. (2000) Schwann cell remyelination is restricted to astrocyte-deficient areas after transplantation into demyelinated adult rat brain. *J Neurosci Res,* 60**,** 571-8.

SHIELDS, S. D., CHENG, X., GASSER, A., SAAB, C. Y., TYRRELL, L., EASTMAN, E. M., IWATA, M., ZWINGER, P. J., BLACK, J. A., DIB-HAJJ, S. D. & WAXMAN, S. G. (2012) A channelopathy contributes to cerebellar dysfunction in a model of multiple sclerosis. *Ann Neurol,* 71**,** 186-94.

SHRAGER, P. (1993) Axonal coding of action potentials in demyelinated nerve fibers. *Brain Res,* 619**,** 278-90.

SIEGEL, R. W. A. (2005) *Basic Neurochemistry: molecular, cellular, and medical aspects*.

SINGER-LAHAT, D., DASCAL, N. & LOTAN, I. (1999) Modal behavior of the Kv1.1 channel conferred by the Kvbeta1.1 subunit and its regulation by dephosphorylation of Kv1.1. *Pflugers Arch,* 439**,** 18-26.

SKRIPULETZ, T., HACKSTETTE, D., BAUER, K., GUDI, V., PUL, R., VOSS, E., BERGER, K., KIPP, M., BAUMGARTNER, W. & STANGEL, M. (2013) Astrocytes regulate myelin clearance through recruitment of microglia during cuprizone-induced demyelination. *Brain,* 136**,** 147-67.

SMART, S. L., LOPANTSEV, V., ZHANG, C. L., ROBBINS, C. A., WANG, H., CHIU, S. Y., SCHWARTZKROIN, P. A., MESSING, A. & TEMPEL, B. L. (1998) Deletion of the K(V)1.1 potassium channel causes epilepsy in mice. *Neuron,* 20**,** 809-19.

SMITH, K. J. (2007) Sodium channels and multiple sclerosis: roles in symptom production, damage and therapy. *Brain Pathol,* 17**,** 230-42.

SMITH, K. J. (2011) Newly lesioned tissue in multiple sclerosis--a role for oxidative damage? *Brain,* 134**,** 1877-81.

SMITH, K. J., FELTS, P. A. & JOHN, G. R. (2000) Effects of 4-aminopyridine on demyelinated axons, synapses and muscle tension. *Brain,* 123 (Pt 1)**,** 171-84.

SMITH, K. J. & HALL, S. M. (2001) Factors directly affecting impulse transmission in inflammatory demyelinating disease: recent advances in our understanding. *Curr Opin Neurol,* 14**,** 289-98.

SMITH, K. J. & MCDONALD, W. I. (1999) The pathophysiology of multiple sclerosis: the mechanisms underlying the production of symptoms and the natural history of the disease. *Philos Trans R Soc Lond B Biol Sci,* 354**,** 1649-73.

SOBKO, A., PERETZ, A., SHIRIHAI, O., ETKIN, S., CHEREPANOVA, V., DAGAN, D. & ATTALI, B. (1998) Heteromultimeric delayed-rectifier K+ channels in schwann

cells: developmental expression and role in cell proliferation. *J Neurosci,* 18**,** 10398-408.

SODERSTROM, M. (2001) Optic neuritis and multiple sclerosis. *Acta Ophthalmol Scand,* 79**,** 223-7.

SOKOLOV, M. V., SHAMOTIENKO, O., DHOCHARTAIGH, S. N., SACK, J. T. & DOLLY, J. O. (2007) Concatemers of brain Kv1 channel alpha subunits that give similar K+ currents yield pharmacologically distinguishable heteromers. *Neuropharmacology,* 53**,** 272-82.

SONG, S. K., SUN, S. W., RAMSBOTTOM, M. J., CHANG, C., RUSSELL, J. & CROSS, A. H. (2002) Dysmyelination revealed through MRI as increased radial (but unchanged axial) diffusion of water. *Neuroimage,* 17**,** 1429-36.

SPERBER, B. R., BOYLE-WALSH, E. A., ENGLEKA, M. J., GADUE, P., PETERSON, A. C., STEIN, P. L., SCHERER, S. S. & MCMORRIS, F. A. (2001) A unique role for Fyn in CNS myelination. *J Neurosci,* 21**,** 2039-47.

SQUIRE, L. R., DARWIN BERG, FLOYD E. BLOOM, SASCHA DU LAC, ANIRVAN GHOSH & SPITZER, N. C. (2008) *Fundamental Neuroscience*, Elsevier

STEFOSKI, D., DAVIS, F. A., FAUT, M. & SCHAUF, C. L. (1987) 4-Aminopyridine improves clinical signs in multiple sclerosis. *Ann Neurol,* 21**,** 71-7.

STIDWORTHY, M. F., GENOUD, S., SUTER, U., MANTEI, N. & FRANKLIN, R. J. (2003) Quantifying the early stages of remyelination following cuprizone-induced demyelination. *Brain Pathol,* 13**,** 329-39.

STYS, P. K. (1998) Anoxic and ischemic injury of myelinated axons in CNS white matter: from mechanistic concepts to therapeutics. *J Cereb Blood Flow Metab,* 18**,** 2-25.

STYS, P. K. (2004) White matter injury mechanisms. *Curr Mol Med,* 4**,** 113-30.

SUN, S. W., LIANG, H. F., TRINKAUS, K., CROSS, A. H., ARMSTRONG, R. C. & SONG, S. K. (2006) Noninvasive detection of cuprizone induced axonal damage and demyelination in the mouse corpus callosum. *Magn Reson Med,* 55**,** 302-8.

SUSUKI, K. & RASBAND, M. N. (2008) Molecular mechanisms of node of Ranvier formation. *Curr Opin Cell Biol,* 20**,** 616-23.

SUZUKI, K. (1969) Giant hepatic mitochondria: production in mice fed with cuprizone. *Science,* 163**,** 81-2.

SUZUKI, K. & KIKKAWA, Y. (1969) Status spongiosus of CNS and hepatic changes induced by cuprizone (biscyclohexanone oxalyldihydrazone). *Am J Pathol,* 54**,** 307-25.

SWARTZ, K. J. (2004) Towards a structural view of gating in potassium channels. *Nat Rev Neurosci,* 5**,** 905-16.

TASAKI, I. (1953) *Nervous Transmission* Charles C. Thomas, Springfield,IL.

TEMPEL, B. L., JAN, Y. N. & JAN, L. Y. (1988) Cloning of a probable potassium channel gene from mouse brain. *Nature,* 332**,** 837-9.

TOMLINSON, D. R. & GARDINER, N. J. (2008) Glucose neurotoxicity. *Nat Rev Neurosci,* 9**,** 36-45.

TRAPP, B. D. & NAVE, K. A. (2008) Multiple sclerosis: an immune or neurodegenerative disorder? *Annu Rev Neurosci,* 31**,** 247-69.

TRAPP, B. D., PETERSON, J., RANSOHOFF, R. M., RUDICK, R., MORK, S. & BO, L. (1998) Axonal transection in the lesions of multiple sclerosis. *N Engl J Med,* 338**,** 278-85.

TRAPP, B. D. & STYS, P. K. (2009) Virtual hypoxia and chronic necrosis of demyelinated axons in multiple sclerosis. *Lancet Neurol,* 8**,** 280-91.

TRIFILIEFF, P., RIVES, M. L., URIZAR, E., PISKOROWSKI, R. A., VISHWASRAO, H. D., CASTRILLON, J., SCHMAUSS, C., SLATTMAN, M., GULLBERG, M. & JAVITCH, J. A. (2011) Detection of antigen interactions ex vivo by proximity ligation assay: endogenous dopamine D2-adenosine A2A receptor complexes in the striatum. *Biotechniques,* 51**,** 111-8.

TSUDA, M., TASHIRO, T. & KOMIYA, Y. (2000) Selective solubilization of high-molecular-mass neurofilament subunit during nerve regeneration. *J Neurochem,* 74**,** 860-8.

UTSUNOMIYA, I., YOSHIHASHI, E., TANABE, S., NAKATANI, Y., IKEJIMA, H., MIYATAKE, T., HOSHI, K. & TAGUCHI, K. (2008) Expression and localization of Kv1 potassium channels in rat dorsal and ventral spinal roots. *Exp Neurol,* 210**,** 51-8.

VABNICK, I., TRIMMER, J. S., SCHWARZ, T. L., LEVINSON, S. R., RISAL, D. & SHRAGER, P. (1999) Dynamic potassium channel distributions during axonal development prevent aberrant firing patterns. *J Neurosci,* 19**,** 747-58.

VELUMIAN, A. A., WAN, Y., SAMOILOVA, M. & FEHLINGS, M. G. (2010) Contribution of fast and slow conducting myelinated axons to single-peak compound action potentials in rat spinal cord white matter preparations. *J Neurophysiol,* 105**,** 929-41.

VENTER, J. C., ADAMS, M. D., MYERS, E. W., LI, P. W., MURAL, R. J., SUTTON, G. G., SMITH, H. O., YANDELL, M., EVANS, C. A., HOLT, R. A., GOCAYNE, J. D., AMANATIDES, P., BALLEW, R. M., HUSON, D. H., WORTMAN, J. R., ZHANG, Q., KODIRA, C. D., ZHENG, X. H., CHEN, L., SKUPSKI, M., SUBRAMANIAN, G., THOMAS, P. D., ZHANG, J., GABOR MIKLOS, G. L., NELSON, C., BRODER, S., CLARK, A. G., NADEAU, J., MCKUSICK, V. A., ZINDER, N., LEVINE, A. J., ROBERTS, R. J., SIMON, M., SLAYMAN, C., HUNKAPILLER, M., BOLANOS, R., DELCHER, A., DEW, I., FASULO, D., FLANIGAN, M., FLOREA, L., HALPERN, A., HANNENHALLI, S., KRAVITZ, S., LEVY, S., MOBARRY, C., REINERT, K., REMINGTON, K., ABU-THREIDEH, J., BEASLEY, E., BIDDICK, K., BONAZZI, V., BRANDON, R., CARGILL, M., CHANDRAMOULISWARAN, I., CHARLAB, R., CHATURVEDI, K., DENG, Z., DI FRANCESCO, V., DUNN, P., EILBECK, K., EVANGELISTA, C., GABRIELIAN, A. E., GAN, W., GE, W., GONG, F., GU, Z., GUAN, P., HEIMAN, T. J., HIGGINS, M. E., JI, R. R., KE, Z., KETCHUM, K. A., LAI, Z., LEI, Y., LI, Z., LI, J., LIANG, Y., LIN, X., LU, F., MERKULOV, G. V., MILSHINA, N., MOORE, H. M., NAIK, A. K., NARAYAN, V. A., NEELAM, B., NUSSKERN, D., RUSCH, D. B., SALZBERG, S., SHAO, W., SHUE, B., SUN, J., WANG, Z., WANG, A., WANG, X., WANG, J., WEI, M., WIDES, R., XIAO, C., YAN, C., et al. (2001) The sequence of the human genome. *Science,* 291**,** 1304-51.

VENTURINI, G. (1973) Enzymic activities and sodium, potassium and copper concentrations in mouse brain and liver after cuprizone treatment in vivo. *J Neurochem,* 21**,** 1147-51.

VERCELLINO, M., MASERA, S., LORENZATTI, M., CONDELLO, C., MEROLA, A., MATTIODA, A., TRIBOLO, A., CAPELLO, E., MANCARDI, G. L., MUTANI,

R., GIORDANA, M. T. & CAVALLA, P. (2009) Demyelination, inflammation, and neurodegeneration in multiple sclerosis deep gray matter. *J Neuropathol Exp Neurol,* 68**,** 489-502.

VICARIO-ABEJÓN, C. (2004) *Long Term Culture of Hippocampal Neurons*, Wiley Online Library.

WACKER, S. J., JURKOWSKI, W., SIMMONS, K. J., FISHWICK, C. W., JOHNSON, A. P., MADGE, D., LINDAHL, E., ROLLAND, J. F. & DE GROOT, B. L. (2012) Identification of Selective Inhibitors of the Potassium Channel Kv1.1-1.2((3)) by High-Throughput Virtual Screening and Automated Patch Clamp. *ChemMedChem.*

WALZ, W. (2000) Role of astrocytes in the clearance of excess extracellular potassium. *Neurochem Int,* 36**,** 291-300.

WANG, F. C., PARCEJ, D. N. & DOLLY, J. O. (1999) alpha subunit compositions of Kv1.1-containing K+ channel subtypes fractionated from rat brain using dendrotoxins. *Eur J Biochem,* 263**,** 230-7.

WANG, H., ALLEN, M. L., GRIGG, J. J., NOEBELS, J. L. & TEMPEL, B. L. (1995) Hypomyelination alters K+ channel expression in mouse mutants shiverer and Trembler. *Neuron,* 15**,** 1337-47.

WANG, H., KUNKEL, D. D., MARTIN, T. M., SCHWARTZKROIN, P. A. & TEMPEL, B. L. (1993) Heteromultimeric K+ channels in terminal and juxtaparanodal regions of neurons. *Nature,* 365**,** 75-9.

WANG, H., KUNKEL, D. D., SCHWARTZKROIN, P. A. & TEMPEL, B. L. (1994) Localization of Kv1.1 and Kv1.2, two K channel proteins, to synaptic terminals, somata, and dendrites in the mouse brain. *J Neurosci,* 14**,** 4588-99.

WAXMAN, S. G. (2005) *Multiple Sclerosis as a Neuronal Disease*, Elsevier.

WAXMAN, S. G. (2006) Axonal conduction and injury in multiple sclerosis: the role of sodium channels. *Nat Rev Neurosci,* 7**,** 932-41.

WESTENBROEK, R. E., NOEBELS, J. L. & CATTERALL, W. A. (1992) Elevated expression of type II Na+ channels in hypomyelinated axons of shiverer mouse brain. *J Neurosci,* 12**,** 2259-67.

WHEELER, D., BANDARU, V. V., CALABRESI, P. A., NATH, A. & HAUGHEY, N. J. (2008) A defect of sphingolipid metabolism modifies the properties of normal appearing white matter in multiple sclerosis. *Brain,* 131**,** 3092-102.

WHITE, J. A., MCALPINE, P. J., ANTONARAKIS, S., CANN, H., EPPIG, J. T., FRAZER, K., FREZAL, J., LANCET, D., NAHMIAS, J., PEARSON, P., PETERS, J., SCOTT, A., SCOTT, H., SPURR, N., TALBOT, C., JR. & POVEY, S. (1997) Guidelines for human gene nomenclature (1997). HUGO Nomenclature Committee. *Genomics,* 45**,** 468-71.

WICKENDEN, A. (2002) K(+) channels as therapeutic drug targets. *Pharmacol Ther,* 94**,** 157-82.

WISSMANN, R., BILDL, W., OLIVER, D., BEYERMANN, M., KALBITZER, H. R., BENTROP, D. & FAKLER, B. (2003) Solution structure and function of the "tandem inactivation domain" of the neuronal A-type potassium channel Kv1.4. *J Biol Chem,* 278**,** 16142-50.

WU, C. Y., KAUR, C., SIVAKUMAR, V., LU, J. & LING, E. A. (2009) Kv1.1 expression in microglia regulates production and release of proinflammatory cytokines, endothelins and nitric oxide. *Neuroscience,* 158**,** 1500-8.

WULFF, H., CASTLE, N. A. & PARDO, L. A. (2009) Voltage-gated potassium channels as therapeutic targets. *Nat Rev Drug Discov,* 8**,** 982-1001.

WYMORE, R. S., KORENBERG, J. R., KINOSHITA, K. D., AIYAR, J., COYNE, C., CHEN, X. N., HUSTAD, C. M., COPELAND, N. G., GUTMAN, G. A., JENKINS, N. A. & ET AL. (1994) Genomic organization, nucleotide sequence, biophysical properties, and localization of the voltage-gated K+ channel gene KCNA4/Kv1.4 to mouse chromosome 2/human 11p14 and mapping of KCNC1/Kv3.1 to mouse 7/human 11p14.3-p15.2 and KCNA1/Kv1.1 to human 12p13. *Genomics,* 20**,** 191-202.

WYMORE, R. S., NEGULESCU, D., KINOSHITA, K., KALMAN, K., AIYAR, J., GUTMAN, G. A. & CHANDY, K. G. (1996) Characterization of the transcription unit of mouse Kv1.4, a voltage-gated potassium channel gene. *J Biol Chem,* 271**,** 15629-34.

XU, Z., CORK, L. C., GRIFFIN, J. W. & CLEVELAND, D. W. (1993) Increased expression of neurofilament subunit NF-L produces morphological alterations that resemble the pathology of human motor neuron disease. *Cell,* 73**,** 23-33.

XU, Z., MARSZALEK, J. R., LEE, M. K., WONG, P. C., FOLMER, J., CRAWFORD, T. O., HSIEH, S. T., GRIFFIN, J. W. & CLEVELAND, D. W. (1996) Subunit composition of neurofilaments specifies axonal diameter. *J Cell Biol,* 133**,** 1061-9.

YABE, J. T., JUNG, C., CHAN, W. K. & SHEA, T. B. (2000) Phospho-dependent association of neurofilament proteins with kinesin in situ. *Cell Motil Cytoskeleton,* 45**,** 249-62.

YANG, J. W., VACHER, H., PARK, K. S., CLARK, E. & TRIMMER, J. S. (2007a) Trafficking-dependent phosphorylation of Kv1.2 regulates voltage-gated potassium channel cell surface expression. *Proc Natl Acad Sci U S A,* 104**,** 20055-60.

YANG, L., FUNG, C. W., CHO, E. J. & ELLINGTON, A. D. (2007b) Real-time rolling circle amplification for protein detection. *Anal Chem,* 79**,** 3320-9.

YANG, Q., CHEN, S. R., LI, D. P. & PAN, H. L. (2007c) Kv1.1/1.2 channels are downstream effectors of nitric oxide on synaptic GABA release to preautonomic neurons in the paraventricular nucleus. *Neuroscience,* 149**,** 315-27.

YELLEN, G., SODICKSON, D., CHEN, T. Y. & JURMAN, M. E. (1994) An engineered cysteine in the external mouth of a K+ channel allows inactivation to be modulated by metal binding. *Biophys J,* 66**,** 1068-75.

YIN, X., CRAWFORD, T. O., GRIFFIN, J. W., TU, P., LEE, V. M., LI, C., RODER, J. & TRAPP, B. D. (1998) Myelin-associated glycoprotein is a myelin signal that modulates the caliber of myelinated axons. *J Neurosci,* 18**,** 1953-62.

ZHOU, L., ZHANG, C. L., MESSING, A. & CHIU, S. Y. (1998) Temperature-sensitive neuromuscular transmission in Kv1.1 null mice: role of potassium channels under the myelin sheath in young nerves. *J Neurosci,* 18**,** 7200-15.

ZHU, J., GOMEZ, B., WATANABE, I. & THORNHILL, W. B. (2007) Kv1 potassium channel C-terminus constant HRETE region: arginine substitution affects surface protein level and conductance level of subfamily members differentially. *Mol Membr Biol,* 24**,** 194-205.

ZHU, J., WATANABE, I., GOMEZ, B. & THORNHILL, W. B. (2003) Heteromeric Kv1 potassium channel expression: amino acid determinants involved in processing and trafficking to the cell surface. *J Biol Chem,* 278**,** 25558-67.